N° d'ordre : 09 ISAL 0069 **Année 2009**

THESE

Présentée devant

(INSTITUT NATIONAL DES SCIENCES APPLIQUEES DE LYON)

Pour obtenir

LE GRADE DE DOCTEUR

Ecole Doctorale des Sciences de l'Ingénieur de Lyon:

Mécanique, Energétique, Génie civil, Acoustique (MEGA)

Spécialité:

MECANIQUE – GENIE MECANIQUE – GENIE CIVIL

Par

Muhammad Zain-ul-abdein

EXPERIMENTAL INVESTIGATION AND NUMERICAL SIMULATION OF LASER BEAM WELDING INDUCED RESIDUAL STRESSES AND DISTORTIONS IN AA 6056-T4 SHEETS FOR AERONAUTIC APPLICATION

Thèse soutenue le 30 septembre 2009 devant la commission d'examen

Jury :

Jean-Michel BERGHEAU	Professeur (ENISE – LTDS)	Rapporteur
John BOUCHARD	Professeur (The Open University UK)	Rapporteur
Dominique DELOISON	Expert Materials Simulation (EADS)	Examinateur
Philippe GILLES	Expert International (AREVA)	Examinateur
Bertrand JOURNET	Expert Senior (EADS)	Examinateur
Michel CORET	Maître de Conf. (INSA-Lyon)	Examinateur
Daniel NELIAS	Professeur (INSA-Lyon)	Directeur
Jean-François JULLIEN	Professeur (INSA-Lyon)	Directeur

LaMCoS, INSA-Lyon, CNRS UMR5259, F69621.
(Laboratoire de Mécanique des Contacts et des Structures)
20, Av. Albert Einstein, 69621 Villeurbanne Cedex, France.

To home,

Pakistan

ACKNOWLEDGMENTS

I would like to express my deepest gratitude to the project directors Prof. Daniel Nélias and Prof. Jean-François Jullien for their support, contribution and enthusiasm for this work. Had it not been their consistent help and valuable guidance, none of this would have been possible.

I owe my sincere thanks to Mr. Dominique Deloison and Dr. Frédéric Boitout for their expert opinions, extended cooperation and fruitful suggestions in making this thesis a success.

I am also extremely grateful to Prof. Jean-Michel Bergheau and Prof. John Bouchard for accepting to be the Reviewers and dedicating their valuable time for this dissertation. I would express my appreciation for Mr. Philippe Gilles, Mr. Bertrand Journet and Dr. Michel Coret who took interest in evaluating this work.

I would like to express my indebtedness to Dr. Patrice Clerk, Dr. Fabrice Morestin, Dr. Tarek Mabrouki, Mr. Philippe Chaudet, Mr. Daniel Maisonnette, Dr. Yannick Vincent, Mr. Emmanuel Josserand, Mr. Luc Dishert and Mr. Xavier Noe for their willingness to share their knowledge and extending their assistance in performing experimental and numerical tasks.

I would like to acknowledge the financial support provided by EADS, AREVA-NP, EDF-SEPTEN, ESI Group and Rhône-Alpes Région through the research program INZAT4. I would also like to acknowledge the financial assistance provided by Higher Education Commission (HEC) of Pakistan in collaboration with Government of France through an Overseas Research Scholarship Program.

Finally, I would like to take this opportunity to express my heartfelt thanks to my parents, for their utmost love and constant encouragement. Special thanks to my wife, for her unremitting support, friendship and understanding during this time. Love for my son Abdullah.

Résumé

La fabrication des panneaux de fuselage des structures aéronautiques par soudage laser comporte un double avantage sur le rivetage conventionnel. Premièrement, la réduction de poids, car il n'est plus nécessaire d'ajouter de la matière pour les rivets et le chevauchement des plaques; et, deuxièmement, le gain de temps, car le procédé de soudage est très rapide. Cependant, des inconvénients tels que les distorsions et les contraintes résiduelles sont des conséquences inévitables de la soudure. Ces panneaux de fuselage sont soudés à des raidisseurs dans une configuration de joints en « T » et la longueur typique de soudure des joints atteint plusieurs mètres.

Ce travail se concentre sur les mesures expérimentales et les simulations numériques des contraintes résiduelles et des distorsions induites par le soudage laser utilisant les conditions aux limites mécaniques et thermiques, appliquées dans le milieu industriel sur des plaques minces d'un alliage d'aluminium AA 6056-T4. Plusieurs expériences de petites échelles ont été réalisées avec différents instruments, comme des thermocouples et des capteurs LVDT qui ont été utilisés pour enregistrer, respectivement, les températures et les déplacements pendant le soudage. La caméra infrarouge a été aussi utilisée pour qualifier l'évolution de la température de bain fondu en fonction du temps. Les mesures de déplacements dans le plan et hors-plan ont été obtenues par stéréo-corrélation d'images. Une micrographie a été réalisée pour mesurer les dimensions de la zone de fusion. La base de données ainsi préparée a servi de point de référence pour la validation des résultats de simulation numérique. La caractérisation thermomécanique du 6056-T4 est également effectuée pour identifier les propriétés des matériaux à utiliser lors de la simulation numérique.

Les simulations par éléments finis sont effectuées avec le logiciel commercial Abaqus et les modèles de source de chaleur volumétrique avec distribution Gaussienne du flux sont programmés en Fortran. Les conditions aux limites thermiques et mécaniques utilisées dans l'industrie sont intégrées aux modèles. Les analyses thermiques sont effectuées en premier pour atteindre la géométrie de zone de fusion et les champs de température souhaitées. Les analyses mécaniques sont effectuées ensuite pour prédire la déformation et l'état de contraintes résiduelles. La loi de comportement du matériau est considérée élasto-plastique / élasto-viscoplastique avec écrouissage isotrope (modèle de plasticité de von Mises). Les analyses comparatives entre les résultats expérimentaux et les simulations présentent une bonne concordance des valeurs. Enfin, les états de contraintes et déformations résiduelles sont évaluées par calcul.

Mots-Clés: soudage laser, AA 6056-T4, caractérisation de matériau, simulation par éléments finis, analyse thermique, analyse mécanique, modèle de source de chaleur, distorsions, déplacement hors plan, contrainte résiduelle, déformation plastique.

Abstract

Fabricating the fuselage panels of aircraft structures with laser beam welding has a two-fold advantage over conventional riveting. First, the weight reduction, since the material to be added as rivets and the sheets overlap is no more required; and second, the time saving, as welding process is very fast. However, the inconveniences like distortions and residual stresses are inevitable consequences of welding. These fuselage panels are welded with stringers in a T-joint configuration and the typical length of weld joints reach several meters.

The effort is made in this work to experimentally measure and numerically simulate the residual stresses and distortions induced by laser beam welding with industrially used thermal and mechanical boundary conditions on the thin sheets of an aluminium alloy AA 6056-T4. Several small scale experiments were carried out with various instrumentations like thermocouples and LVDT sensors, which were used to record the temperatures and displacements during welding, respectively. Infra-red camera was also used to qualify the evolution of weld pool temperature as a function of time. Measurements of in-plane and out-of-plane displacements were achieved by stereo image correlation technique. Micrography was carried out to measure the dimensions of fusion zone. The database so prepared served as benchmark for the validation of numerical simulation results. Thermo-mechanical characterisation of 6056-T4 was also performed in order to identify the material properties to be used during numerical simulation.

Finite element (FE) simulations are performed with the commercial FE software Abaqus and the volumetric heat source models with Gaussian distribution of flux are programmed in Fortran. The industrially used thermal and mechanical boundary conditions are integrated in the numerical models. Heat transfer analyses are performed first in order to achieve the required weld pool geometries and temperature fields. Mechanical analyses are performed next so as to predict the distortion and the residual stress state. The material is assumed to follow elasto-plastic and/or elasto-viscoplastic law with isotropic hardening (von Mises plasticity model). The comparative analyses between the experimental and simulation results have shown good agreements. Finally, the residual stress and strain states are evaluated through simulations.

Keywords: laser beam welding, AA 6056-T4, material characterisation, finite element simulation, thermal analysis, mechanical analysis, heat source model, distortions, out-of-plane displacement, residual stress, plastic strain.

CONTENTS

Nomenclature

ρ	Density
C_p	Specific heat capacity
λ	Thermal conductivity
H_e	Enthalpy
Q_i	Internal heat generation rate
$\partial\Omega_q$	Part of the boundary $\partial\Omega$ at which flux is applied
$\partial\Omega_T$	Part of the boundary $\partial\Omega$ at which temperature is imposed
q	Surface density of heat flux
q_{conv}	Surface density of heat flux representing convection
q_{rad}	Surface density of heat flux representing radiation
q_{tcr}	Surface density of heat flux representing thermal contact resistance
T	Temperature
T_p	Temperature imposed
T_0	Ambient/reference temperature
T_{abs}	Absolute zero
T_s	Temperature of the surrounding media
T_{req}	Required temperature
$T_{solidus}$	Solidus temperature
$T_{liquidus}$	Liquidus temperature
σ_{SB}	Stefan-Boltzmann constant
ξ	Emissivity of radiating surface
h_{conv}	Convective heat transfer coefficient of air
$h_{forced\ conv}$	Convective heat transfer coefficient for air suction
h_{tcr}	Heat transfer coefficient due to thermal contact resistance
A_0	Original cross-sectional area
L_0	Original gauge length
F	Force
δ	Displacement
A_i	Instantaneous area
L_i	Instantaneous length
σ_i	Initial residual stress
σ^I	First order residual stress
σ^{II}	Second order residual stress
σ^{III}	Third order residual stress
$\boldsymbol{\sigma}$	Stress tensor
σ_e	Engineering stress
σ_t	True stress
σ_y	Yield strength
σ^{VM}	Von Mises equivalent stress
σ_1, σ_2, σ_3	Principal stresses
σ_{xx}	Longitudinal stress
σ_{yy}	Transverse stress

σ_{zz}	Through-thickness stress
σ_{xy}, σ_{yz}, σ_{zx}	Shear stress components
$\boldsymbol{S}$	Deviatoric stress tensor
J_2	Second deviatoric stress invariant
$\boldsymbol{\varepsilon}$	Strain tensor
ε_e	Engineering strain
ε_t	True strain
ε^e	Elastic strain
ε^{th}	Thermal strain
ε^{in}	Inelastic strain
ε^p	Plastic strain
ε^{vp}	Viscoplastic strain
ε^{pt}	Strain due to transformation plasticity
ε_{xx}	Longitudinal strain
ε_{yy}	Transverse strain
ε_{zz}	Through-thickness strain
ε_{xy}, ε_{yz}, ε_{zx}	Shear strain components
D_e	Elastic domain
$\boldsymbol{\Lambda}$	4^{th} order stiffness tensor
f	Plasticity criterion
E	Young’s modulus
ν	Poisson’s ratio
α	Linear thermal dilatation coefficient
p	Cumulated plastic deformation
R	Isotropic hardening variable
H	Hardening modulus
$\boldsymbol{X}$	Kinematic hardening variable
$\boldsymbol{X}^{\mathrm{d}}$	Deviatoric part of the tensor $\boldsymbol{X}$
C, γ	Kinematic hardening parameters
$\psi(<f>)$	Function of viscosity
n, K, m	Material parameters for viscoplasticity
Q_v	Volumetric heat flux
Q_0	Net heat input
η	Efficiency of welding process
U	Voltage
I	Current
P	Power
Q_c	Volumetric heat flux in cone
r_c	Flux distribution parameter for cone
z_e	z-coordinate of top surface of cone
z_i	z-coordinate of bottom surface of cone
r_e	Radius at the top of cone
r_i	Radius at the bottom of cone
Q_s	Volumetric heat flux in sphere
d_s	Flux distribution parameter for hollow sphere
r_{os}	Outer radius of sphere
r_{is}	Inner radius of sphere

CHAPTER 1

GENERAL INTRODUCTION

Contents

GENERAL INTRODUCTION

Through the course of its evolution, the world has continuously been blessed by the revolutionary and dynamic achievements of science and technology. As far as structural integrity of the manufactured components is concerned, welding engineering is one such domain that has played a decisive role. Starting from the production of simple cola-tin, welding has shown its unending applications in the fields of aircraft manufacturing, ship building, power plant fabrication etc.

The aeronautic industry is in a permanent quest of achieving reduction in weight of aircraft structure. This is accomplished, in the first place, by making use of light weight alloys for the manufacturing and, in the second place, by introducing innovative fabrication techniques. Aluminium alloys have, therefore, found a great deal of applications in the manufacturing of aerospace structures, e.g. fuselage panels are generally manufactured from thin sheets of an aluminium alloy AA 6056-T4 (Al-Mg-Si-Cu). The aeroplanes of series Airbus A3XX, make extensive use of aluminium alloys, particularly of series 2XXX, 6XXX and 7XXX, in their construction. Figures 1.1 and 1.2 show the applications of welded panels for the front and central parts of A3XX.

Figure 1.1. Aluminium alloy structures used in A3XX [DARC][DITJ][ADRT]

Figure 1.2. a. Front, b. Central fuselage panels [DARC][DITJ][ADRT]

Until recently, riveting was being used for the fabrication of fuselage panels with stringers. The advancements in manufacturing processes, however, have successfully replaced riveting with laser beam welding technique (Fig. 1.3). This is because several millions of rivets, which were used to add up an additional amount of weight to an aircraft, are no longer required. Moreover, welding is comparatively a much faster process than riveting. The maximum attainable speed of welding is 10 m/min as compared to 10 cm/min during riveting [DARC]. Nevertheless, accompanied with its blessings, welding always brings some inconveniences like distortions and residual stresses. These distortions and residual stresses are at times so crucial that they may lead to the sudden damage or collapse of the structure. This is why in order to optimize the welding process and / or to introduce pre- and post-heat treatment techniques; the knowledge of stress distribution and distortion pattern is a must. These stresses can be measured with the help of X-ray diffraction, neutron diffraction and hole drilling techniques etc. From practical point of view, however, these techniques are not only difficult to apply directly on the entire aircraft structure but are also quite expensive.

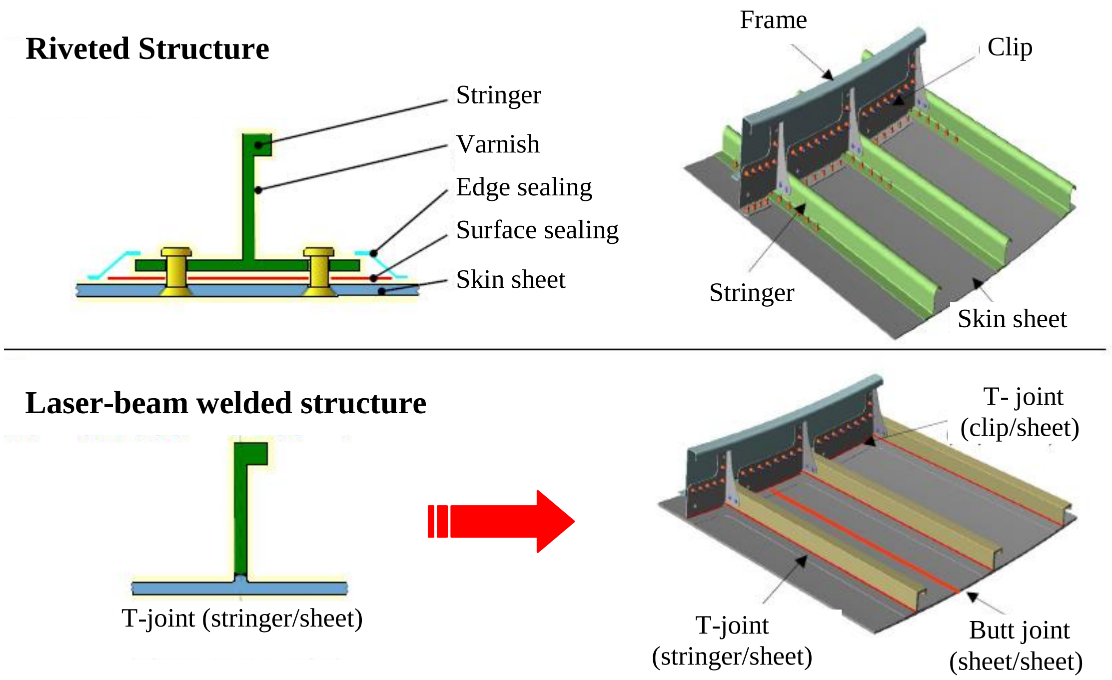

Figure 1.3. Comparison between riveted and welded structure [TEMG]

In the recent years, finite element simulation has proven itself to be a useful tool in predicting these welding induced distortions and residual stresses. The principal of numerical simulation of welding entails the knowledge of a comprehensive database with reference to geometry, material properties, initial conditions, boundary and loading conditions. The more the information regarding these parameters is accurate, the more the simulation is robust. Once the input database is furnished, numerical simulation may now be performed; however, while post-processing, another experimental database is generally required to establish the comparison with simulation results. The results of such a database should also be good enough to validate the numerical model. This may be achieved by adopting sufficient instrumentation during the experiments (usually small-scale) and by verifying the reproducibility of the experimental observations. The predicted state of residual stress distribution and distortion pattern may then help exercising better control over the undesirable aspects of the process.

1.1 Project INZAT

INZAT is a research program, which was launched in year 1994 in Rhône-Alpes with the collaboration of various laboratories. The program was joined by LaMCoS of INSA-Lyon in year 2004. The main objective of this program is to predict the residual stresses and distortions of the welded structures. In fact, the word INZAT stands for two words; ‘IN’ and

'ZAT' (Zone Affecté Thermiquement) and may be understood from the phrase "what is IN the ZAT ?". The numbers that follow the name of project like INZAT1, INZAT2, INZAT3 etc. indicate the different phases of the project. Presently this program is in its fourth phase and hence the name INZAT4. Depending upon the various phases, the project INZAT has been supported by various industrial partners including EADS, AREVA-NP, EDF-SEPTEN, EDF/R&D, DSIN/BCCN, CEA Saclay, ESI Group and Rhône-Alpes Région [ELAW].

1.2 Historical Background

The progress made by the program INZAT has been a step-by-step process and is mainly comprised of performing simple academic test cases, analysing material behaviour, identifying material parameters, studying thermo-mechanical response of material, modelling welding processes and coupling phenomenon etc. In the pursuit of these goals, various theses have been produced over a period of time, which include the works of Nathalie Cavallo [CAVN] 1998, who prepared a database related to the characterisation of a steel alloy 16MnD5 that could be used for the numerical simulation of 'INZAT Disk'. Later on, Sophie Petit-Grostabussiat [PETS] 2000, and Yannick Vincent [VINY] 2002, continued their efforts in further developing the numerical simulation for 'INZAT Disk' on finite element softwares like Sysweld and Code Aster. Y. Vincent additionally developed the metallurgical and mechanical consequences of welding operation in a 'SATOH' type test case. Lionel Depradeux [DEPL] 2004, sought for numerical simulation of TIG welding induced distortions and residual stresses in 316L steel. Walid El-Ahmar [ELAW] 2007, focussed on factors affecting the numerical simulation results while performing simulation tasks on a test case of NET-TG1. He particularly placed emphasis on the sensitivity of simulation results with reference to thermo-mechanical properties of the material. Tong Wu [WUTO] 2007, performed experimental and numerical investigation of welding induced damage in 15-5PH stainless steel focussing largely upon transformation plasticity effects.

With special reference to the welding of aluminium alloys, Damien Fabrègue [FABD] 2004, studied, at microscopic scale, a rather common welding defect called hot cracking in aluminium alloy structures of series 6000. Alexandra Asserin-Lebert [ASSA] 2005, discussed the fracture mechanism of laser beam welded sheets of aluminium alloy (6056) at microstructure level. Claudie Darcourt [DARC] 2005, performed numerical simulation of AA 6056-T4 and predicted the distortion phenomenon occurring at local and global levels as a result of laser beam welding of thin sheets. Christophe Gallais [GALC] 2005, also studied the characterisation and modelling of friction stir welded joints of AA 6056-T4. He identified the two distinct zones in the vicinity of weld joint as heat affected zone and thermo-mechanically affected zone and developed microstructural model to take the precipitation of alloying additions into account. Emmanuel Josserand [JOSE] 2007, have also tried to anticipate the laser beam welding induced distortions on small-scale specimens of thin sheets for the same aluminium alloy (6056). His findings show that the initial surface profiles of the test plates due to pre-processing, like rolling, etc., play an important role in defining the distortion level of welded test plates.

1.3 Dissertation – At a Glance

The work presented in this dissertation is a part of the project INZAT4, co-sponsored by EADS, AREVA-NP, EDF-SEPTEN, ESI Group and Rhône-Alpes Région. It involves the collaboration of LaMCoS, MATEIS and CETHIL of INSA Lyon, LTDS of ENISE and IUT du Creusot. It encompasses the following major tasks:

- Thermo-mechanical characterisation of the aluminium alloy AA 6056-T4
- Experimental campaigns of laser-beam welding on test plates and T-joints
- Numerical simulation of laser-beam welding on Abaqus® /Standard

Chapter 1 describes the context and the historical background of the problem under investigation. A brief introduction is given about the industrial application of AA 6056-T4 and its fabrication in the forms of fuselage panels of aircraft structure using laser-beam welding technique.

Chapter 2 provides the literature review of laser-beam welding process, its merits and demerits. Classification of residual stresses and distortions induced during welding is defined. Various modes of distortions are also explained. A discussion about the thermo-metallo-mechanical nature of the welding process is developed. Thermal and mechanical modelling is given special emphasis. The laws governing material constitutive behaviour are also introduced. The development of residual stresses in the welded structures is explained in detail.

Chapter 3 explains the thermo-mechanical characterisation of AA 6056-T4. A series of tensile tests performed at various temperatures and different strain rates is described. The thermo-mechanical properties of the material (Young's modulus, yield strength etc.) are determined from the stress-strain curves. Dilatometric test is also performed and calculation of thermal expansion coefficient is also explained. The data-base is prepared in order to furnish the material parameters for numerical simulation.

Chapter 4 gives an account of laser-beam welding experimental campaigns performed on the laboratory-scale specimens. Efforts are made to imitate the industrial loading and boundary conditions. Various types of test cases, which include fusion, filler and T-joint welding, are discussed. An extensive data-base of experimental observations with special reference to qualitative and quantitative results is prepared. The experimental results are later used for the validation of the numerical models.

Chapter 5 discusses the development of Finite Element (FE) models. Sequentially coupled thermo-mechanical analyses are performed to simulate various test cases. Heat source models are defined to integrate the volumetric heat flux. Comparative study of experimental and simulated results is carried out so as to ensure the reliability of numerical models. Based on numerical results, the development and distribution of residual stresses and distortions are described.

Chapter 6 summarizes the conclusions inferred from the experimental work and numerical simulations. Suggestions and recommendations are given to improve the FE models. Future work with reference to the present dissertation is also suggested.

CHAPTER 2

STATE-OF-THE-ART LASER-BEAM WELDING

Contents

State-of-the-Art – Laser Beam Welding

The ability to weld aluminium alloys in aircraft structure is critical to their successful exploitation. Fusion welding involves the application of a heat source to melt the edges of two surfaces, with or without the help of a filler wire. The mixing of molten material from the work-piece and molten drops of filler material creates a weld pool, which when solidifies, forms a joint between the two components. The method by which heat is generated in order to fuse the base metal and filler wire defines the nature of the welding process. Welding significantly affects the optimised microstructure in the region next to the weld metal, and hence three distinct zones appear viz. weld bead/fusion zone (FZ), heat affected zone (HAZ) and unaffected base metal.

The welding process causes a highly non-uniform heating of the parts being joined. The local heating and subsequent cooling induce volumetric changes producing transient and residual stresses and deformations. The developments of these stresses and deformations are closely related phenomena. During heating and cooling, thermal strains occur in the weld bead and HAZ. The strains produced during the heating stage of welding are always accompanied by plastic deformation of the metal. The stresses resulting from these strains combine and react to produce internal forces that cause a variety of welding distortions.

Residual deformations introduce severe problems in assembling the welded structure and reduce its quality. Distorted shapes and dimensional inaccuracies reduce the usefulness of the structure. These kinds of problems help in understanding the importance of stress and strain development in the welded structures at manufacturing stages. It is important for the estimation of structural reliability, and development of suitable methods for the improvement of dimensional accuracies.

2.1 Welding Processes

High quality welding processes are a must for welding an aerospace structure. Various techniques are already in use including Tungsten Inert Gas (TIG) welding, Metal Inert Gas (MIG) welding, Plasma welding, Laser beam and Electron beam welding. The choice of a particular process depends largely upon the application of the component to be welded, material of the component, process parameters, cost, residual distortions etc. The classification of these processes is shown in Fig. 2.1 as a function of power densities [MAZJ].

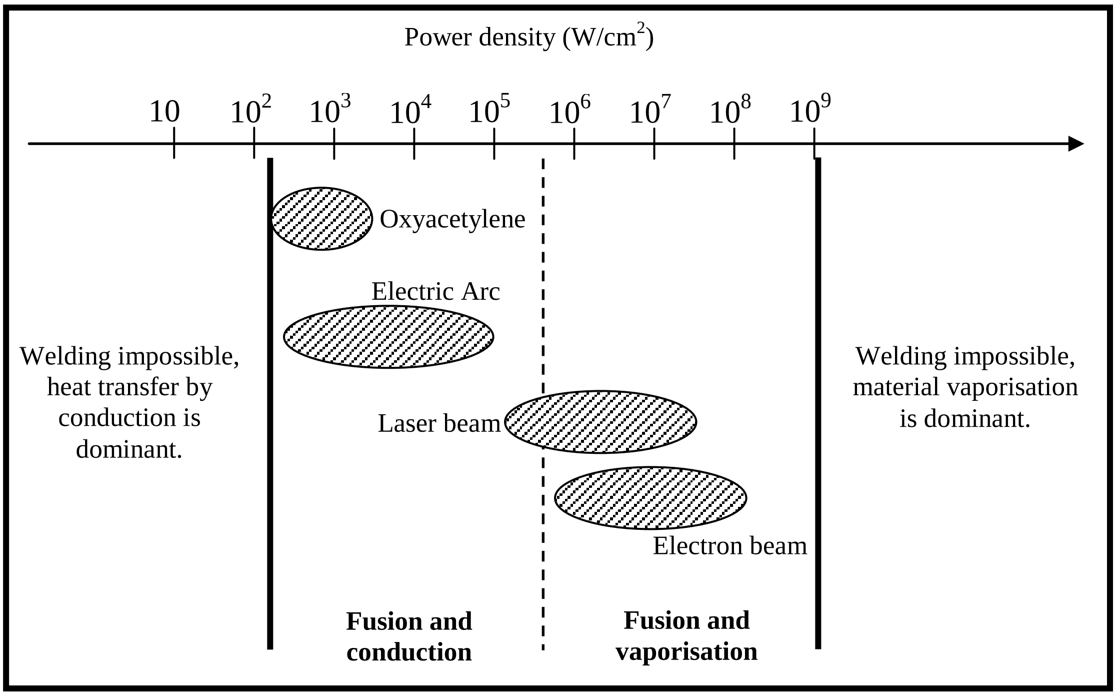

Figure 2.1. Power density of different welding processes [MAZJ]

Table 2.1 summarizes salient features of some of the welding techniques with respect to their productivity, merits and demerits. With particular reference to laser-beam welding (LBW), it is advantageous in comparison to TIG, MIG etc. because it has high welding speed and produces relatively smaller HAZ; additionally, compared to electron beam welding, LBW does not require vacuum nor does it produces harmful X-rays during its operation.

Welding process	Welding speed	One pass penetration	Merits	Demerits
Oxy-acetylene	10 cm/min	2-3 mm	• Low cost • Portable	• Slow speed • High deformation
MIG-MAG	50-100 cm/min	3-4 mm	• Low cost	• High deformation • Groove preparation
TIG	10-50 cm/min	3-4 mm	• High quality • Portable	• High deformation • Slow speed • Larger HAZ
Laser beam	1-5 m/min	upto 10 mm (6 kW)	• High speed • Less deformation	• High installation cost • Non-portable
Electron beam	1-10 m/min	upto 80 mm (25 kW)	• High speed • Greater thickness	• Vacuum required • High cost

Table 2.1. Comparison amongst different welding processes [DARC]

2.2 Laser Beam Welding (LBW)

The term 'LASER' is an acronym for Light Amplification by Stimulated Emission of Radiation. As the name suggests the laser action occurs when an atom is excited by an external energy source. The absorbed energy causes the atom's electrons to move from their ground state to one of the discrete and exact energy orbits; characteristic of the specific atom. Therefore, when these orbiting electrons return spontaneously to their ground state, they release the energy difference as a photon. This photon when passes near an excited electron of the same energy causes the approached electron to return to its ground state and in doing so this electron also releases its photon of light. The two photons travel as a coherent pair and in the exact same direction. As these two paired photons continue on, they trigger other electrons by stimulated emission creating an enormous amplification of photons travelling in the exact same direction dependent on their origin. All of the photons that compose the laser beam are of the same energy and hence are of the same wavelength (monochromatic). Additionally, this generated beam is in-phase (coherent) and of low divergence (collimated).

2.2.1 Working Principal of Nd:YAG LBW

A Neodymium-Yttrium Aluminium Garnet (Nd:YAG) solid state laser is one of the most popular lasers used industrially. It consists of the element neodymium dispersed in the host yttrium aluminium garnet (YAG) crystal. Figure 2.2 presents the working principal of Nd:YAG laser beam welding.

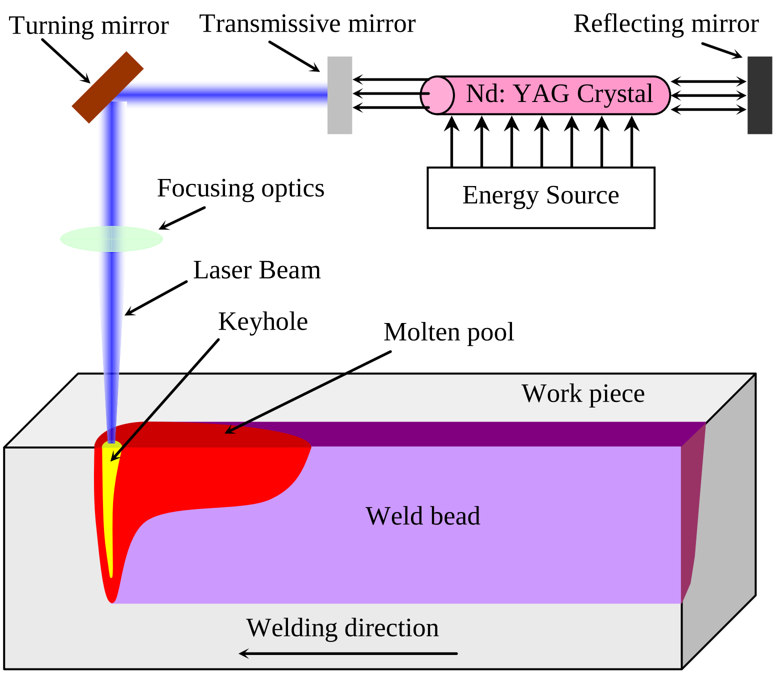

Figure 2.2. Principal of Nd:YAG LBW

Since neodymium atoms are capable of producing lasing action they are excited with an external energy source. Absorbing energy, the neodymium doped YAG crystal results in the release of photons in random spatial directions by the combined mechanism of spontaneous and stimulated emission. The equipment is provided with a rear fully reflecting mirror and a front transmissive (partially reflective) mirror. By coincidence, the spatial direction of some of the photon groups causes them to travel along the longitudinal axis of the cavity. The result is the impingement of these photons on the mirrors from where they are returned to the crystal by reflection and continue to stimulate the emission of other photons. This activity creates an enormous amplification of photons travelling back and forth between the mirrors, continually stimulating and aligning their travel direction. The front mirror, designed to allow a controlled transmission of light, lets the laser beam escape from the apparatus. This beam, being monochromatic, coherent and collimated, may then be directed to the target with the help of turning mirrors and focusing optics.

2.2.2 Weld Pool Formation

The high energy LBW is fundamentally different from classical arc welding processes like TIG, MIG etc. In arc welding processes, the surface of the metal to be welded is heated with relatively lower power density and weld pool appears as a result of heat conduction within the work piece; whereas the highly energised laser beam vaporises the material and creates a 'keyhole' in the work piece. When the welding torch advances the keyhole is filled by surrounding molten metal of the work piece or of the filler wire. Figure 2.2 shows schematic sketch of keyhole, followed by molten weld pool and solidified weld bead. Figure 2.3 presents the stages of the formation of keyhole and the weld pool.

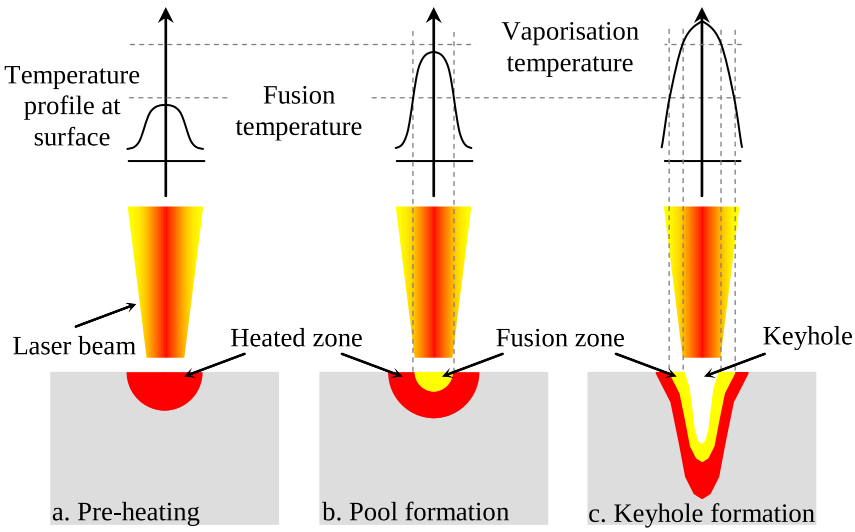

Figure 2.3. Weld pool formation [ROBY]

Although the laser-material interaction depends largely upon the surface condition of the material, the formation of capillary-shaped keyhole may be decomposed in four distinct stages [CHIS][KANM] as shown in Fig. 2.3.

- Preheating of the surface of material under the lasing action (Fig. 2.3.a); reflection of laser beam is predominant.
- Localised fusion of metal accompanying high rate of absorption of laser beam by the material (Fig. 2.3.b); the temperature increases rapidly.
- Evaporation of metal in the highest temperature zone (Fig. 2.3.c); formation of fine capillary due to partially ionized metallic vapours, allowing the incident laser to penetrate the material.
- Ionisation of metallic vapours in the capillary forming a keyhole (Fig. 2.3.c).

The formation and sustenance of keyhole during LBW is the result of various equilibrium forces that tend to either open or close it. The pressure created by metallic vapours helps maintaining the keyhole; while the surface tension of molten metal, gravity and dynamic pressure resulting from to and fro movement of liquid metal are responsible for its closure.

2.3 Welding Consequences

Heat transfer phenomenon plays an important role in welding. It involves large gradient of temperature which range from as high as 3000°C (weld pool) to as low as 20°C (base metal). Due to this large thermal gradient the material experiences several phenomenon occurring simultaneously, e.g. transformation from solid to liquid and then again to solid, phase transformations, volumetric changes, etc. The local heating and subsequent cooling induces volumetric changes producing temporary and residual stresses and deformations.

Residual stresses are self balanced internal stresses that exist in the component without any external load. Since the welding process heats the material locally, the temperature distribution is not uniform. In the melted weld pool stresses are released and can be assumed to zero. During the solidification of the molten pool the metal starts to shrink and exerts stresses on the surrounding weld metal and HAZ. The stress level in the base metal area is proportionately low, but increases in the weld area and can be as high as the yield limit of the base material. This may cause unwanted and sudden failure of the material.

Distortions are simply permanent deformations that result due to the non-uniform expansions and contractions of the weldments. They can be minimised by the use of fixtures and clamping. But in this case residual stresses are increased.

2.4 Classification of Welding Stresses and Deformations

Stresses arising during the welding process are referred to as internal or locked-in stresses. As already mentioned, internal stresses are those which exist in a body without external forces applied. These kinds of stresses usually arise in forming intricate shapes of structures during processing. For example, these stresses develop in complex structures subjected to cutting, grinding, bending or many other types of metal-working. A bolted joint, where the bolt body is stretched and the joined pieces are compressed, is also an example of internal stresses equilibrium [RADD][PILA].

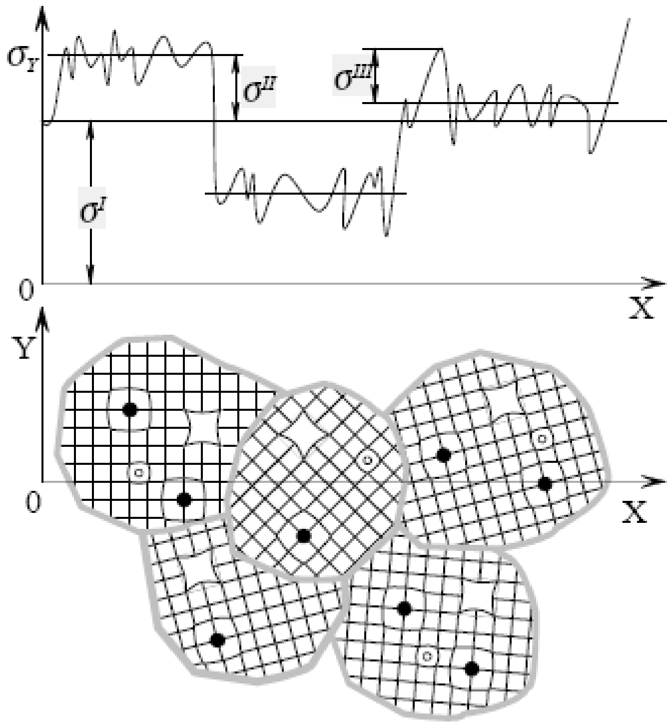

Figure 2.4. First, second and third order residual stresses; defects – foreign substitution atoms, Frenkel defect (vacancy and internode atom) [RADD]

Internal stresses are subdivided into macro- and micro-stresses (first, second, and third order, Fig. 2.4). First order residual stress, σ^I, extend over macroscopic areas and is the averaged stress over a volume with several material grains. Second order residual stress, σ^{II}, acts between adjacent grains. It is averaged within each grain. Third order residual stress, σ^{III}, acts on the inter-atomic level. It is a kind of deviation from the averaged σ^{II}, caused by different impurities of the atomic lattice (examples shown in Fig. 2.4 are: foreign substitution atom; Frenkel defect (vacancy and internode atom)).

First order residual stresses are in equilibrium with themselves within the limits of the structure or structural element, and an isotropic material formulation is usually suitable for the determination of such stresses. Micro-stresses do change significantly over the grain. They depend on crystal anisotropy. In evaluating the influence of the internal stresses on a deformation process, attention should be paid to the macro-stresses. The usual stresses caused by an external force are macro-stresses. And welding stresses are also ranked among those.

Welding stresses can be classified by these characteristics: lifetime, direction and origin of. According to the first characteristic, welding stresses can be temporary or residual. The temporary stresses do exist only in a specific moment of the non-stationary process of heating and cooling. The residual stresses can be found after the whole process of welding is completed and structure is cooled down to the room temperature. Directionally, the welding stresses subdivide into longitudinal (parallel to the weld seam) and transverse (perpendicular to the weld seam) stresses. By origin the welding stresses are subdivided into [PILA]:

- Thermal stress (caused by non-uniform temperature distribution);
- Stresses caused by the plastic deformation of the metal;
- Stresses caused by phase transformations.

Thermal stresses vanish after temperature equalisation. Phase-transformation stresses may appear during welding of some alloyed steels. In processing, low-alloyed structural steels' phase transformation occurs at elevated temperatures. The material, being soft, accommodates volume change caused by phase transformation without significant change in the stress development process. Stresses caused by plastic deformation almost always exist in the areas close to the weld and weld seam itself. A typical stress distribution pattern in welded T-joint is shown in Fig. 2.5. The negative and positive sign conventions are representatives of compressive and tensile stresses, respectively.

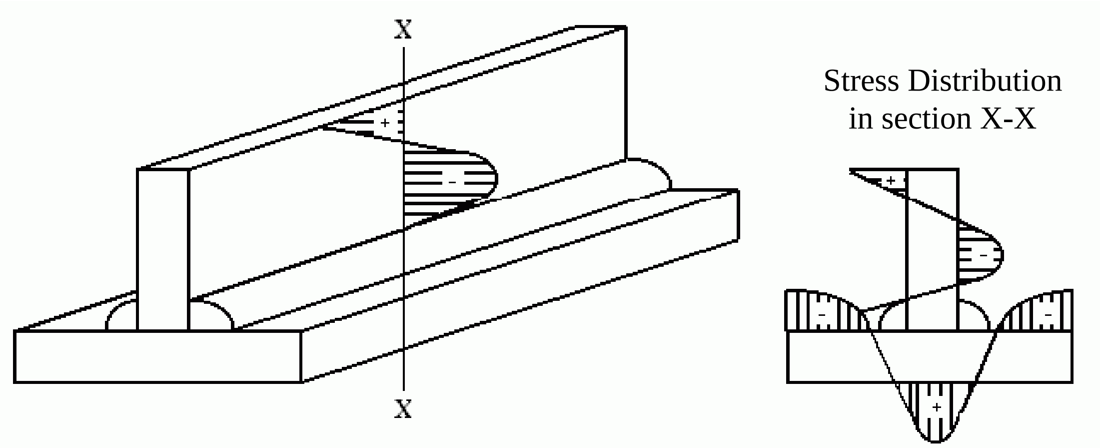

Figure 2.5. Residual stress distribution in a T-joint [FRAJ]

In classifying welding deformations, it should be mentioned that this term covers not only the strain at various points, but also the integral characteristics, such as deflection, angular displacement and change in linear dimensions. As in the case of stresses, welding deformations can also be temporary or residual. Three fundamental dimensional changes of the welded plate are:

- Transverse shrinkage;
- Longitudinal shrinkage;
- Angular distortion (rotation around the weld line).

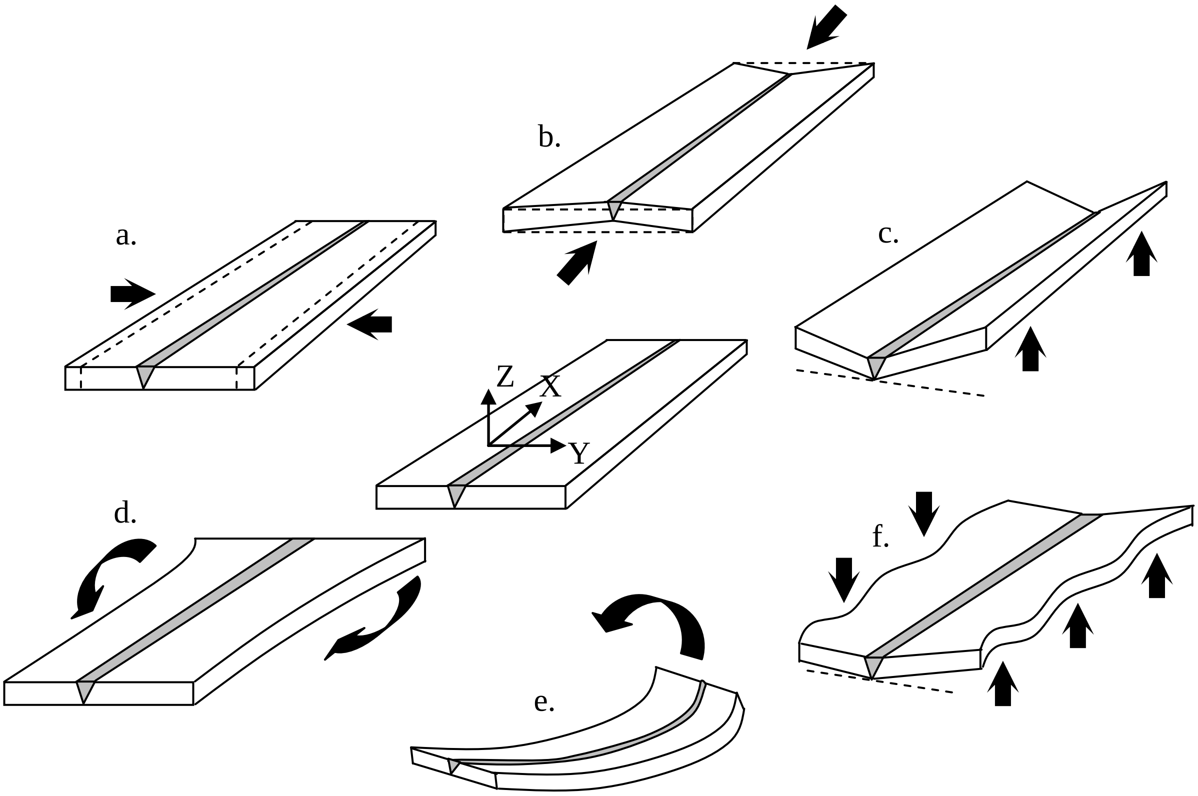

Figure 2.6. Various deformation modes during welding [BERD]

From a more detailed point of view, the welding deformations (in other terms – shrinkage, distortion or warpage) can be classified as:

- *Transverse shrinkage* – shrinkage perpendicular to the weld centreline (Fig. 2.6.a);
- *Longitudinal shrinkage* – shrinkage in the direction of the weld line (Fig. 2.6.b);
- *Angular distortion* – distortion caused by non-uniform temperature distribution in the through-thickness direction (Fig. 2.6.c);

- *Rotational distortion* – angular distortion in the plane of the plate due to thermal expansion or contraction (Fig. 2.6.d);
- *Bending distortion* – distortion in a plane through the weld line and perpendicular to the plate (Fig. 2.6.e);
- *Buckling* – distortion caused by compressive stresses inducing instability when the plates are thin (Fig. 2.6.f).

2.5 Historical Account of Weld Modelling

One of the most important steps towards resolving of any kind of deformation and stress problem in welding applications is to find the appropriate resolution of the temperature distribution. Over the years many different scientific approaches to the solution of this problem were developed. These approaches include:

- A whole series of analytical models, from the simplest 1D solutions to complicated 3D models taking into account 3D heat source distribution and heat losses from work piece surfaces;
- Finite difference analysis (FDA);
- Finite element analysis (FEA).

Over the period of time the main techniques for solving heat transfer problems were changing with growing computer capacity. The analytical solutions were introduced over 60 years ago [ROSD][ROS1][ROS2][ROS3][RYKN][RYK1][WALJ]. Then about 30 years ago numerical methods, viz. finite difference method (FDM) and finite element analysis (FEA) were introduced as solutions for the heat transfer problems [WESO][MAKV][MAK1]. To be more precise, FDM was introduced to the welding applications in the early 60s. And the first published materials concerning FEA in welding made its appearance ten years later [UEDY][GATK][BELG][FRIE]. The part of the doctoral thesis of Ola Westby [WESO] was the first publication concerning the use of FE method for mechanical problems in welding applications. But FEA methods gained a wide acceptance only over the last decade [VOLL][MOLT][RUNH][WIKL].

Analytical methods are capable of computing, with reasonable accuracy, temperature distributions in geometrically simple weldments. The accuracy of the analysis is reasonably high in dealing with temperature changes in areas not so close to the welding arc. An advantage of this method is that it allows analysing the effect of main factors: welding parameters, dimensions of the work piece and material properties. The computing time for solving the analytical models usually ranges between 1 – 100 seconds [PILA]. One of the main drawbacks of the analytical solution is that it does not give possibility to solve non-linear problems.

The use of finite difference methods is more a transition between analytical and finite element methods. The main advantage of the FDM is that it is rather simple and easily understandable physically (the variables are: temperature, time, and spatial coordinates; in contrast to some mathematical functional, involved in FEA solution). But with this method approximation of curvilinear areas is quite complicated. In addition, the FDM uses uniform steps over the space co-ordinates (it is possible to avoid this but it also severely complicates the task).

The history of finite element simulations of the thermal and mechanical behaviour during welding could be traced back to the 1970s [ANDB][FRIE][UEDY][HIBH][RYBE]. Over the past 10 years the FEM has become the most popular and powerful technique of solving the heat transfer problems [GOLJ][GOL1][LINL][NASM]. During these years, together with the powerful super computers, many different commercial programs based on FEA showed up in the market [ABAQ][SYSW][CODA][CAST]. There are several commercial packages with user-friendly programming environment and understandable graphical interfaces that are able to help the user to create the program just by some clicks. But, of course, in order to obtain reliable results the user has to know and understand the main principles and algorithms the program is based on. In FEM a structure is represented as an assembly of the finite elements. In the earliest developments of finite element methods all the attention was drawn to the development of effective finite elements for the solution of specific problems. However, more general techniques were developed as soon as the great potential of the method was discovered. In his works, Lindgren [LINL] introduced different modelling aspects of the application of the finite element method to predict the thermal, material and mechanical effects of welding. Besides, he also introduced complexity of welding simulation, material modelling of welding and computational strategies of welding simulation [LIN1] [LIN2][LIN3][LIN4][LIN5][LIN6].

The subsequent sections of this chapter will present some of the elementary steps necessary to develop understanding of the numerical simulation of welding. For any further details, the reader is referred to the works produced by Masubuchi [MASK] and Radaj [RADD].

2.6 A Thermo-metallo-mechanically Coupled Phenomenon

The definition of welding process as a thermo-metallo-mechanically coupled phenomenon essentially implies that there are various thermal, metallurgical and mechanical processes happening simultaneously in the fusion and heat affected zones throughout the heating and cooling phases. In order to capture the residual stress state and resulting distortions, it is, therefore, necessary to model all these phenomena as accurately as possible. However, depending upon the type of material, certain simplifications may be adopted at this stage. For example, during welding certain steels show phase transformations in solid state while some other alloys, once solidified, do not show any change of phase. Almost all the aluminium alloys fall into the second category of materials (i.e. with no solid state phase transformation). Hence, after taking latent heat of fusion into consideration, the remaining metallurgical aspects may be ignored. Figure 2.7 presents the interaction and coupling of thermal, metallurgical and mechanical aspects of the process. In this dissertation, the emphasis is placed on thermo-mechanical modelling only.

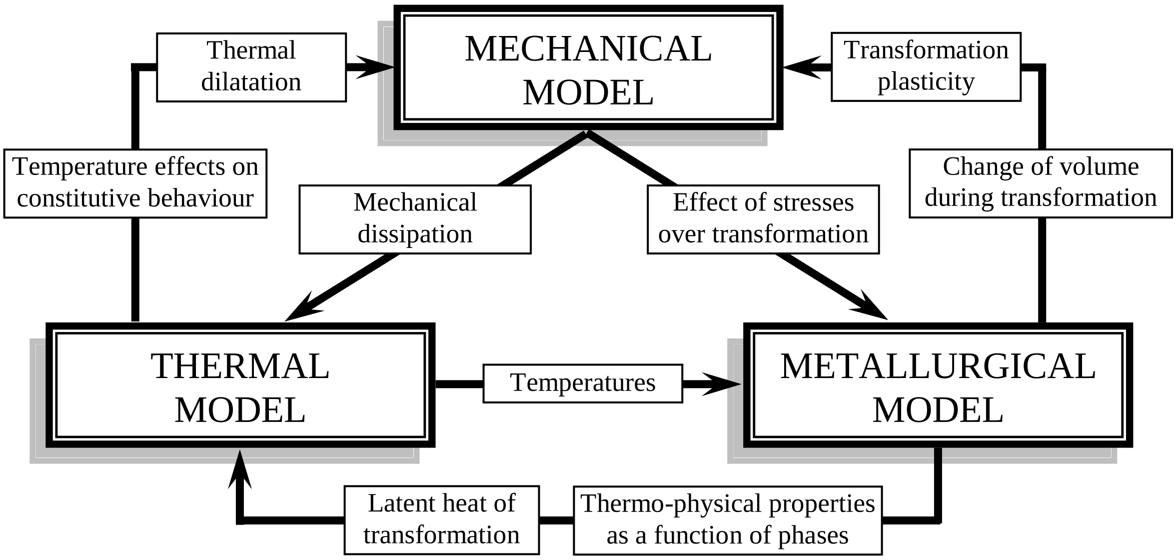

Figure 2.7. Coupling of physical phenomena in welding [BERJ][ELAW][DUAY]

In the absence of metallurgical phase transformations, the mechanical effects induced by heat transfer are the expansion and contraction of material and the mechanical characteristics of the material depend accordingly on temperature. On the other hand, the thermal effect induced mechanically is intrinsic dissipation: evolution of irreversible deformation such that the internal hardening variables dissipate energy in the form of heat. This rise in temperature due to mechanical work done is often trivial as compared to the increase in temperature due to the heat energy injected in the work piece during welding.

Consequently, it is a highly adopted practice that in welding simulation an uncoupled thermo-mechanical analysis approach is used. Therefore, thermal analysis is first performed followed by mechanical analysis.

2.7 Thermal Modelling

The purpose of modelling the thermal problem is to calculate the temperature histories associated with the welding of the work piece. This calculation consists of resolving the heat equation while considering the thermal loading and boundary conditions. The heat equation is based upon the principal of conservation of energy as defined in the first principle of thermodynamics. The thermal behaviour is mostly modelled by Fourrier's Law which defines the heat flux as a function of temperature gradient [DEPL][PETM]. Heat transfer in a solid medium of domain Ω is, therefore, modelled by following equations:

$$\rho.C_p.\frac{\partial T}{\partial t} - div(\lambda.gradT) - Q_i = 0 \quad \text{in } \Omega \tag{2.1}$$

Equation 2.1 may be rewritten as Eq. 2.3 in terms of enthalpy of material, where enthalpy is defined as:

$$H_e(T) = \int_{T_0}^{T} \rho.C_p(u).du \tag{2.2}$$

$$\frac{\partial H_e}{\partial t} - div(\lambda.gradT) - Q_i = 0 \tag{2.3}$$

In Eq. 2.1, the conditions may be applied at the boundary $\partial\Omega$ such that $\partial\Omega = \partial\Omega_q \cup \partial\Omega_T$ and $\partial\Omega_q \cap \partial\Omega_T = \varnothing$.

$$\lambda.gradT.n = q(T,t) \quad \text{on } \partial\Omega_q \tag{2.4}$$

$$T = T_p(t) \quad \text{on } \partial\Omega_T \tag{2.5}$$

with, ρ density in kg.m^{-3},

C_p specific heat capacity in J.kg^{-1}.°C^{-1},

λ thermal conductivity in W.m^{-1}.°C^{-1},

T temperature in °C,

Q_i internal heat generation rate in W.m^{-3},

$\partial\Omega_q$ part of the boundary $\partial\Omega$ at which flux is applied,

$\partial\Omega_T$	part of the boundary $\partial\Omega$ at which temperature is imposed,
n	normal vector directing outward from $\partial\Omega$,
$q(T,t)$	surface density of heat flux representing convection and/or radiation,
$T_p(t)$	temperature imposed,
$H_e(T)$	enthalpy as a function of temperature.

Heat transfer takes place by means of conduction, convection and radiation. During welding the work piece gets heated due to the conduction of heat energy within the material, while heat loss in the surrounding environment takes place through convection and radiation. Additional amount of heat loss may also take place when a hot body comes in contact with a colder one and heat dissipates from hot to cold media. This type of heat exchange depends upon the thermal conductivities of the two media, contact area, heat conduction property of any other medium present at the interface of two bodies, and applied pressure. The heat transfer phenomena as general boundary conditions are now being described in the following equations:

$$q_{conv} = h(T)(T - T_0) \tag{2.6}$$

$$q_{rad} = \sigma_{SB}\xi((T - T_{abs})^4 - (T_0 - T_{abs})^4) \tag{2.7}$$

$$q_{tcr} = h_{tcr}(T_s - T) \tag{2.8}$$

with,

$h(T)$	convective heat transfer coefficient as a function of temperature in W.m^{-2}.°C^{-1},
T_0	ambient temperature in °C,
T_{abs}	absolute zero,
T	temperature of the component being welded in °C,
σ_{SB}	Stefan-Boltzmann constant, 5.68 x 10^{-8} J.K^{-4}.m^{-2}.s^{-1},
ξ	emissivity of the radiating surface,
h_{tcr}	heat transfer coefficient due to thermal contact resistance in W.m^{-2}.°C^{-1},
T_s	temperature of the surrounding body in contact with work piece being welded.

The thermal boundary conditions may, therefore, be defined as Eq. 2.4 where $q(T,t)$ may present the sum of q_{conv} and q_{rad}. It is, therefore, quite customary to find in literature that both the natural convection and radiation are written in the form of a combined heat transfer coefficient. Following two forms are common:

$$q(T,t) = B(T - T_0)^a \tag{2.9}$$

$$q(T,t) = B(T)(T - T_0) \tag{2.10}$$

Here, *B* and *a* or *B(T)* are the combined coefficients of heat transfer by free convection and radiation. As during welding the fusion zone (FZ) changes its phase from solid to liquid and then solid, a considerable amount of latent heat of fusion is to be taken into account and this is often achieved by integrating it in the specific heat capacity C_p. The solution of this type of non-linear thermal problem is classical in its nature and does not pose any particular problem, except while identifying the parameter for boundary and loading conditions. It is for this reason that the parameters for loading and boundary conditions are identified with reference to geometry of FZ and the temperature fields obtained through experimental measurements. This is often acquired by the method of inverse identification.

2.8 Mechanical Modelling

In order to quantify the residual stresses and deformations in a welded structure through an FE code, it is necessary to describe the mechanical model of the material behaviour [DEPL][PETM]. This is based upon the equation of conservation of momentum:

$$div(\boldsymbol{\sigma}) - F = 0 \tag{2.11}$$

And it is completed by the appropriate constitutive behaviour and boundary conditions. The constitutive equations are based on the hypothesis of decomposition of deformation and are presented in the subsequent sections. Various constitutive behaviours that are frequently used in numerical simulation of welding are also presented and the effect of material properties and boundary conditions are discussed.

2.8.1 Strain Decomposition

The symmetric strain tensor is composed of various parts [PETM]:

- ***Elastic strain***, $\boldsymbol{\varepsilon}^e$ is a function of variation of stress tensor between initial state (initial residual stress, $\boldsymbol{\sigma}_i$, at a given reference temperature, T_0) and the actual state, $\boldsymbol{\sigma}$. It is expressed with compliance tensor, inverse of 4th order stiffness tensor, $\boldsymbol{\Lambda}(T)$:

$$\boldsymbol{\varepsilon}^e = \boldsymbol{\Lambda}(T)^{-1} : (\boldsymbol{\sigma} - \boldsymbol{\sigma}_i) \tag{2.12}$$

where $\Lambda(T)$ is defined by the two elastic coefficients Young's modulus $E(T)$ and Poisson's ratio $\nu(T)$ for an isotropic material.

- ➢ ***Thermal dilatation***, $\boldsymbol{\varepsilon}^{th}$ is a function of actual temperature T and the reference temperature T_0. It is written in terms of linear thermal dilatation coefficient $\alpha(T)$:

$$\boldsymbol{\varepsilon}^{th} = \alpha(T)(T - T_0)\boldsymbol{I} \tag{2.13}$$

- ➢ ***Inelastic strain***, $\boldsymbol{\varepsilon}^{in}$ may be decomposed in two parts as plastic strain $\boldsymbol{\varepsilon}^{p}$ and viscoplastic strain $\boldsymbol{\varepsilon}^{vp}$.
- ➢ ***Transformation plasticity***, $\boldsymbol{\varepsilon}^{pt}$ is described in terms of transformation plasticity coefficient, which is measured experimentally. It defines the plastic deformation during the transformation of ferrite, pearlite, bainite or martensite with the application of stress.

It is from here that the overall decomposition of strain follows:

$$\boldsymbol{\varepsilon} = \boldsymbol{\varepsilon}^{e} + \boldsymbol{\varepsilon}^{th} + \boldsymbol{\varepsilon}^{p} + \boldsymbol{\varepsilon}^{vp} + \boldsymbol{\varepsilon}^{pt} \tag{2.14}$$

Or it may be written in incremental form as:

$$\dot{\boldsymbol{\varepsilon}} = \dot{\boldsymbol{\varepsilon}}^{e} + \dot{\boldsymbol{\varepsilon}}^{th} + \dot{\boldsymbol{\varepsilon}}^{p} + \dot{\boldsymbol{\varepsilon}}^{vp} + \dot{\boldsymbol{\varepsilon}}^{pt} \tag{2.15}$$

Remarks:

i) The additive decomposition rule, valid for the hypothesis of small deformations, may be derived from multiplicative decomposition of the symmetric part of strain gradient.

ii) Stress increment is calculated from the strain increment. In case of large deformation, an objective stress rate has to be selected (Jaumann derivative, for example).

iii) Equation 2.15 shows plastic and viscoplastic strain rates. In general, these two rates do not intervene simultaneously in the numerical implementation. The plastic deformation mechanism, being dependent upon the temperature, is often chosen as purely viscoplastic behaviour at high temperatures and purely plastic behaviour at low temperatures.

2.8.2 Constitutive Behaviour Laws

Plastic deformation of the material is an inevitable consequence of a welding operation. It is, therefore, required that in order to calculate the stresses and deformations the plastic behaviour of metallic materials be defined comprehensively. The plastic behaviour is defined by following three properties:

- ***Criterion for plasticity***, specifies the three dimensional stress state with reference to the start of plastic flow and determines, therefore, the elastic domain (defined in space in terms of stress, hardening variables $\boldsymbol{H}_{var}$ and the temperature). At certain given temperature and hardening level, the elastic domain may be written in vector space of dimension 6 of second order symmetric tensor as:

$$D_e = \{\boldsymbol{\sigma} \,/\, f(\boldsymbol{\sigma}, \boldsymbol{H}_{var}, T) \leq 0\} \tag{2.16}$$

The state $f(\boldsymbol{\sigma},\boldsymbol{H}_{var},T) = 0$ is the criterion for plasticity that defines the elastic domain. The function *f*, also called plasticity criterion, has to be independent of the orientation of system coordinates and this is the reason for which it is defined with the help of three invariants of stress tensor.

For the plasticity independent of time, the model that is mostly used for numerical simulation of welding is the criterion of von Mises. Criterion of Tresca is amongst other famous models. The formulation of criteria taking care of hydrostatic pressure, for instance Drucker-Prager criterion and Mohr-Coulomb criterion, are rarely used for numerical simulation of welding.

- ***Flow rule*** relates the incremental plastic deformation to the incremental stress. This rule helps defining the plastic or viscoplastic deformation rate when the material behaviour is no more elastic. It, therefore, postulates the plastic flow, normal to the loading surface, by virtue of the principle of maximum work done (Drucker).
- ***Hardening law*** specifies the evolution of plasticity criterion during the plastic flow resulting because of the rearrangement of internal structure of material. The hardening laws are actually the rules that characterise the evolution of hardening variables during the inelastic deformation. The deformation may lead to unchanged elastic domain D_e (no hardening, elastic perfectly plastic), may reduce it (negative hardening) or increase it (positive hardening).

2.8.2.1 Elastic Perfectly Plastic Model

Using the criterion of von Mises, the function *f* may be written as:

$$f(\boldsymbol{\sigma}) = \sqrt{3J_2} - \sigma_y \tag{2.17}$$

Where σ_y is the yield strength and J_2 is the second deviatoric stress ($\boldsymbol{S}$) invariant and are defined in Eq. 2.18

$$J_2 = \frac{1}{2}\boldsymbol{S}:\boldsymbol{S} \qquad \text{with} \qquad \boldsymbol{S} = \boldsymbol{\sigma} - \frac{tr(\boldsymbol{\sigma})}{3}\boldsymbol{I} \tag{2.18}$$

Also, $$\sqrt{3J_2} = \sigma^{VM} = \sqrt{\frac{3}{2}\boldsymbol{S}:\boldsymbol{S}} = \sqrt{\frac{1}{2}\left[(\sigma_1-\sigma_2)^2 + (\sigma_2-\sigma_3)^2 + (\sigma_3-\sigma_1)^2\right]} \tag{2.19}$$

Here, σ^{VM} is von Mises equivalent stress and σ_1, σ_2 and σ_3 are the principal stresses.

For the plastic mode, being zero in perfect plasticity, there exist infinite equivalent positions of plastic deformation for a given admissible state of stress, such that $f = 0$. The plastic multiplier $\dot{\lambda}$ may be determined by combining elastic constitutive law and the condition of coherence:

$$n:\dot{\boldsymbol{\sigma}} = 0 \qquad \text{with} \qquad n = \frac{\partial f}{\partial \boldsymbol{\sigma}} \tag{2.20}$$

For a particular case of isotropic elasticity and von Mises criterion, it leads to: $\dot{\lambda} = \frac{2}{3} n:\dot{\boldsymbol{\varepsilon}}$

The elastic perfectly plastic behaviour is defined by the Eqs 2.21 and 2.22:

Elastic behaviour: $$\boldsymbol{\sigma} = \boldsymbol{\Lambda}:(\boldsymbol{\varepsilon} - \boldsymbol{\varepsilon}^p - \boldsymbol{\varepsilon}^{th}) \tag{2.21}$$

Flow rule: $$\dot{\boldsymbol{\varepsilon}}^p = \dot{\lambda}\frac{df}{d\boldsymbol{\sigma}} = \dot{\lambda}\frac{3}{2}\cdot\frac{\boldsymbol{S}}{\sigma^{VM}} \tag{2.22}$$

For such a model, the material dependent coefficients are Young's modulus E, Poisson's ratio ν, thermal dilatation coefficient α and yield strength σ_y.

2.8.2.2 Elasto-plastic Model with Isotropic Hardening

Materials that possess purely isotropic hardening behaviour, their elastic domains transform without the translation of the origin. The hardening, therefore, depends upon a scalar parameter known as isotropic hardening variable R. The relation obtained using von Mises criterion and isotropic hardening behaviour leads to a particular law of plasticity known as Prandtl-Reuss Law. In this case the function f is defined as follows:

$$f(\boldsymbol{\sigma}, R) = \sqrt{3J_2(\boldsymbol{\sigma})} - \sigma_y - R(p) \tag{2.23}$$

The isotropic hardening is denoted by the function *R(p)*, which in linear case is expressed by:

$$R(p) = H\boldsymbol{\varepsilon}^p \qquad \text{also} \qquad \dot{p} = \sqrt{(2/3)\dot{\varepsilon}^p : \dot{\varepsilon}^p} \tag{2.24}$$

Here, p represents the cumulated plastic deformation. Independent of the form chosen for R, the coherence condition allows finding the plastic multiplier:

$$\dot{\lambda} = \frac{(n:\dot{\boldsymbol{\sigma}})}{H} = \dot{p} \tag{2.25}$$

The elasto-plastic (EP) model with linear isotropic hardening may, therefore, be defined by the Eqs 2.26 and 2.27.

$$\textit{Elastic behaviour:} \qquad \boldsymbol{\sigma} = \boldsymbol{\Lambda} : (\boldsymbol{\varepsilon} - \boldsymbol{\varepsilon}^p - \boldsymbol{\varepsilon}^{th}) \tag{2.26}$$

$$\textit{Flow rule:} \qquad \dot{\boldsymbol{\varepsilon}}^p = \dot{\lambda}\frac{df}{d\boldsymbol{\sigma}} \qquad \text{with} \qquad \dot{\lambda} = \frac{(n:\dot{\boldsymbol{\sigma}})}{H} \tag{2.27}$$

For such a model, the material dependent coefficients are Young's modulus E, Poisson's ratio ν, thermal dilatation coefficient α, initial yield strength σ_y and the hardening modulus H.

2.8.2.3 Elasto-plastic Model with Linear Kinematic Hardening

Materials that possess kinematic hardening behaviour, their elastic domains rather than transforming translate into stress space. The hardening, therefore, depends upon a vector parameter known as kinematic hardening variable $\boldsymbol{X}$. The relation obtained using von Mises criterion and kinematic hardening behaviour leads to another particular law of plasticity known as Prager Law. The kinematic hardening variable $\boldsymbol{X}$ associated with plastic deformation gives the function f the following form:

$$f(\boldsymbol{\sigma},\boldsymbol{X}) = \sqrt{3J_2(\boldsymbol{\sigma} - \boldsymbol{X})} - \sigma_y \tag{2.28}$$

$$\text{where,} \qquad \boldsymbol{X} = (2/3)H\boldsymbol{\varepsilon}^p \tag{2.29}$$

The elasto-plastic (EP) model with linear kinematic hardening may, therefore, be defined by Eqs. 2.30 and 2.31.

Elastic behaviour: $$\boldsymbol{\sigma} = \boldsymbol{\Lambda} : (\boldsymbol{\varepsilon} - \boldsymbol{\varepsilon}^{p} - \boldsymbol{\varepsilon}^{th}) \quad (2.30)$$

Flow rule: $$\dot{\boldsymbol{\varepsilon}}^{p} = \dot{\lambda} \frac{df}{d\boldsymbol{\sigma}} \quad \text{with} \quad \dot{\lambda} = \frac{(n : \dot{\boldsymbol{\sigma}})}{H} \quad (2.31)$$

For such a model, the material dependent coefficients are Young's modulus E, Poisson's ratio ν, thermal dilatation coefficient α, initial yield strength σ_y and the hardening modulus H.

2.8.2.4 Elasto-viscoplastic Model with Non-Linear Kinematic Hardening

The kinematic hardening behaviour is generally subdivided into linear and non-linear kinematic formulation. The linear kinematic formulation is already defined above in section 2.8.2.3. In order to define the non-linear kinematic formulation, the function f using von Mises criterion may be written as follows:

$$f(\boldsymbol{\sigma}, \boldsymbol{X}) = \sqrt{3J_2(\boldsymbol{\sigma} - \boldsymbol{X})} - \sigma_y \quad (2.32)$$

The elasto-viscoplastic (EVP) model with non-linear kinematic hardening may be defined by Eqs. 2.33, 2.34 and 2.35.

Elastic behaviour: $$\boldsymbol{\sigma} = \boldsymbol{\Lambda} : (\boldsymbol{\varepsilon} - \boldsymbol{\varepsilon}^{p} - \boldsymbol{\varepsilon}^{th}) \quad (2.33)$$

Non-linear kinematic hardening: $$\dot{\boldsymbol{X}} = \frac{2}{3} C.\gamma.\dot{\boldsymbol{\varepsilon}}^{p} - C.\boldsymbol{X}.\dot{p} \quad (2.34)$$

Flow rule: $$\dot{\boldsymbol{\varepsilon}}^{p} = \dot{p} \frac{df}{d\boldsymbol{\sigma}} \quad \text{and} \quad \dot{p} = \left\langle \frac{f}{K} \right\rangle^{n} \quad (2.35)$$

In such a model, the material dependent coefficients are Young's modulus E, Poisson's ratio ν, thermal dilatation coefficient α, initial yield strength σ_y, the hardening parameters C and γ, exponent of viscoplasticity n and viscoplastic resistance K.

2.8.2.5 Classical Viscoplastic Models

In plasticity the intensity of plastic flow is imposed by the condition of coherence, while in viscoplasticity it is defined as a function of viscosity $\psi(<f>)$[DEPL], such that:

$$\dot{\boldsymbol{\varepsilon}}^{vp} = \psi(< f >)\frac{\partial \phi}{\partial \boldsymbol{\sigma}} \tag{2.36}$$

Here, $\dot{\boldsymbol{\varepsilon}}^{vp}$ is the viscoplastic strain rate tensor, f is the same criterion for plasticity as well as for viscoplasticity, ϕ is the plastic potential. The possible choice for f and ϕ belongs to the origin of various models, while the function $\psi(<f>)$ is responsible for viscoplasticity. The latter is characterised such that the inelastic strain rate does not depend upon stress rate rather only upon the instantaneous state of stress and of hardening. The selection of this function varies according to the models (linear, power, exponential, etc.). There exist different kinds of classical viscoplasticity models which may be defined as follows:

- *Perfect viscoplasticity (Odqvist):*

$$\dot{\boldsymbol{\varepsilon}}^{vp} = \frac{3}{2}\left(\frac{\left\langle \sigma^{VM} - \sigma_y \right\rangle}{K}\right)^n \frac{\boldsymbol{S}}{\sigma^{VM}} \tag{2.37}$$

- *Viscoplasticity with isotropic hardening (multiplicative)*

$$\dot{\boldsymbol{\varepsilon}}^{vp} = \frac{3}{2}\left(\frac{\left\langle \sigma^{VM} - \sigma_y \right\rangle}{K.p^{1/m}}\right)^n \frac{\boldsymbol{S}}{\sigma^{VM}} \tag{2.38}$$

- *Viscoplasticity with isotropic hardening (additive)*

$$\dot{\boldsymbol{\varepsilon}}^{vp} = \frac{3}{2}\left(\frac{\left\langle \sigma^{VM} - \sigma_y - R \right\rangle}{K}\right)^n \frac{\boldsymbol{S}}{\sigma^{VM}} \tag{2.39}$$

- *Viscoplasticity with kinematic hardening*

$$\dot{\boldsymbol{\varepsilon}}^{vp} = \frac{3}{2}\cdot \dot{p} \cdot \frac{(\boldsymbol{\sigma} - \boldsymbol{X})^d}{(\boldsymbol{\sigma} - \boldsymbol{X})^{VM}} \tag{2.40}$$

with
$$\dot{p} = \left(\frac{\left\langle (\boldsymbol{\sigma} - \boldsymbol{X})^{VM} - \sigma_y \right\rangle}{K}\right)^n \tag{2.41}$$

The notations used are already defined in the previous sections except for $\boldsymbol{X}^d$ which is the deviatoric part of the tensor $\boldsymbol{X}$ and m which is a material parameter for viscoplasticity. Equation 2.39 is used in Abaqus simulations in chapter 5.

2.8.3 Boundary Conditions

In order to determine the stress state prevailing in the structure, the solution of equation of conservation of momentum (Eq. 2.11) has to be established which verifies the imposed boundary conditions in terms of forces and displacements. Determination of mechanical boundary conditions during welding is an extremely delicate step and is specific to the experiment being simulated. These boundary conditions are required to take care of holding and clamping devices used to maintain the work piece in position during welding. Considering the difficulty in estimating the rigidity of clamping devices, it is a common practice to assume zero displacement of the parts of the work piece in contact with clamps. It is for this reason that efforts are made to use as simple boundary conditions as possible and for certain academic scale experiments the test pieces are simply placed upon the support where they stay in position under the action of gravity. In industry, however, clamping conditions for welding of huge structures are relatively more complicated. The integration of complex boundary conditions is likely to increase the computation time of an already prolonged calculation of mechanical simulation. It should, however, be noted that a little change in mechanical boundary conditions may affect the mechanical response to a great extent.

2.9 Modelling the Thermo-mechanical Behaviour of Material

Various authors agree to the fact that thermo-mechanical properties of the material have significant effect over the simulation results. Lindgren [LIN2] attempted to classify the precision of numerical simulation results according to different criteria. One of these criteria is the selection of a cut-off temperature (T_{cut}), above which change in material properties is not taken into account for mechanical simulation. In this case, the EP models used for welding simulation are furnished with the material properties defined from ambient temperature till T_{cut} while beyond this temperature the properties remain constant. The use of cut-off temperature helps avoiding the problems related to numerical solution at high temperatures where the values of material properties are very low. These modelling aspects shall be discussed in detail in next chapter.

2.10 Transient stress field

During welding the process of stress-strain field development is characterised by the elastic-plastic behaviour of the metal, non-stationary temperature conditions with a high temperature limit (up to several thousands °C), and very high temperature gradients (locally of the order of 10^3 °C/mm). The transient and residual stress development is based on volumetric change of the structure elements. With the heat propagating through the body and the temperature equalisation, the stress distribution continues.

Kinetics of the stress field during welding is a process of stress development lasting the whole period of welding and subsequent cooling. The stress kinetics investigation is quite a complicated task because of the huge amount of variables affecting the process. At the same time, the physical nature of the stress development process can be evaluated by means of quite simple examples.

2.10.1 Longitudinal Stress Development during Welding

A typical thermal cycle is considered in Fig. 2.8 [PILA]. In order to monitor the stress development at any point, an elementary volume element is chosen. The case of thin plate welding is considered so that the through-thickness temperature gradient may be assumed as negligible. The elementary element is also shown in Fig. 2.8. The temperature inside the cubic element may be considered constant as its volume is quite small.

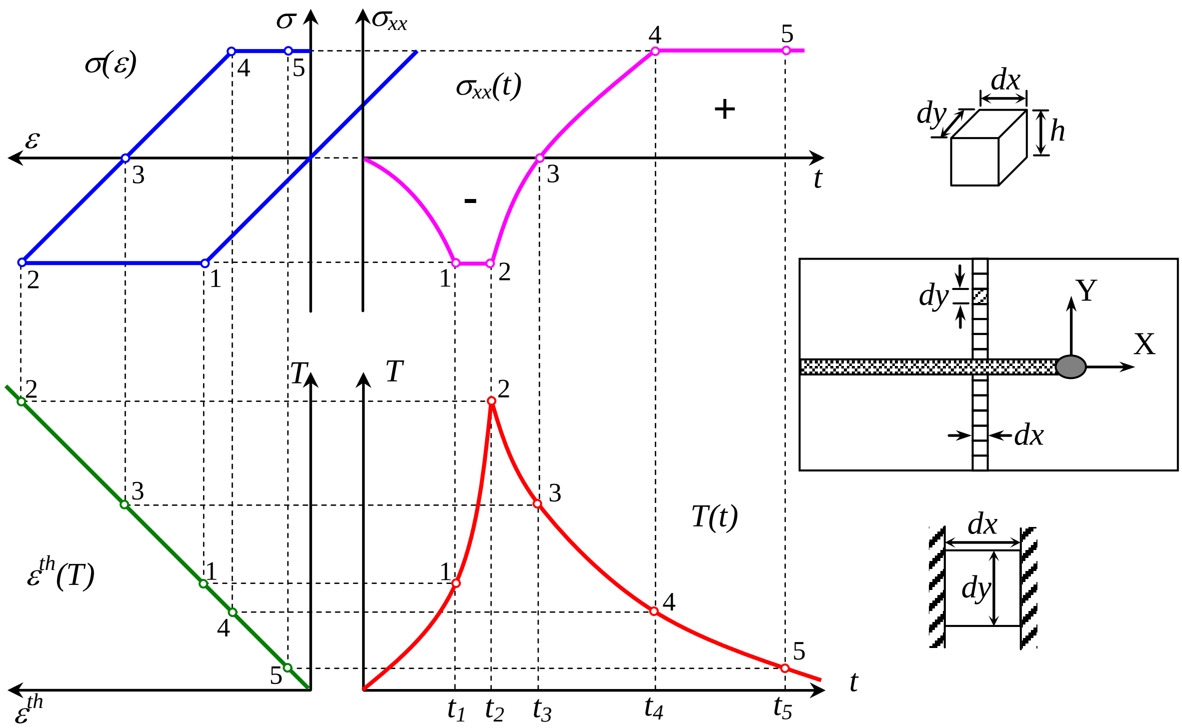

Figure 2.8. Kinetics of stress generation during welding [PILA]

Usually, a welded structure is stiff enough to keep the total deformation along the welding direction (in this case - ε_{xx}) significantly smaller than the unrestrained thermal deformation ε^{th}. This state is true for the elements situated close to the weld seam. This is why it may also be assumed that the element does not change its dimensions in the x-direction as shown in Fig. 2.8. At the same time, during the heating and cooling stages, longitudinal stresses σ_{xx} develop in the elements.

For simplification, 1D-stressed case is being considered, and it is also assumed that σ_{yy} is equal to zero i.e. in the *y*-direction the element can be deformed stress-free. Summarising, in the longitudinal direction $\sigma_{xx} \neq 0$, $\varepsilon_{xx} = 0$, but in the transverse direction $\sigma_{yy} = 0$, $\varepsilon_{yy} \neq 0$. To analyse the stress-cycles in the elements, data about the metal volume expansion due to the elevated temperatures (the dilatometric curve) and curves of material deformation (the stress-strain curves) are needed. Neglecting the structural changes in the material, the dilatometric curve can be approximated as a straight line i.e. the thermal expansion coefficient α is constant. The set of stress-strain curves can, as a first approximation, be substituted by an idealised stress-strain curve as shown in Fig. 2.8. The stress-strain $\sigma(\varepsilon)$, dilatometry $\varepsilon^{th}(T)$, time-longitudinal stress $\sigma_{xx}(t)$ and time-temperature $T(t)$ curves are juxtaposed and arbitrarily scaled in order to facilitate the overall analysis. Now, the stress-cycle $\sigma_{xx}(t)$ can be plotted following the tracings in Fig. 2.8.

For example, at the time t_1 the temperature T_1 is characterised by the point *1*. From this point a horizontal line, characterising the thermal expansion corresponding to T_1, will determine the point *1* on the dilatometric curve. For the case of a cubic element in the x-direction, the $\varepsilon^{th}{}_1$ will determine the thermal expansion. Extending vertically up onto the $\sigma(\varepsilon)$ curve, another point *1* is obtained. This point is characterised by σ_{xx} and ε_{xx} at t_1 and coincident with the moment in time when the σ_{xx} reaches the yielding limit σ_y. Now the required point *1* on the time-stress curve can be found by the intersection of the perpendiculars from the thermal cycle and the stress-strain curve. In the same manner the rest of the points characterising the stress-cycle can be found. The point *2* corresponds to the maximum temperature on the thermal cycle and the maximum of the plastic compressive strain. After t_2 the cooling process and, hence, the unloading starts and lasts until t_3. At t_3 the elastic stress and strain are both equal to zero. From t_3 to t_4 the elastic tensile strain is growing. At t_4 the second plastic deformation with opposite sign begins. The time t_5 corresponds to the completely cooled down state.

Figure 2.9 gives a schematic representation of the temperature and the resulting longitudinal stress distribution that occur during welding [PILA]. In this example a simple bead-on-plate case is analysed (Fig. 2.9.a). The weld pool, which is moving along the *x*-axis with a speed *v*, is indicated by an arrow.

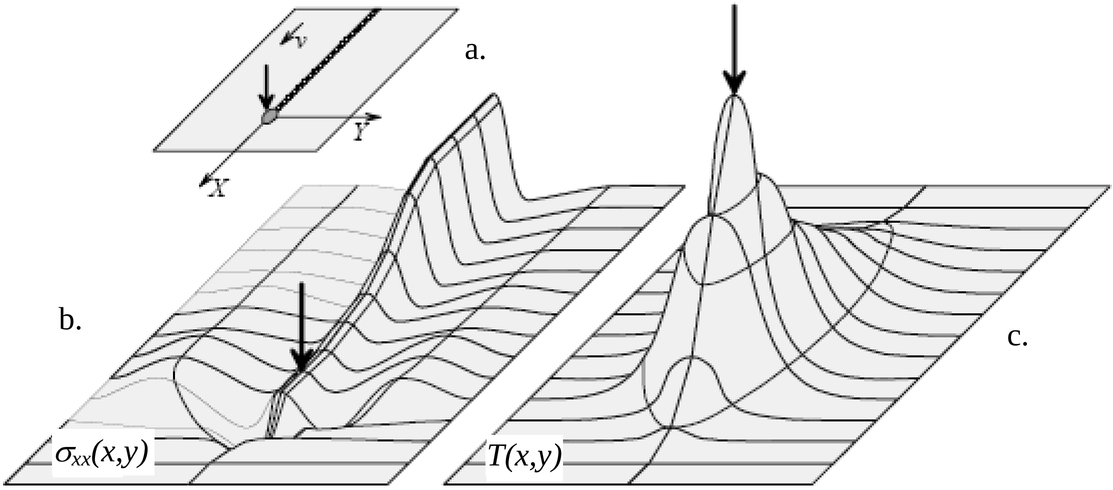

Figure 2.9. Schematic representation of temperature and longitudinal stress distribution during welding [PILA]

Far ahead from the heat source the temperature is constant and the stress is equal to zero at all the points. Moving in the negative direction of the x-axis, a point is reached where the temperature starts to rise. The points close to the weld line experience compression in the longitudinal direction immediately in front of weld pool. This deep fall changes to a fast rise of the longitudinal stress immediately behind the fusion zone. The rate of stress change is proportional to the temperature gradient ahead of the source. It is caused by the yielding point σ_y changing with temperature. At elevated temperatures the material begins to soften. After some particular temperature the material reaches the stage when σ_y is almost zero and so, the points situated close to the centreline reach the softening temperature, and climb up to a zero value of the longitudinal stress.

Stresses in the regions in the immediate vicinity of FZ are compressive, because the expansion of these areas is restrained by the surrounding metal where the temperature is still lower. However, stresses in the areas next to these compressive zones are the balancing tensile stresses. Going further, at some distance behind the FZ, the temperature drops sufficiently for the material to be stiff enough to resist the deformation caused by the temperature change. The FZ contracts due to cooling and as a result the tensile stresses arise. After a certain time, the temperature change due to welding diminishes. High tensile longitudinal stresses (usually reaching up to the yielding stress) are produced in the FZ. In the regions away from the FZ, compressive stresses exist.

Radaj [RADD] has classified various plastic zones in the vicinity of FZ for a case of quasi-stationary temperature field caused by a moving line heat source (Fig. 2.10). As mentioned earlier, the material reaching some critical temperature looses its strength. Beyond this temperature limit the material is almost free of stress because of the reduced yield limit at elevated temperatures. The broken parabolic line in Fig. 2.10 indicates the local temperature maximum and hence serves as the demarcation for compressive (ahead of heat source) and tensile (behind the source) regions.

The point *a.* marked in Fig 2.10 is the area somewhat ahead of heat source and hence experiences only elastic compression due to the expansion of FZ. Point *b.* is located inside the plastic compression zone, the region immediately in front of FZ. This plastic compression zone, when becomes part of the moving weld pool releases all the stresses in the molten metal. But if it remains outside the FZ, as for the case of Point *c.*, then after passing the maximum temperature isotherm it experiences tension due to the local contraction of the region behind the FZ. Point *d.* is the region where this tensile loading passes into plastic tension zone, whereas point *e.* experiences some relaxation of stresses due to localised annealing of high temperature isotherms following the FZ. All the regions from point a. to e. may be regarded as HAZ, as the release of stresses in the melt pool does not take place at these points. However, points *f.* and *g.*, located on the weld line, are the ones that do become part of FZ. It is for this reason that the moment material softening isotherm or FZ goes beyond these points, for instance point *g.*, they start experiencing tensile stresses due to the solidification shrinkage / contraction of the material. However, when heat source moves further ahead the points located on the weld line, for instance point *f.*, experience annealing due to trailing high temperature isotherms and hence some release of tensile stresses also takes place in these regions.

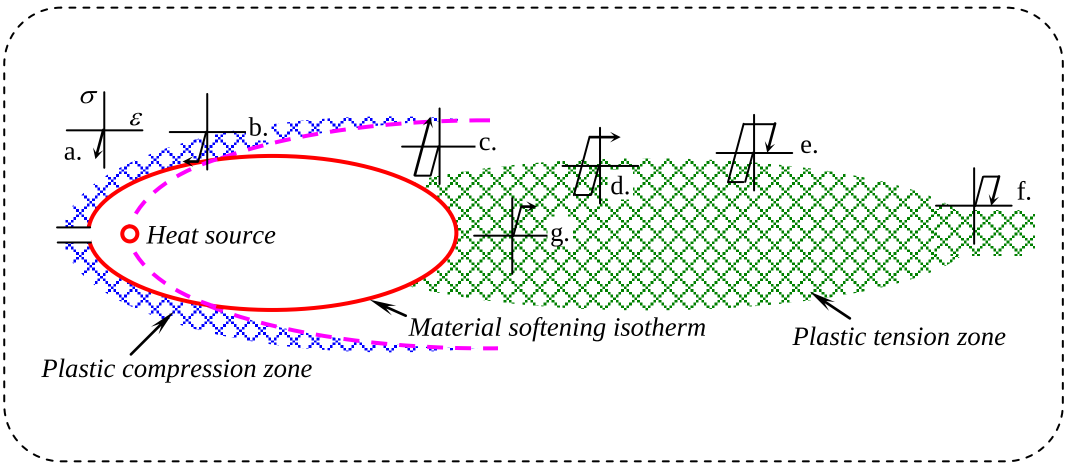

Figure 2.10. Stress-strain cycles in the quasi-stationary temperature field [RADD][ELAW]

2.10.2 Transverse Stress Development during Welding

Transverse residual stresses are generated by the transverse contraction of the weld during the cooling phase. It can also be generated indirectly due to the longitudinal contraction [RADD].

The development of transverse stresses during welding is somewhat similar to the longitudinal stress development. The stress distribution may be split into three regions; base metal (the unaffected material), HAZ and FZ. The base metal, as it experiences negligible temperature change, has zero stress level. Moving from the base metal to HAZ in the direction transverse to the weld line, a large hump of tensile stresses is met that grows into compressive stresses as FZ is approached. It is to be noted that for longitudinal stress development the stresses in HAZ and FZ are generally compressive and tensile in nature, respectively; however transverse stresses appear, in most cases, opposite in nature i.e. tensile in HAZ and compressive in FZ. The fact that residual stresses are in a self-equilibrium state explains the reason. Hence, independent of the stress distribution in the work piece, the stresses in any cross-section should be balanced by the sum of the forces and the sum of moment of forces.

Radaj [RADD] suggests that after the cooling of welded plates, due to the transverse and longitudinal material shortening, residual transverse stresses arise in the structure. If the plates were welded in a free condition (without tack welds and additional clamps), then the transverse stresses are not too large. The greatest values are reached near the ends of the weld. Stresses there can be both compressive and tensile.

A weld deposited instantaneously between two plates produces a gaping section in the middle of the weld length if the weld cools down without transverse restraint. The compressive stresses are initiated due to longitudinal shortening of the plastic deformation zone, and the plate edge tends to bend the way shown in Fig. 2.11.d. Transverse compression arises at the weld ends with a change to transverse tension when approaching the middle section of the weld length. During welding of short and narrow plates with a high welding speed, the plate edges move towards each other during cooling. The longitudinal shortening tries to bend plates in the plane. As a result, the residual stresses illustrated in Fig. 2.11.b are formed along the weld centreline.

If the welding speed is low enough for the weld metal to cool down to the temperature when the material is able to withstand loading, and it happens not so far behind the welding arc, then the end of the weld seam experiences tensile stresses as shown in Fig. 2.11.c. The additional clamping has a serious effect on the residual transverse stress distribution in welds.

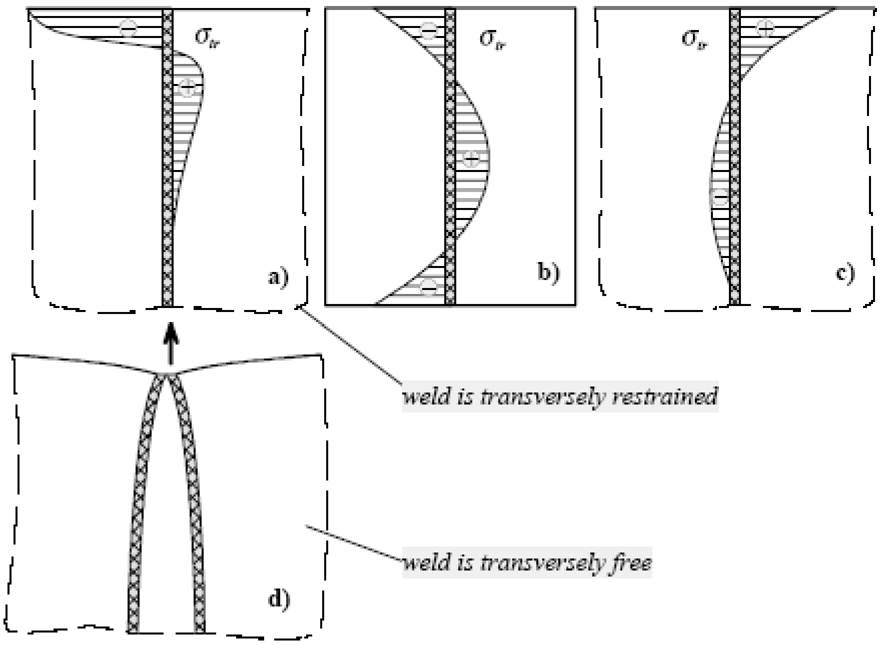

Figure 2.11. Transverse residual stresses in: (a) rapidly deposited weld in long plate; (b) rapidly deposited weld in short plate; (c) slowly deposited weld in long plate [RADD]

It should be mentioned that transverse stresses in the through-thickness direction also exist in weldments. Their level is high enough in some cases of welding to pay serious attention to them. An example [PILA] for the case in Fig. 2.12.a can be a one-pass sub-merged arc welding used for joining two medium-thick plates or any kind of welding in thin plates. Such processes are usually characterised by a relatively wide plastically deformed zone. The material in the area close to the welding line is able to “breath” in the through-thickness direction more or less freely. Hence, transverse stresses are low. To Fig. 2.12.b corresponds the case of highly concentrated electron-beam welding in thick and middle-thick plates. The metal of the narrow area close to the welding line is restricted in a through-thickness movement. And, in such a way, high residual stresses in the through-thickness direction are initiated.

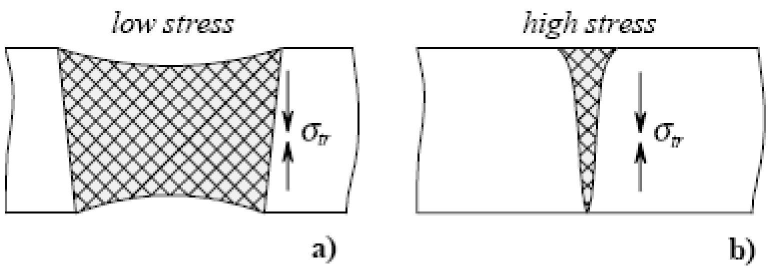

Figure 2.12. Transverse weld stress in through-thickness direction; (a) with relatively wide plastically deformed zone; (b) with narrow plastically deformed zone. [PILA]

2.11 Concluding Remarks

In this chapter, the principal of laser-beam welding process is briefly described. The welding consequences are given special emphasis. Various thermal and mechanical models are explained at length. It is established that being a thermo-mechanically coupled phenomenon the residual stress generation during welding is of complex nature. Moreover, metallurgical aspects are of importance, if there are solid state phase transformations in the material. Since, this is not the case with AA 6056-T4, the metallurgical aspects are ignored. Finally, the theory of residual stress development is discussed, and it is also established that the longitudinal residual stresses are of utmost significance.

CHAPTER 3

AA 6056-T4 THERMO-MECHANICAL CHARACTERISATION

Contents

SUMMARY

This chapter describes the material characteristics of AA 6056-T4 in detail. AA 6056-T4 is an aluminium alloy with Mg and Si as its major alloying additions. Here, term T4 indicates the naturally aged state of the alloy after having quenched from the phase α (a solid solution). Since welding involves heating of the component to very high temperatures, the mechanical properties of AA 6056-T4 are also identified at very high temperatures. Secondly, the effect of low and high strain rates is also studied in order to quantify the visco-plastic behaviour of the material. The material parameters which are presented in this chapter include Young's Modulus, yield strengths (at 0%, 0.1% and 0.2% offsets), hardening curves and dilatation coefficient.

The tensile tests, which were performed using conventional tensile testing machine and induction heating, are split into two categories with respect to strain rates; 0.0001 s^{-1} (low strain rate) and 1 s^{-1} (high strain rate). Further classification, for each strain rate, is based on the temperature attained in the area of interest. The desired temperature values are 20°C, 100°C, 200°C, 250°C, 300°C, 350°C, 400°C and 450°C. A dilatometric test was also performed in a dilatometer to measure the thermal expansion coefficient of the material. Some of the experiments were repeated to ensure the precise measurement of material properties.

Problems encountered during induction heating include high temperature gradient within the gauge length (especially at temperatures beyond 250°C) and very slow heating rate (1 – 15°C/s). Though efforts were made to heat the tensile test specimens at high temperature rate so as to avoid the precipitation/dissolution of various precipitates and compounds; the acquired heating rate of 1°C/s beyond 300°C, however, was likely to alter the material properties due to metallurgical phase transformations.

MAJOR CONCLUSIONS

The material properties like Young's modulus, yield strengths and hardening slopes are found to be decreasing with increasing temperatures; while with increasing strain rates their evolution shows an increasing trend. The effect of strain rates is such that it is negligible at lower temperature; while at higher temperature the viscous phenomenon dominates. Moreover, for the temperatures including and beyond 250°C, the material shows strain softening behaviour.

AA 6056-T4
Thermo-mechanical Characterisation

Understanding the way the materials respond to their surrounding conditions, whether static or dynamic, primarily entails a great deal of knowledge regarding their thermomechanical properties. Tensile tests performed under various thermal and mechanical loading conditions, generally, provide sufficient information about the material being used for certain application. With special reference to numerical simulation of welding, the material properties like Young's modulus, yield strength, proof strength, hardness parameters etc. are usually required as a function of temperature. These properties may easily be acquired from monotonic tensile tests; however, the hardening behaviour, whether isotropic or kinematic, may only be investigated with the help of cyclic and/or tensile-compression tests.

3.1 Aluminium Alloys

Aluminium alloys are amongst the most widely used alloys in modern aircraft construction. They are vital to the aviation industry because of their high strength to weight ratio, corrosion-resisting qualities, ductility, malleability and their comparative ease of fabrication. Aluminium alloys, in which the principal alloying ingredients are either manganese, magnesium, chromium or magnesium and silicon, show little attack in corrosive environments. On the other hand, those in which substantial percentages of copper are used are more susceptible to corrosive action. The total percentage of alloying elements is seldom more than 6 – 7% in the wrought aluminium alloys. These alloys may be divided into two categories; non-heat treatable and heat treatable. The non-heat treatable alloys may only be hardened by cold-working (strain-hardening); while the heat treatable alloys may be hardened either by heat treatment or by cold-working.

The International Alloy Designation System is the most widely accepted naming scheme for wrought alloys. Each alloy is given a four-digit number, where the first digit indicates the major alloying elements.

- 1000 series are essentially pure aluminium with a minimum 99% aluminium content by weight and can be work hardened.
- 2000 series are alloyed with copper, can be precipitation hardened to strengths comparable to steels, susceptible to stress corrosion cracking.

- 3000 series are alloyed with manganese and are work-hardenable.
- 4000 series are alloyed with silicon.
- 5000 series are alloyed with magnesium and derive most of their strength from work-hardening.
- 6000 series are alloyed with magnesium and silicon and can be precipitation-hardened.
- 7000 series are alloyed with zinc and can be precipitation-hardened to the highest strengths of any aluminium alloy.
- 8000 series is a category mainly used for lithium alloys.

3.2 AA 6056-T4 – An Introduction

AA 6056-T4 is an aluminium alloy that essentially contains Mg and Si as alloying additions. It is easy to machine and has strong weldability. Its chemical composition is shown in Table 3.1.

Mg	Si	Mn	Cu	Zn	Zr	Al
0.6-1.2	0.7-1.3	0.4-1.0	0.5-1.1	0.1-0.7	~ 0.2	Rest

Table 3.1. Chemical composition of AA 6056-T4 by % weight [DARC]

The term T4 represents the heat treatment process, which is given to the material. Heat treatment to increase strength of aluminium alloys is, generally, a three step process:

- Solution treatment: dissolution of soluble phases in solid state
- Quenching: development of supersaturated solid solution
- Age hardening: precipitation of solute atoms either at room temperature (natural ageing) or at elevated temperature (artificial ageing / precipitation heat treatment).

The heat treated aluminium alloys that involve natural ageing are designated as T4; while those which are artificially aged with precipitation hardening are nominated as T6. Owing to its better weldability, AA 6056-T4 is used to manufacture the fuselage panels and stringer assembly of aircraft structure. Figure 3.1 shows the aluminium-metal (Al-M) binary phase diagram, where M stands for any major metallic alloying addition. The diagram presents various liquid and solid phases and intermetallic compounds. The phase α is a solid solution of Al and M free of any compound (Al_xM_y) and precipitates.

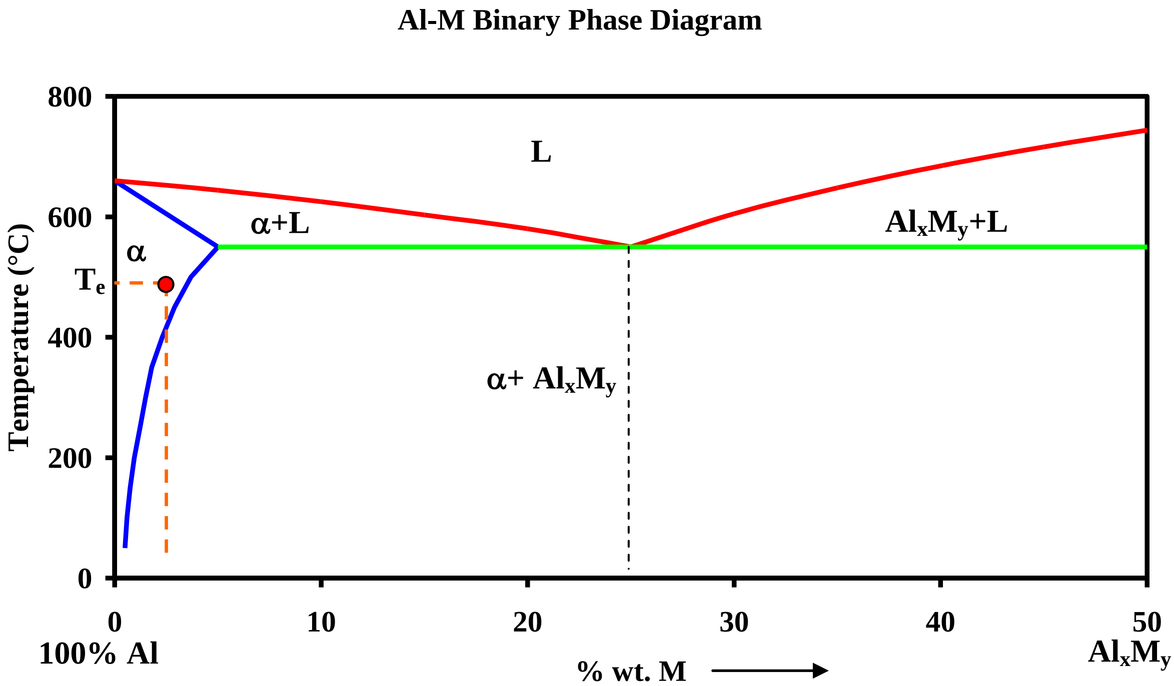

Figure 3.1. Al-M binary phase diagram

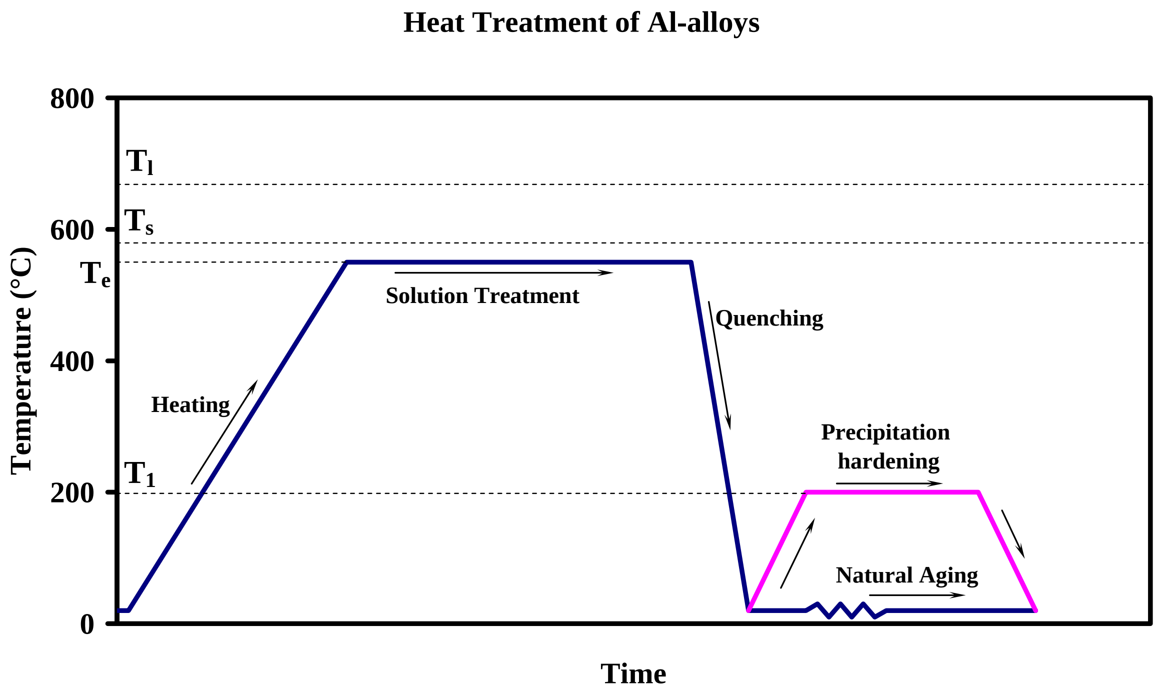

Figure 3.2. Heat treatment of Al-alloys

Figure 3.2 illustrates the complete heat treatment cycle of solution treatment and natural/artificial ageing. AA 6056-T4 is heated to an elevated temperature (T_e), and is held at this temperature for a certain length of time. This is done to completely dissolve all other phases in the phase α. The solid solution is then quenched to room temperature to avoid any diffusion and accompanying formation of the phase Al_xM_y. The super-saturated solution, so obtained, tends to release minute clusters of Al_xM_y in the matrix phase α. In some cases this precipitation occurs at room temperature and is known as natural ageing; while in some other cases, precipitation hardening is required to be performed at certain higher temperature (T_1) and is regarded as artificial ageing.

Table 3.2 presents approximate values of Young's modulus (E) and yield strength (σ_y) at different temperatures for aluminium alloy series 6XXX. The reported values are adopted from literature [SHAS][LEDH].

Temperature (°C)	Young's Modulus (GPa)	Yield Strength (MPa)
20	72.144	48~360
100	70.467	55~338
200	67.251	37~263
250	64.718	25~159
300	61.359	32~72
350	56.611	14~25
400	50.998	10~17
450	44.518	8~13
500	37.196	5~10

Table 3.2. Approximate values of E and σ_y for Al alloy series 6XXX

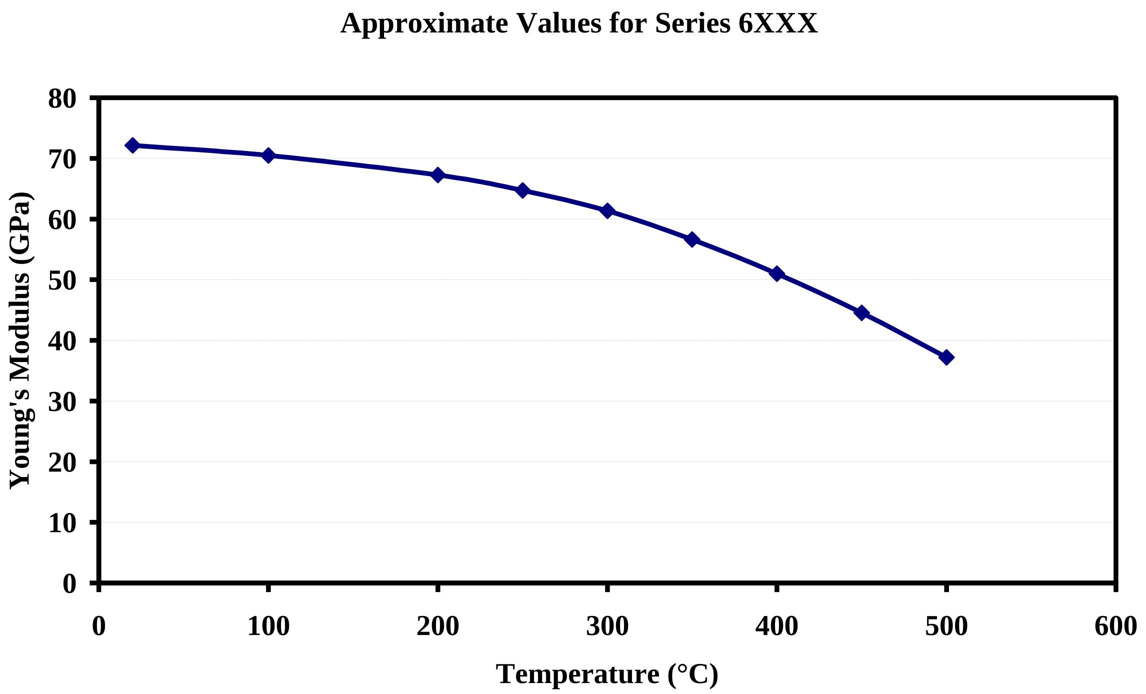

Figure 3.3. Young's modulus of Al-alloys series 6XXX

Evolution of Young's modulus as a function of temperature for aluminium alloy series 6XXX is presented in Fig. 3.3. The values of Young's modulus change from 72 GPa (at 20°C) to 37 GPa (at 500°C). The values of Young's modulus as a function of temperature for AA 6056-T4 lie in close approximation to these values. However, yield strength values for series 6XXX vary greatly even at a single temperature. For instance, this value may be as low as 48 MPa for one alloy, while for the other it may be as high as 360 MPa; each at room temperature. It is, therefore, difficult to develop any comparison of yield strength values with those of AA 6056-T4.

3.3 Experimentation Scheme

The experiments for thermo-mechanical characterisation were performed on a tensile (compression) testing machine Schenck of LaMCoS, INSA-Lyon. The machine operates hydraulically and has the capacity of 10 kN, with a load control range of 2-10 kN in tension, strain control of 20% and displacement control of ± 50 mm. Specimens of thickness 2.5 mm were machined from the plates provided by EADS. Schematic sketch of a typical tensile test specimen with the gauge length of 15 mm and a width of 10 mm is shown in Fig. 3.4 (see Annex B for detailed sketch).

A total of 5 K-type thermocouples (TCs) were welded on the specimens to record the temperatures. TC 3 pointing at position 'C' was installed in the middle of the specimen for controlling the temperature values through inductor, while the remaining TCs were welded at a distance of 3 mm from each other to record the temperature values of the specimen. The specimens were strained to 5% deformation for each given temperature and strain rate. For the tests carried out at temperatures greater than 20°C, sufficient holding time, without loading, was given to each specimen so as to attain homogeneous temperature within the gauge length and to compensate for the thermal dilatation. After 5% deformation, each specimen was unloaded and then reloaded only when the temperature reached a value of 20°C. This was done to observe the effect of thermo-mechanical history, if any. Table 3.3 gives the list of tensile tests carried out during the experimental campaign.

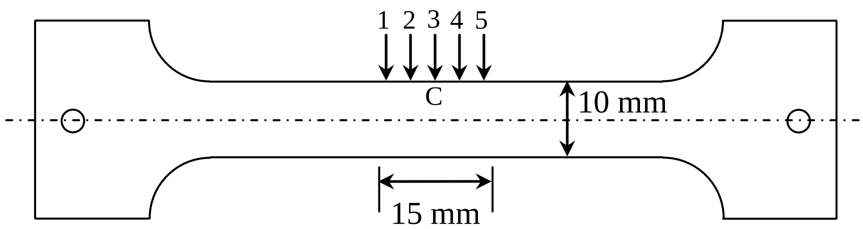

Figure 3.4. Tensile test specimen (Schematic sketch)

Temperature (°C)	**Strain Rate (s^{-1})**	**Specimen No.**
20	1	6056T4-06 6056T4-16
	0.0001	6056T4-04
100	1	6056T4-17
	0.0001	6056T4-03
200	1	6056T4-18
	0.0001	6056T4-05 6056T4-11
250	0.0001	6056T4-12
300	1	6056T4-19 6056T4-24
	0.0001	6056T4-07 6056T4-13
350	1	6056T4-21
400	1	6056T4-20
	0.0001	6056T4-08 6056T4-15
435	0.0001	6056T4-09
445	0.0001	6056T4-10
450	1	6056T4-22

Table 3.3. Layout plan of tensile tests

A few tests were repeated to ensure the reliability of results. Although the inductor was set to heat the specimens at a maximum rate of 25°C/s in each case, yet the actual recorded temperature rate was between 10 – 15°C/s. Following temperature rates were programmed for heating the specimens:

- For temperature up to 200°C, temperature rate = 25°C/s
- From 200°C to 300°C, temperature rate = 5°C/s
- From 300°C to 450°C, temperature rate = 1°C/s

To compute the dilatation coefficient an additional test was also performed at the end.

3.4 Loading Conditions

Figure 3.5 shows the thermal and mechanical loading conditions employed during tests. First loading for each test was carried out at required temperature (T_{req}) while second loading was performed at ambient temperature (T_0). The purpose of second loading was to observe the effect of thermal and mechanical history upon the properties of material; however the results of second loading are not included in this dissertation. Specimens were strained up to 5% and 10% during 1st and 2nd loadings, respectively. Second loading was carried out only for the tests with strain rate 0.0001 s^{-1}.

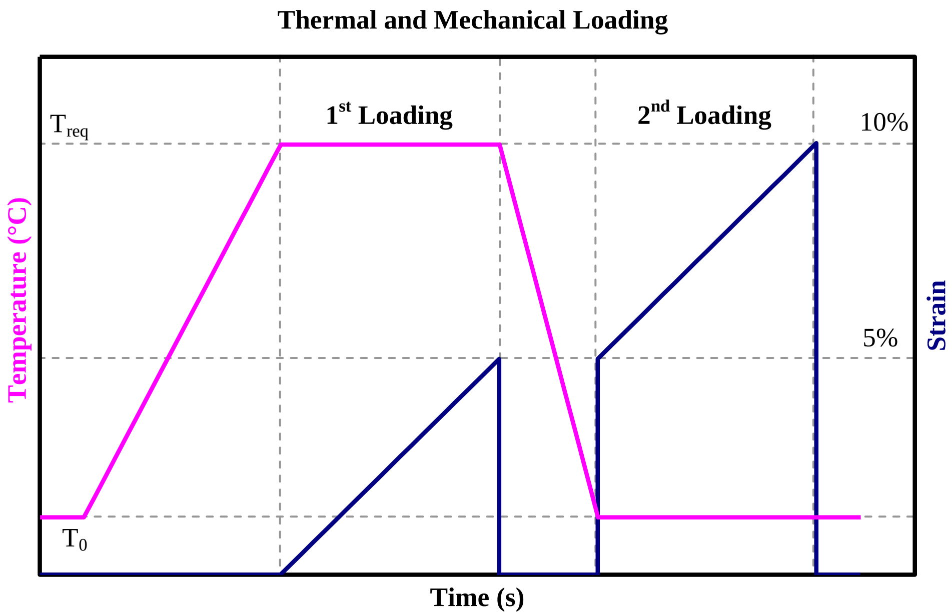

Figure 3.5. Thermal and mechanical loading

3.5 Results Treatment

The treatment of test results is performed with respect to the requirements of the FE code Abaqus. As far as the data related to the temperature dependent mechanical properties is concerned, Abaqus requires the definition of Young's modulus, Poisson's ratio, yield strength, dilatation coefficient and strain hardening curves all as a function of temperature and / or strain rates. Since Abaqus is capable of treating the hardening curves in the form of point data; the tensile tests exploited here, present the method of determining Young's modulus and yield strength. However, the strain-hardening curves are required to be entered in terms of true stress and true strain. Moreover, in order to define rate dependent plasticity, the values of yield strengths at various strain rates are to be provided.

3.5.1 Strain Rate: 0.0001 s^{-1}

A few cases of the tensile tests are now being presented so as to explain how the resulting stress-strain curves have been treated. Figure 3.6 presents the result of tensile test carried out at 20°C and at a strain rate of 0.0001 s^{-1}. The term engineering stress means force (N) per unit original area (mm^2); total strain gives originally recorded values from extensometer while engineering strain represents adjusted strain values (set to zero strain at the start of 1st loading). Figure 3.7 shows same curve up to 5% engineering strain.

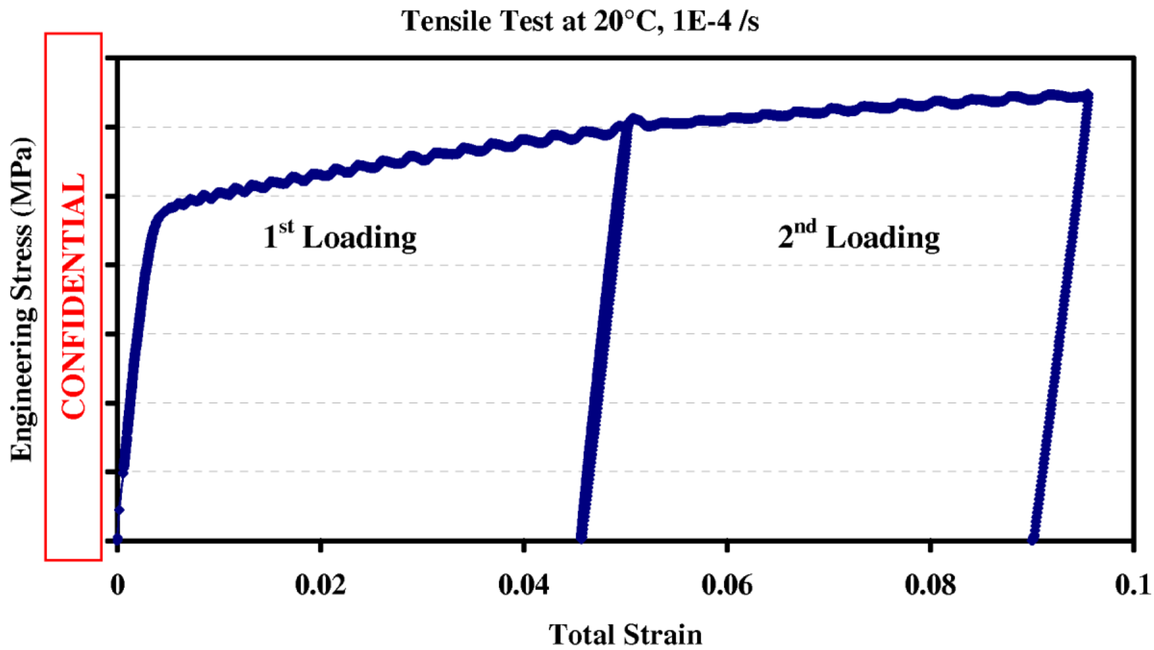

Figure 3.6. Stress-strain curve at 20°C and 0.0001 s^{-1}; Specimen no. 6056T4-04

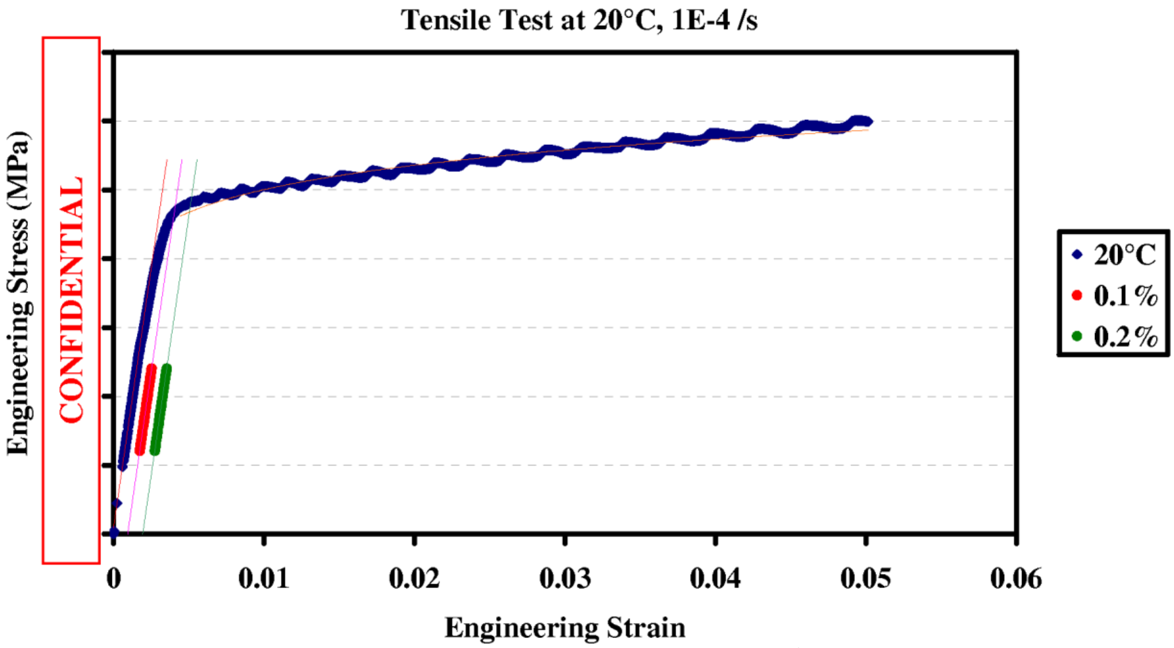

Figure 3.7. Stress-strain curve at 20°C, 0.0001 s^{-1} up to 5% strain

The materials that do not show a well-defined yield point, an offset value of 0.1% or 0.2% is taken as standard to calculate yield strength. Three trend lines parallel to elastic part of the curve are drawn to mark the yield strength values at 0%, 0.1% and 0.2%. These lines also serve to calculate the Young's modulus, which, in turn, is determined from the slope of a straight line drawn between the stress values starting from 10% of maximum stress to 50% of maximum stress recorded; wherever possible. The plastic part of the curve is filtered to obtain smooth lined curve. Filtering is done using moving average algorithm of MATLAB.

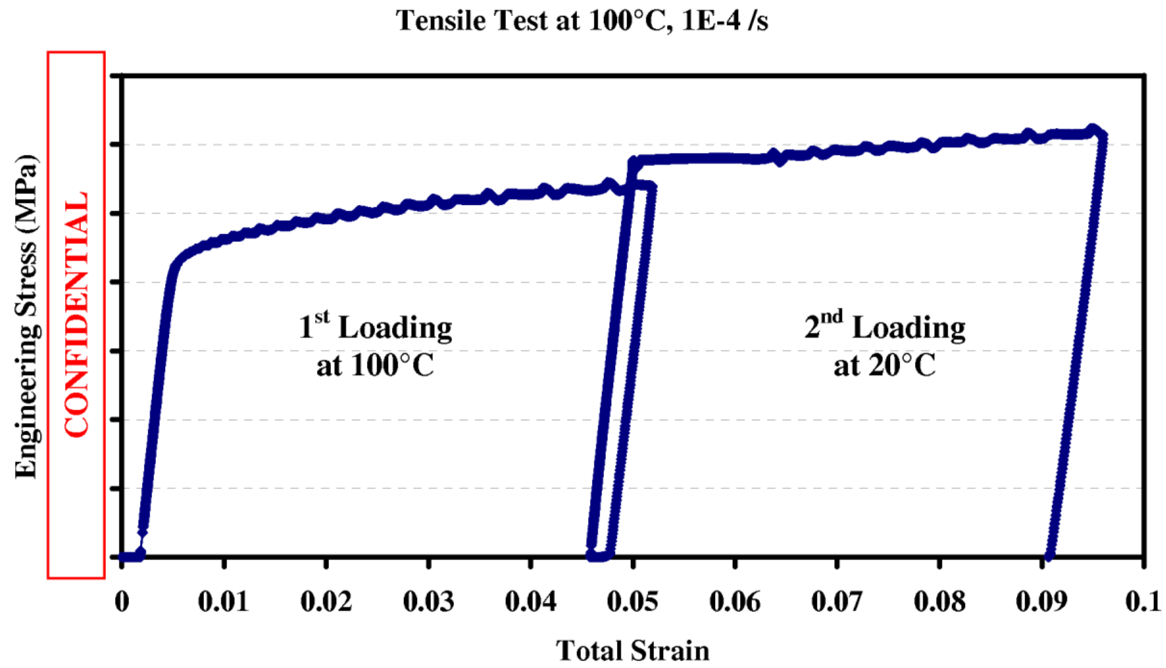

Figure 3.8. Stress-strain curve at 100°C and 0.0001 s^{-1}; Specimen no. 6056T4-03

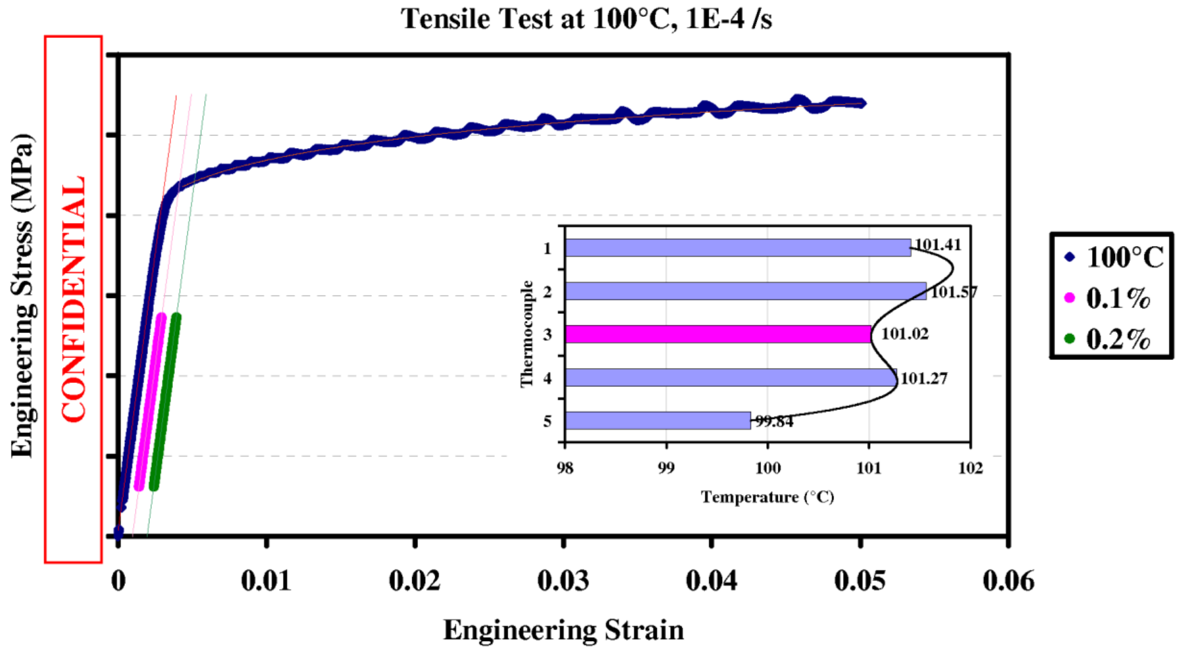

Figure 3.9. Stress-strain curve at 100°C, 0.0001 s^{-1} up to 5% strain

Figure 3.8 presents the stress-strain curve at a temperature of 100°C and at a strain rate of 0.0001 s^{-1}. What differentiates this curve from the one at 20°C is the initial thermal expansion. The non-zero value of deformation at zero stress level just before the start of tensile test is because of the thermal dilatation of AA 6056-T4. A delay time of few seconds is given at zero stress so as to accommodate the dilatation effects and allow the temperature homogenization in the area of interest. Once the inherent level of dilatation at any specific temperature is reached, the specimen is strained up to 5%. Temperature is kept constant until unloading is complete. Thermal contraction is observed after first unloading when the temperature drops to room temperature. Figure 3.9 shows the separated part of the curve in Fig. 3.8 up to 5% of strain. The acquired temperature values at various thermocouples are also shown. A temperature difference of approximately 3°C is observed in the gauge length of 15 mm. Young's modulus and yield strength are determined in a way similar to the tensile test at ambient temperature (20°C).

Two of the tensile tests at same strain rate but at different temperatures have so far been explained. The subsequent tests at elevated temperatures for this strain rate have been treated the same way, and hence are not being discussed to avoid repetition.

Generally, at higher temperatures and with constant strain rate, a gradually decreasing level of stress is observed to cause the same level of strain; or in other words with increasing temperature and constant strain rate the slope of the elastic region decreases, which, in turn, decreases Young's modulus of material.

3.5.2 Strain Rate: 1 s^{-1}

Along with high temperature rates, welding processes involve high strain rates as well. Efforts have, therefore, been made to carry out the tensile tests at strain rates as high as 1 s^{-1}. The problem encountered, while carrying out these tensile tests, was the performing of tests in deformation mode, which at high strain rate is likely to cause severe damage to machine since in deformation mode the pulling action of tensile testing machine takes command from extensometer. At such a high strain rate, just a little slip of extensometer may cause the pulling shaft of machine to move unexpectedly in upward / downward direction, thereby causing serious damage. Therefore, the tests had been carried out in displacement mode. Attempts had been made to adjust such a displacement rate that could give strain rates in near approximation to 1 s^{-1}. A very fast acquisition of data points was used, since slower acquisition was found unable to record sufficient information.

Figure 3.10 presents the stress-strain curve obtained at a temperature of 20°C and strain rate of 1 s^{-1}. The specimen is deformed up to 5% strain. A filtered curve is obtained from raw data curve. The slope of the curve between strain and time gives a value of 0.9967 s^{-1} (~ 1 s^{-1}). The values of Young's modulus and yield strengths at 0%, 0.1% and 0.2% are calculated from filtered data and are presented in Fig. 3.11. The initial one third values of stress are taken as standard to determine Young's modulus.

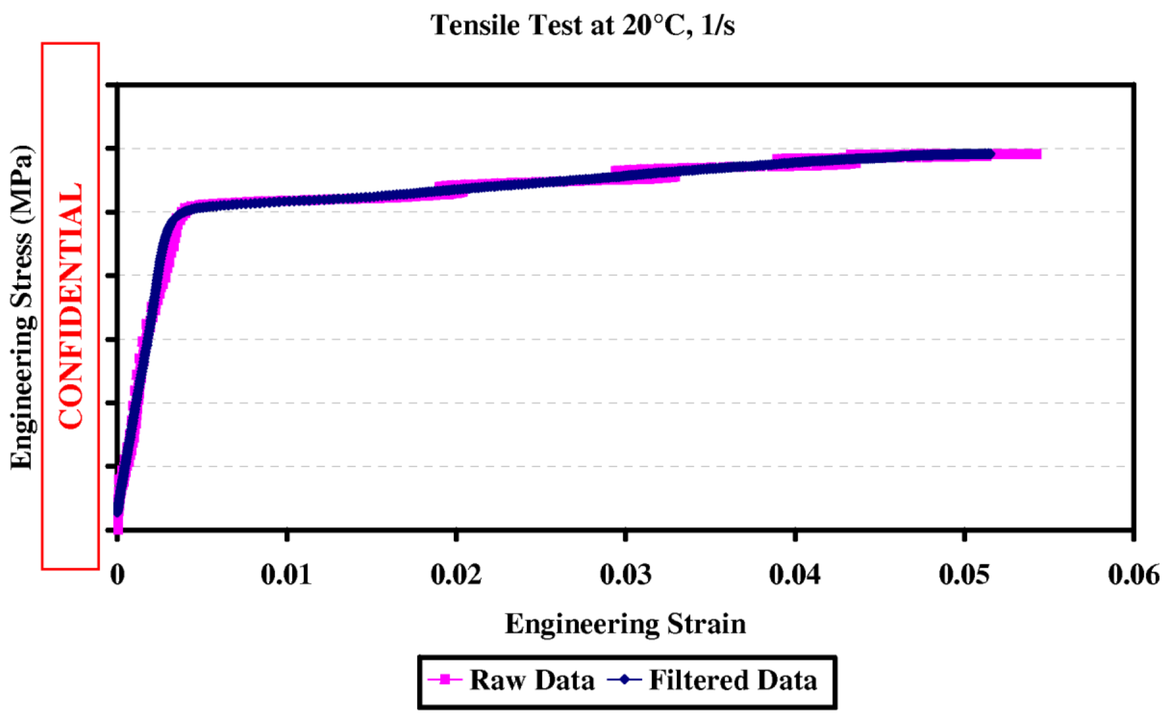

Figure 3.10. Stress-strain curve at 20°C and 1 s^{-1}; Specimen no. 6056T4-16

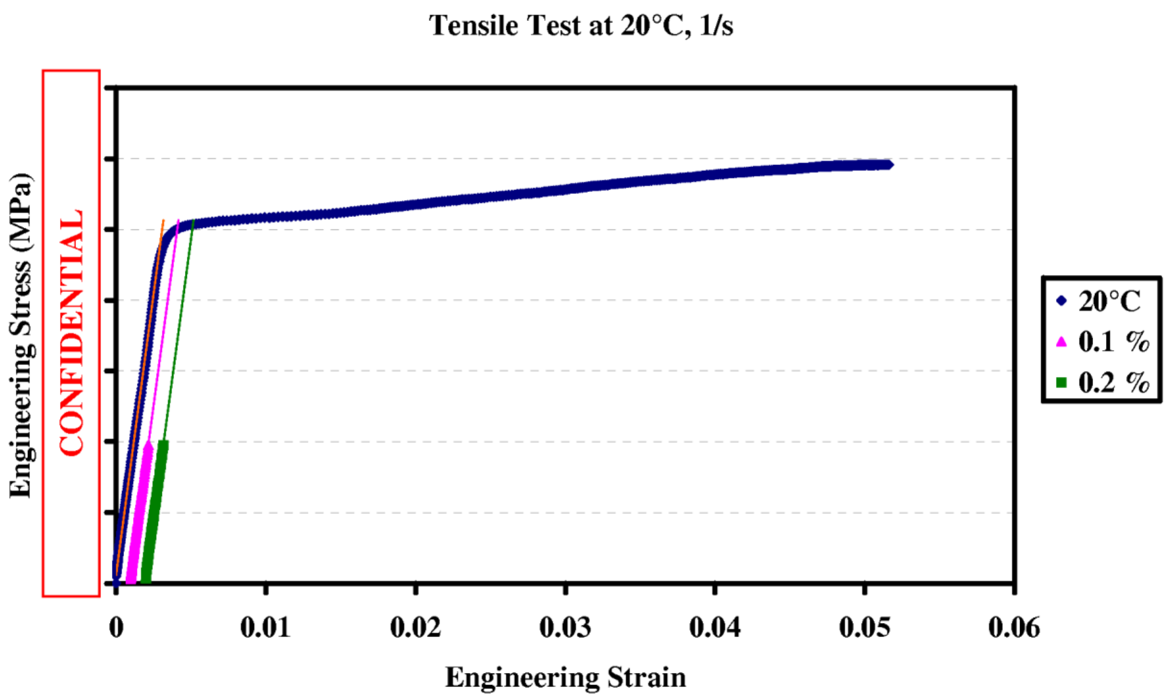

Figure 3.11. Stress-strain filtered curve at 20°C, 1 s^{-1} up to 5% strain

Similarly, Fig. 3.12 presents the stress-strain curve obtained at the temperature of 100°C and at strain rate of 1 s^{-1}. The filtered data is separated from raw data and is further used to calculate the Young's modulus and yield strengths at 0%, 0.1% and 0.2% (Fig. 3.13). The strain rate value during the test is found to be 1.019 s^{-1} (~ 1 s^{-1}), while the temperature difference within the gauge length is less than 1°C and is also shown in Fig. 3.13.

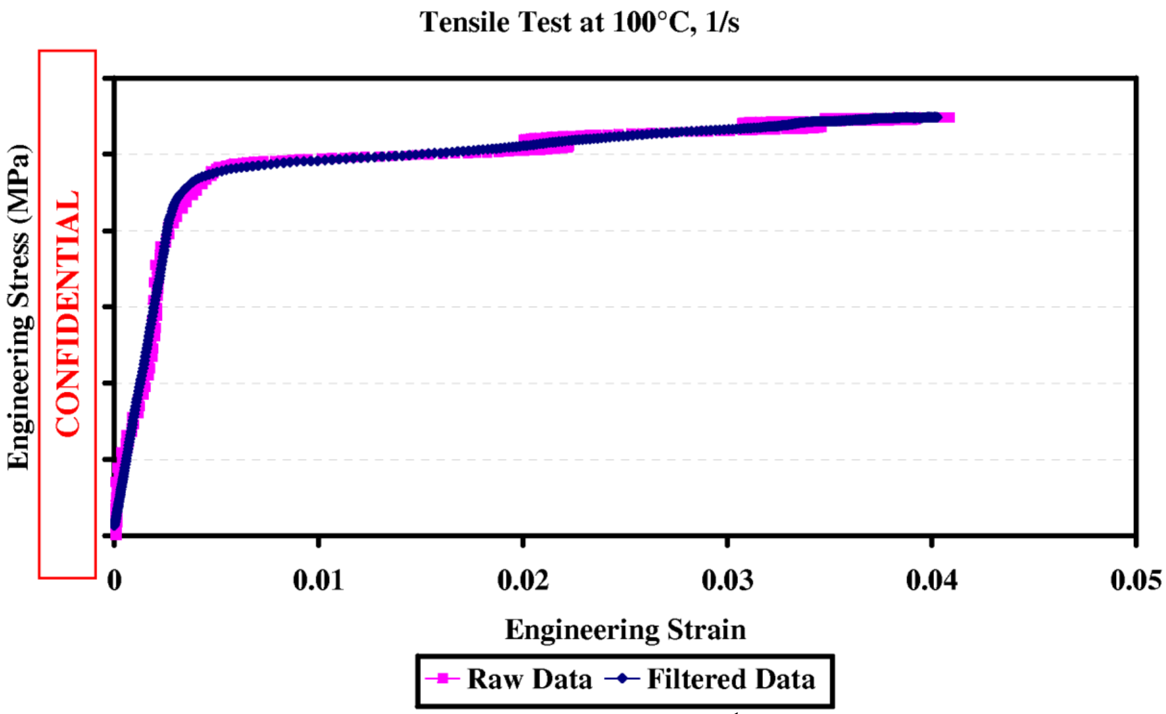

Figure 3.12. Stress-strain curve at 100°C and 1 s^{-1}; Specimen no. 6056T4-17

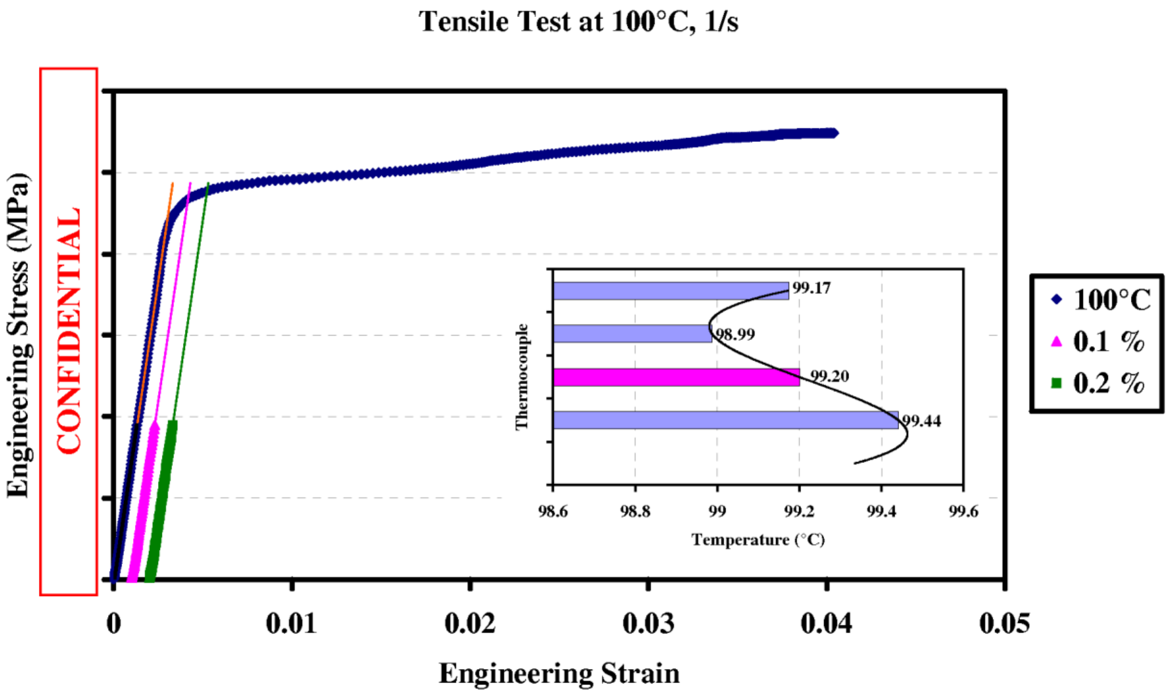

Figure 3.13. Stress-strain filtered curve at 100°C, 1 s^{-1} up to 5% strain

The remaining stress-strain curves are treated the same way. For the temperatures greater than 300°C, the elastic part of the curves are found difficult to be exploited because, due to the high strain rate, very few points are available in the elastic region. However, the curves at higher temperatures show elastic-perfectly plastic behaviour, which implies that the values of yield strengths at 0%, 0.1% and 0.2% may be calculated with reasonable accuracy.

3.6 Stress-strain Curves

Engineering stress-strain curves assume that the stress and strain depend upon the original cross-sectional area (A_0) and original gauge length (L_0), respectively. The tensile testing machine records the force (F) and the extensometer measures the displacement (δ) from where engineering stress (σ_e) and strain (ε_e) are calculated as follows:

$$\sigma_e = F / A_0; \qquad \varepsilon_e = \delta / L_0 \tag{3.1}$$

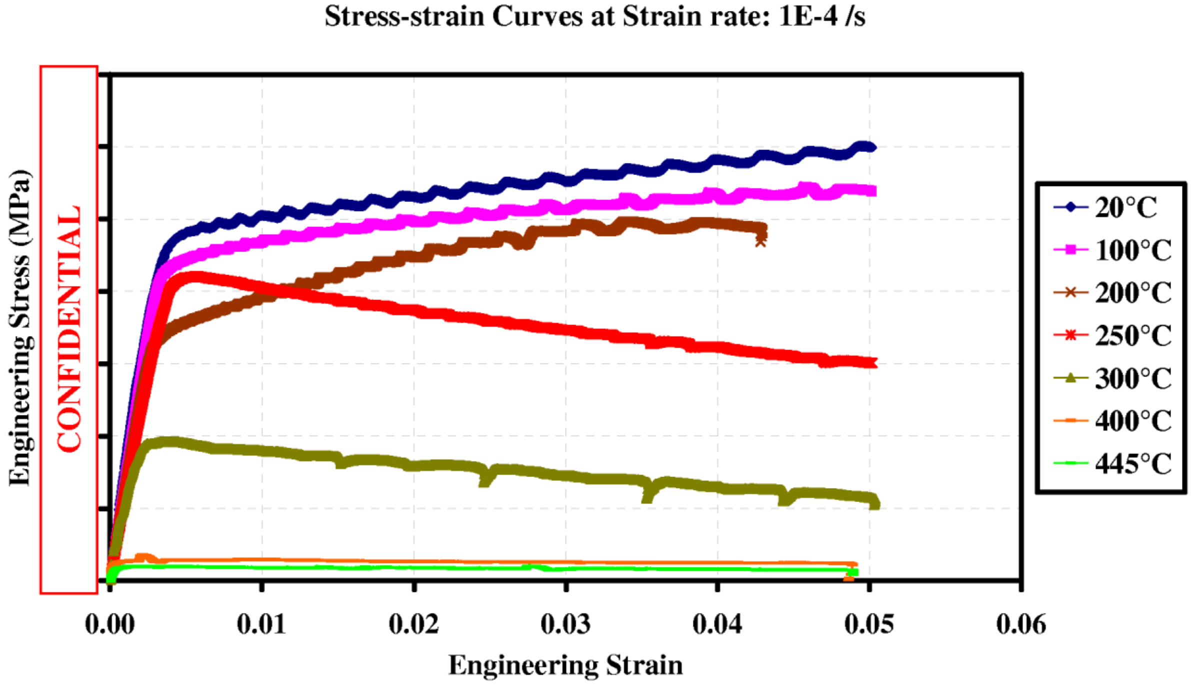

Figure 3.14. Engineering stress-strain curves at 0.0001 s^{-1}

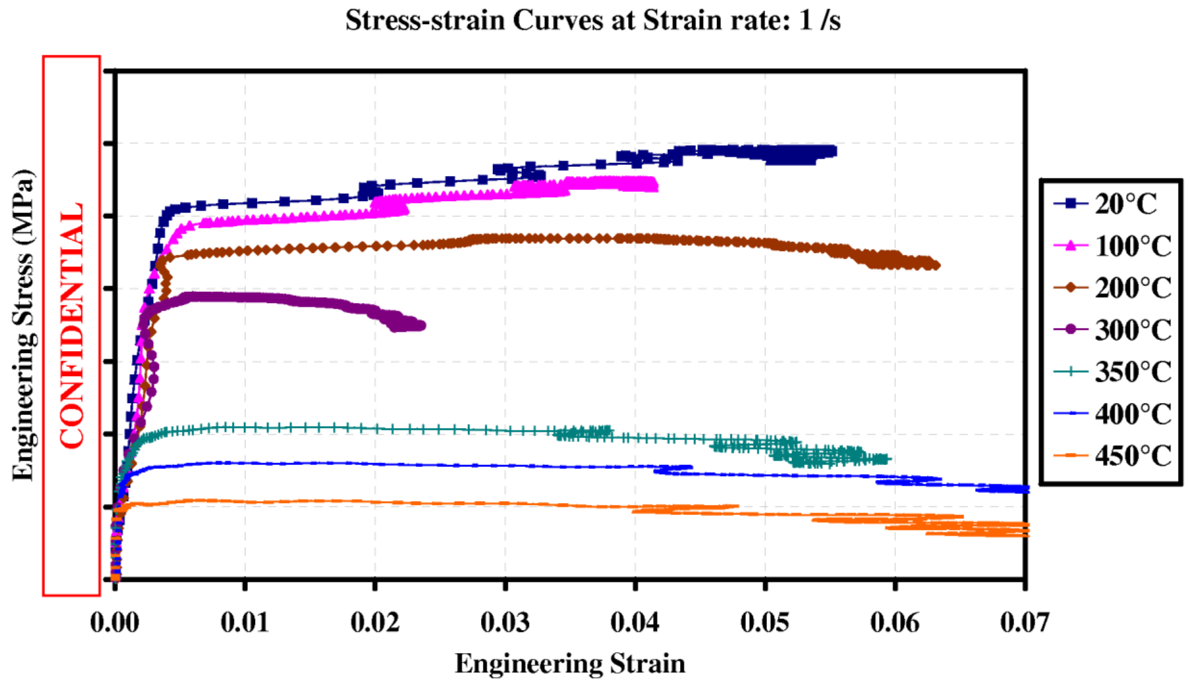

Figure 3.15. Engineering stress-strain curves at 1 s^{-1}

Figures 3.14 and 3.15 illustrate the engineering stress-strain curves in untreated form for the strain rates of 0.0001 s^{-1} and 1 s^{-1}, respectively. These curves provide reliable information during elastic deformation. However, since beyond the elastic limit the specimen dimensions experience substantial changes from their original values; the instantaneous area (A_i) and instantaneous length (L_i) play vital role in measuring the material response in the plastic flow range. The true stress (σ_t) and true strain (ε_t) are, therefore, defined to obtain true stress-strain curves.

$$\sigma_t = \frac{F}{A_i}; \qquad \varepsilon_t = \int_{L_0}^{L_i} \frac{1}{L_i} dL = \ln \frac{L_i}{L_0} \tag{3.2}$$

During yield and the plastic-flow regime following yield, the material flows with negligible change in volume; increases in length are offset by decreases in cross-sectional area. Prior to necking, when the strain is still uniform along the specimen length, this volume constraint can be written:

$$dV = 0 \Rightarrow A_i L_i = A_0 L_0 \Rightarrow L_i / L_0 = A_0 / A_i \tag{3.3}$$

From where:

$$\sigma_t = \sigma_e (1+\varepsilon_e); \qquad \varepsilon_t = \ln(1+\varepsilon_e) \tag{3.4}$$

These equations can be used to derive true stress-strain curves. Figures 3.16 and 3.17 show the true stress-strain curves at 0.0001 s^{-1} and 1 s^{-1}, respectively.

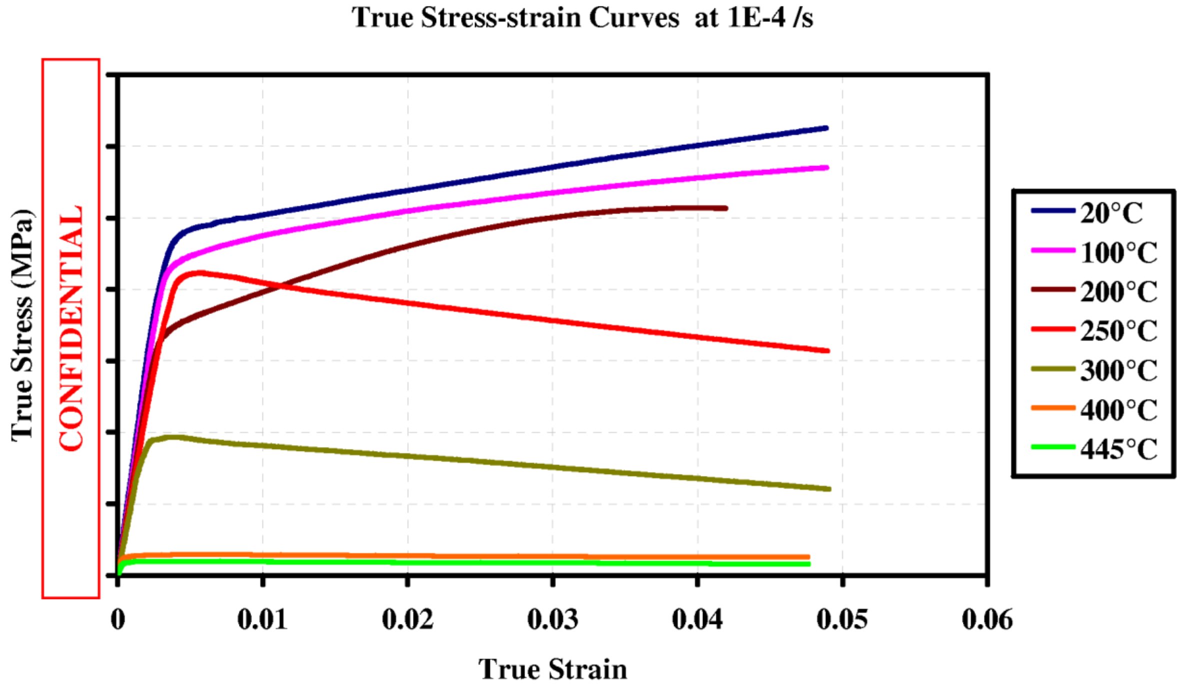

Figure 3.16. True stress-strain curves at 0.0001 s^{-1}

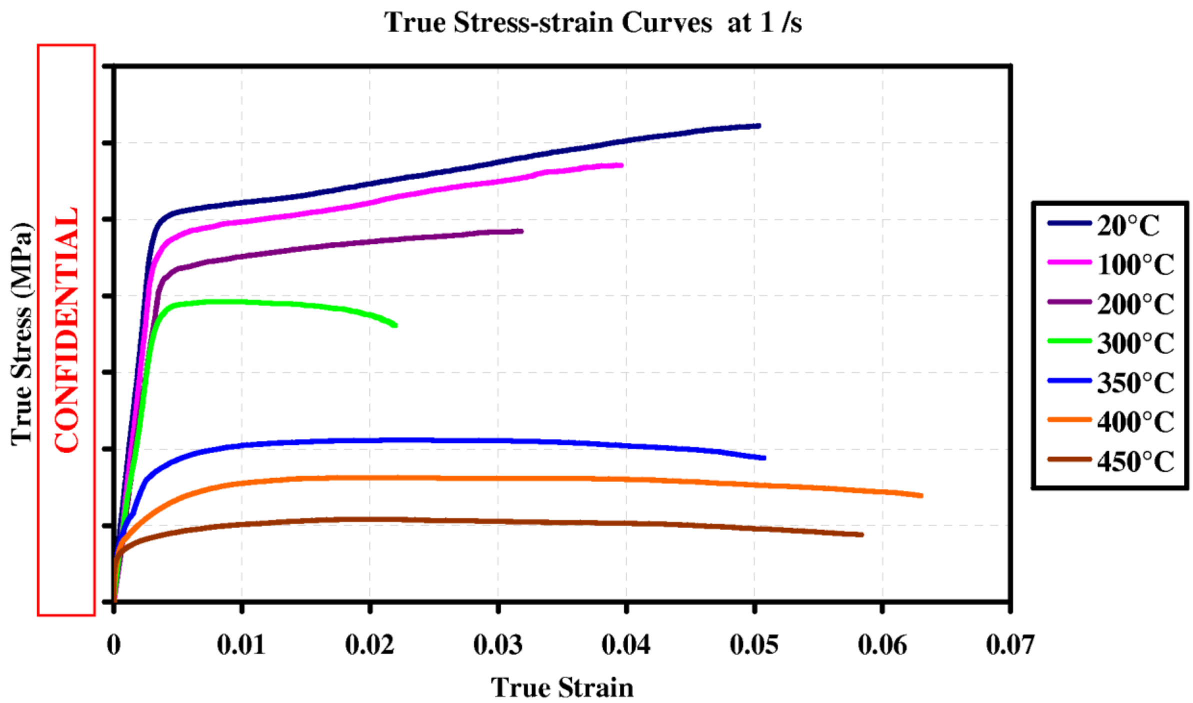

Figure 3.17. True stress-strain curves at 1 s^{-1}

A regular trend of decreasing hardening slopes with increasing temperatures is observed for both types of tests (Figs. 3.16 and 3.17). Tensile tests performed at the strain rate of 0.0001 s^{-1} show strain softening effects starting from temperature 250°C; while the ones performed at 1 s^{-1} illustrate elastic-perfectly plastic behaviour beyond 300°C. The true stress-strain curve at 250°C and 0.0001 s^{-1} shows a comparatively different evolution of stress values as a function of strain. It will be observed in the subsequent sections that for a constant strain rate the yield strength values decrease with increasing temperature; however, contrary to the trend, the yield strength value at 250°C surpass the ones determined at 200°C. Metallurgical studies [MONF][HERR] show that dynamic recrystallization is responsible for such kind of behaviour. This phenomenon appears during straining of metals at high temperature, characterised by a nucleation rate of low dislocation density grains and a posterior growth rate that can produce a homogeneous grain size when equilibrium is reached. It occurs only after a critical amount of strain which is dependent on the type of strain path, the initial grain size, temperature and strain rate. When the critical strain is reached, strain-hardening and dynamic recovery cease to be the principle mechanisms responsible for the stress-strain response; dynamic recrystallization accompanies the process. At micro-structural level strain hardening can no longer store more immobile dislocations. At the peak stress level grain boundaries bulge until a new grain is formed. Upon reaching the equilibrium state the stress level drops to steady state.

3.7 Material Properties

The qualification of material properties is one of the most important steps to be considered cautiously. Various sources of errors arising during testing and data exploitation may lead to erroneous determination of elastic / plastic parameters. Performing all or few of the tensile tests twice or thrice is one of the ways of establishing consistent results. Persistent trend in the evolution of properties may also serve as benchmark for their qualification.

3.7.1 Strain Rate: 0.0001 s^{-1}

Figures 3.18 to 3.21 present evolution of Young's modulus and yield strengths at 0%, 0.1% and 0.2% as a function of temperature. These curves show the point data determined from each tensile test. Some of these tests are repeated to ensure the reliability of results. A trend line is drawn for each material parameter in such a way that most of the points lie on or close to it. Since enough data is available the values lying away from the trend line may be ignored.

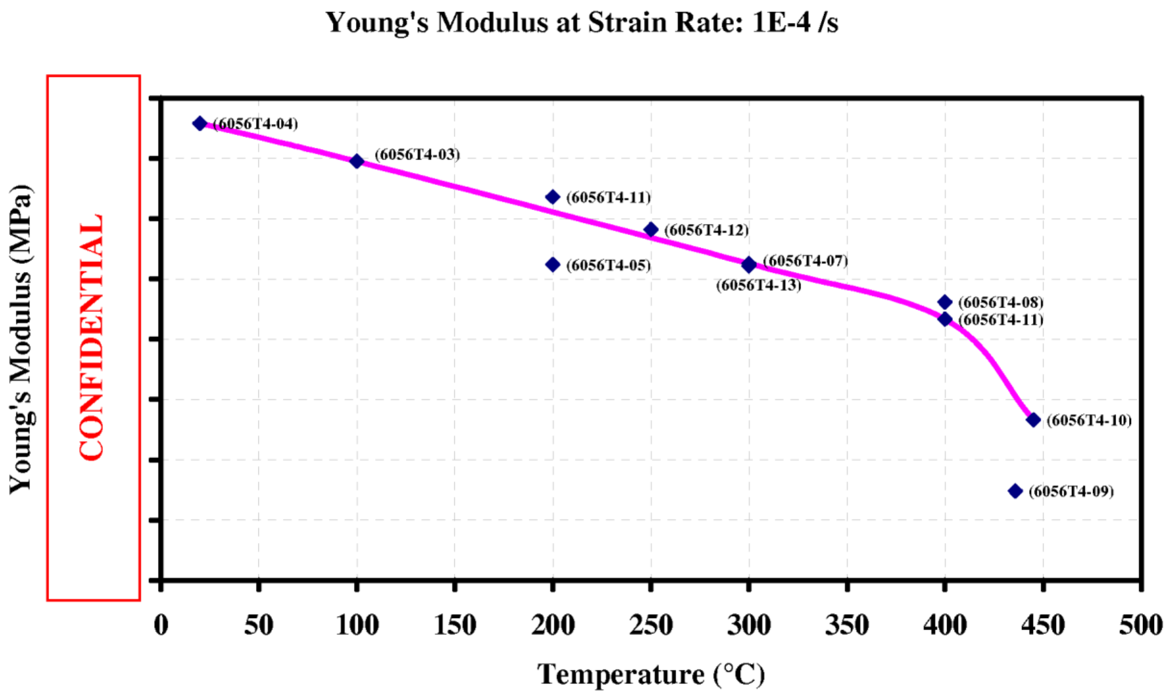

Figure 3.18. Young's modulus as a function of temperature at strain rate: 0.0001 s^{-1}

The evolution of 0% yield strength (Fig. 3.19) shows somewhat different trend as compared to 0.1% and 0.2% yield strengths (Figs. 3.20 and 3.21). The reason for this difference is the uncertainty in determining the yield strength at 0%. As yield strengths at 0.1% and 0.2% are calculated from the offset lines drawn parallel to elastic region of the stress-strain curves; they intersect the curves at a distinct level of stress and hence provide the precise values. However, yield strength at 0% is noted at the stress where slope of the elastic region separates the stress-strain curve; which, in fact, is a qualitative way of determining a value. An important observation is the abrupt increase in the values of 0.1% and 0.2% yield strengths at a temperature of 250°C. It has been discussed in the previous section that an increased value of yield strength results due to the dynamic recrystallization.

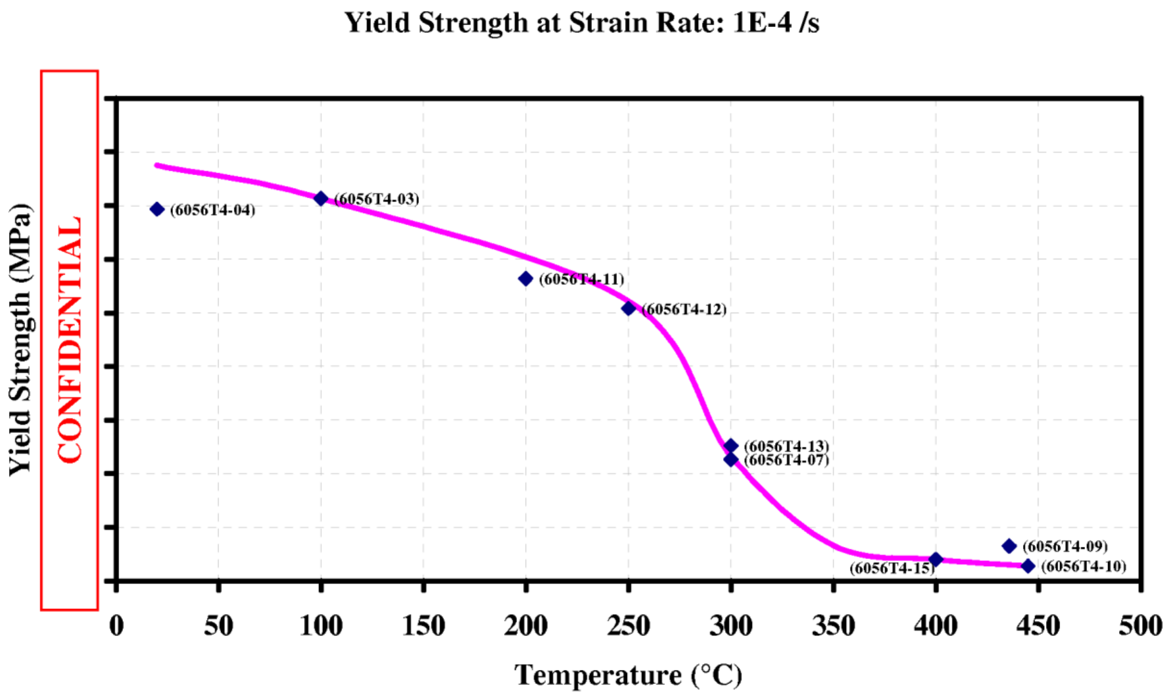

Figure 3.19. Yield strength (0%) as a function of temperature at strain rate: 0.0001 s^{-1}

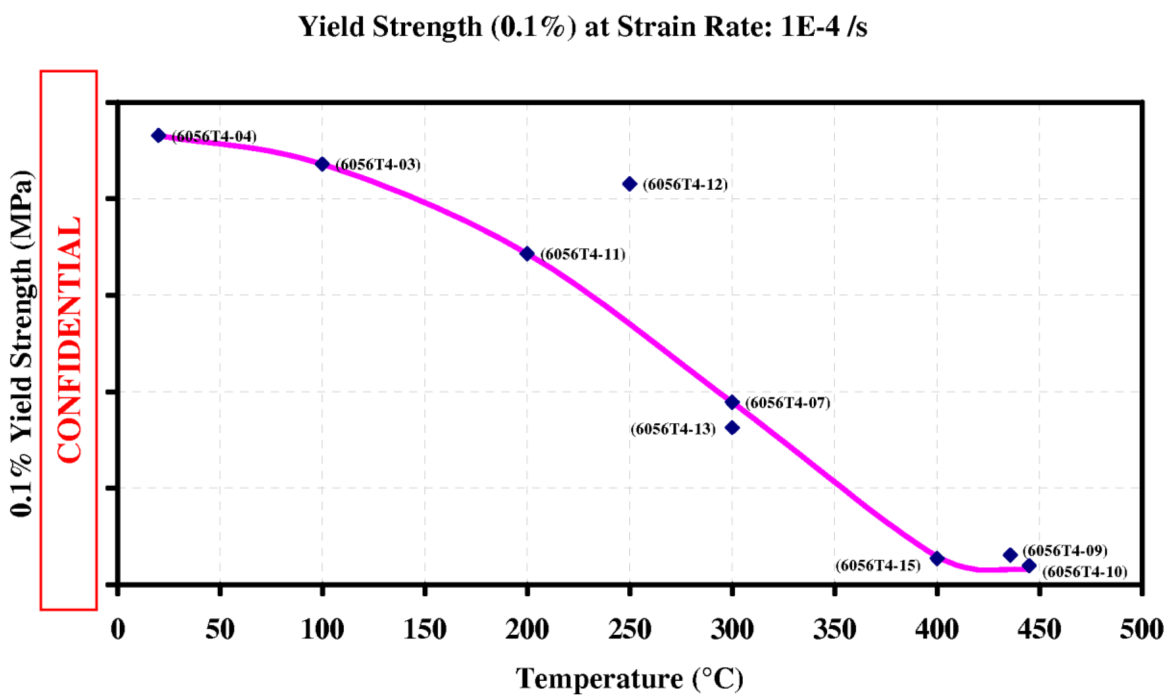

Figure 3.20. Yield strength (0.1%) as a function of temperature at strain rate: 0.0001 s^{-1}

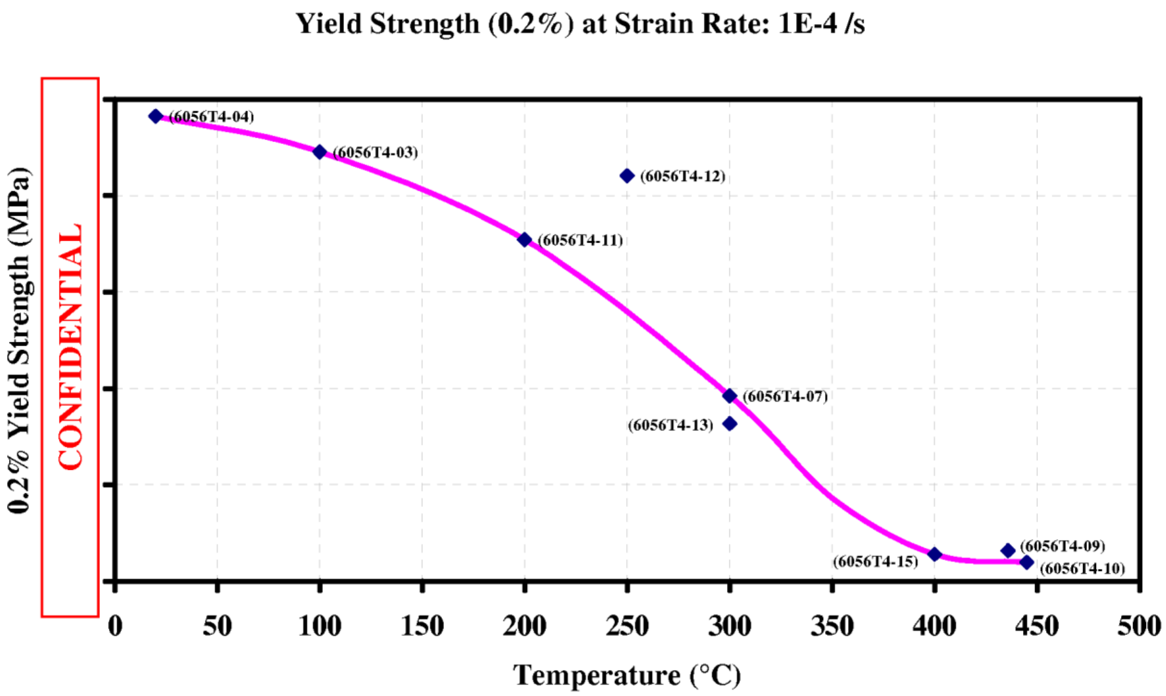

Figure 3.21. Yield strength (0.2%) as a function of temperature at strain rate: 0.0001 s^{-1}

3.7.2 Strain Rate: 1 s^{-1}

Figure 3.22 presents evolution of Young's modulus as a function of temperature. The curve is produced in a similar fashion as described in the previous section. Most of the data points lie on the trend line. Not much deviation from general trend is observed. The values of Young's modulus decrease with increasing temperature.

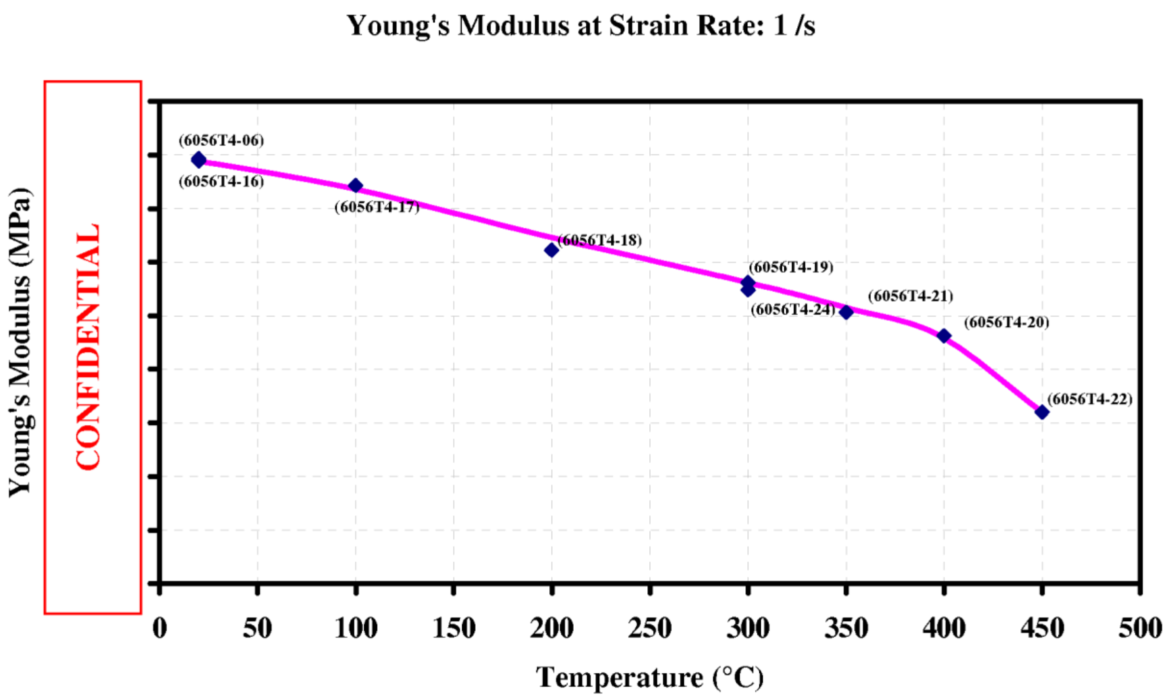

Figure 3.22. Young's modulus as a function of temperature at strain rate: 1 s^{-1}

Yield strength values at 0%, 0.1% and 0.2% as a function of temperature are presented in Figs. 3.23, 3.24 and 3.25, respectively. Tensile tests performed at 300°C show two distinct values in each case. One of these values is ignored because the variation in temperatures recorded at thermocouple position is found to be more than 30°C; and as the material properties change abruptly at higher temperatures, little variation on temperature distribution may lead to uncertain results.

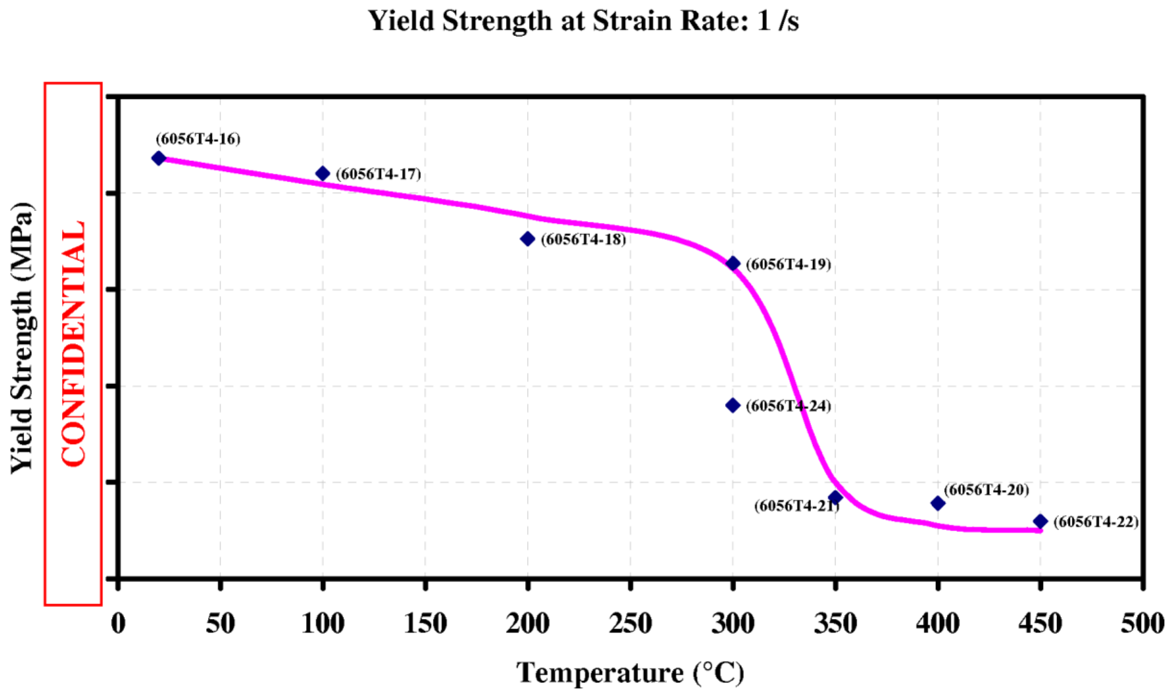

Figure 3.23. Yield strength (0%) as a function of temperature at strain rate: 1 s^{-1}

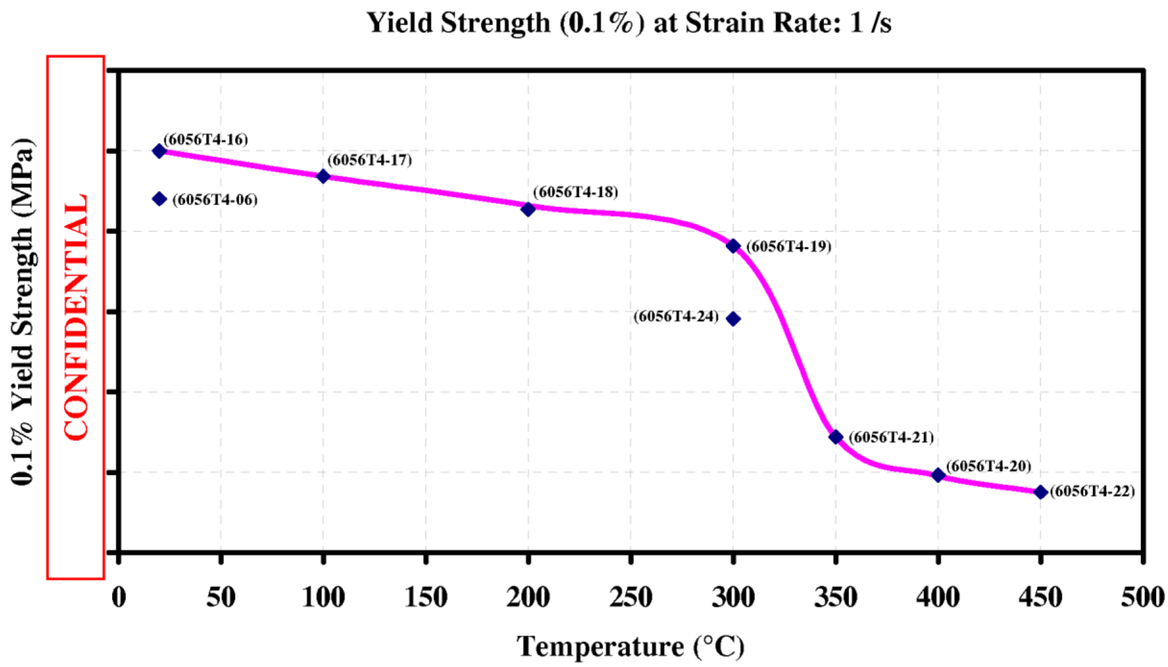

Figure 3.24. Yield strength (0.1%) as a function of temperature at strain rate: 1 s^{-1}

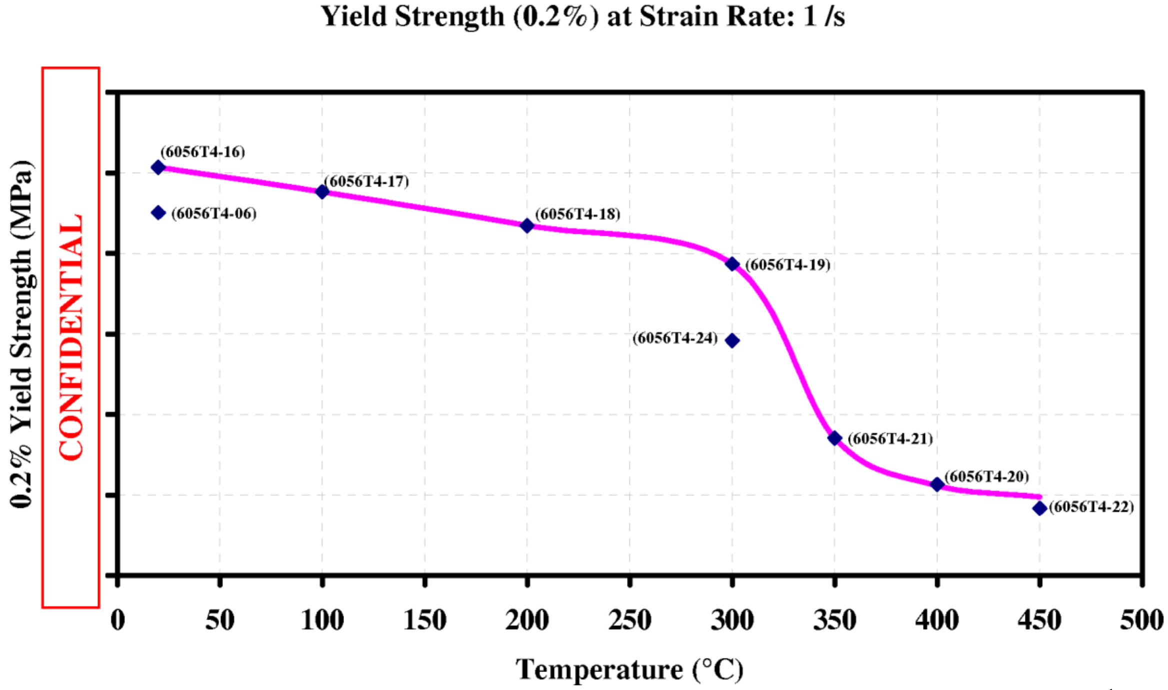

Figure 3.25. Yield strength (0.2%) as a function of temperature at strain rate: 1 s^{-1}

3.7.3 Comparative Analysis

As a general rule, the slope of stress-strain curve decreases with increasing temperature for a constant strain rate; while it increases with increasing strain rate provided the temperature is kept constant. Figures 3.26 to 3.29 show various properties following the similar pattern.

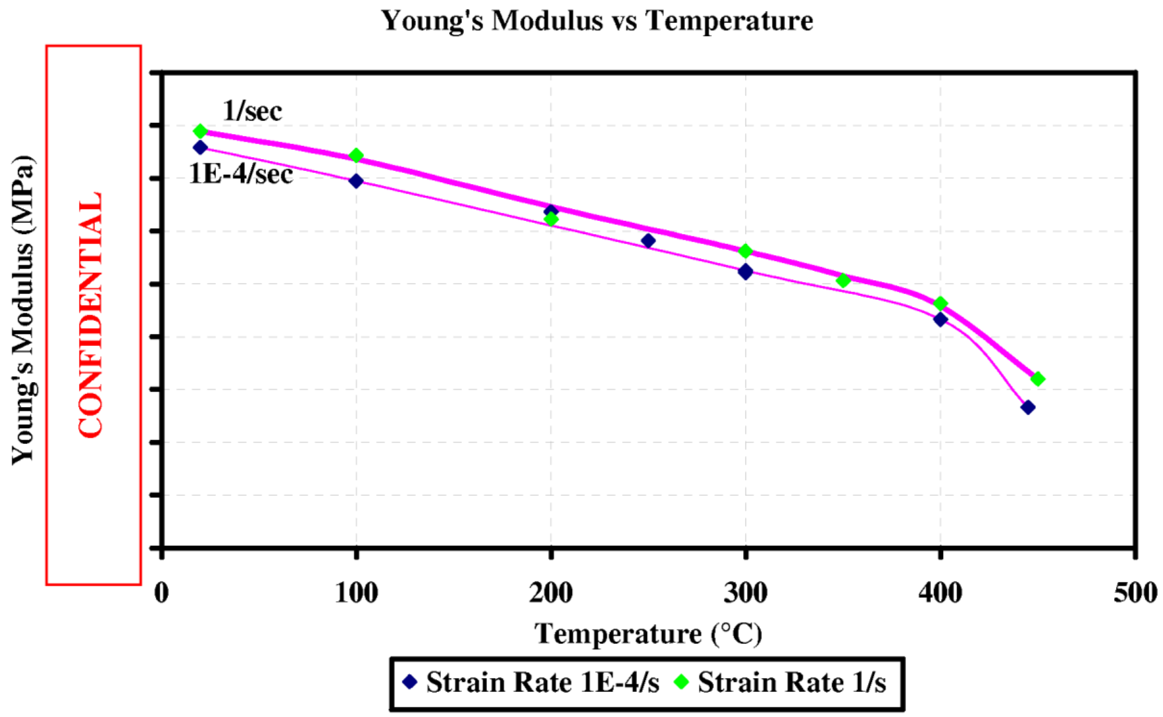

Figure 3.26. Comparison between Young's modulus as a function of temperature

The material properties vary rapidly between the temperatures 250°C and 400°C. This is because at higher temperatures (usually 0.5 times the melting temperature), the diffusion phenomenon is greatly pronounced, which, in turn, assists the annihilation of dislocation by a process of climb and / or glide. Moreover, the precipitation of alloying additions is also highly dominant and the new phases appearing in the parent matrix affect the properties.

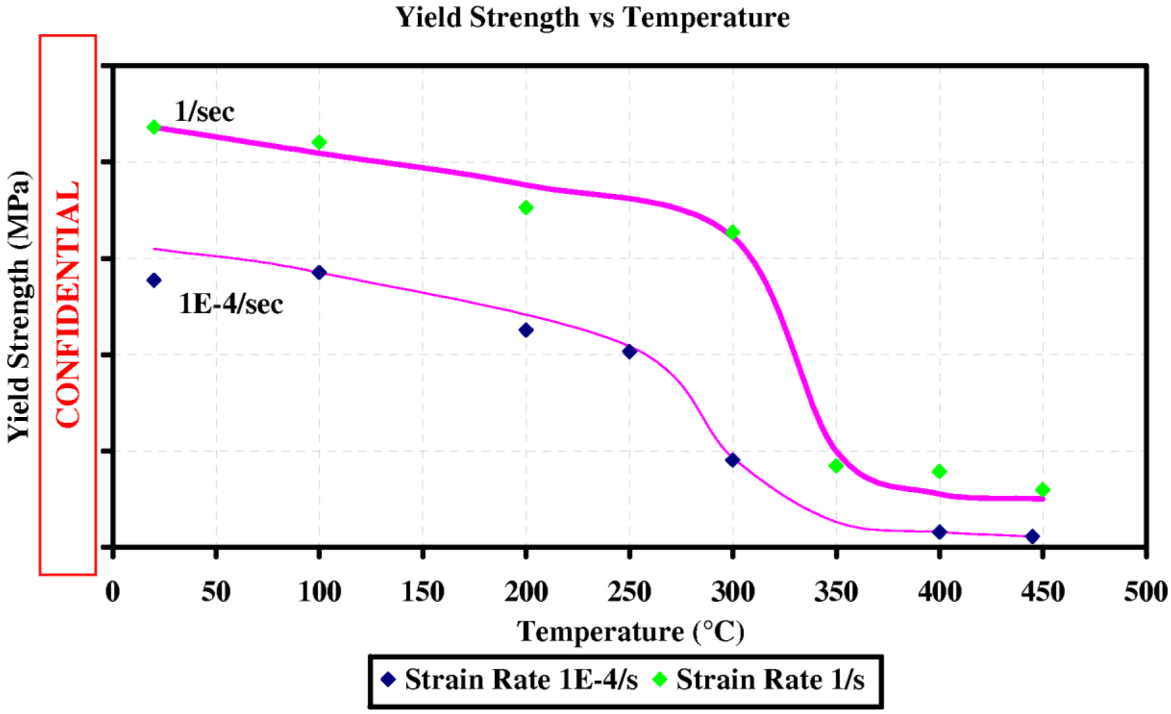

Figure 3.27. Comparison between 0% yield strength as a function of temperature

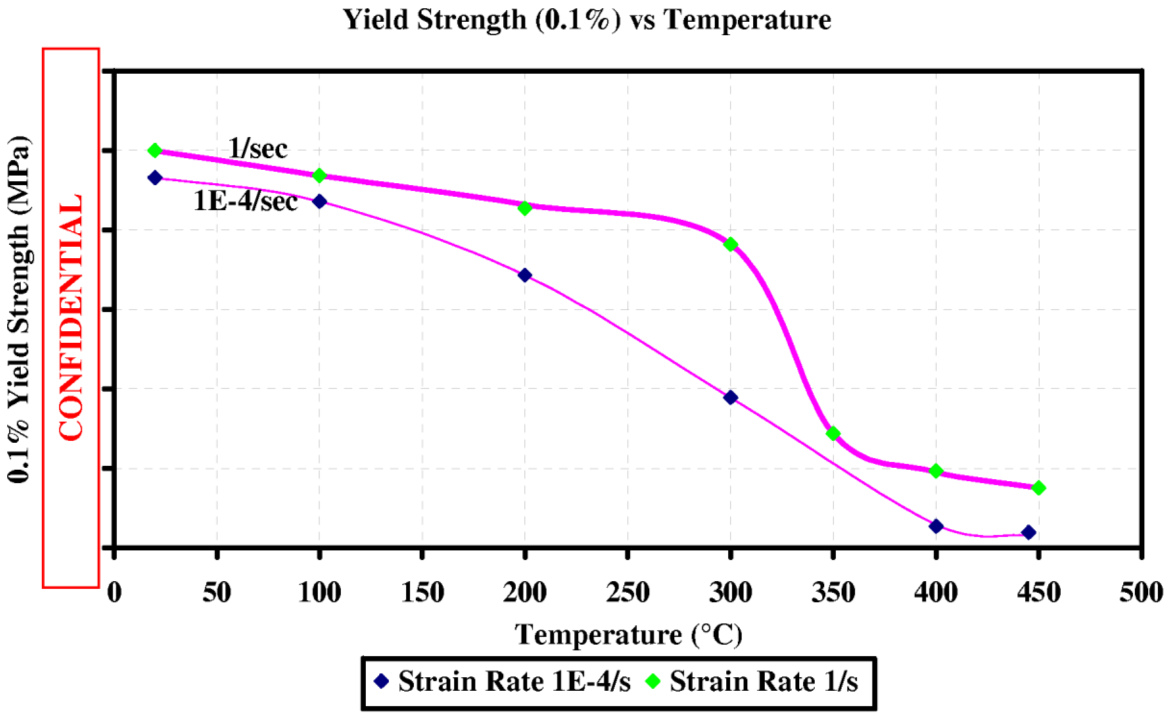

Figure 3.28. Comparison between 0.1% yield strength as a function of temperature

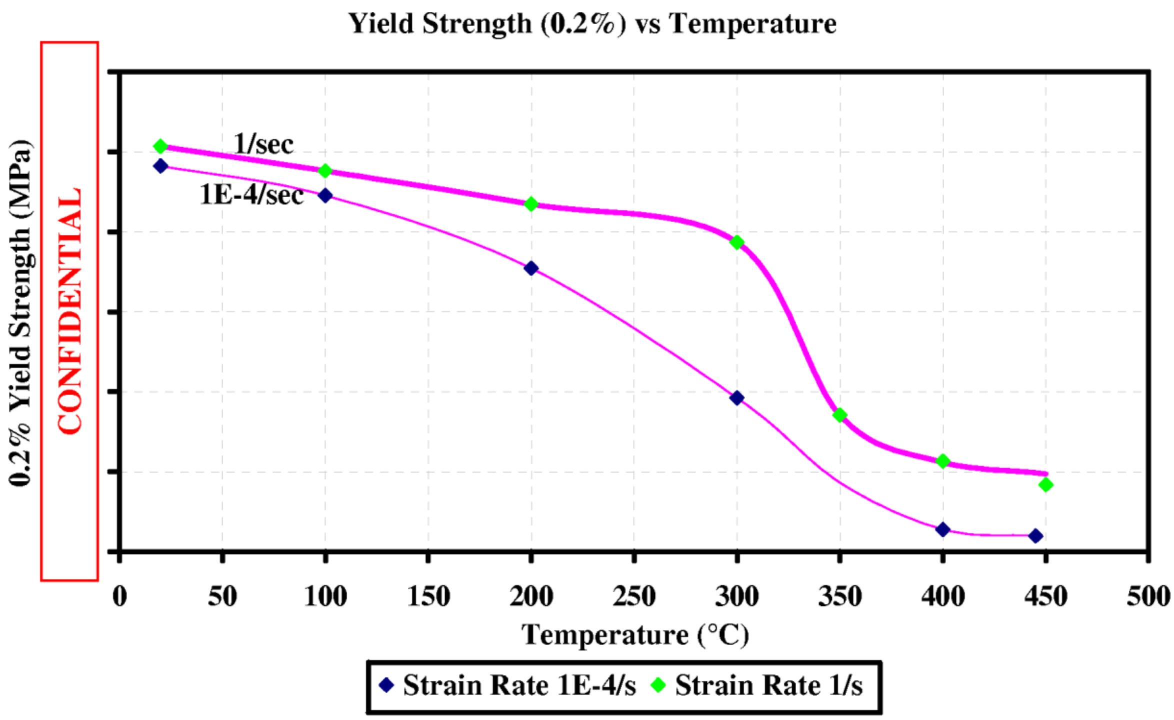

Figure 3.29. Comparison between 0.2% yield strength as a function of temperature

Table 3.4 summarizes the thermo-mechanical properties obtained from the tensile tests performed at various temperatures and strain rates.

Specimen No.	Temperature (°C)	Strain Rate (s^{-1})	Young's Modulus (MPa)	Yield Strength (MPa)		
				0%	0.1%	0.2%
6056T4-04	20	0.0001	CONFIDENTIAL			
6056T4-03	100	0.0001				
6056T4-11	200	0.0001				
6056T4-12	250	0.0001				
6056T4-07	300	0.0001				
6056T4-15	400	0.0001				
6056T4-10	445	0.0001				
6056T4-16	20	0.997				
6056T4-17	100	1.019				
6056T4-18	200	1.136				
6056T4-19	300	0.994				
6056T4-21	350	1.165				
6056T4-20	400	1.229				
6056T4-22	450	1.114				

Table 3.4. Thermo-mechanical properties

3.8 Dilatometry

The coefficient of thermal expansion (α), also called dilatation coefficient, is an inherent characteristic of material that defines the response of material to temperature change. In order to give a general overview, the approximate values of thermal expansion coefficient for aluminium alloy series 6XXX are shown in Fig. 3.30, which is reproduced from literary sources [SHAS][LEDH]. Figure 3.30 indicates that the values of dilatation coefficient lie between 22.5 x 10^{-6} /°C at a temperature of 20°C and 28.7 x 10^{-6}/°C at 300°C.

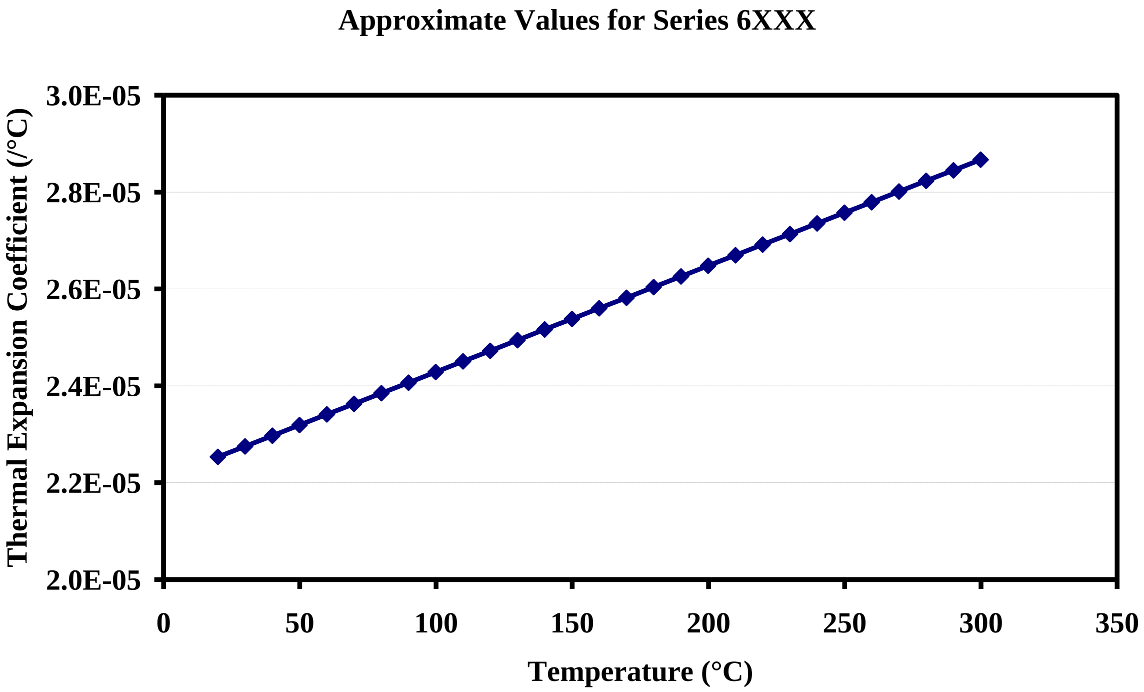

Figure 3.30. Thermal expansion coefficient of Al-alloys series 6XXX

In addition to the tensile tests discussed in previous sections, a dilatometric test was also performed to determine the dilatation coefficient of AA 6056-T4. A specimen of length (L_0) 30 mm was placed in a dilatometer, heated to a temperature of 500°C and then cooled down to room temperature in a controlled environment. The displacement (L) due to increase and decrease in temperature was recorded. The thermal loading cycle shown in Fig. 3.31 demonstrates that the heating of the specimen follows a constant temperature rate. However, despite the controlled environment, the cooling part of the curve shows non-linear decrease in temperature. It is for this reason that the dilatation curve of Fig 3.32 shows linear evolution of displacement upon heating and non-linear upon cooling. Thus, the dilatation coefficient as a function of temperature is calculated from heating part of the dilatometric curve only. Figure 3.32 also shows schematic representation of original length (L_0) and displacement (L).

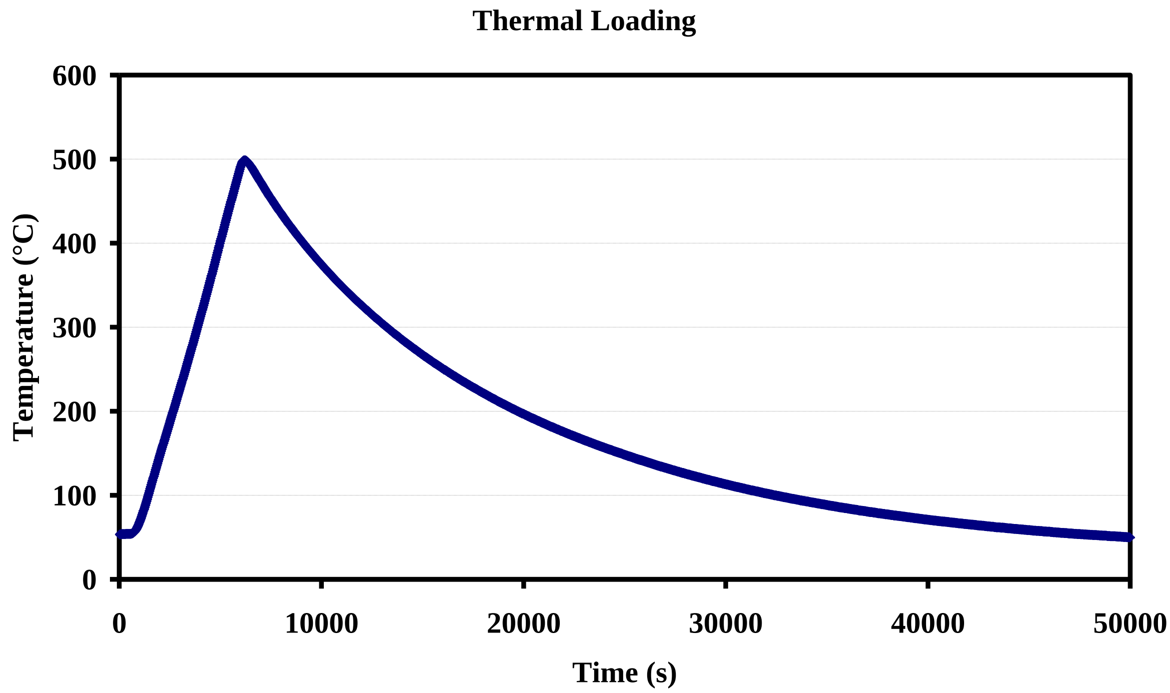

Figure 3.31. Thermal loading cycle for dilatometric test

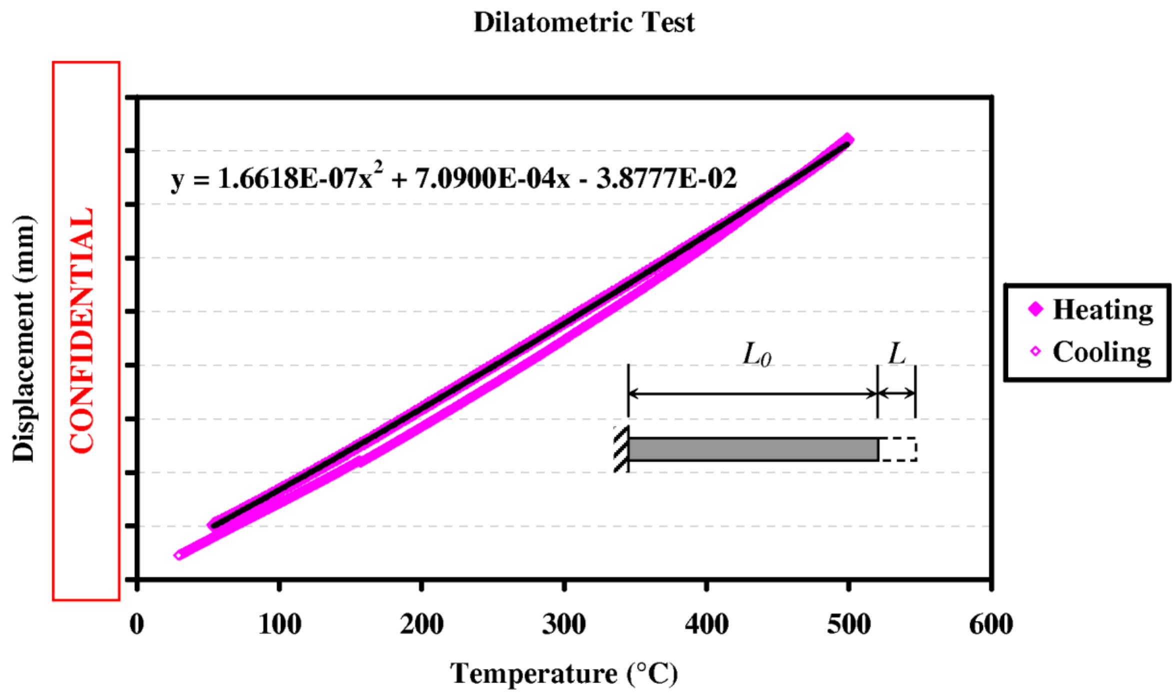

Figure 3.32. Thermal dilatation as a function of temperature

Since displacement is a function of temperature, i.e. $L = f(T)$, the thermal expansion coefficient (α) may be determined from Eq. 3.5. Figure 3.33 presents the dilatation coefficient as a function of temperature.

$$\alpha = \frac{1}{L_0} \cdot \frac{dL}{dT} \tag{3.5}$$

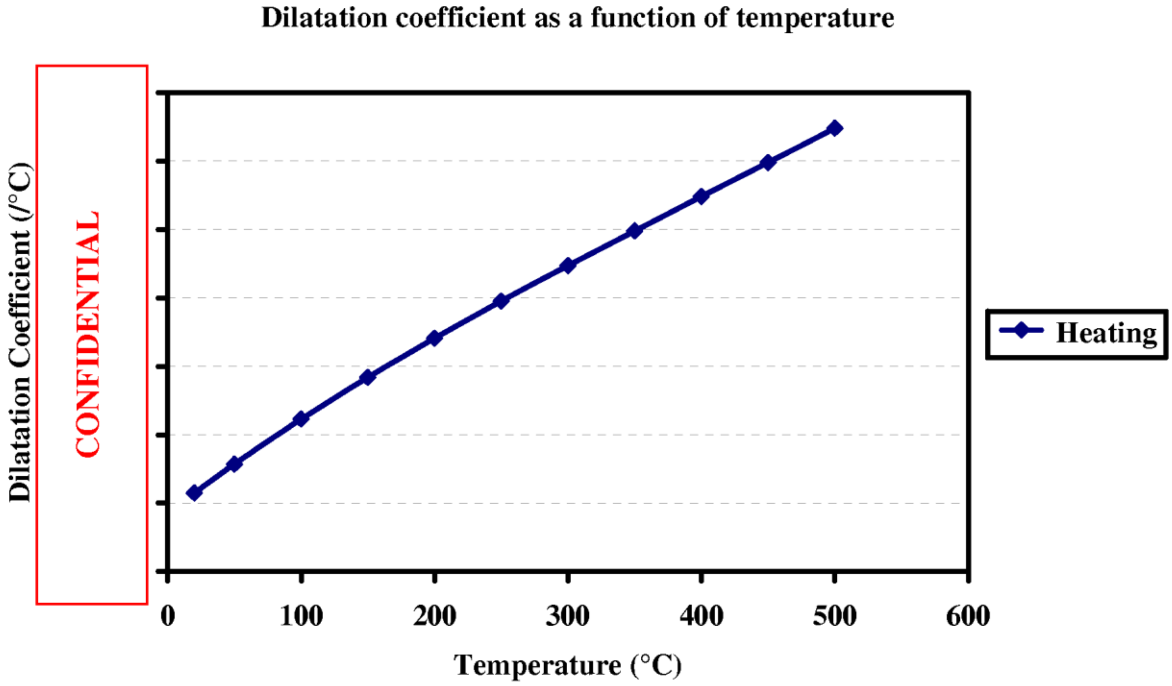

Figure 3.33. Dilatation coefficient of AA 6056-T4 as a function of temperature

3.9 Influence of Material Properties over Simulation Results

The definition of mechanical properties as a function of temperature constitutes, along with the definition of heat source, one of the key-points of numerical simulation [LIN3]. These properties are sometimes difficult to obtain especially at higher temperatures. Some authors have studied the influence of material parameters (i.e. mechanical properties) and the effect of their temperature dependency over numerical simulation with particular reference to residual stresses and distortions. Generally, the results of residual stresses depend essentially upon the mechanical properties at lower temperatures. The mechanical properties at higher temperatures have less effect over the residual stresses, but influence greatly the residual distortions [BRUD].

Given that the mechanical properties are difficult to obtain at high temperatures and that their effect over the residual stresses is low; numerous simulations make use of 'cut-off' temperature (T_{cut}). Thus, the mechanical properties like Young's modulus, yield strength, hardening slopes etc. are temperature dependent up to a certain temperature limit, T_{cut}. Beyond this temperature, the properties are constant, which then permit avoiding the numerical problems arising due to their extremely low level [LIN4]. The criterion of cut-off temperature may be applied to a few or all the properties. Lindgren [LIN4] defined four levels of precision for simulations on the basis of cut-off temperature.

Table 3.5 shows the classification of precision level with respect to the ratio $T/T_{solidus}$, where T is the actual temperature and $T_{solidus}$ is the temperature at the start of fusion.

Simulation Precision	Characteristics
Elementary	$T_{cut}/T_{solidus} \leq 0.5$: The volume change related to solid-state phase transformation are not taken care of, yet the effect of phase change over the yield strength at ambient temperature is taken into account. Temperature dependent material properties along with latent heat of fusion are used.
Classic	$T_{cut}/T_{solidus} \leq 0.7$: The volume change related to solid-state phase transformation and their effect over mechanical properties are taken into account. Temperature dependent material properties along with latent heat of fusion are used.
Precise	Similar to the classic simulation with a more significant precision level such that very fine modelling of material properties is used.
Very Precise	$T_{cut}/T_{solidus} = 1$: Required to include the effect of material flow within the weld pool in order to capture the accurate behaviour at higher temperature. Temperature dependent material properties along with latent heat of fusion are used. It may be required to use more detailed description of latent heat of fusion.

Table 3.5. Characteristics of simulation precision

Zhu [ZHUX] carried out the numerical simulations considering the dependency and non-dependency of mechanical properties over temperature. According to him, the Young's modulus may be taken as constant and it is preferred that its value be taken at ambient temperature rather than average temperature. Poisson's ratio may also be taken as constant because it has less influence over the numerical results [TEKP]. However, as mentioned earlier, the temperature dependency of yield strength value may not be ignored as it has great influence over the simulation results [BRUD][LIN4]. As far as hardening behaviour (isotropic, kinematic or mixed) is concerned, the researchers have divided opinion [LIN4]. It is, however, expected that the hypothesis of kinematic hardening yields better results than that of isotropic hardening in case of numerical simulation of multi-pass welding [BRUD]. Thus, it appears that not much systematic research work is performed to establish the effect of hardening behaviour upon simulation results. It should also be noted that the effect of hardening behaviour may be masked by some other parameters which influence greatly the simulation results; for example, thermo-mechanical properties, heat source application, type of model (2D or 3D) etc.

Summarizing from the perspective of material properties, it is still not well understood as to what level of details is required to accurately predict the residual stresses and distortions. However, researchers agree to the fact that material properties are of vital importance for the numerical simulation of welding.

3.10 Material Characterisation using Gleeble System

One of the major problems encountered during induction heating of tensile test specimens was that the acquired heating rate was as low as 1°C/s. Since the T4 state of AA 6056 comprises of a super-saturated solid solution of alloying elements with some precipitates of the form Al_xM_y, at such a low temperature rate the precipitates get enough diffusion time and may result in dissolution of new precipitates. These newly formed precipitates are then likely to impart their own properties to the material. This is why the tensile specimens are required to be heated at a very high temperature rate so that the dissolution of precipitates may be avoided. The solution to such a problem is the heating of specimen by Joule effect where temperature rate of the order of 100°C/s are easily achievable.

In this section the results of material characterisation using Gleeble system are presented. This machine (available at LaMCoS, INSA-Lyon) is equipped with Joule heating system and hence may be successfully adopted for thermal and mechanical tests involving high temperature rate and requiring controlled metallurgical transformations.

The stress-strain curves are obtained with similar type of specimens as used for conventional tensile testing machine. The monotonic tensile tests were performed at various strain rates and at different temperatures. The heating rate was maintained at 25°C/s for all the tests. Tensile loading was applied only when the required temperature had reached. All the tests were performed in ‘displacement’ mode, which means the pulling action of the shaft was controlled by displacement rate and not by strain rate. The efforts were made to adjust such a displacement rate so that the strain rates of 0.001 s^{-1} (high) and 0.0001 s^{-1} (low) could be reached.

Figures 3.34 and 3.35 present the true stress-strain curves obtained from all the tensile tests performed. Figures 3.36, 3.37, 3.38 and 3.39 show the evolution of Young’s modulus and yield strengths at 0%, 0.1% and 0.2%, respectively. It may be noticed here that yield strengths measured at 250°C are once again more than those observed at 200°C. It has already been explained in previous sections that this observation may result due to dynamic recrystallization of material.

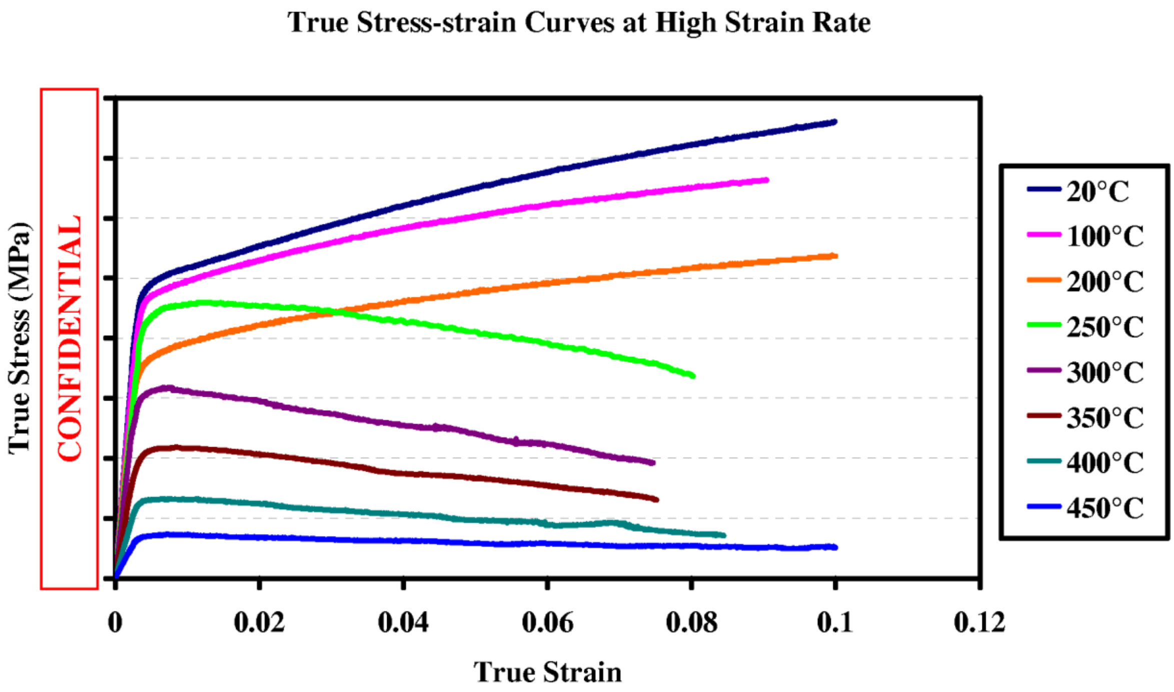

Figure 3.34. True stress-strain curves at high strain rate obtained from Gleeble system

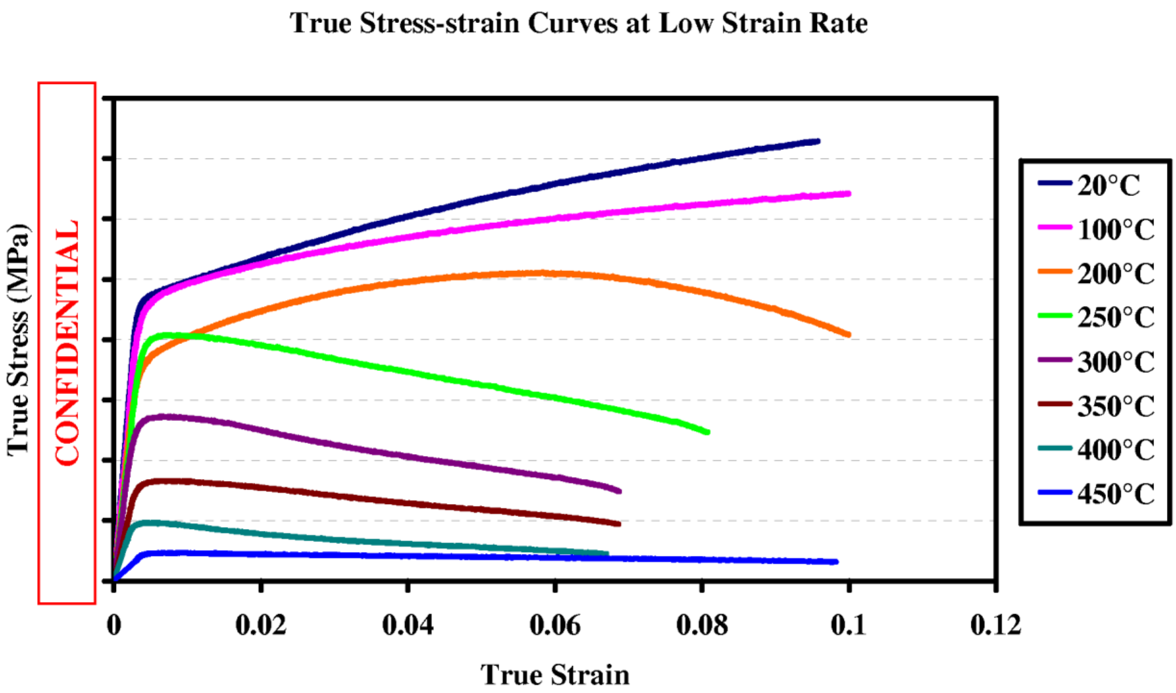

Figure 3.35. True stress-strain curves at low strain rate obtained from Gleeble system

The true stress-strain curves illustrate that the material AA 6056-T4 follow strain hardening behaviour till the temperature of 200°C, while from 250°C onward it shows strain softening behaviour.

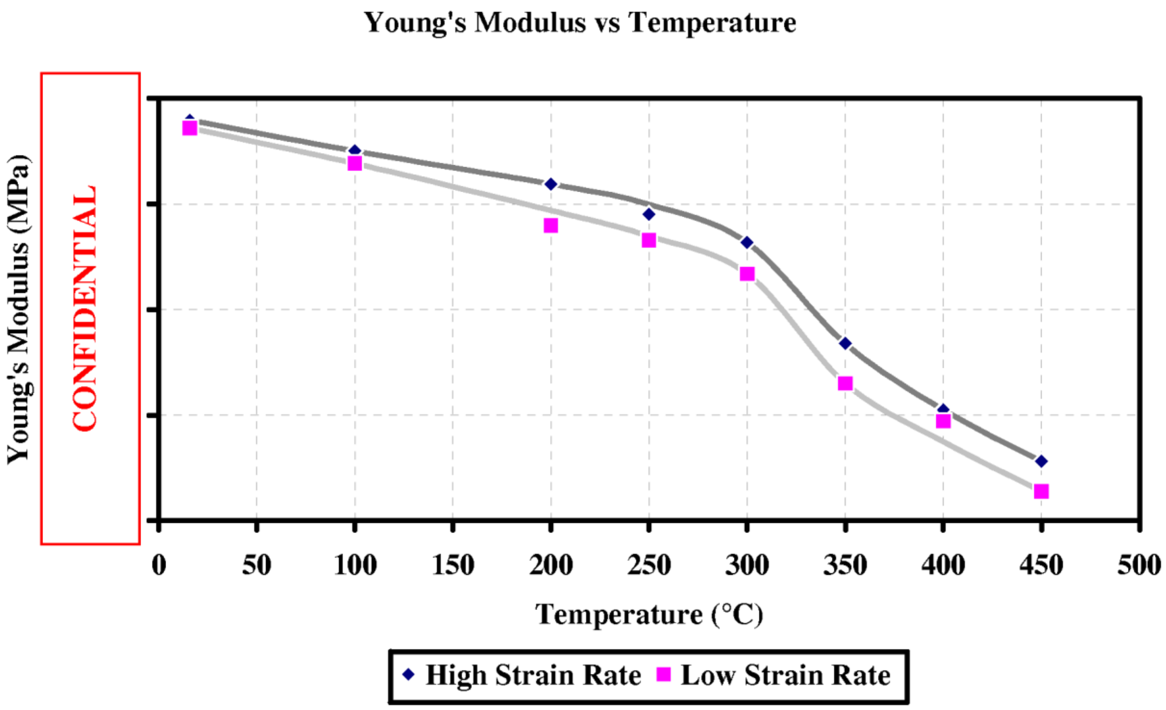

Figure 3.36. Young's moduls as a function of temperature - Gleeble system

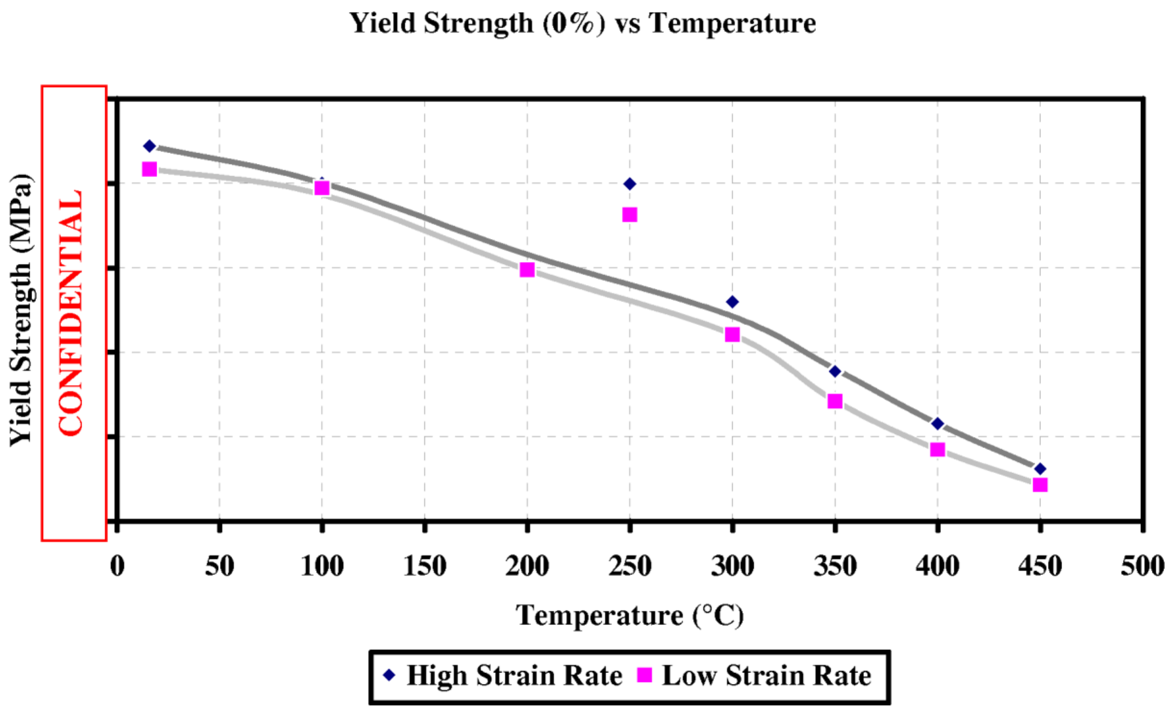

Figure 3.37. Yield strength (0%) as a function of temperature - Gleeble system

The evolution of material properties shows a rather little influence of strain rates at low temperatures; however at high temperatures since the magnitude of material parameters decreases the effect of strain rate becomes significant.

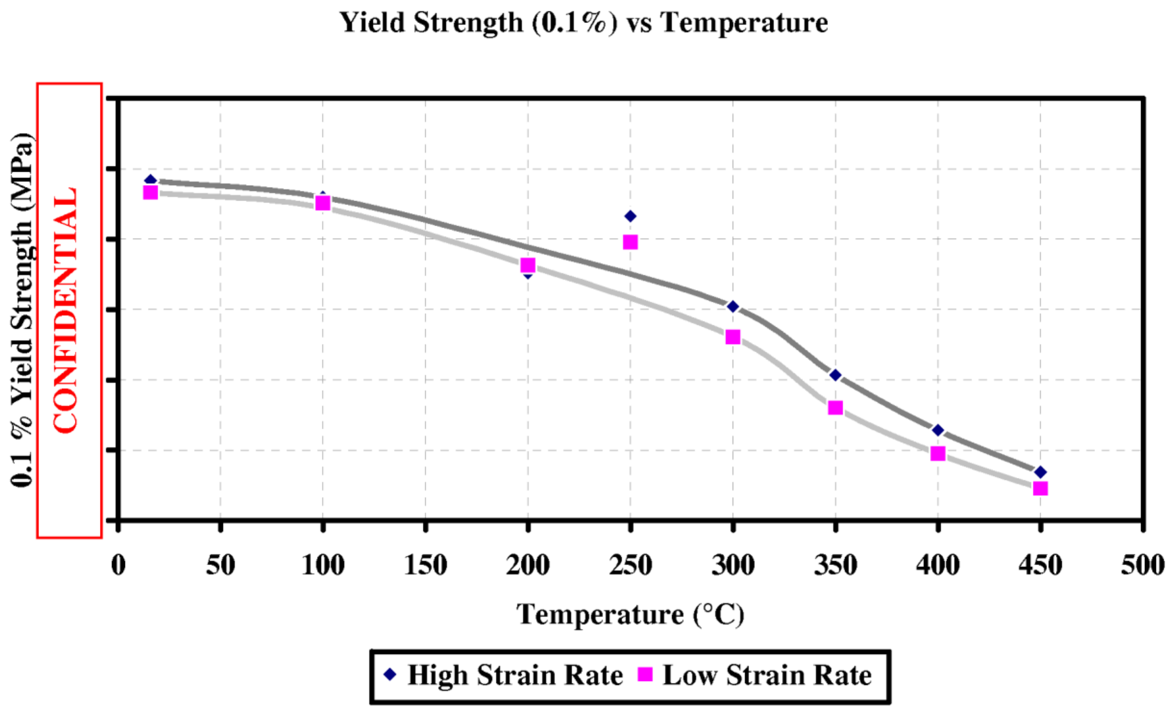

Figure 3.38. Yield strength (0.1%) as a function of temperature - Gleeble system

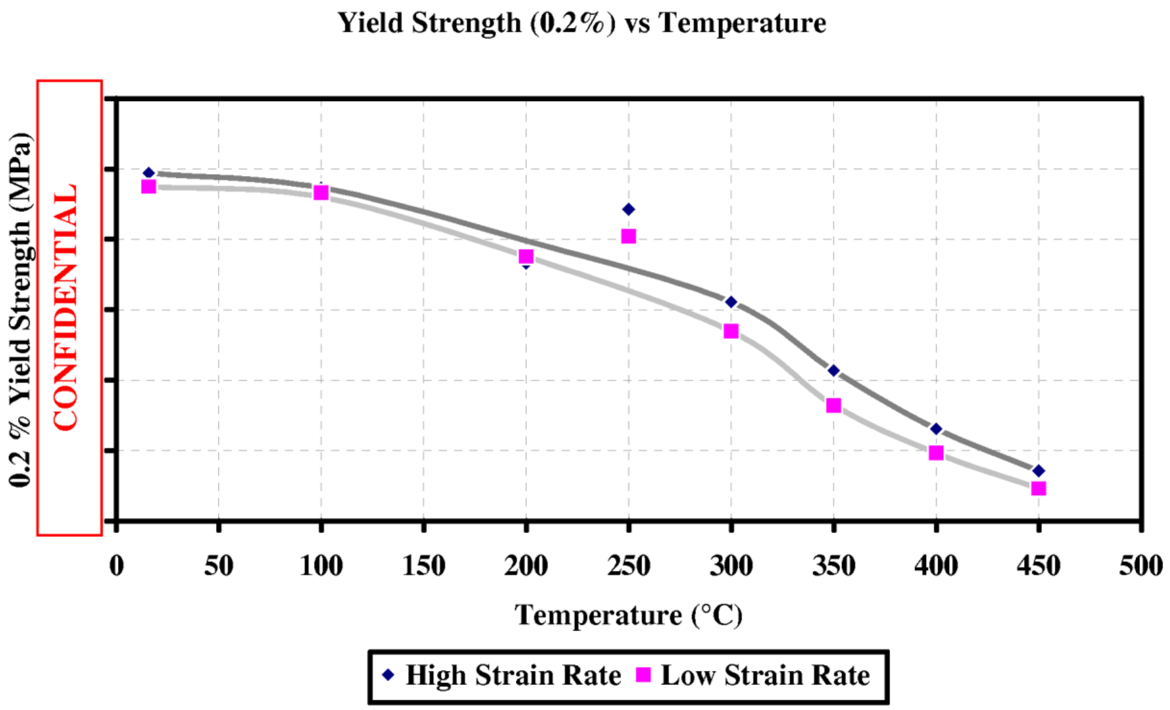

Figure 3.39. Yield strength (0.2%) as a function of temperature - Gleeble system

Table 3.6 shows the material parameters identified using Gleeble system. The comparison between the results obtained from two different systems, Gleeble using Joule heating and conventional tensile testing using induction heating (Table 3.4), shows that the material properties remain almost identical at room temperature; however, the difference amongst them increases with increasing temperatures. For instance, the measured values of Young's modulus at 450°C and 0.0001 s^{-1} using induction heating and Joule heating are 26628 MPa and 5560 MPa, respectively. The former is five times as high as latter. This observation suggests that the heating rate considerably influences the material properties and hence the materials involving phase transformations (precipitation, dissolution etc.) should preferably be tested using maximum possible temperature rate.

Specimen No.	Temperature (°C)	Strain Rate (s^{-1})	Young's Modulus (MPa)	Yield Strength (MPa)		
				0%	0.1%	0.2%
S26	16	0.000866				
S01	100	0.001079				
S02	200	0.001331				
S06	250	0.002218				
S03	300	0.001937				
S07	350	0.002093				
S04	400	0.00168				
S05	450	0.001787	CONFIDENTIAL			
S08	16	0.0000857				
S09	100	0.000125				
S10	200	0.000082				
S12	250	0.000214				
S13	300	0.000183				
S14	350	0.000222				
S15	400	0.00017				
S16	450	0.000198				

Table 3.6. Identified material properties using Gleeble system

3.11 Conclusions

Following conclusions are drawn based on the monotonic tensile tests and dilatometric test observations.

- With increasing temperatures, the values of Young's modulus and yields strengths (0%, 0.1% and 0.2%) decrease. In addition, the material properties vary rapidly beyond 250°C.

- The increasing strain rates cause an increase in the values of Young's modulus and yield strengths. This change in properties is found to be trivial at lower temperatures; however, at higher temperatures the difference in material properties is found to be 2 – 3 times higher for a strain rate of 1 s^{-1} than for $0.0001 s^{-1}$.

- With respect to strain hardening slopes of stress-strain curves, it is found that at a constant strain rate of 0.0001 s^{-1}, the hardening slopes tend to decrease with increasing temperatures. Moreover, for the temperatures beyond 200°C the material shows strain softening behaviour.

- For the stress-strain curves obtained at a strain rate of 1 s^{-1}, the strain-hardening slopes reduce till a temperature of 200°C; however, beyond this temperature the material tends to show elastic perfectly-plastic behaviour.

- The true stress-strain curve at 250°C and 0.0001 s^{-1} shows a relatively different evolution of stress values as a function of strain. It is found that the yield strength values are higher than those determined at 200°C due to dynamic recrystallization of the material.

- The thermal dilatation coefficient increases linearly with increasing temperature.

- Improvement in results is observed using Gleeble system which involves heating by Joule effect. It is found that very slow heating rate is likely to change metallurgical state of the material which further influences the material properties to great extent. On the other hand with the use of high heating rate the material does not get sufficient time for phase transformation and hence the thermo-mechanical properties remain less affected due to the limited precipitation / dissolution occurrences.

CHAPTER 4

EXPERIMENTAL INVESTIGATION

Contents

SUMMARY

The experimental approach adopted to study the response of the material AA 6056-T4 when subjected to laser beam welding is discussed in the following chapter. Various welding experiments with increasing complexities are performed on test plates and T-joints. Small-scale specimens of dimensions 300 mm x 200 mm x 2.5 mm are used for experimentation. The welding test cases are performed in two phases, viz. test plates welding and T-joints welding. With respect to the type of welding, the test cases are subdivided into fusion welding case (Test Case 01), filler welding case (Test Case 02) and T-joint welding case (Test Case 03).

Further classification for test plate welding cases is based upon boundary conditions. Two types of boundary conditions are used; where the first type uses an aluminium suction table to maintain the test plates in position during welding, while the second type involves simple holding of plates in air at the far ends across the weld joint. No such distinction of boundary conditions is made in T-joints welding. However, T-joints are categorized with respect to the number and position of tack welds amongst the base plate and stiffener.

Measurements are taken before, during and after welding of specimens. The temperatures are measured during welding with the help of thermocouples installed in the vicinity of fusion zone. The evolution of weld pool surface temperature is acquired with Infra-red camera. High-speed camera is used to observe the material ejection due to welding in keyhole regime. The in-plane displacements during welding are recorded with LVDT sensors. Stereo image correlation technique is employed to measure residual in-plane and out-of-plane displacements. Micrography is performed after welding so as to measure the fusion zone geometry.

MAJOR CONCLUSIONS

A database of experimental results is prepared to validate the numerical models. It is found that increased heat input yields higher peak temperature values at thermocouple positions, which further leads to increased distortion levels. However, the factors like filler wire addition and boundary conditions influence these findings. For instance, welding cases with aluminium support result in lower level of distortions due to rapid heat dissipation from the welding specimens. Similarly, the use of filler wire considerably reduces the amount of heat energy transmitted to the test specimens and hence results in less deformed structure as compared to fusion welding cases.

Experimental Investigation

In the previous chapters, the discussion regarding the laser-beam welding and its consequences is developed. This chapter is primarily concerned with the approach adopted to analyse the response of the material AA 6056-T4 when subjected to laser-beam welding with various thermal and mechanical boundary conditions. Recapitulating, the aluminium alloy 6056-T4 is used in aeronautic industry for the manufacturing of fuselage panels. The fabrication process used is laser-beam welding, which is employed in a T-joint configuration joining AA 6056-T4 sheets with stringer assemblies (Fig. 1.3). The laboratory scale experiments, presented in this chapter, were organised in a way so that the industrial loading and boundary conditions could be integrated at relatively smaller scale. All the welding test cases were performed in two different experimental campaigns; the first one comprised of welding of test plates while the second one involved welding of T-joints. Various instrumentations were employed to capture the experimental data. Much of this database is used in the next chapter for developing a comparative analysis with numerical models.

4.1 Aim of Campaigns

The primary aim of these campaigns is to prepare a database of the experimental measurements and observations. This database should necessarily contain enough information which may serve as benchmark for the comparison and validation of the numerical simulation results. Other secondary purposes of these campaigns are to observe and analyse the following:

- Material response to laser-beam welding in keyhole regime.
- Effect of initial surface profiles of sheets.
- Variation of heat energy absorbed by the material during welding.
- Effect of heat energy dissipation in the support made of aluminium.
- Distortion patterns.

The information gathered during experimental campaigns is exploited and treated to a considerable extent and conclusions based on experimental observations are also drawn.

4.2 Scheme of Test Cases

The experimental campaigns, as mentioned earlier, were carried out in two phases. In the first phase only the test plates were welded, while in the second phase T-joints were welded from both sides of the stiffener. With reference to weld joint configuration, the following three types of test cases have been performed:

- ***Test Case 01***: Fusion pass welding of test plates
- ***Test Case 02***: Filler pass welding of test plates
- ***Test Case 03***: T-joint welding

Single pass laser-beam welding experiments were carried out in 'keyhole' regime for all the test cases. As the name suggests the fusion pass welding of test plates involves welding without filler wire addition, whereas filler pass welding means welding with filler wire addition. T-joint welding is performed with the addition of filler wire on the both sides of fillet.

Industrially, the fuselage panels are held in position with the help of a suction table. Large thin sheets of AA 6056-T4, usually several meters in length, are placed on a table made of aluminium and a suction force is applied through the bottom. The stiffeners are then placed vertically upon these thin sheets and welded with two welding heads moving simultaneously on each side of the fillet joint. Efforts are made in these experimental campaigns to integrate the industrially employed boundary conditions. The following two types of boundary conditions were, therefore, introduced.

- Welding in air (free convection and radiation) with simplest clamping of the test plates, lengthwise from the far edges.
- Welding while holding test plates and T-joints on aluminium suction table from the bottom side of the plates with a suction force of approx. 1 bar.

It may be noticed that the T-joints were welded with the help of aluminium suction table only. No distinction was made with reference to the welding parameters for the same type of test cases. Although the sheet thickness used was 2.5 mm, the welding parameters were selected such that the complete penetration of fusion zone could be avoided. Welding of T-joints additionally involved tack welds with varying sequence. Efforts were made to perform each test case at least two to three times so that the repeatability of experimental results could be established. Visual inspection of test plates was also done to differentiate the plates with convex and concave profiles. The terms convex and concave are relative to the placement of test plates on the support or clamping device. The test plate with its edges, not the mid-section, touching the platform on which it is placed is assumed to have a convex profile; while the one with its mid-section touching the platform instead of edges is regarded as having concave profile. Table 4.1 and 4.2 summarize all the welding test cases with the symbolic representation and weld parameters. The test case numbers / symbols shall be used frequently in subsequent sections.

Test Case	Welding Operation	Support	Plates Welded	Welding Parameters	Symbol
01A	Fusion without filler metal	Aluminium	P06 (concave) P14 (convex) P15 (convex)	Power: 2300 W Speed: 8 m/mn	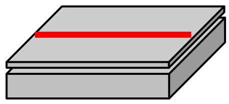
01B	Fusion without filler metal	No support	P03 (concave) P01 (convex) P12 (convex)	Power: 2300 W Speed: 8 m/mn	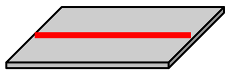
01C	Fusion without filler metal	Aluminium	P20 (convex)	Power: 3000 W Speed: 8 m/mn	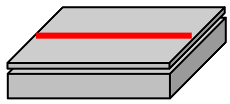
02A	Fusion with filler metal	Aluminium	P07 (concave) P17 (convex) P19 (convex)	Power: 3000 W Speed: 8 m/mn Wire feed: 5 m/mn	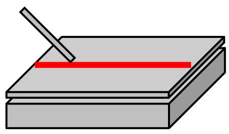
02B	Fusion with filler metal	No support	P04 (concave) P11 (convex) P13 (convex)	Power: 3000 W Speed: 8 m/mn Wire feed: 5 m/mn	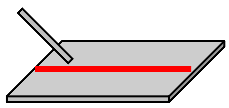

Table 4.1. Test cases performed during first experimental campaign

According to table 4.1, a constant welding speed of 8 m/mn was used for all the test cases. The laser beam power, however, was different for fusion and filler welding test cases; 2300 W for the former and 3000 W for the latter. This is because the filler metal consumes a substantial amount of beam power during melting while becoming the part of fusion zone (FZ). One of the test cases named 01C was carried out at the beam power of 3000 W but with no filler wire. This test case was actually aimed at observing the effect of increased beam power on the weld specimen without using filler metal wire. For all the test cases of type 02, the wire made of an aluminium alloy 4047 (diameter: 1 mm) was used as filler material.

Moreover, the weld bead was created for a total length of 290 mm leaving aside a distance of 5 mm on each end of the bead from the edge of the plate.

Table 4.2 presents the scheme of T-joints welded in the second phase of experimentation. The distinction amongst different test cases is based on tack weld numbers and positions. Test cases 03A, 03B and 03C were carried out with one (at start), two (at start and end) and three (at start, mid and end) tacks, respectively. Test case 03D was performed without tack welds. The tack length was maintained as 5 mm. Two welding heads were used; one on each side of T-joint. The details of experimental setup are explained in the next section. The beam power of 2500 W was used on each side of stiffener, while maintaining the welding speed of 5 m/mn. AA 4047 with a diameter of 1 mm was used as filler wire. All the T-joints were welded using aluminium suction table.

Test Case	**Welding Operation**	**Support**	**T-joints Welded**	**Welding Parameters**	**Symbol**
03A	1 Tack at start + Fusion with filler metal	Aluminium	T01 (concave) T02 (convex)	Power (P): 2 x 2500 W Weld Speed: 5 m/mn Ar gas flow rate: 20 l/mn Wire feed rate: 3 m/mn Wire diameter: 1 mm Wire material: Al 4047 Tack length: 5 mm	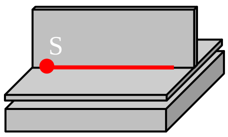
03B	1 Tack at start + 1 Tack at end + Fusion with filler metal	Aluminium	T03 (concave) T06 (concave)		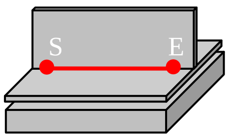
03C	1 Tack at start + 1 Tack at end + 1 Tack in middle + Fusion with filler metal	Aluminium	T05 (concave) T07 (convex)		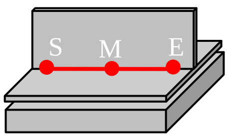
03D	No Tacks at all, Only fusion with filler metal	Aluminium	T08 (convex) T09 (convex)		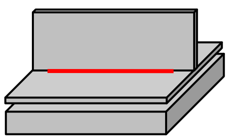

Table 4.2. Test cases performed during second experimental campaign

4.3 Experimental Setup

The experimental campaigns have been carried out on the laser beam welding machine of Pole Laser Bourgogne Technology (PLBT) at IUT du Creusot (Fig. 4.1). This machine is equipped with a movable platform, while its welding head remains static during the operation. The work piece is placed underneath the welding head on the movable platform. The laser beam spot is focused at the location of weld joint. The beam power, speed of the platform, wire feed rate and other related parameters are adjusted through a digital control system. Additional devices like infra red camera, high speed camera, extra welding head etc. can also be mounted on the static welding head. Further mounting of clamping devices on the movable platform, designed as per the work piece, is also achievable.

Two types of clamping equipments were used for the experimental campaigns; the first being the aluminium suction table upon which the test plates were placed (Test case 01A, 02A and 03), while the second being the simple bars used to hold the test plates from the far edges while avoiding the contact of the remaining surfaces with the platform (Test case 01B, 01C and 02B). Various instrumentations have been used during the experimentation. For instance, the temperature measurements in the vicinity of weld joint during welding were taken with K-type thermocouples, the surface temperature of weld pool was recorded with the help of infra red camera and the ejection of material from the keyhole was observed with high speed camera. Similarly, Linear Variable Differential Transducer (LVDT) sensors were used for measuring the in-plane displacements during welding and image correlation technique was employed to record the in-plane and out-of-plane displacements before and after the welding.

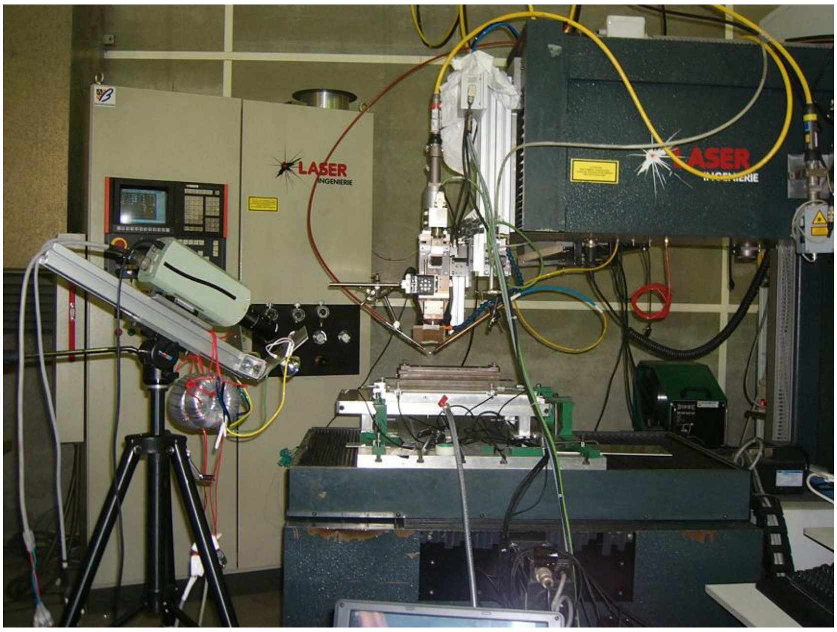

Figure 4.1. Pôle Laser Bourgogne Technologie

The schematic representation of test plate using aluminium suction table as support and the actual experimental setup are shown in Figs. 4.2 and 4.3, respectively.

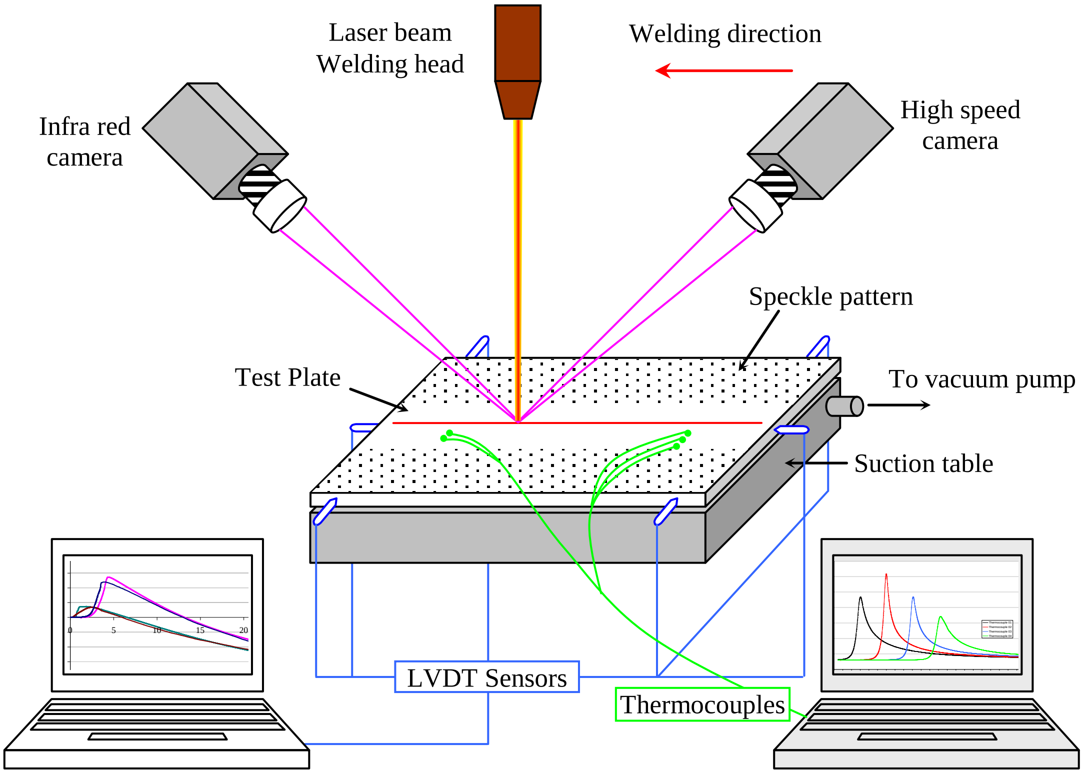

Figure 4.2. Schematic representation of Test plate welding

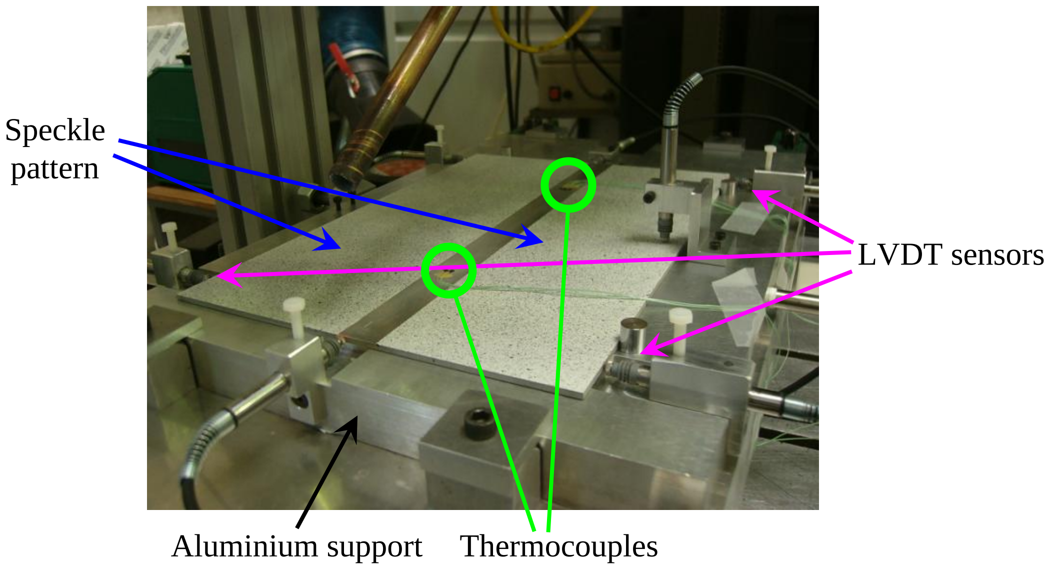

Figure 4.3. Experimental Setup of Test plate welding

Similarly, the schematics of T-joint welding and the experimental setup are shown in Figs. 4.4 and 4.5, respectively. A pressure value of 1 bar is applied through a vacuum pump to maintain the test plates and base plates of T-joints in position during welding.

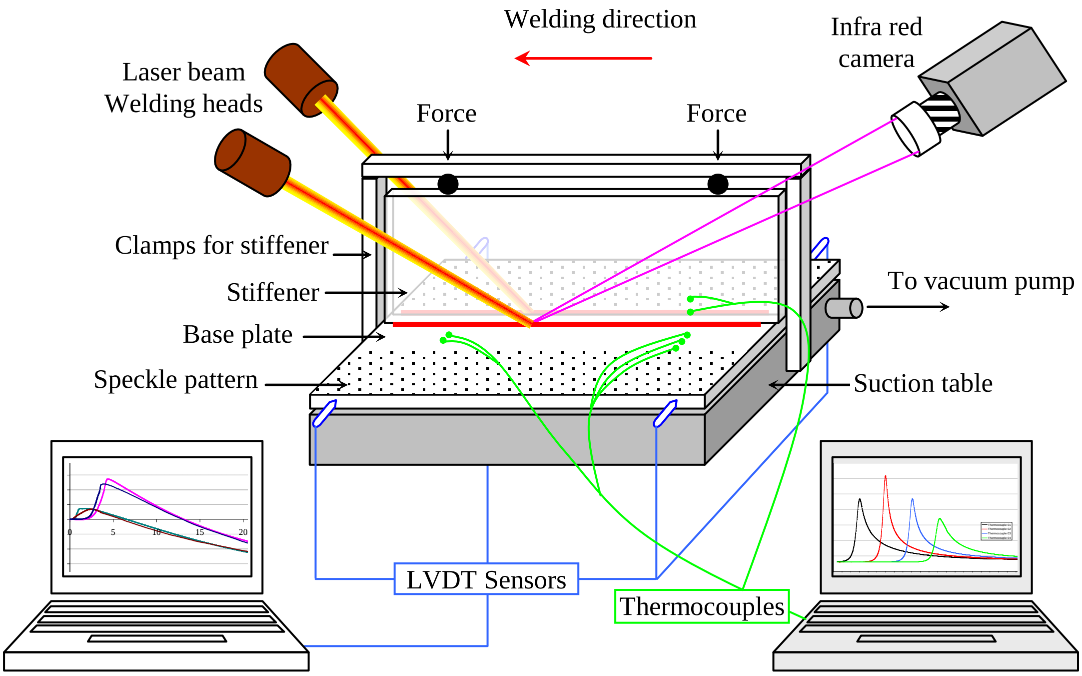

Figure 4.4. Schematic representation of T-joint welding

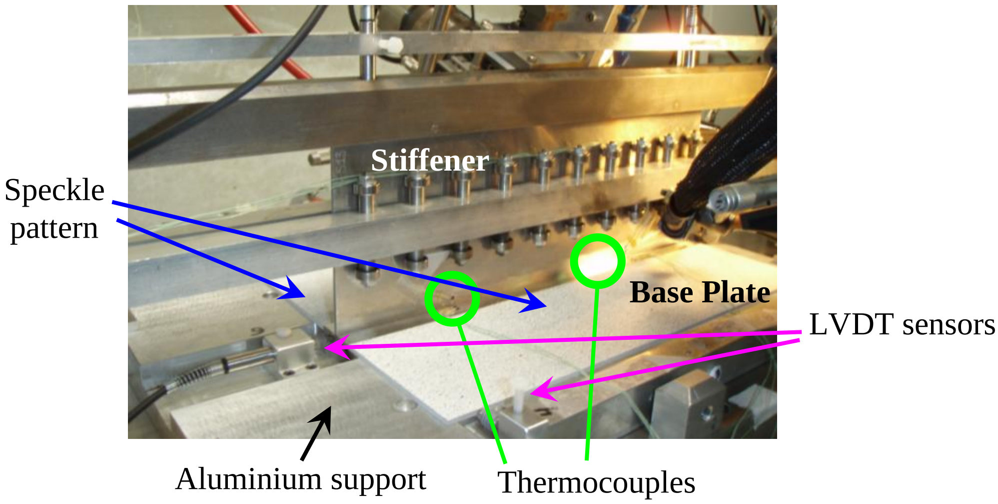

Figure 4.5. Experimental Setup of T-joint welding

4.4 Geometry of Test Specimens

Since the test cases are performed on laboratory scale to serve the academic level research purpose, the sizes of the specimens are kept relatively small. Nevertheless, these specimens are still large enough to furnish the required results and exploitable information regarding temperature and displacement measures. The dimensions of the test plates and base plates of T-joints were 300 mm x 200 mm x 2.5 mm, while those of stiffeners were 300 mm x 100 mm x 2.5 mm. Figures 4.6 and 4.7 present the geometry and layout plan of instrumentation for test plates (test cases 01 and 02) and T-joints (test case 03), respectively.

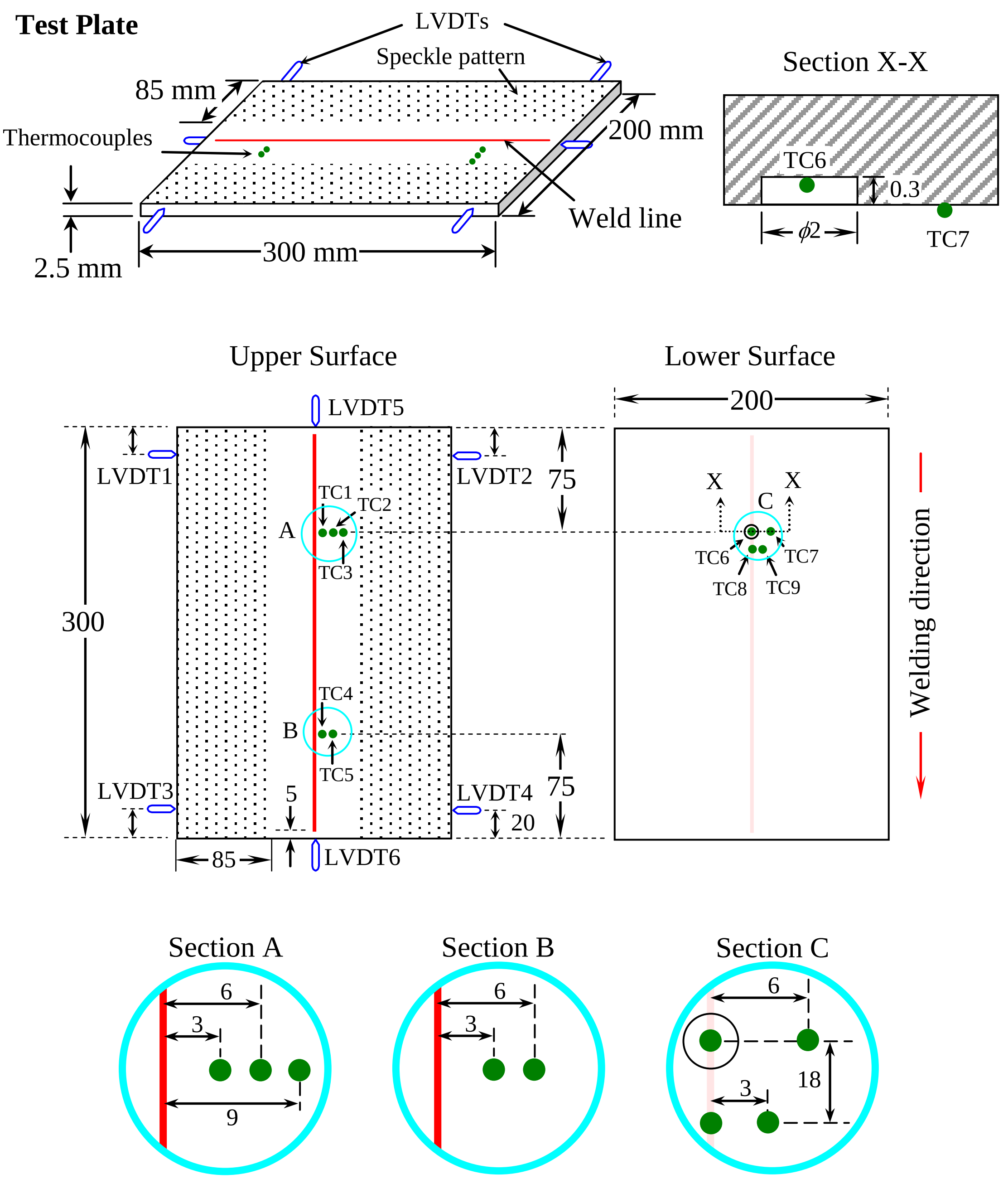

Figure 4.6. Geometry of the plates and layout plan of instrumentation (dimensions in mm)

According to Fig. 4.6, a total of nine thermocouples (TCs) are installed on the test plates; the first five (TC1, TC2, TC3, TC4 and TC5) and the next four (TC6, TC7, TC8 and TC9) are welded on the upper and lower surfaces of the test plate, respectively. TC6 and TC8 are positioned directly underneath the weld center line. Additionally, TC6 is placed in a very fine drilled hole in a depth of 0.3 mm from the bottom surface. LVDT sensors are placed in the direction perpendicular and parallel to welding; where the pairs of LVDTs 1 and 2, LVDTs 3 and 4 and LVDTs 5 and 6 are placed in line with each other. The speckle pattern is created only on the upper surface of the plates away from weld joint (85 mm on each side).

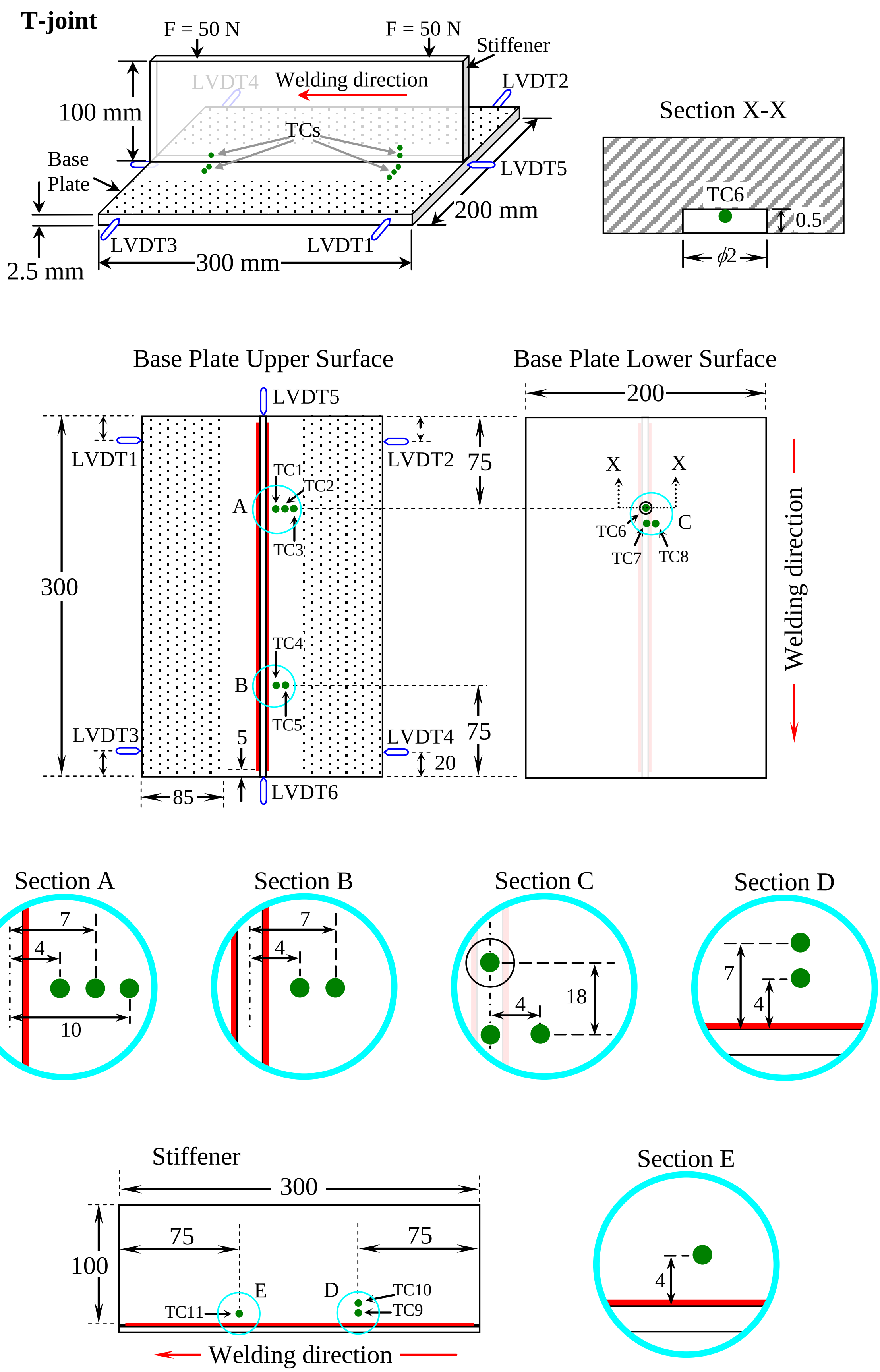

Figure 4.7. Geometry of T-joint and layout plan of instrumentation (dimensions in mm)

Similarly, Fig. 4.7 shows a total of eleven thermocouples (TCs) welded on T-joint assembly; five of them, namely TC1, TC2, TC3, TC4 and TC5, are installed on the upper surface of base plate, three (TC6, TC7 and TC8) are placed on the lower surface of base plate, while the remaining three (TC9, TC10 and TC11) are welded on one side of the stiffener. The distance of TCs from the weld center line is also shown in Fig. 4.7. TC6 and TC7 are placed directly underneath the weld center line, where TC6 is welded inside a small hole of depth 0.5 mm. The pairs of LVDTs 1 and 2 and LVDTs 3 and 4, are placed in line with each other perpendicular to weld bead; while LVDTs 5 and 6 are placed parallel to weld bead. Like in case of test plates, the speckle pattern is created on the upper surface of base plate for a width of 85 mm on each side of welding joint. Two forces of 50 N each are applied vertically on the stiffener through the clamping device, so as to keep it in position during welding.

4.5 Boundary Conditions

Since the experimental campaigns are meant to replicate the laser beam welding application on AA 6056-T4 as it is currently in-practice in aircraft industry; the efforts are made to integrate the industrial boundary conditions during experimentation. The industrial boundary conditions, both thermal and mechanical, are extremely complex in nature, due to the application of a large metallic suction table. As already mentioned, with reference to thermal boundary conditions the test cases are sub-divided into two categories; the first one, using simplest boundary conditions (e.g. test cases 01B, 01C and 02B) and the second one, using suction table (e.g. test case 01A, 02A and 03). Both of these categories are being discussed in the following.

4.5.1 Simplest Supporting Conditions

Test cases 01B, 01C and 02B (table 4.1) make use of simplest supporting conditions. Since the test plates are very thin, they are clamped at the farthest ends from above and below. The schematic representation is shown in Fig. 4.8. Moreover, LVDTs are removed due to the presence of clamps.

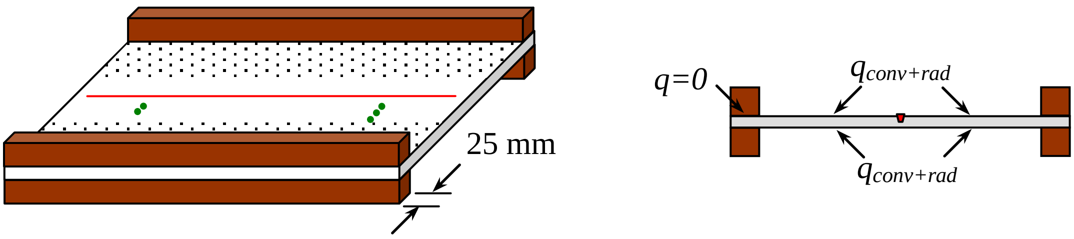

Figure 4.8. Simplest supporting conditions

The heat transfer in the surrounding environment is due to free convection and radiation only. At the interface of test plate and insulated clamps (25 mm wide), the heat loss is assumed to be zero. With reference to the mechanical boundary conditions, the out-of-plane displacement at the plate/clamp interface is considered as zero, while all other regions are free to expand and/or contract in any direction under the action of heat source. Figure 4.9 shows the actual experimental setup for such type of test cases.

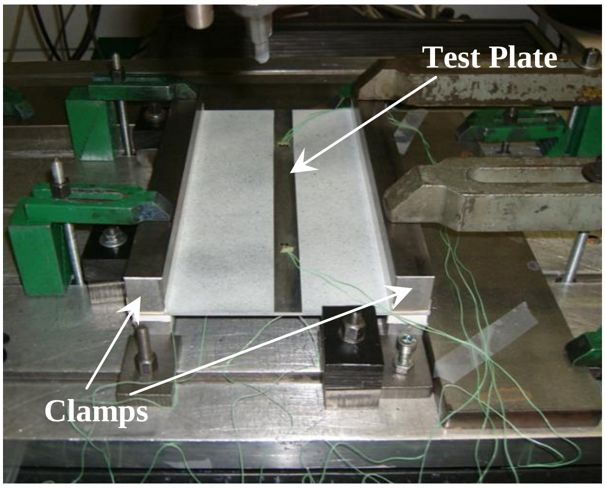

Figure 4.9. Experimental setup of simplest supporting conditions

4.5.2 Aluminium Suction Table

The aluminium suction table is made out of 25 mm thick plate of an aluminium alloy 6061. The size of the table is just sufficient to take care of the test plates with dimensions 300 mm x 200 mm. The test cases 01A, 02A and 03 have been carried out using this table. The aluminium suction table not only serves as a support to maintain the test plates in position but it is also capable of applying mechanical load of 1 bar in the form of suction force at the bottom surface of the test plates. Figure 4.10 shows the schematic sketch as well as the actual table. In Fig. 4.10 the red dotted line marks the position of test plate, where it must be placed to perform welding. The stoppers, shown in the figure, are meant to assist positioning of test plate; however, they are removed just before the start of welding after the application of pressure. The drilled holes and grooved regions of the table are designed to create vacuum. Although the table is provided with a fine rubber joint, meant to serve as a seal to avoid leakage, near the outer edge of test plate; yet the measured value of pressure ($\approx$ 0.8 bar) shows a significant presence of leakage. This is why the forced convection is assumed to be present at the bottom surface of the test plates.

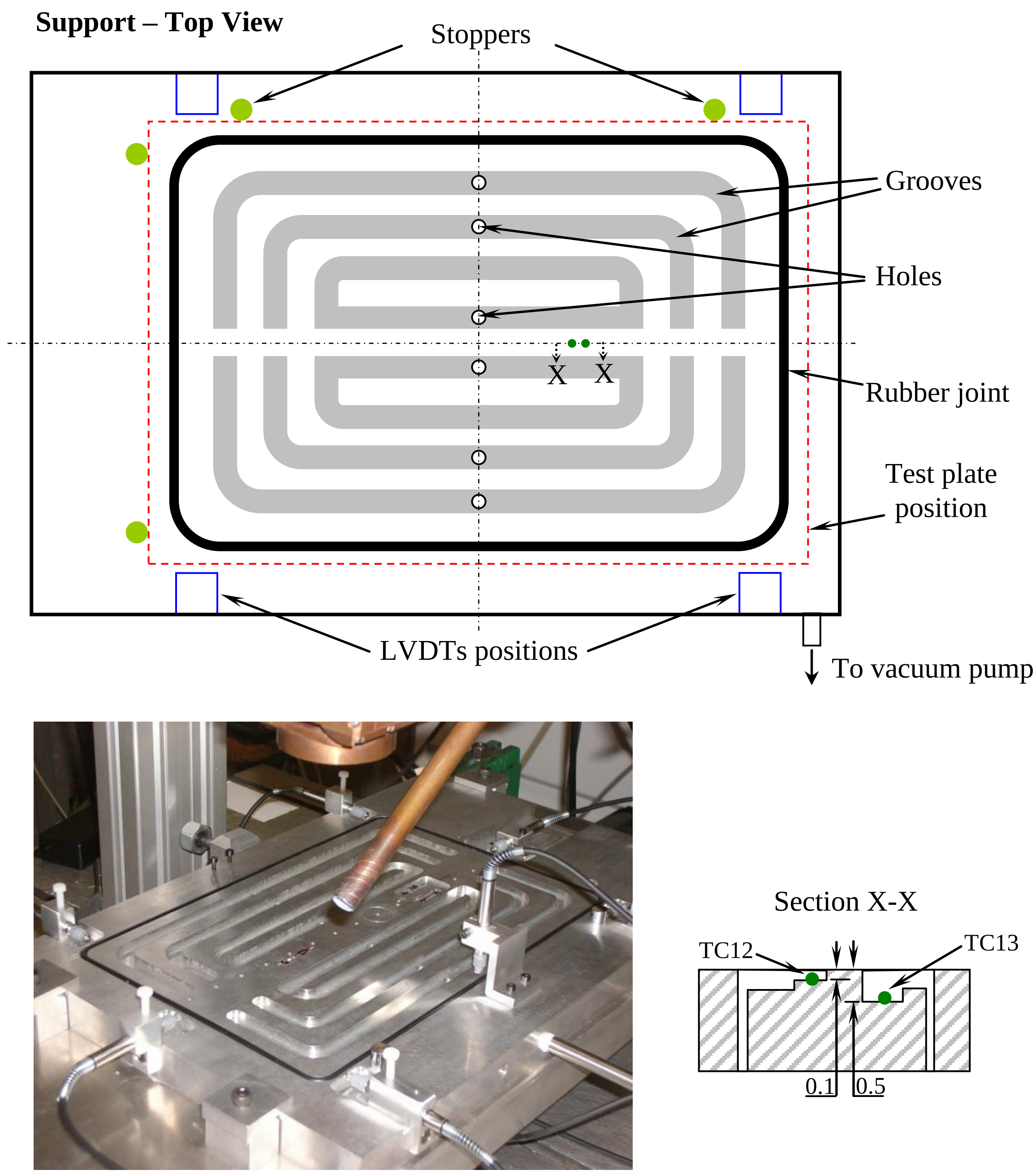

Figure 4.10. Aluminium suction table (dimensions in mm)

Two of the thermocouples (TC12 and TC13) are also installed on the suction table beneath the weld line. This is done to ensure the heat transfer in the support due to its possible contact with the test plate during welding. It will be shown in the subsequent sections that some heat loss takes place at the interface of the test plate and support.

The resultant thermal boundary conditions are shown in Fig. 4.11. It is believed that at the plate / support interface the heat transfer is of two types: forced convection ($q_{forced\ conv}$) and thermal conductance (q_{cond}); while the remaining surfaces experience free convection and radiation conditions ($q_{conv+rad}$).

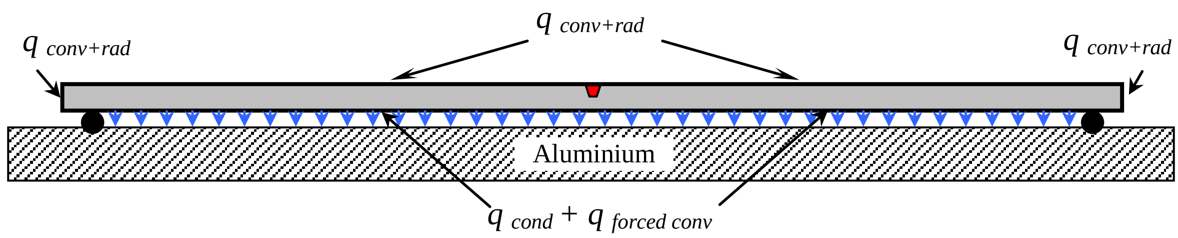

Figure 4.11. Thermal boundary conditions due to aluminium support

4.6 Methodology

In the previous sections the experimental setup, geometry and boundary conditions used during the experimental campaigns have been discussed at length. The welding parameters are also described in tables 4.1 and 4.2. The complete methodology adopted is being summarized here. Following steps have been performed for all the test cases:

- ***Visual inspection:*** To establish convex or concave curvature of test plates.
- ***Creation of speckle pattern:*** To measure the initial surface profiles of test plates by image correlation.
- ***Welding of thermocouples:*** To record the temperature values in the vicinity of fusion zone (FZ).
- ***Installation of LVDTs:*** To record the in-plane displacements during welding occurring as a result of local expansion and contraction of FZ and HAZ.
- ***Clamping of test specimens:*** To keep the test plates and T-joints in position during welding using insulated bars and aluminium suction table.
- ***Laser beam welding:*** To carry out welding on test plates and T-joints (the adjustment of welding parameters is also done at this stage).
- ***Infra-red camera:*** To observe the evolution of surface temperature of weld pool during welding.
- ***High speed camera:*** To observe the phenomenon of material ejection from the molten weld pool.
- ***Image correlation:*** To measure the final surface profiles of plates and T-joints and to observe the difference with initial surface profiles.
- ***Micrography:*** To measure the dimensions of FZ.

Having gathered all the experimental information, a comprehensive database is prepared. The experimental results are being presented in the subsequent sections.

4.7 Experimental Results

This section provides a detailed description of experimental measurements taken before, during and after the welding. These results may broadly be classified into three categories; first being the temperature measurements as taken from thermocouples and infra-red camera, second being the displacement measurements as recorded from LVDT sensors, image correlation technique and visual inspection and third being miscellaneous including micrography and high-speed camera observations. Further classification may be based upon the quantitative and qualitative nature of the results. Table 4.3 summarizes the classification of results.

Measurements	Quantitative	Qualitative
Temperature	Thermocouples	Infra-red Camera
Displacement	LVDT Sensors Image Correlation	Visual Inspection
Miscellaneous	Micrography	High Speed Camera

Table 4.3. Classification of experimental results

4.7.1 Thermocouple Measurements

In his work, Beck [BECT] suggests that K-type thermocouples should be used for measuring the temperatures up to 850°C. Additionally, his findings show that, due to reasons of increasing thermal inertia with increasing wire diameter, TC wires with the smallest possible diameter should be used. Furthermore, if the temperature gradient does not exist upon the workpiece surface, the two wires of TC may be welded separately; which implies that for a workpiece with significant thermal gradient, TC wires should be spot-welded at a single point.

Since the temperatures to be measured in HAZ of laser welded test plates / T-joints remain well below 850°C, the test cases presented in this work make use of K-type (Chromel-Alumel) thermocouple with wire diameter of 79 μm. K-type TCs are capable of measuring temperatures up to +1300°C with an accuracy in temperature measurement of 1.1°C, the sensitivity of 41 μV/°C and the response time of 20 ms. In order to avoid the effect of thermal gradient involved due to directional heating during welding, all the TCs were spot-welded at a single point on specified locations (Fig. 4.12). The spot-welded region and unsheathed wires were then required to be protected from radiations of the laser beam torch. This was done by applying a drop of 'nail polish'. During welding, the solvent ethyl acetate contained by nail polish vaporises at a temperature of 77.1°C, thereby, leaving behind a thin flexible film of plasticizers, which not only protects the TCs from radiations but also serves as an adhesive agent. It was ensured on a separate specimen that the application and the later vaporisation of nail polish do not affect the temperature measurements of TCs. The coordinate positions of TCs for test cases 01, 02 and 03 are shown in table 4.4.

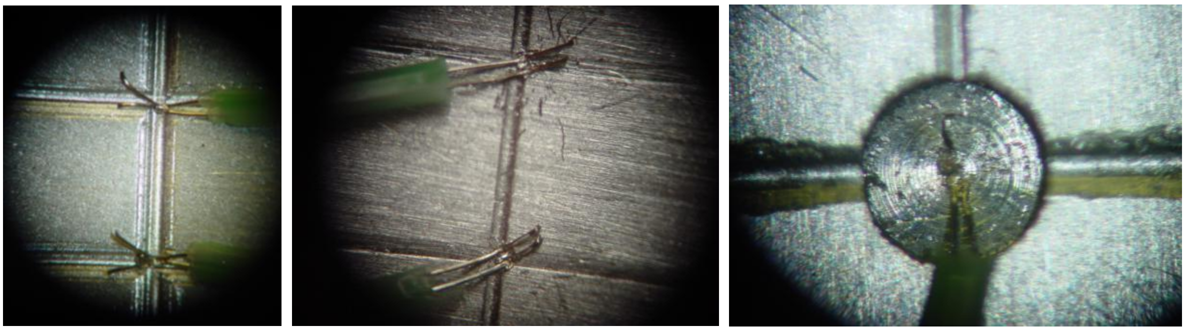

Figure 4.12. Magnified images of welded thermocouples

Test Case		TC1	TC2	TC3	TC4	TC5	TC6	TC7	TC8	TC9	TC10	TC11
01 & 02	**X**	75	75	75	225	225	75	75	93	94	-	-
	Y	3	6	9	3	6	0	6	0	3	-	-
	Z	0	0	0	0	0	-2.2	-2.5	-2.5	-2.5	-	-
03	**X**	75	75	75	225	225	75	93	93	75	75	225
	Y	3.5	7	10	4	7	0	0	4	1.25	1.25	1.25
	Z	0	0	0	0	0	-2.0	-2.5	-2.5	4	7	4

Table 4.4. Coordinate positions of thermocouples (dimensions in mm)

Temperature acquisition during welding was made using FRONTDAQ: FD20 acquisition system, which is capable of treating 20 differential inputs from 2 or 4 wire sensors simultaneously with an acquisition rate of 7680 Hz. The temperature acquisition during laser beam welding experiments was made at a frequency of 200 Hz. The system is capable of using two different ranges of potential differences; range 1 (from ±15 mV to ±1 V) and range 2 (±1 V to ±10V), with an achievable precision of ±10 μV to ±100 μV. The accuracy of temperature measurements for K-type thermocouple (-180°C – +1300°C) using Frontdaq system is ± 1.2 °C.

4.7.1.1 Test Case 01A (Fusion welding on support)

Time-temperature curves as recorded for test case 01A (Table 4.1) at all the thermocouple (TC) positions (Fig. 4.6) are being presented here. Figure 4.13 shows the temperature histories on the upper surface of the test plate along with the legend of TC positions. It is to be noted that TC1 and TC4 are at the same distance from the weld center line, therefore they should, ideally, show the same peak temperatures. However, some differences may be observed for all such thermocouples. These differences may be attributed to, in first place, the delay of 20 ms in the response time of the TCs and, in second place, to the varying amount of heat energy absorbed by the test plates during the key-hole welding process as the latter may be observed from the varying dimensions of FZ. These varying dimensions of the FZ shall be presented in the section of micrography.

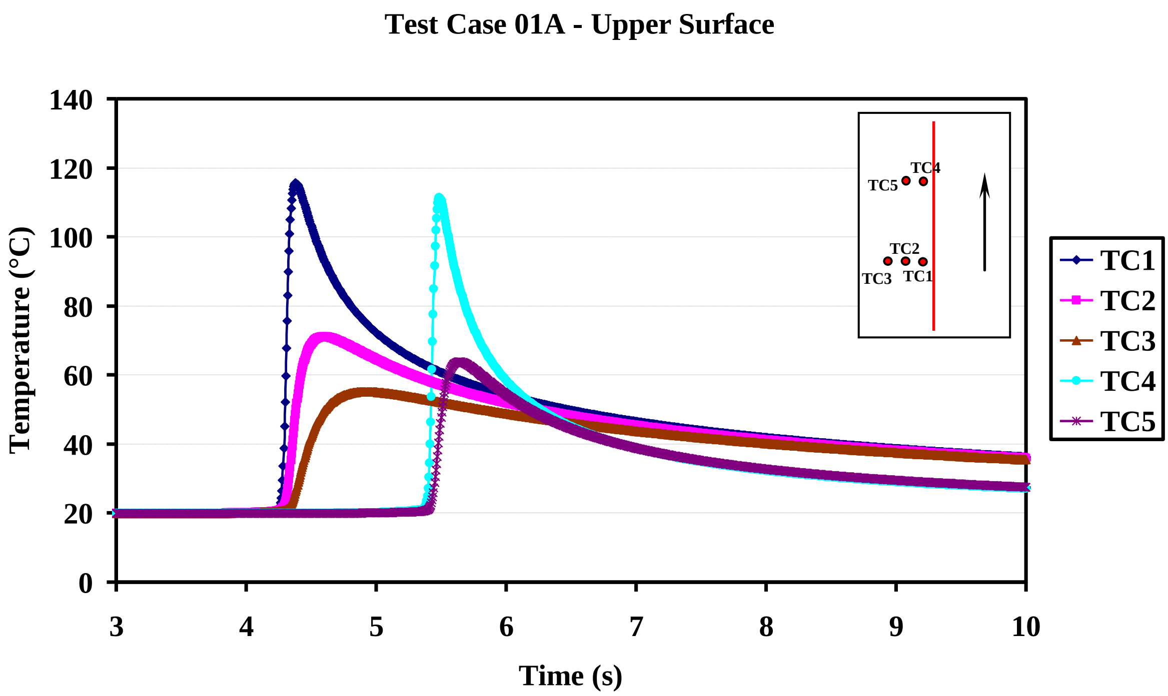

Figure 4.13. Thermal histories at the upper surface of test plate – Test Case 01A

Figure 4.14 presents the thermal histories for the TCs installed at the bottom surface of the test plate. As already mentioned, TC6 was welded directly underneath the weld fusion line in a fine drilled hole of depth 0.3 mm from the bottom surface; it is believed that the temperature values measured at this location shall be least affected by any external factor like radiations from heat source, forced convection by shielding gas (Argon in this case) etc. In addition to that it gives the temperature measure in the closest proximity to the FZ. Similarly, TC8 being immediately below the weld fusion line gives the next highest value of peak temperature measured from any of the TCs.

Test Case 01A - Lower Surface

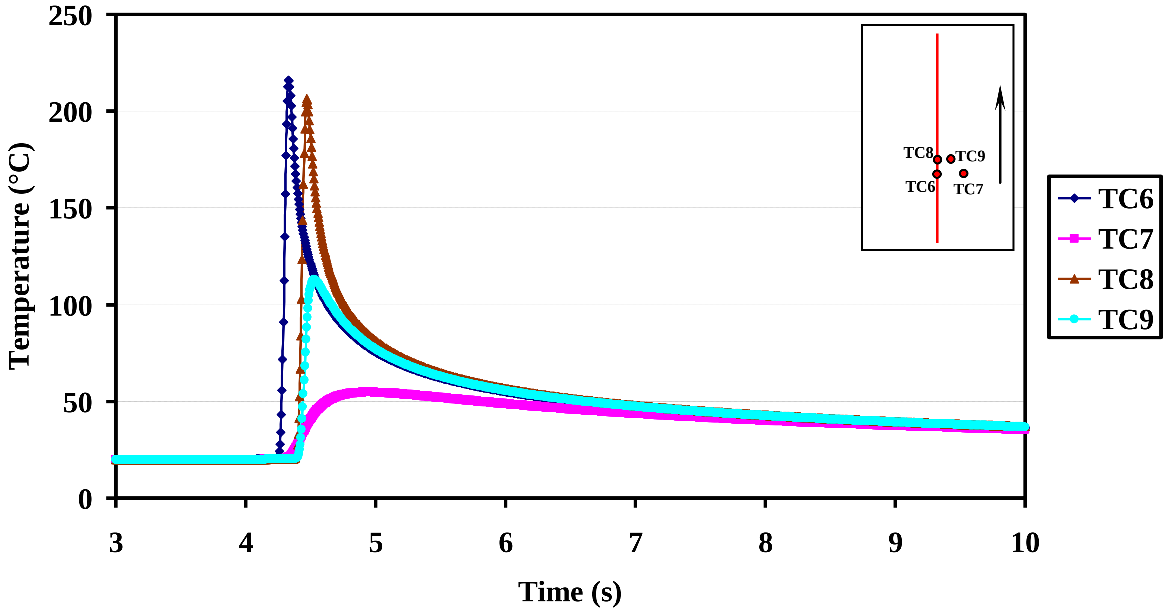

Figure 4.14. Thermal histories at the lower surface of test plate – Test Case 01A

Test Case 01A - Aluminium Support

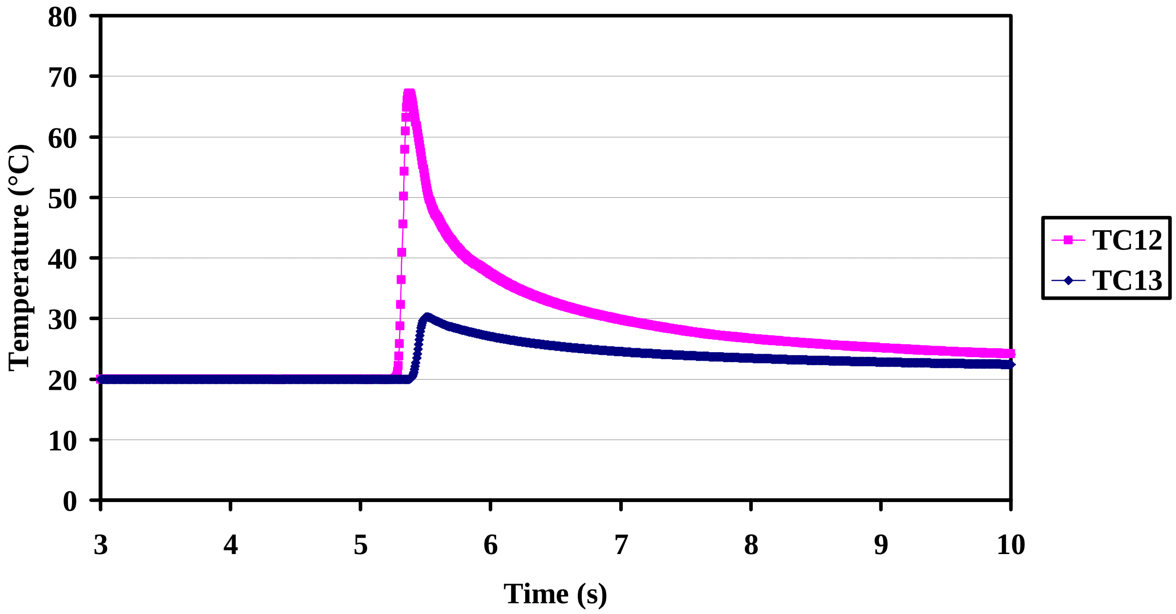

Figure 4.15. Thermal histories on the aluminium support – Test Case 01A

The temperature measurements from the TCs installed on the aluminium support (Fig. 4.10) are shown in Fig. 4.15. TC12 shows a significantly high temperature value of approximately 70°C. This observation verifies the heat dissipation from the test plate to the aluminium support due to contact.

4.7.1.2 Test Case 01B (Fusion welding in air)

Since test case 01B does not involve use of aluminium support, only the time-temperature curves of upper and lower surfaces are presented in Figs. 4.16 and 4.17, respectively. Temperature measures at positions TC1 and TC4, and at TC2 and TC5 show a rather stable heat source and constant absorption of heat energy along the length of FZ.

Test Case 01B - Upper Surface

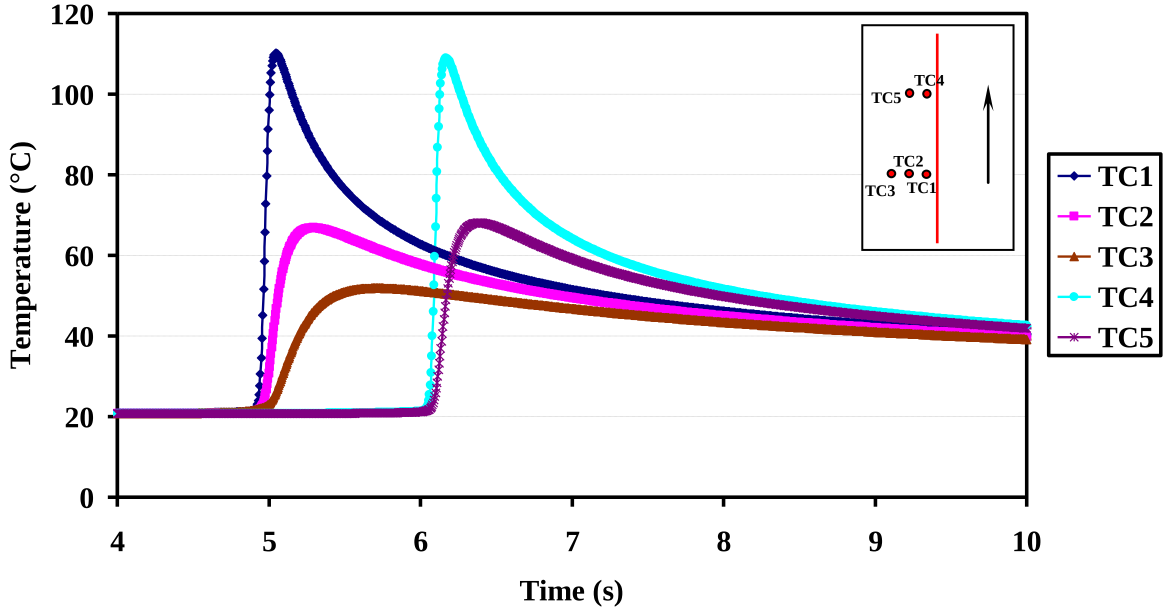

Figure 4.16. Thermal histories at the upper surface of test plate – Test Case 01B

Test Case 01B - Lower Surface

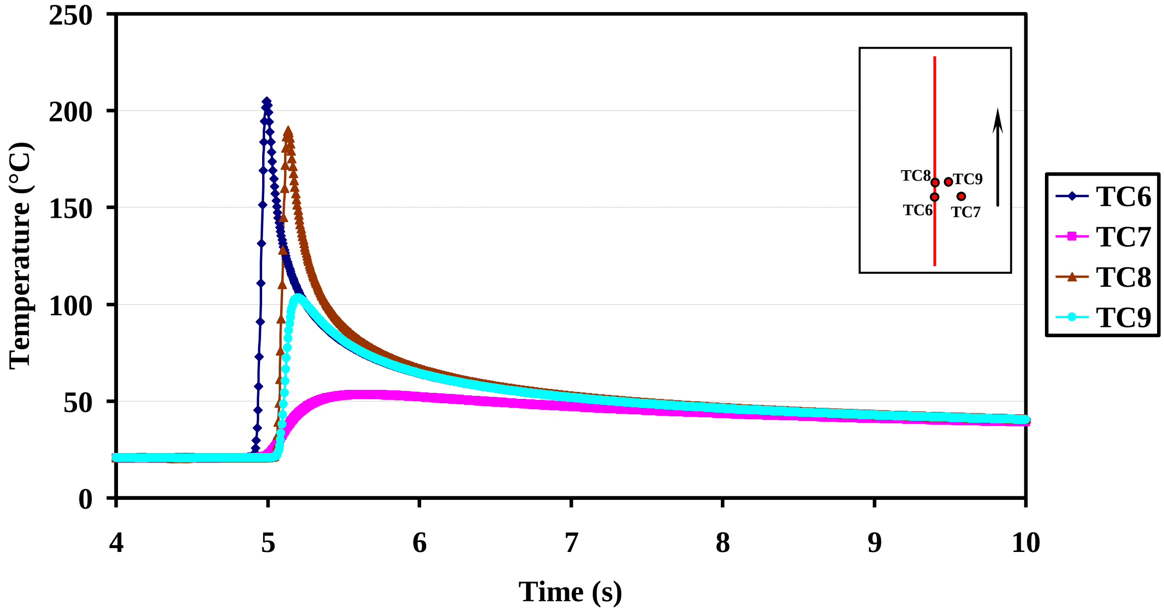

Figure 4.17. Thermal histories at the lower surface of test plate – Test Case 01B

4.7.1.3 Test Case 01C (Fusion welding with high beam power)

Large variation of peak temperatures is observed at positions TC1 and TC4 for this test case (Fig. 4.18), while TC6 and TC8 got completely burnt out and hence are not shown in Fig. 4.19; the reasons being the excessive amount of heat input during welding (Table 4.1) and highly unstable weld pool. Moreover, the response of the test case in terms of displacement measurements has also been highly irregular.

Case Test 01C - Upper Surface

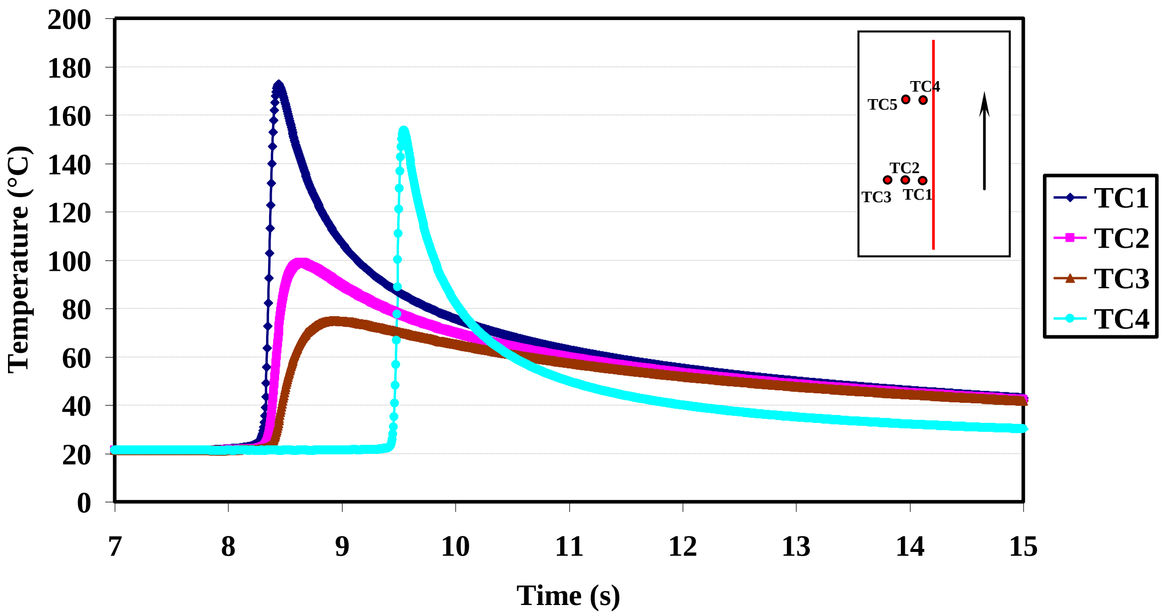

Figure 4.18. Thermal histories at the upper surface of test plate – Test Case 01C

Case Test 01C - Lower Surface

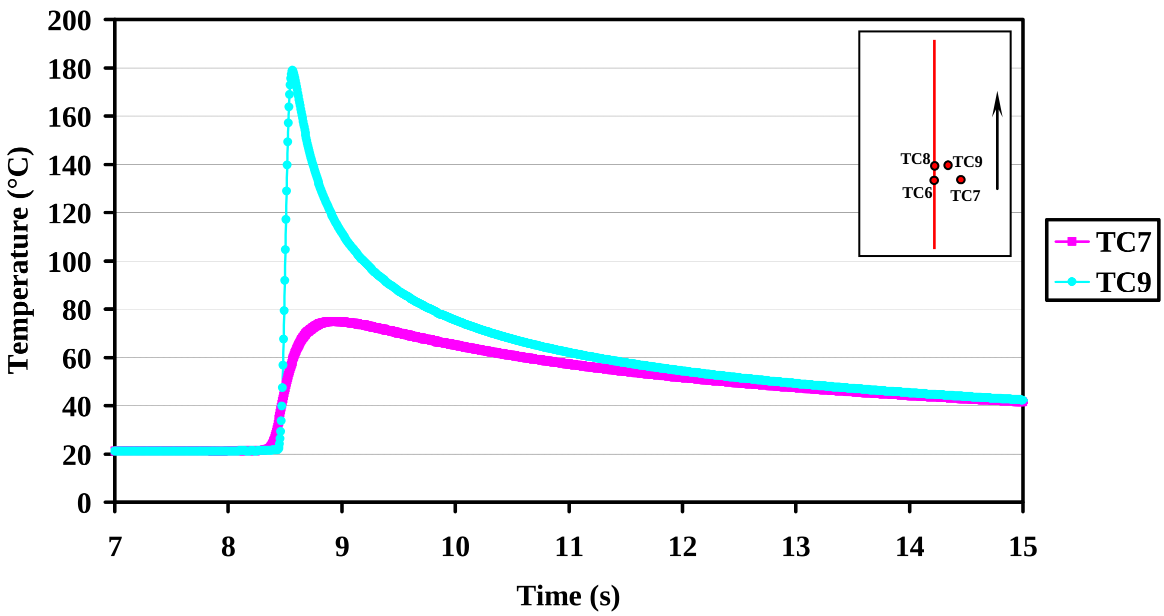

Figure 4.19. Thermal histories at the lower surface of test plate – Test Case 01C

4.7.1.4 Test Case 02A (Filler welding on support)

This test case involves the use of filler metal wire, which acts as an additional source of variation in temperatures at positions TC1 and TC4 (Fig. 4.20); because the moment solid filler wire enters the weld pool it tends to drop its temperature. Although the additional amount of heat energy required for the fusion of filler wire is provided by increasing the laser beam power, minute perturbations in weld pool temperatures are almost inevitable.

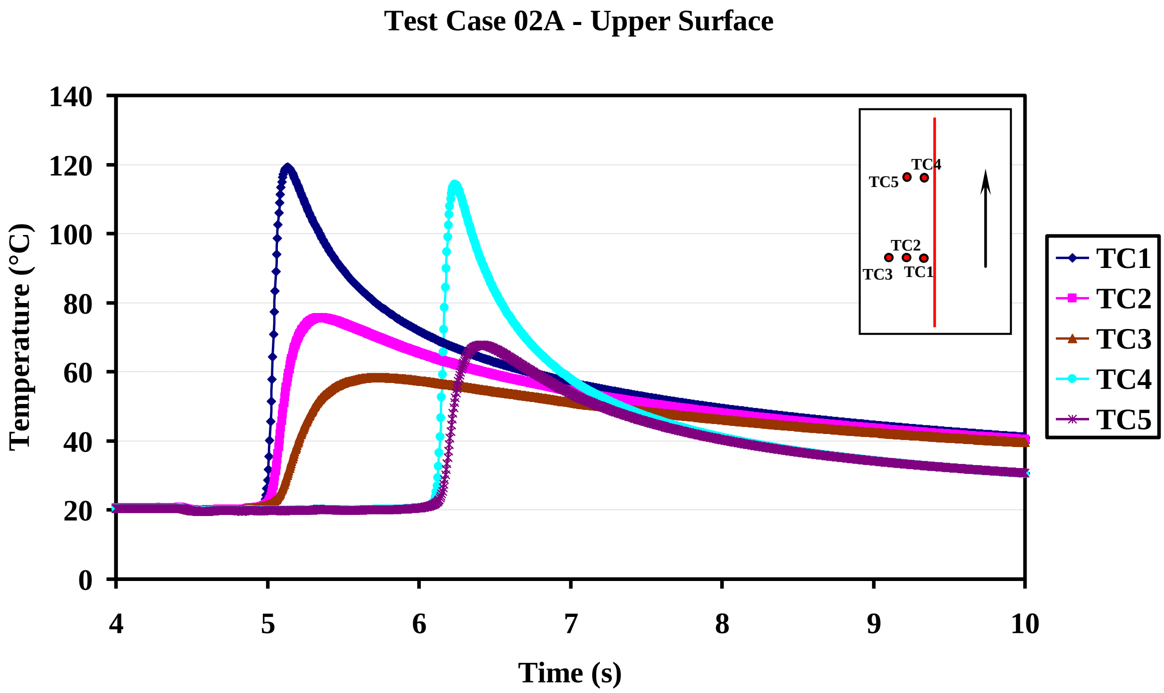

Figure 4.20. Thermal histories at the upper surface of test plate – Test Case 02A

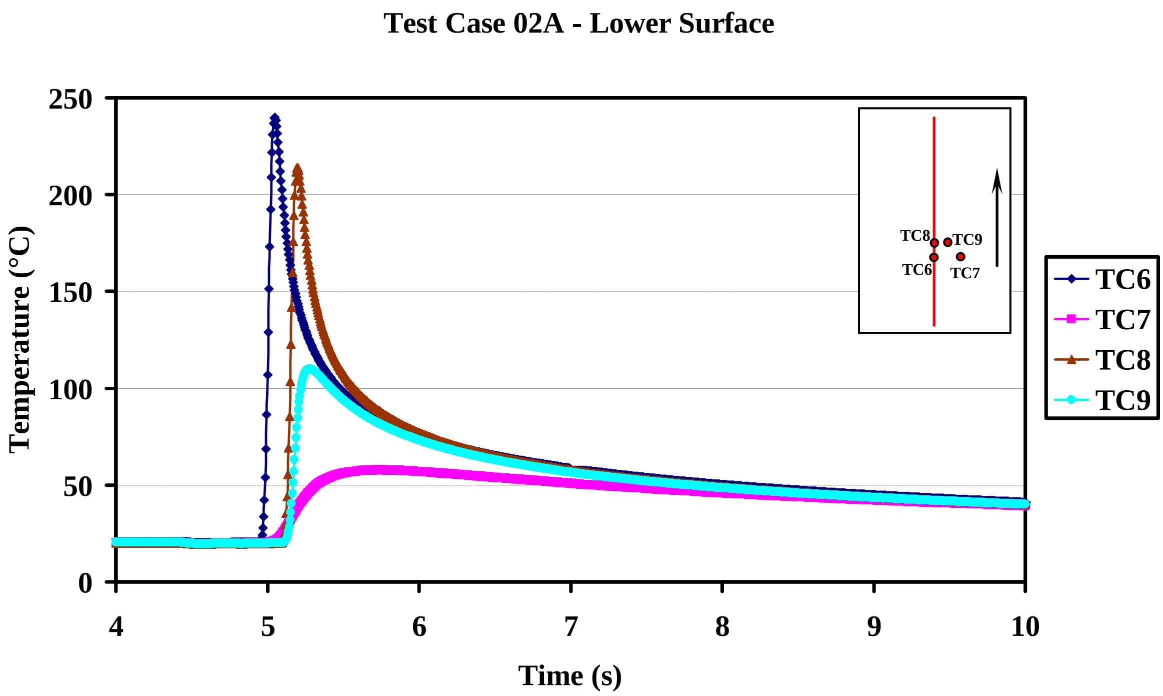

Figure 4.21. Thermal histories at the lower surface of test plate – Test Case 02A

A relatively higher temperature value of over 90°C observed at TC12 (Fig. 4.22) implies more heat dissipation in support as compared to the test case 01A (Fig. 4.15).

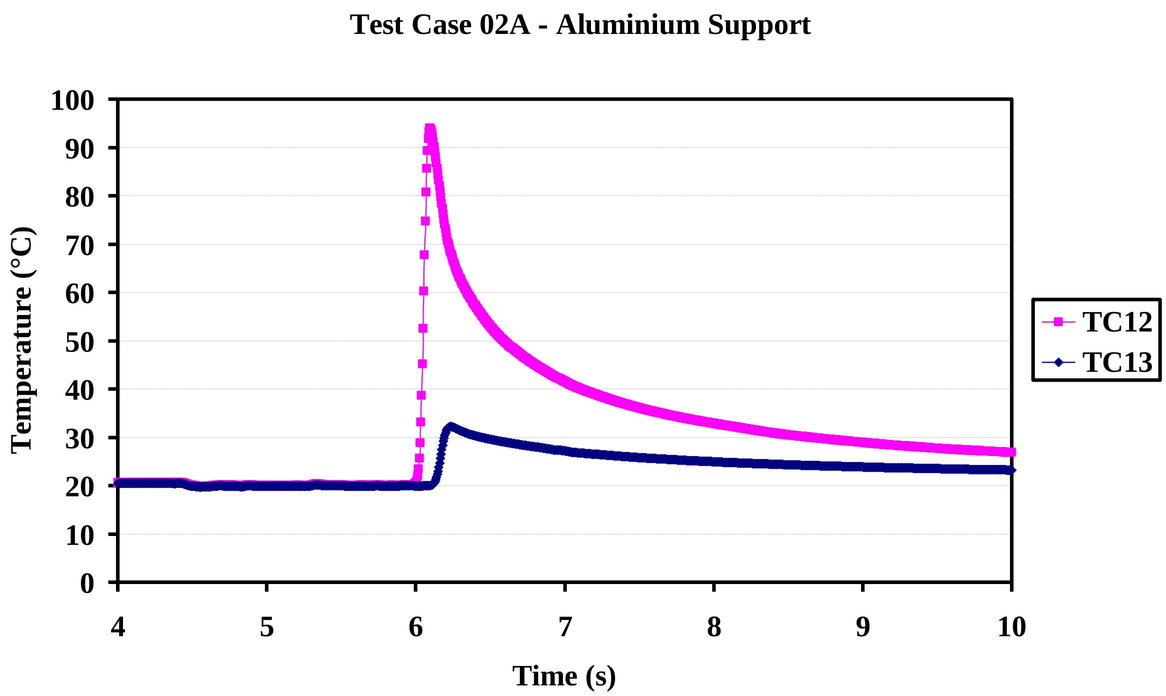

Figure 4.22. Thermal histories on the aluminium support – Test Case 02A

4.7.1.5 Test Case 02B (Filler welding in air)

This test case is performed in air with filler wire addition. The time-temperature curves are presented in Figs. 4.23 and 4.24.

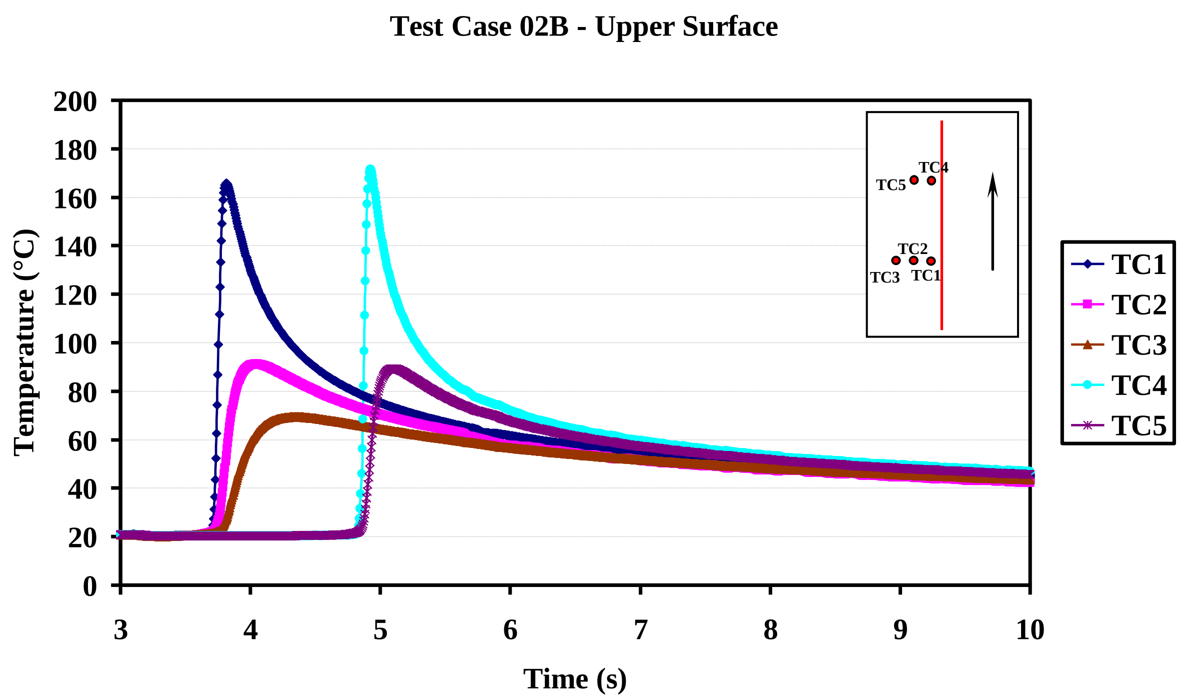

Figure 4.23. Thermal histories at the upper surface of test plate – Test Case 02B

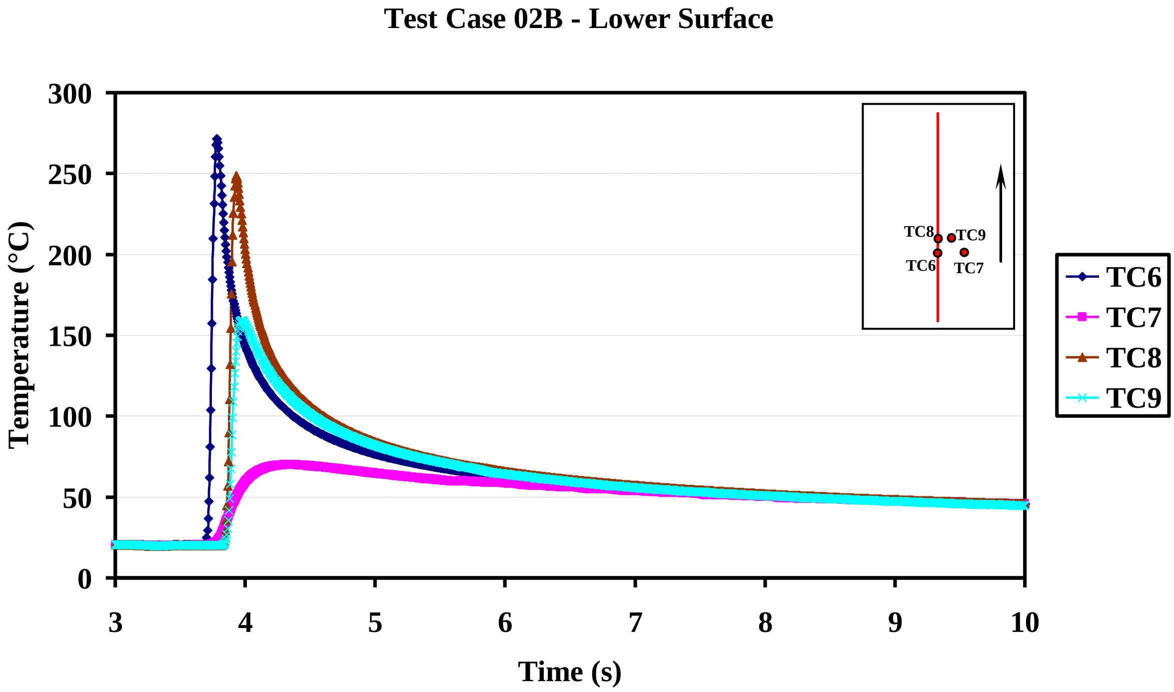

Figure 4.24. Thermal histories at the lower surface of test plate – Test Case 02B

4.7.1.6 Comparison of Peak Temperatures

The comparative analysis of peak temperatures for test cases 01 and 02 is being presented in this section at some of the TC positions. The results of TCs that are closest to the FZ viz. TC1, TC4, TC6 and TC8 are compared with each other. TC12 is selected to compare the test cases with respect to the heat transfer in the aluminium support.

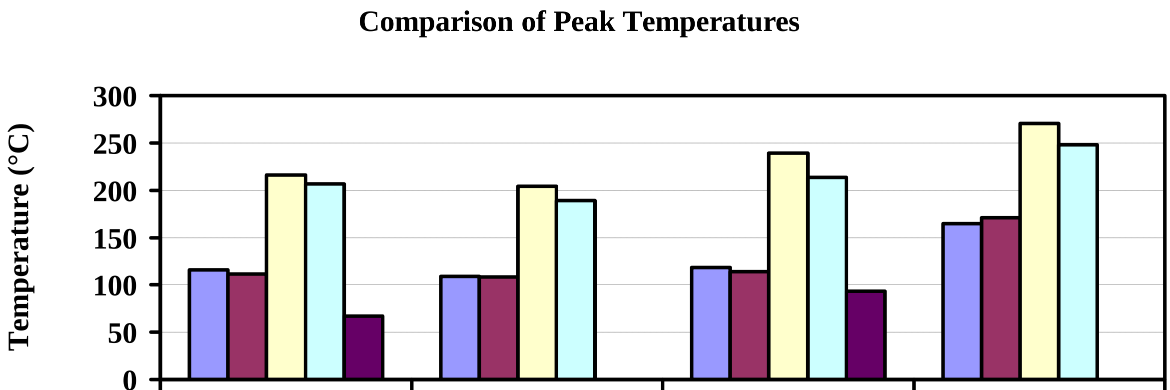

	01A	01B	02A	02B
TC1	115.59	109.27	118.56	164.85
TC4	111.38	108.13	113.84	170.85
TC6	215.84	204.12	239.09	270.82
TC8	206.58	189.17	213.66	247.88
TC12	67.23		93.50	

Test Case

Figure 4.25. Comparative analysis of peak temperatures for test cases 01 and 02

Recapitulating, test cases 01A and 01B were performed with the constant laser beam power of 2300 W, where the thermal boundary conditions for the former includes the use of aluminium support while the latter involves welding in air. Similarly, test cases 02A and 02B were carried out with the beam power of 3000 W and with identical boundary conditions as those of 01A and 01B, respectively; in addition, they involve the use of filler wire.

Comparing peak temperatures for 01A and 01B (Fig. 4.25), it may be observed that the temperature values are in close approximation to each other. For instance, peak temperature at TC1 for 01A is 115.59°C while that of 01B is 109.27°C. Similarly, at positions TC4, TC6 and TC8, the peak temperature values are slightly higher for test case 01A than for 01B. This observation suggests that the peak temperature value is independent of the thermal boundary conditions. Since test case 01A involves the use of aluminium support, which means a relatively rapid heat loss from the test plate to the support, yet the peak temperatures for 01A are higher than for 01B. The thermal boundary conditions have a rather more pronounced effect over the cooling part of the time-temperature curves, as will be shown in the next section. It further suggests that the peak temperature values should necessarily depend upon the amount of heat energy contained by the test plate, which may vary on case to case basis depending upon the efficiency of the process, stable beam power, reflections from the surface of test plate, ejection of material from the key-hole etc.

Test cases 02A and 02B (Fig. 4.25), however, present varying trend. For instance, the peak temperature at TC1 for 02A is 118.56°C while that of 02B is 164.85°C. As these test cases make use of filler metal wire, a considerable part of heat input (laser-beam power) is consumed in melting the solid metallic wire. Since there is no direct way of calculating as to what fraction of heat energy is used by filler wire, the variations in peak temperature values may be expected. A difference of more than 45°C at TC1 and similar differences at TC4, TC6 and TC8 suggest large variations in the amount of heat energy absorbed by the test plates.

Close approximation of peak temperatures for test cases 01A and 02A (Fig. 4.25) directs towards another interesting observation. Test case 01A differs from 02A on the basis of laser beam power, which are 2300 W for the former and 3000 W for the latter. This implies that the additional amount of heat energy provided in the form of laser beam power for the test case 02A is almost entirely utilised for the fusion of filler wire. These test cases, hence, are also of great interest from numerical simulation point of view.

The peak temperatures observed at TC12 for test cases 01A and 02A suggest that a relatively higher amount of heat energy goes into the support for 02A.

4.7.1.7 Comparison of Thermal Boundary Conditions

The effect of thermal boundary conditions upon temperature histories is being discussed in this section. Figure 4.26 presents time-temperature curves at TC1 and TC4 for test cases 01A (using aluminium support) and 01B (free convection in air). Although both the test cases are performed using identical welding parameters (Table 4.1), yet the effect of thermal boundary conditions on peak temperatures is negligible. However, cooling parts of the curves vary as a result of different boundary conditions. In Fig. 4.26 the specimen of test case 01A, being in contact with aluminium support, shows a comparatively faster cooling rate due to rapid heat dissipation within the support than that of test case 01B. The net difference of around 7°C may be observed at time 30 sec.

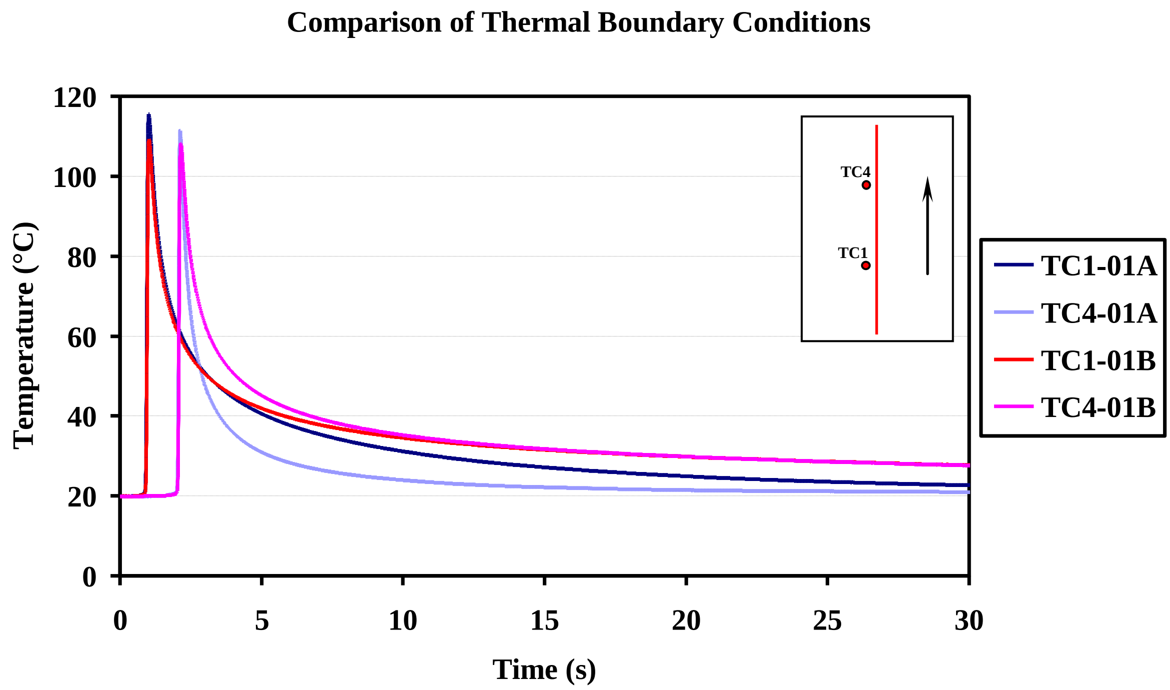

Figure 4.26. Comparative analysis of thermal boundary conditions for test case 01

The cooling curve of 01A at TC1, installed closer to the weld start end, shows little divergence from that of 01B at the start of cooling. The reason being the continued application of heat source heading towards the weld stop end while cooling at TC1 has already started. The trailing high temperature isotherms do not allow rapid cooling at position TC1. Once the heat source is removed, both the cooling curves of 01A and 01B for TC1 separate, thereby showing the influence of different thermal boundary conditions.

The rapid divergence of the cooling curve of test case 01A at TC4 from the test case 01B is, however, observed even at the very start of the cooling. This is because TC4, installed near the weld stop end, experiences a sudden removal of heat source, and hence the thermal boundary conditions show an immediate pronounced effect over the cooling curves. A large fraction of heat energy goes into aluminium support for the case 01A in a very short interval of time, while 01B continues to cool down slowly under the action of free convection and radiation in air. It may, therefore, be established that at least for a specific length of time, the amount of heat energy contained by the specimens of test case 01B is higher than those of test case 01A.

4.7.1.8 Test Case 03 (T-joint welding)

The TC positions for test case 03 are shown in Fig. 4.7. Since the welding parameters and the boundary conditions for all the test cases type 03 are identical (Table 4.2) and the sub-classification is based only upon the numbers and locations of tack welds, the thermal histories recorded for the cases 03A, 03B, 03C and 03D are mostly identical with some differences in peak temperatures due to TC positioning and welding heat input uncertainties. The results of one of the test cases are being presented here.

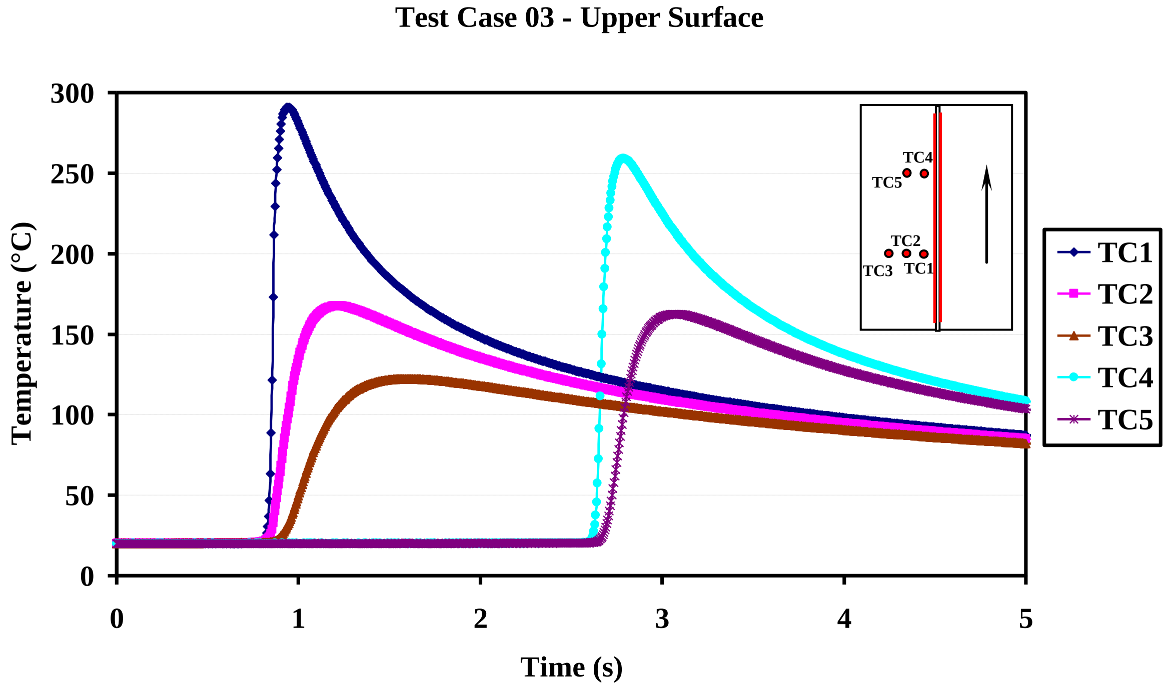

Figure 4.27. Thermal histories at the upper surface of base plate of T-joint – Test Case 03

Figure 4.27 shows the time-temperature curves recorded at the upper surface of the base plate of T-joint. It may be observed that peak temperature at TC1 is comparatively higher than the one at TC4. In addition to the various other reasons mentioned in previous sections, it is observed that the distance of TC from the weld fusion line also plays an important role in defining the peak temperature values. The thermocouples TC1 and TC4, being very close to weld fusion zone, are located in the region where thermal gradient is extremely high. Therefore, a slight variation in positioning of TCs may lead to such kind of differences. Upon measuring the distance after welding, it is found that TC1 is closer to FZ by a distance of 0.5 mm as compared to TC4. This observation is interesting from numerical simulation point of view, where the temperature calculation may be carried out taking care of exact location of thermocouples.

The temperature histories at the lower surface of the base plate are shown in Fig. 4.28. The thermocouples TC6 and TC7 have shown very high values of peak temperature (over 400°C), as they are located immediately underneath the weld center line. Additionally, TC6 is positioned in a depth of 0.5 mm from the bottom surface and, hence, has shown slightly higher peak temperature compared to TC7. The peak temperature as observed at TC8 is slightly higher than 250°C, which is in fact quite close to the one measured at TC4 (Fig. 4.27). It is to be noted from Fig. 4.7 that TC4 and TC8 are installed at the same distance (4 mm) from the weld center line, but at the opposite faces of base plate. Therefore, it may be concluded that the isotherms in the through-thickness direction become constant at a distance of 4 mm maximum from the weld center line.

Figure 4.29 presents the time-temperature curves recorded on the stiffener of the T-joint. The thermocouples TC9 and TC11 are installed at a distance of 4 mm from the base plate. The repeatability of the results is also established on the basis of peak temperature (around 275°C) measured from each TC.

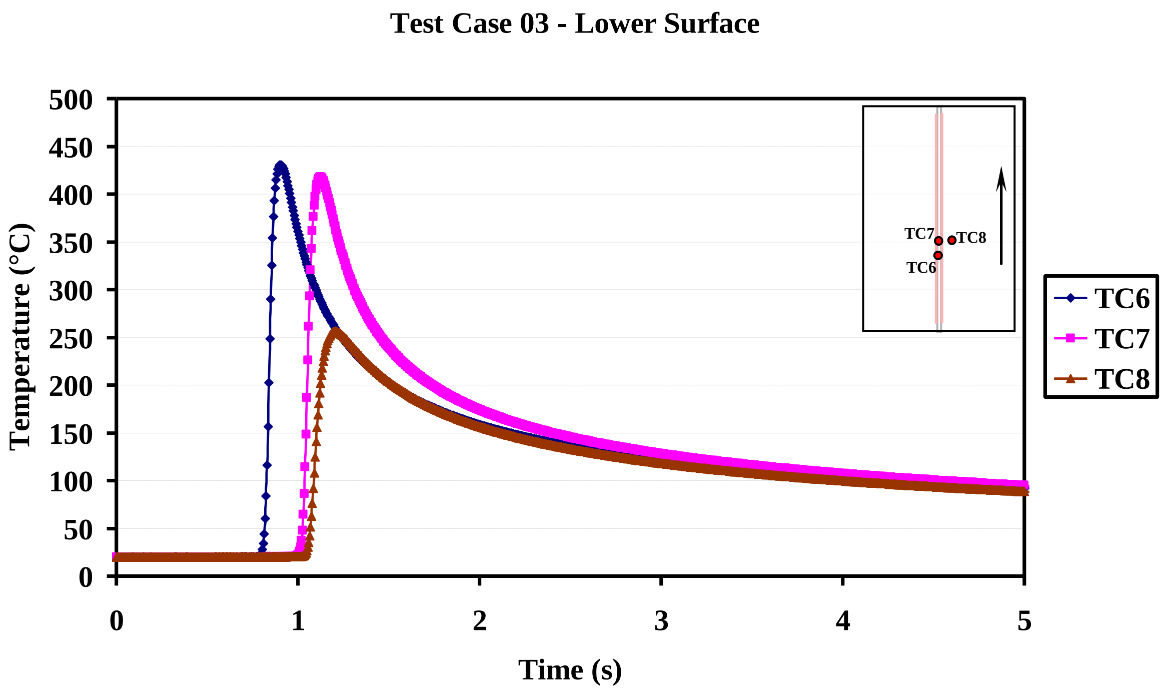

Figure 4.28. Thermal histories at the lower surface of base plate of T-joint – Test Case 03

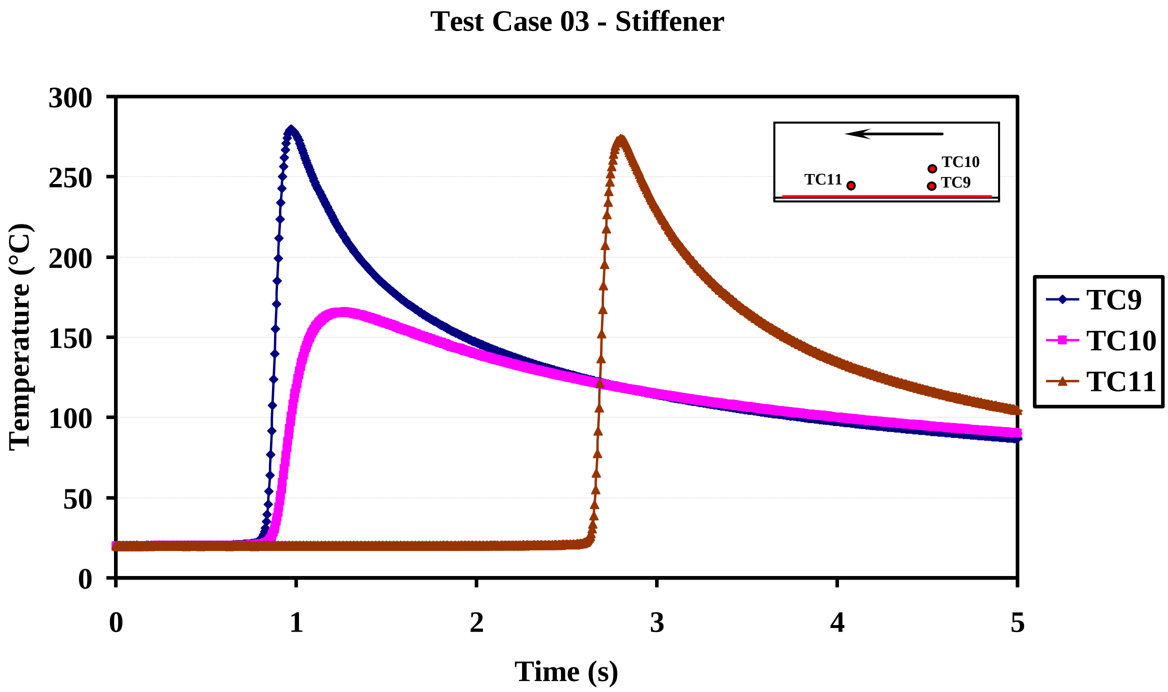

Figure 4.29. Thermal histories on the stiffener of T-joint – Test Case 03

4.7.2 LVDT Sensors

The linear in-plane displacements occurring due to localized expansion and contraction of test plates and T-joints during welding is measured with the help of LVDT sensors. A total of 6 LVDT sensors are used for each test case (Figs. 4.6 and 4.7). For convenience, the set of LVDT1 and LVDT2 is being called here as Set A, since both the LVDT sensors are placed in line to each other perpendicular to the welding direction. Moreover, both the LVDTs are likely to show the similar type of displacement evolution. Likewise, Set B will represent the pair of LVDT3 and LVDT4. Although LVDT5 and LVDT6 are also placed in line to each other, yet they are expected to show different behaviour from each other, as the former is installed near the weld start end and the latter is placed close to the weld stop end.

4.7.2.1 Test Case 01A (Fusion welding on support)

Figure 4.30 shows the displacement evolution during welding for test case 01A at positions LVDT1, LVDT2, LVDT3 and LVDT4. It may well be observed that LVDT1 and LVDT2 follow a unique identical pattern. Likewise, LVDT3 and LVDT4 also follow the trend similar to each other. It will be observed in the subsequent sections that for all the test cases, these LVDTs follow identical evolution of displacements. Analysing the displacement evolution, it is found that the moment heat source is applied; the region immediately beneath the welding torch tends to expand in all directions. Since LVDT1 and LVDT2 are installed near the weld start end, they respond immediately and the displacement values increase rapidly, while at the same time LVDT3 and LVDT4 are far enough to record any displacements as no expansion has yet taken place in the regions next to them. As the heat source advances, the slopes of the displacements at LVDTs 1 and 2 decrease. This is because when heat source moves away from weld start end, the heating rate in that region already starts decreasing though the temperatures are still high enough to induce expansion. The phenomenon continues and the slopes of displacements reduce till the heat source reaches weld stop end.

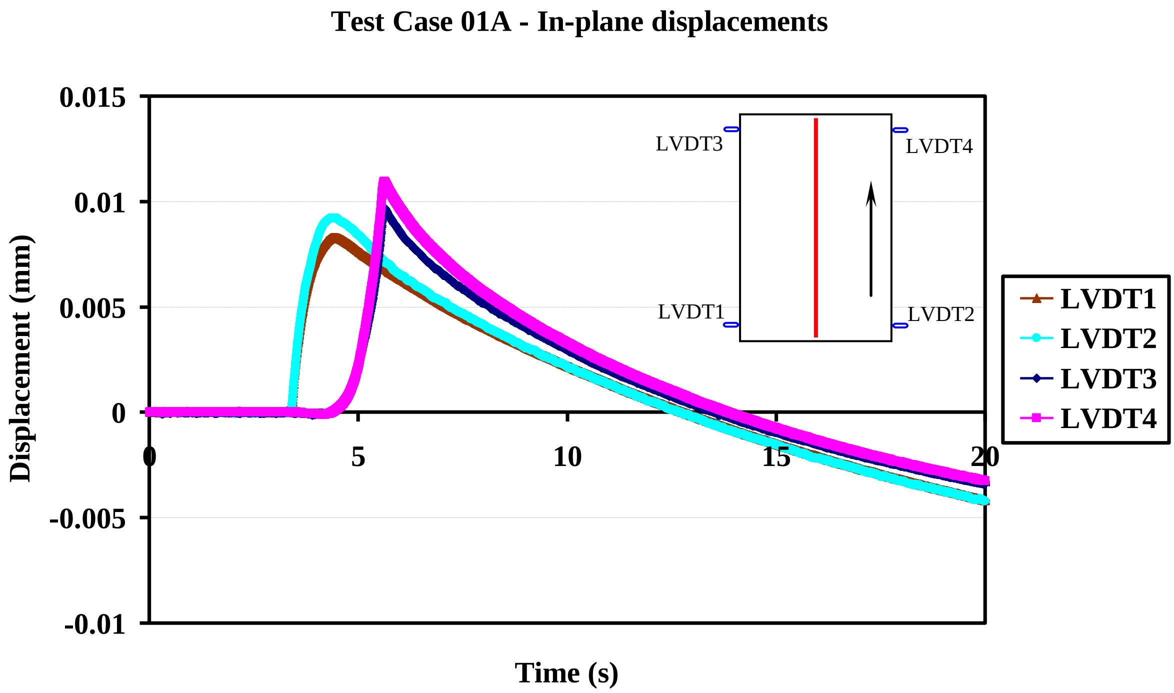

Figure 4.30. Evolution of in-plane displacements for LVDTs 1, 2, 3 and 4 – Test Case 01A

An exact opposite pattern is observed at LVDTs 3 and 4. Since heat source is heading towards these LVDTs, the slope of these curves increase gradually. The response is very slow at the start while it increases rapidly towards the end, as the weld stop end experiences more and more expansion due to heating. However, having reached the maximum attainable value, these LVDTs experience an abrupt decrease in displacement. This is because the moment heat source is removed; the regions next to them immediately start to cool down due to surrounding cooling media (air for example). And now following the contraction due to cooling displacement values start decreasing.

No such discontinuity is observed for LVDTs 1 and 2, as the regions adjacent to them have already started cooling down long before heat source is extinguished. This may be verified from Fig. 4.30; where the time instant at which peak value of displacement is noted for LVDTs 3 and 4, LVDTs 1 and 2 are already showing decreasing displacements.

Ideally, the displacements measured by LVDTs of Set A and Set B should have the same magnitude, yet the little difference observed may be attributed to the slight variations in positioning of LVDTs, placement of the test plates, centering of the weld torch with respect to plate, slipping of plate during welding etc. In order to minimise the effect of some of these factors the averaged displacements of corresponding LVDTs of Set A and Set B are calculated and presented in Fig. 4.31. This is also beneficial from numerical simulation point of view, where a symmetric model will be used and displacements of only a symmetric half of the test plates will be calculated.

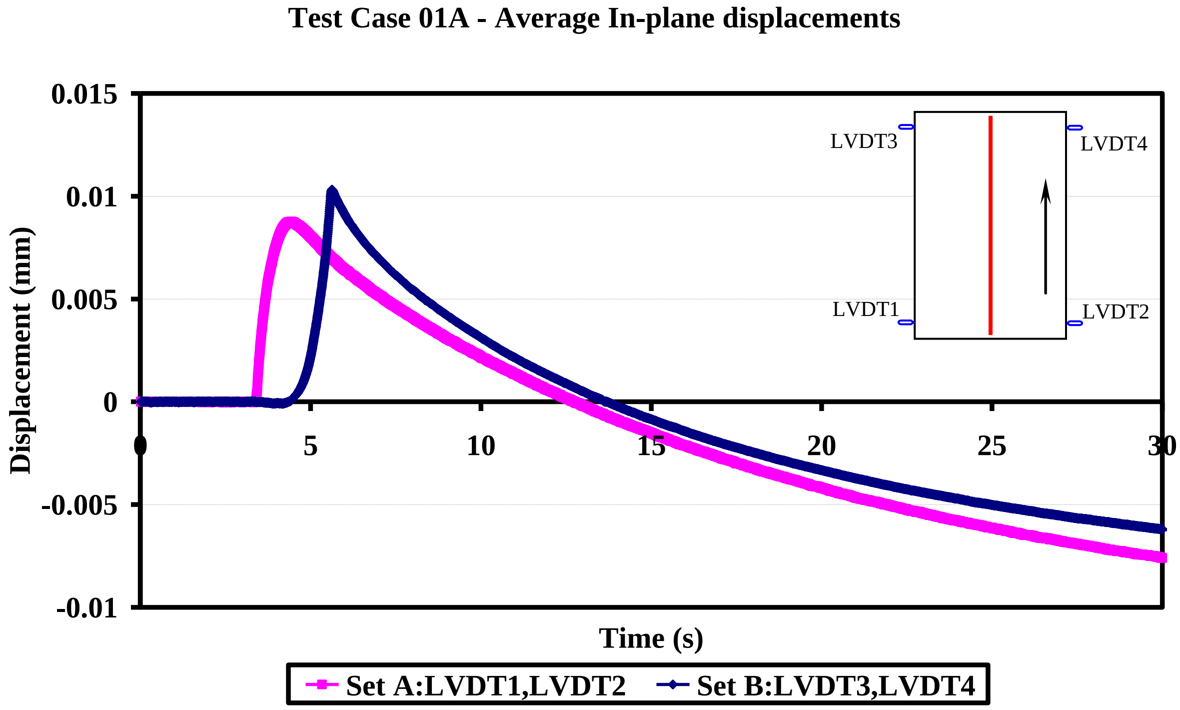

Figure 4.31. Average in-plane displacements for Set A and B – Test Case 01A

Results of LVDTs 5 and 6 are shown in Fig. 4.32. Since LVDTs 5 and 6 are installed near the weld start and stop ends, respectively. Their displacement evolution is very much identical to those of Set A and Set B, respectively. However, the magnitude of displacement recorded by these LVDTs is approximately 5 times as high as those of Sets A and B. The obvious reason is their distance from the weld FZ. LVDTs of Set A and B are installed at a distance of 100 mm from the weld center line while LVDT 5 and 6 are placed at a distance of 5 mm from FZ (Figs. 4.6 and 4.7). These LVDTs are, however, sensitive to the slippage in the direction of welding due to heat source movement.

Test Case 01A - In-plane displcements

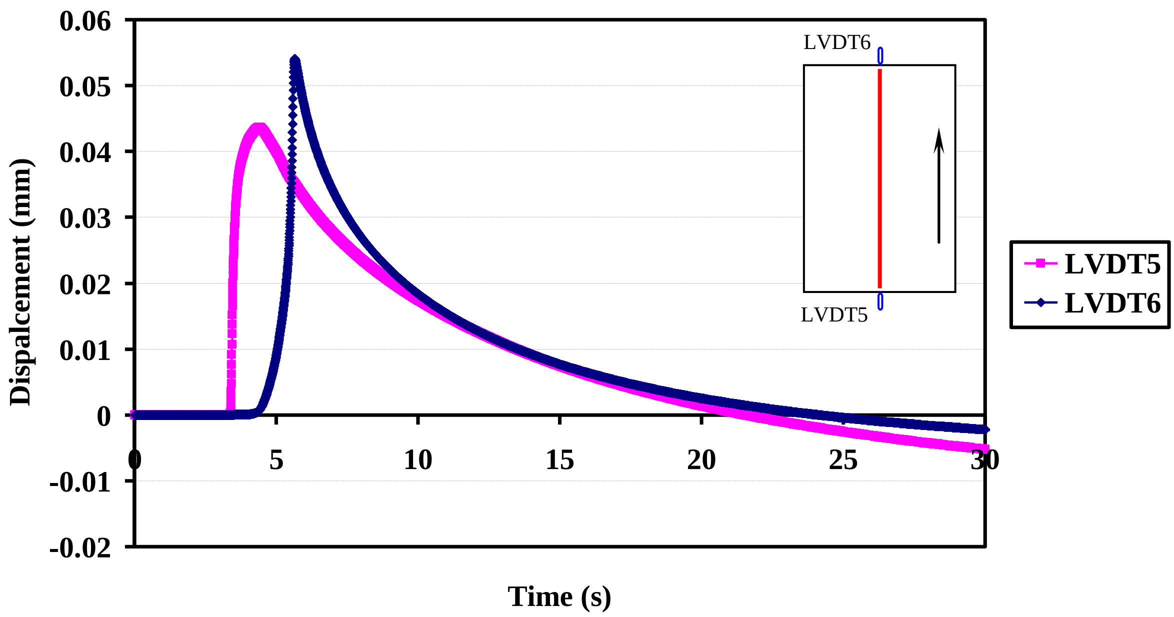

Figure 4.32. Evolution of in-plane displacements for LVDTs 5 and 6 – Test Case 01A

4.7.2.2 Test Case 02A (Filler welding on support)

The evolution of displacement at various LVDT positions has been discussed in detail in previous section. The expansion and contraction of test plates for all the test cases follow similar pattern unless otherwise affected by some additional factor. The difference in magnitudes for various cases may, therefore, be attributed to changing welding parameters.

Test Case 02A - In-plane displacements

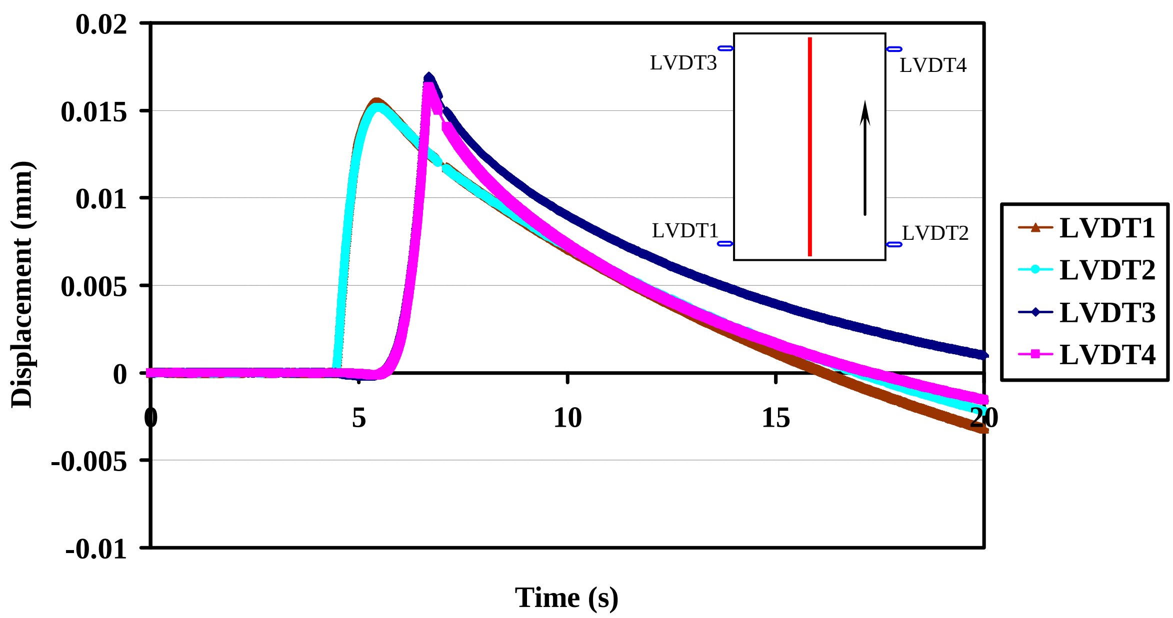

Figure 4.33. Evolution of in-plane displacements for LVDTs 1, 2, 3 and 4 – Test Case 02A

Figures 4.33 and 4.34 present the evolution of in-plane displacements for LVDTs 1, 2, 3 and 4 and average for Sets A and B for test case 02A, respectively. As already mentioned, this test case differs from 01A on the basis of laser-beam power and the use of filler wire material. The beam power of 3000 W with the addition of filler wire metal (table 4.1) results in comparatively higher values of peak displacements.

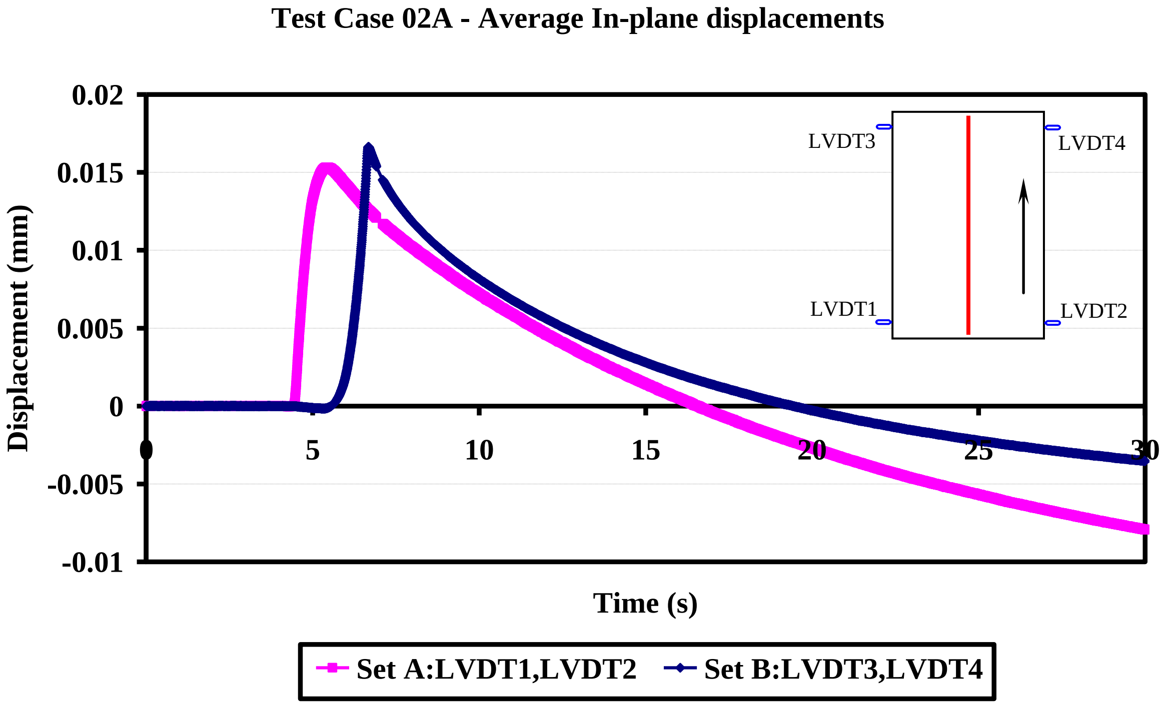

Figure 4.34. Average in-plane displacements for Set A and B – Test Case 02A

4.7.2.3 Test Case 03 (T-joint welding)

Although T-joint welding is unique in a sense that it not only includes the use of filler wire material, rather it welds the stiffener to the base plate making use of two welding torches moving simultaneously on each side of the fillet (Figs. 4.5 and 4.7). Moreover, the clamping device along with the application of two concentrated forces of 50 N is used to keep the stiffener in position. These factors are likely to affect the displacement values.

Figures 4.35 and 4.36 show the displacement evolution and average displacements for LVDTs 1, 2, 3 and 4. It is observed that the displacement evolution follow the similar pattern as those of test cases 01A and 02A. However, the difference is noted with respect to maximum displacement values attained. The maximum displacement values observed for Set A are of the same order as those of test case 01A and 02A; while Set B shows the peak displacement almost 3 times higher than Set A. It is noticed that Set A behaves in a way similar to the test cases 01A and 02A; since in the very beginning of welding, stiffener is still not the part of T-joint and, hence, affects least the displacement values of Set A. Whereas the displacement values recorded by Set B include the combined effect of expansion/contraction of base plate and stiffener. Additionally, Set B results reflect the higher weld heat input (2 weld torches in parallel).

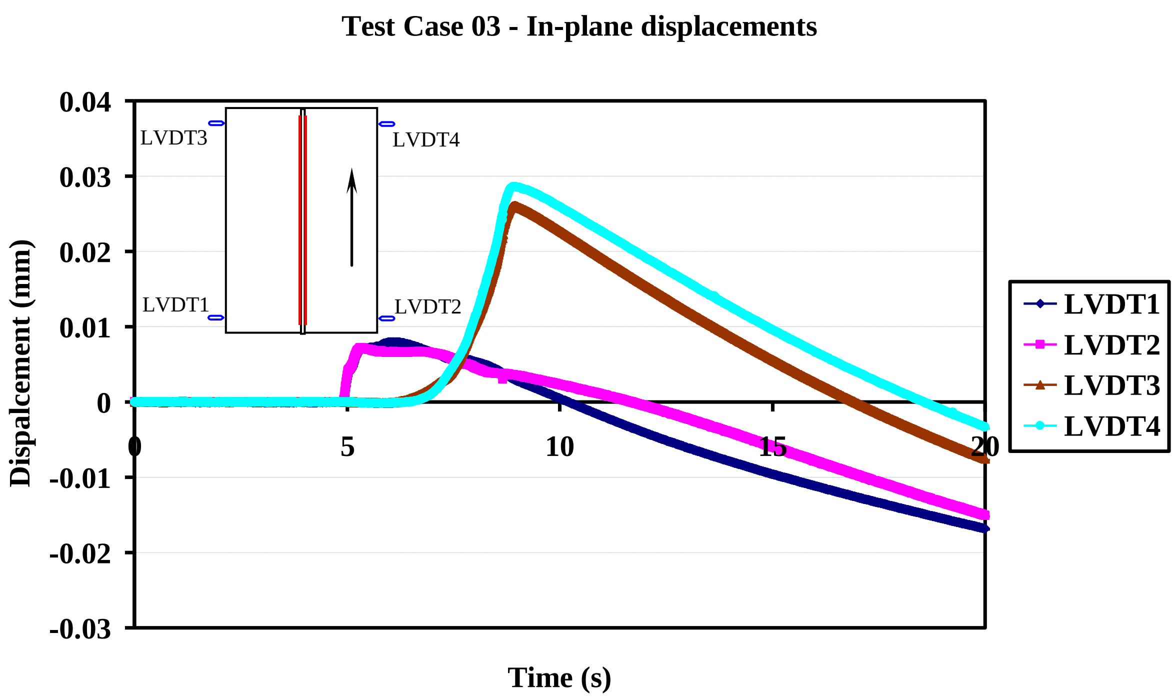

Figure 4.35. Evolution of in-plane displacements for LVDTs 1, 2, 3 and 4 – Test Case 03

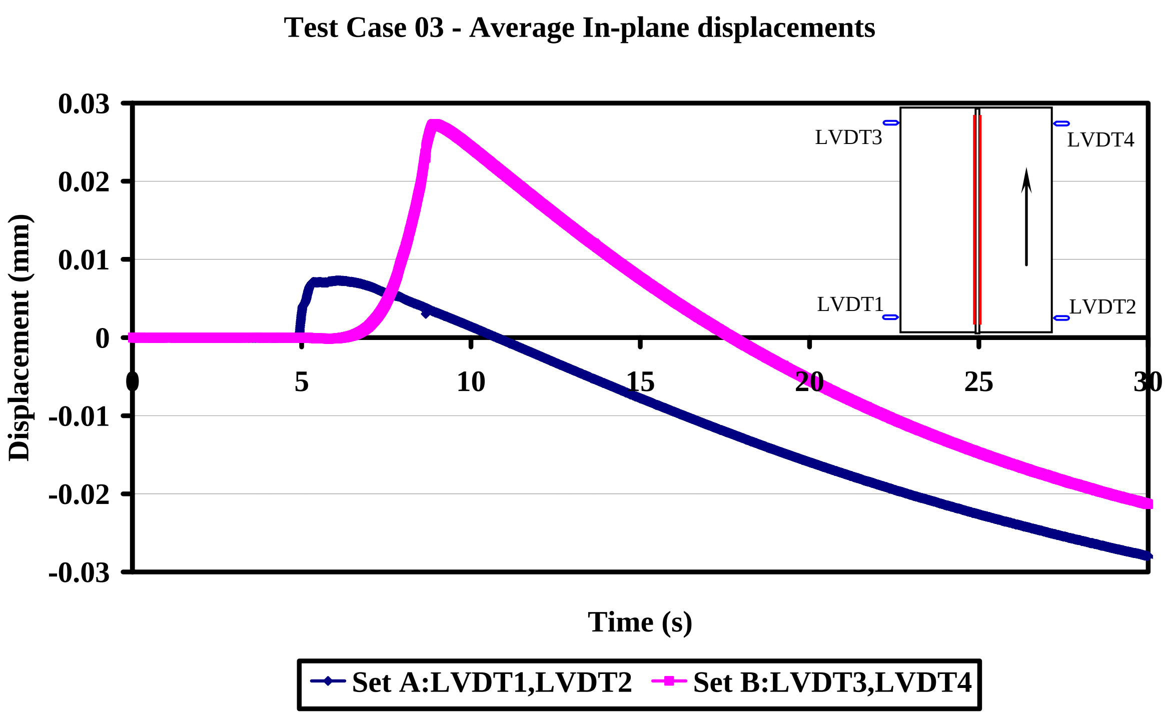

Figure 4.36. Average in-plane displacements for Set A and B – Test Case 03

Another factor that may influence the maximum displacement values is the slippage of T-joint in the direction of welding. Figure 4.37 clearly depicts the significant slippage of base plate during welding. The encircled region of Fig. 4.37 showing the result of LVDT5 should ideally present regular increasing and decreasing displacements; instead it shows the missing peak. What actually happened at this location is a result of two opposing factors. Under normal conditions the LVDT sensor should record increasing displacement due to expansion, but owing to the slippage of the base plate in the direction of heat source movement (away from LVDT5) the T-joint is actually carried away from its original position. This carrying away effect of T-joint is large enough to compensate the expansion in the opposite direction and hence an irregular drop of peak displacement value is observed. LVDT6, however, shows a regular curve, because in this case the expansion and slippage shall have additive effect.

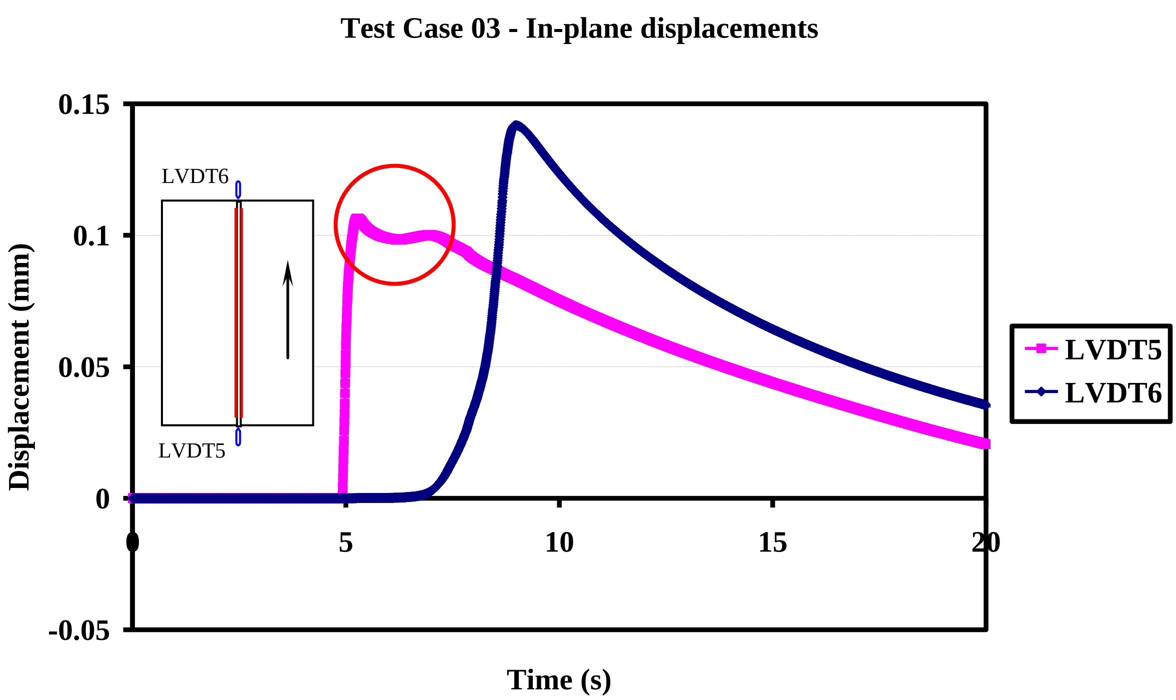

Figure 4.37. Evolution of in-plane displacements for LVDTs 5 and 6 – Test Case 03

The difference in peak values for Sets A and B (Fig. 4.36) may, therefore, be considered a result of slippage in the direction of welding, since the LVDT positions for Sets A and B before welding are updated during welding. This change in position is also quite systematic. Owing to the carried-away effect of T-joint, LVDTs from Set A tend to record displacement values on a line closer to the edge of base plate; while Set B measures displacements on a line more towards the mid of the base plate.

4.7.3 Stereo Image Correlation

It was observed during the visual inspection of test plates that none of them was perfectly straight before welding (a problem very common to the thin sheets). The pre-welding processes like rolling, machining, etc. are some of the reasons for these initial geometric imperfections. Josserand [JOSE] has shown that the initial geometric imperfections influence the final distortion levels of the test plates. It is for this reason that stereo correlation, also known as digital image correlation (DIC), technique is employed to measure the global 3D surface profiles of test plates. These surface profiles are measured both in initial (before welding) and final (after welding) states. The difference profiles are then calculated through the software Vic3D. Since these difference profiles are seen for the states just before and after the welding, it is expected that they will provide a measure of distortions/displacements induced by welding only.

DIC offers contact less and full field measurement of three dimensional displacements of an object surface. The image correlation technique requires digital images of a deformed object (final state) and a reference image of the object (initial state), which are taken by means of two charge-coupled device (CCD) cameras. Before carrying out image correlation of the object, calibration of these cameras is necessary. The calibration of cameras is performed using 20 images of a translated and rotated planar dot pattern of known spacing called target. The target used in this work contains equally spaced 12 and 9 black dots on a white background in the *x*- and *y*-directions, respectively. The grid spacing between the dots is 18.02 mm. In this work, the calibration of the stereo-system is performed using commercial software Vic-3D 2007. The calibration results are defined in terms of the following parameters:

- *Center x* and *Center y*: image plane center in pixels for each camera.
- *Focal length x* and *Focal length y*: focal length in pixels for each camera.
- *Skew*: deviation from orthogonality between the row and column directions in the sensor plane.
- *Kappa 1*: radial distortion coefficient.
- *Alpha*, *Beta* and *Gamma*: relative orientation of camera 2 with respect to camera 1 in degrees, where *alpha* is the relative tilt, *beta* is the relative pan angle and *gamma* is the swing angle.
- *Tx, Ty, and Tz*: position of pinhole in camera 2 relative to camera 1 in mm.

Having performed the calibration, Vic-3D yields standard deviation of residuals for all views, which was found to be 0.0199 pixels for the cases under investigation. A higher value of calibration residuals leads to higher value of error in the measure of correlation accuracy for the image correlation of object surface. The components and settings of image correlation, and the calibration results are as follows:

Components and settings of image correlation technique

Cameras	2 LIMESS 12 bit grey scale CCD 1.34”
Cameras resolution	2048 x 2048 pixels
Lenses	2 Nikon Micro-NIKKOR (*f* = 55mm, 1:2.8 D)
Lighting	2 Compact fluorescent lamps, Osram Delux EL 30W/840
Object	AA 6056-T4 plates
Software	Vic-3D 2007
Calibration target	12 x 9 black dots on white background; spacing: 18.02 mm
Standard deviation of residuals for all views	0.0199133 pixels
Subset size (pixels)	21 x 21
Step size (pixels)	5
Interpolation function	Quintic B-spline
Correlation criterion	Zero-Normalized Sum of Squared Differences
Points analysed	over 46497
Pixel size	1 pixel = 0.16 mm
Error	0.0116198 pixel = 1.859168 μm

Calibration results for DIC system

Parameter	**Camera 1**	**Camera 2**
Center x (pixel)	984.65	1045.2
Center y (pixel)	1014.48	1002.33
Focal length x (pixel)	7887.49	7868.11
Focal length y (pixel)	7888.03	7867.1
Skew	-0.8123	-0.1236
Kappa 1	-0.0276	-0.0325

Camera 1➔2 transformation

Alpha (degrees)	-0.1683
Beta (degrees)	-13.301
Gamma (degrees)	+0.00743732
Tx (mm)	+270.68
Ty (mm)	-1.5706
Tz (mm)	+31.871
Baseline (mm)	272.55

A random grey speckle pattern is generally required on the object surface, which is created with the help of white and black paints. A subset window (or correlation window) is subsequently defined in the reference image as a neighbourhood of *m* x *m* pixels that forms a unique stamp of the center point of this neighbourhood. The speckle pattern of this neighbourhood should hold enough contrast and directional information to track the local deformation to the first order of approximation (affine transformation) by using a cross-correlation algorithm. In the correlation algorithm the centers of the neighbouring subset windows are shifted by a step size of *n* pixels. *n* must be smaller than the subset size to enable overlapping of the subsets. Once these settings are defined, the displacement field is calculated as an updated displacement for every subset center.

For all the test cases, over 46497 points were analysed on a surface area of 300 x 170 (mm^2). The error for displacements was found to be 0.0116 pixels. For a pixel size of 0.16 mm, this error value accounts for 1.86 μm (< 2 μm). Since the displacement values of test cases remain of the order of several hundred microns, an error of less than 2 μm is considered small.

The scheme of stereo image correlation is presented in Fig. 4.38. Figure 4.38 shows red line bounded region, which is the area of interest for measuring the distortions. The dimensions of this region are presented in Figs. 4.6 and 4.7. Table 4.5 provides an overview of the initial and final surface profiles of the test plates used for various test cases. It may be observed that the initial surface profiles are by and large irregular, and the final surface profiles follow the trend.

Although the difference profiles are expected to give the net distortions induced by welding, slight variations are observed for various test plates welded under same loading and boundary conditions. This implies that the test plates with different initial surface profiles behave differently when welded. The selection of the test plate that may lead to exploitable results is, therefore, a matter of great concern. The criterion for selection is based upon minimum initial geometric imperfection, constant application of heat flux throughout the welding and maximum data recorded in terms of temperatures from thermocouples and in-plane displacements from LVDT sensors.

Once a particular test plate is selected for the specific test case, the next step is to exploit the results in a way so that they may be compared with numerical simulation results. The net in-plane displacements are found to be identical on both sides of the fusion zone. For the case of out-of-plane displacements, the minimum and maximum displacements are recorded as a function of distance across the weld joint. Since image correlation is not possible in the weld fusion zone and in the region where thermocouples are installed; the out-of-plane displacements are assumed to be emerging linearly from the weld center line.

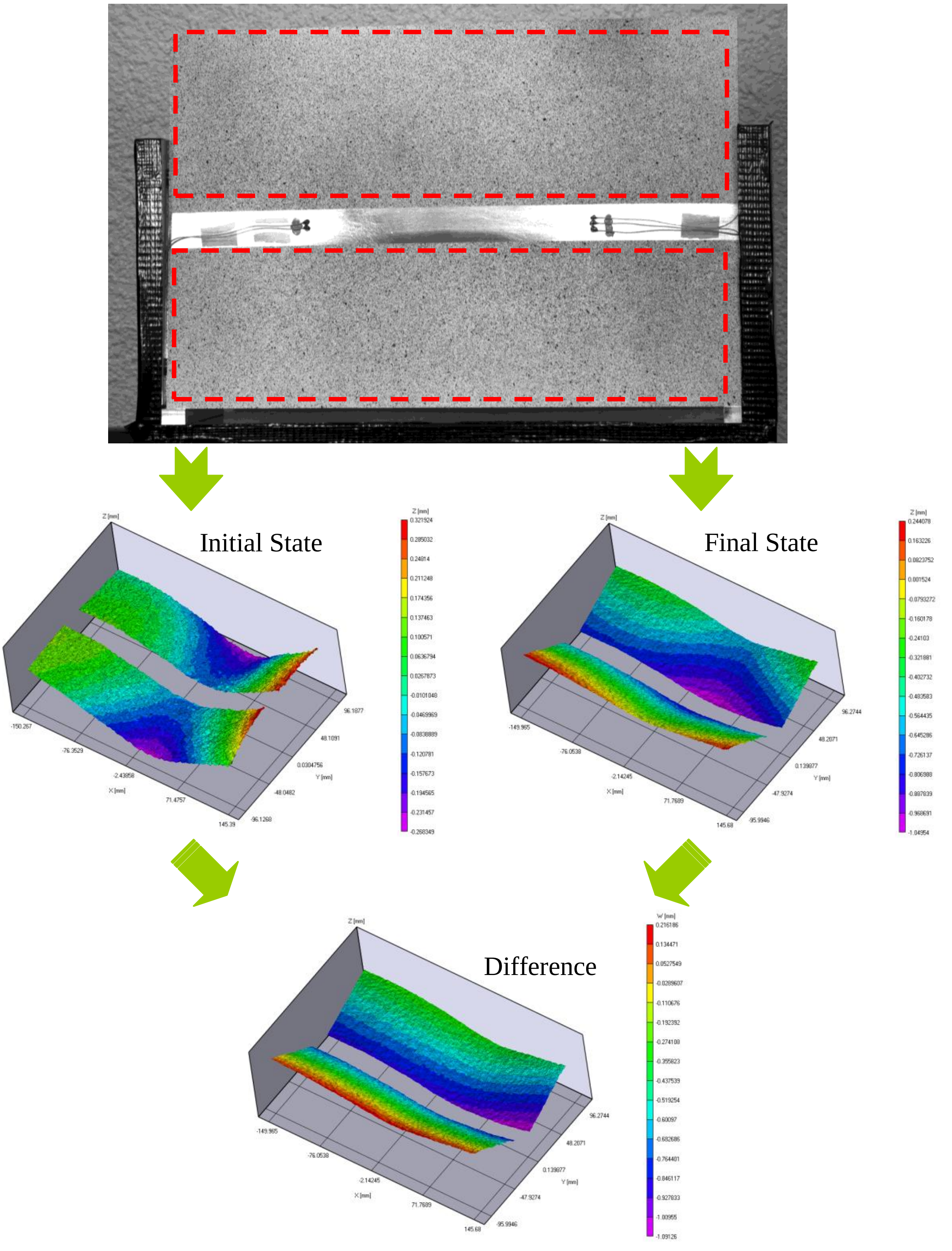

Figure 4.38. Scheme of stereo image correlation technique

Irrespective of the initial geometric imperfections, there are various other factors that influence the distortion pattern. These factors are welding parameters, boundary conditions, amount of heat energy contained and dissipated by the test specimens and use of filler wire. These aspects are being discussed in the subsequent sections.

	Initial State – Before Welding	**Final State – After Welding**
Test Case 01A	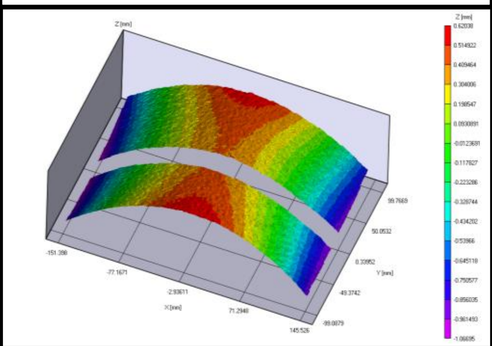	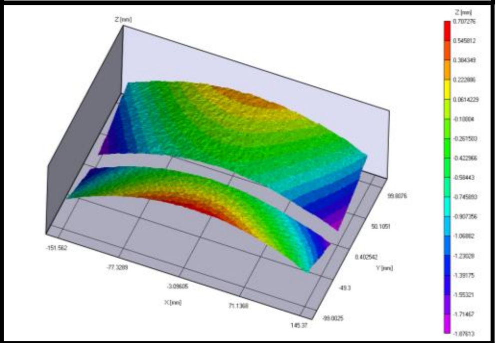
Test Case 01B	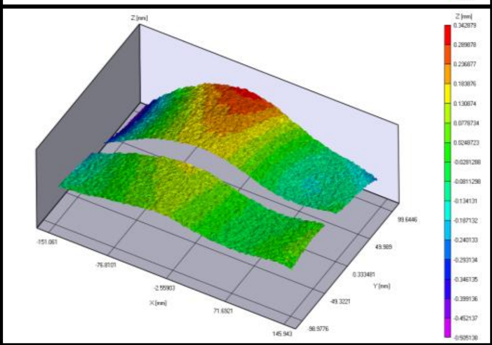	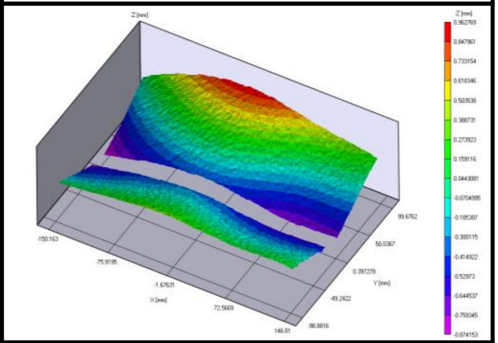
Test Case 02A	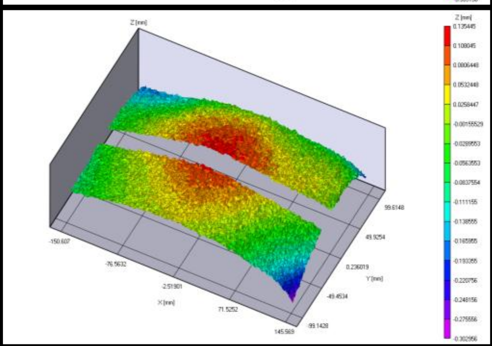	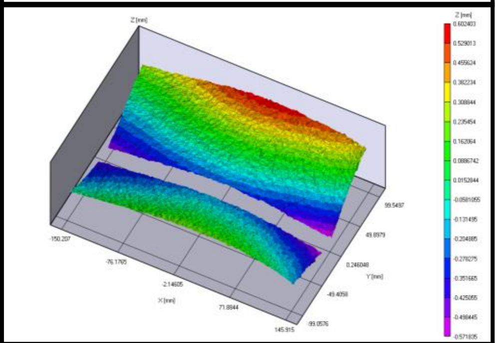
Test Case 02B	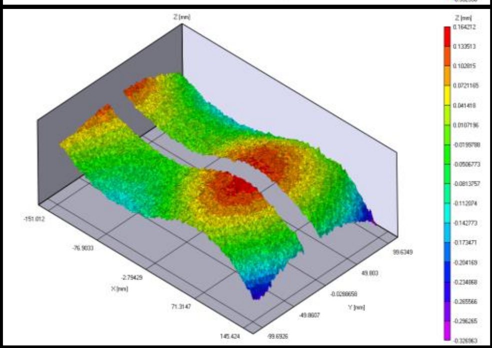	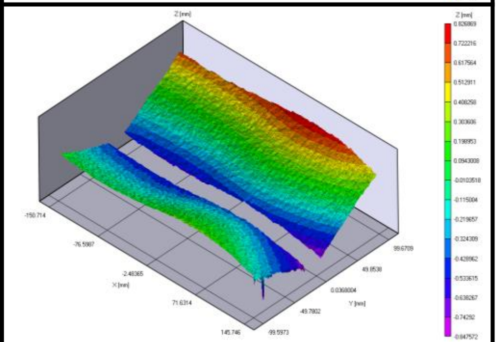
Test Case 03	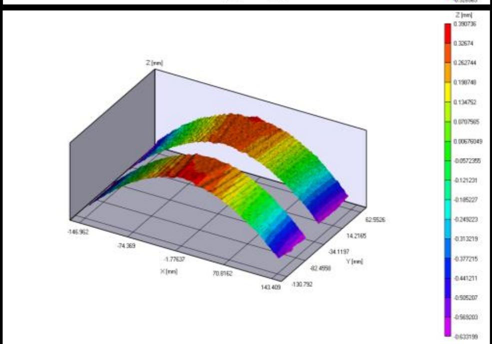	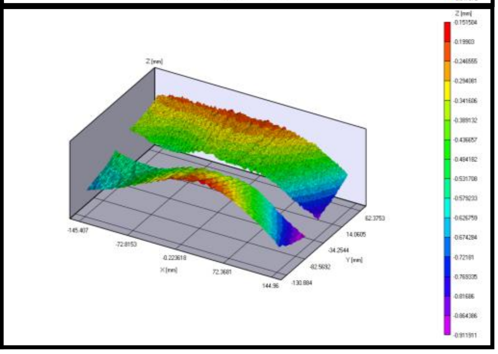

Table 4.5. Initial and final surface profiles of various test cases

4.7.3.1 Test Case 01A (Fusion welding on support) and 02A (Filler welding on support)

With reference to the net out-of-plane and in-plane displacements, the test cases 01A and 02A are compared with each other in Figs. 4.39 and 4.40, respectively. Figure 4.39 presents the maximum and minimum out-of-plane displacements measured from the upper surface of the test plates. It is observed that the test case 01A (a case of fusion welding with beam power of 2300 W) has displacement values higher than the test case 02A (a case of filler welding with beam power of 3000 W). In spite of using higher beam power, the test case 02 shows lower level of displacements. This indicates that a considerably large fraction of beam power is consumed during melting of the filler metal wire.

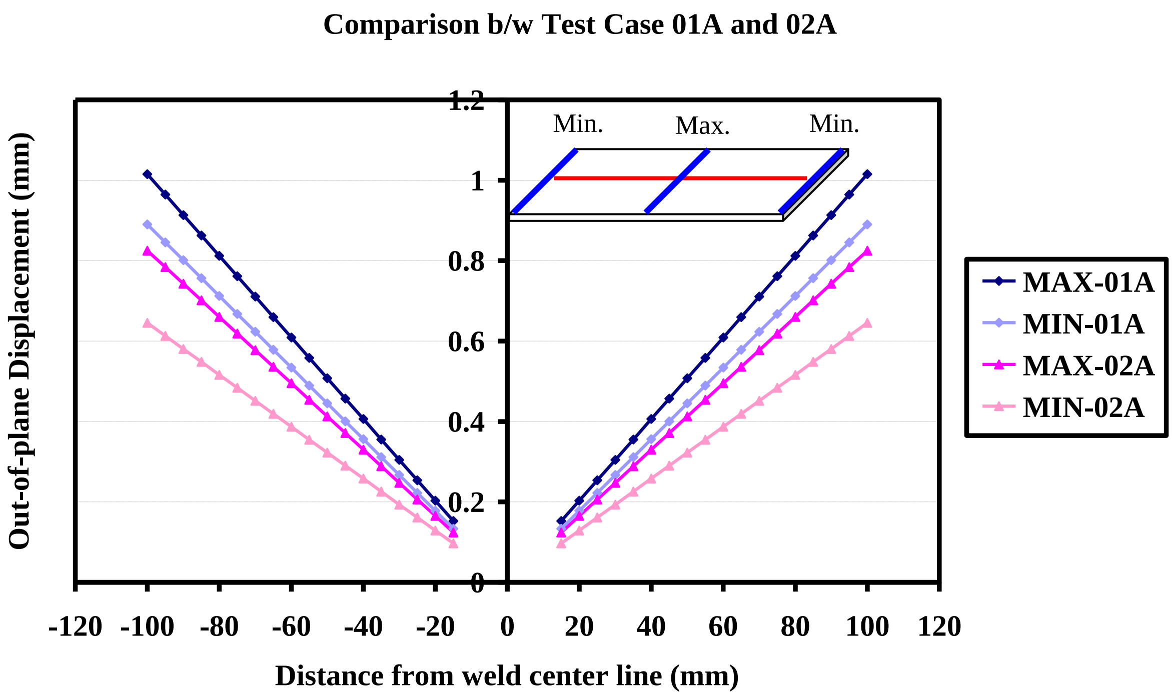

Figure 4.39. Out-of-plane displacements – Test Cases 01A and 02A

This observation has already been established in section 4.7.1.6, where it was noticed that the peak temperatures recorded by thermocouples installed on the test plates for both the test cases were in close approximation. Moreover, Fig. 4.25 depicts that the peak temperature recorded by TC12 (installed on the aluminium support) has shown considerably higher value for test case 02A than for 01A, thereby depicting more heat loss from test plate of case 02A and hence the lesser distortions.

Similarly, the comparison of the net in-plane displacements is presented in Fig. 4.40. It is observed that the in-plane displacements also follow the same trend as that of out-of-plane displacements. Hence they are higher for test case 01A than for 02A.

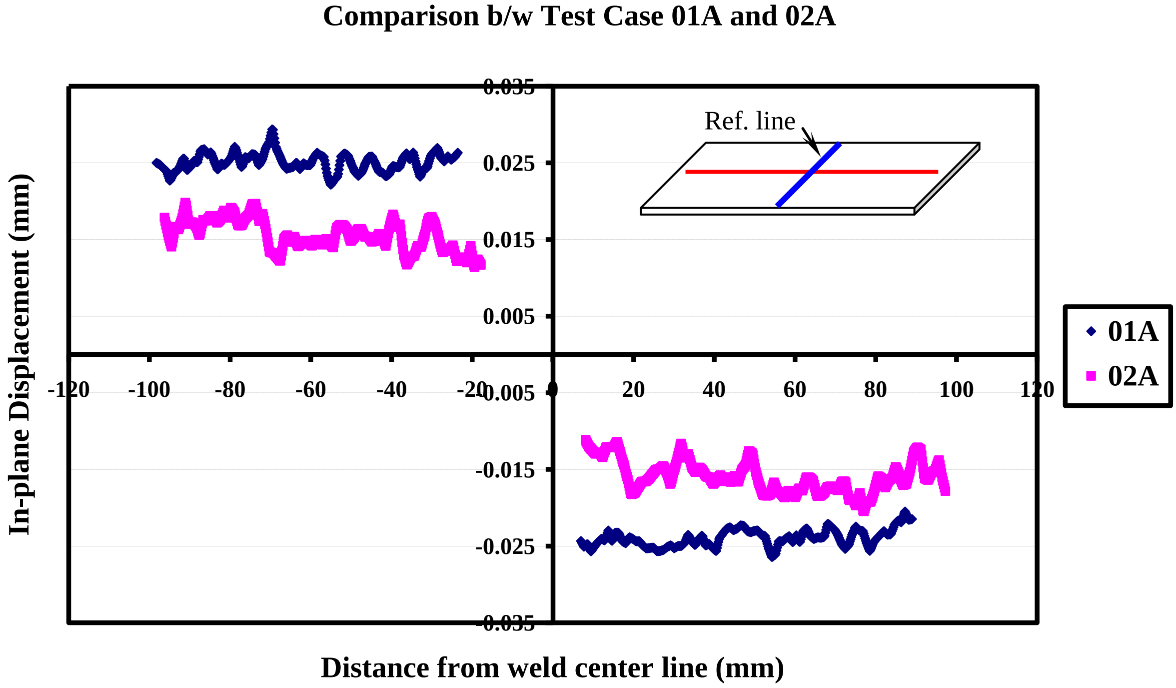

Figure 4.40. In-plane displacements – Test Cases 01A and 02A

4.7.3.2 Test Case 01B (Fusion welding in air) and 02B (Filler welding in air)

Figures 4.41 and 4.42 present the out-of-plane and in-plane displacements measured from the upper surface of the test plates, respectively. It is observed that the test case 01B (a case of fusion welding in air with beam power of 2300 W) has displacement values slightly lesser than the test case 02B (a case of filler welding in air with beam power of 3000 W).

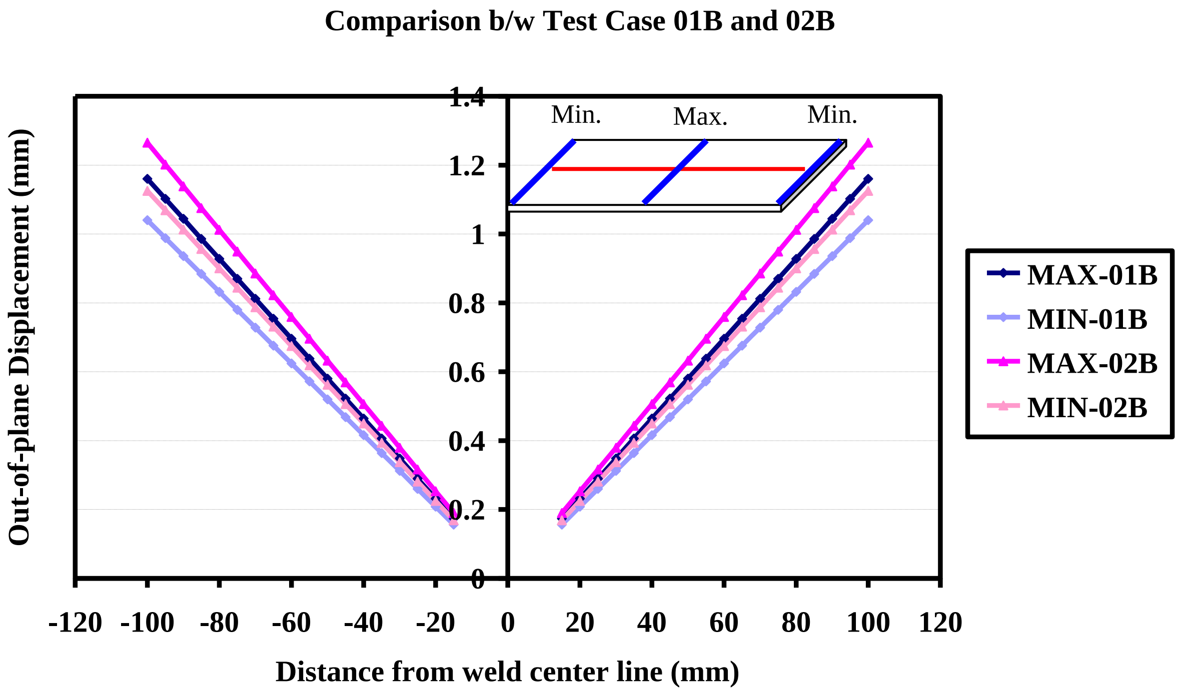

Figure 4.41. Out-of-plane displacements – Test Cases 01B and 02B

Apparently, it seems that these test cases do not follow the same trend as those of 01A and 02A (section 4.7.3.1); rather they show an opposite response i.e. higher displacements for filler welding case and lower for fusion welding. The reason for this difference can be explained with reference to amount of heat energy absorbed by the test plate.

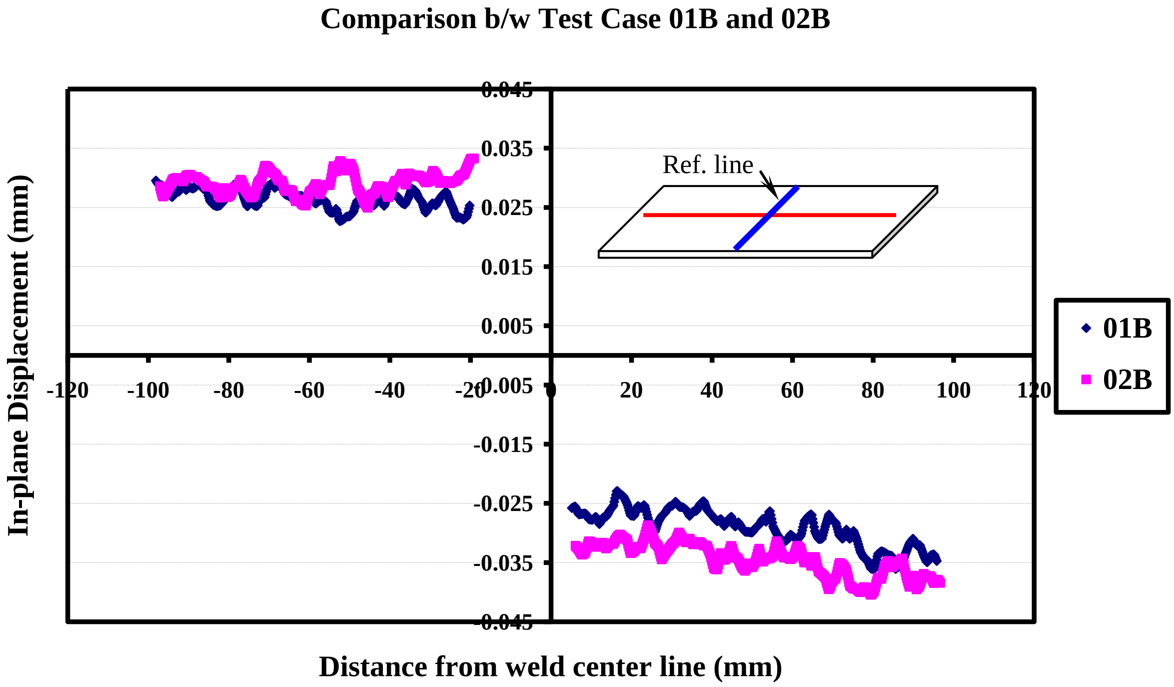

Figure 4.42. In-plane displacements – Test Cases 01B and 02B

An indirect measure of amount of heat energy absorbed by the test plates is already presented in Fig. 4.25, where comparison in peak temperatures for various thermocouple positions for different test cases is shown. It may be observed from Fig. 4.25 that the peak temperatures measured for test case 02B are considerably higher as compared to 01B. This implies that the amount of heat energy contained by the test plate of 02B is more than that of 01B and hence the corresponding effect over distortions is also higher for the former than for the latter.

4.7.3.3 Test Case 03 (T-joint welding)

Figures 4.43 and 4.44 present the out-of-plane and in-plane displacements measured from the upper surface of the base plate of T-joint, respectively. Since T-joint welding is different from other test cases in terms of loading and boundary conditions, the distortion pattern is also quite different. The maximum out-of-plane displacements (≈ 0.25 mm) are almost 4 times less than the test plate welding cases (≈ 1 mm). It is because the stiffener seats vertically downward to some extent at the level of weld joint during welding, thereby inducing high level localised deformations in the fusion and heat affected zones. As the image correlation could not be performed in these zones, the effect of these deformations over the global out-of-plane displacements could not be taken care of. However, the effects of two welding torches each with the laser-beam power of 2500 W and the filler wire addition is evident from the in-plane displacement values (≈ 0.06 mm) which are approximately 2 to 4 times as high as test plate welding cases (≈ 0.015-0.035 mm).

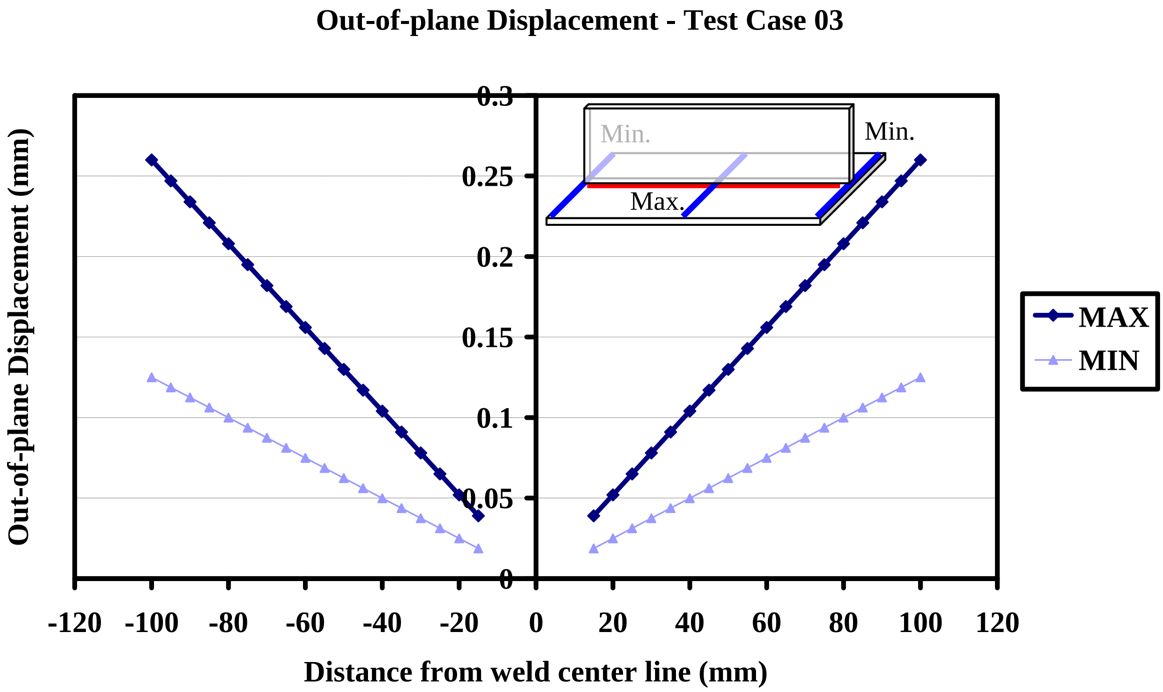

Figure 4.43. Out-of-plane displacements – Test Case 03

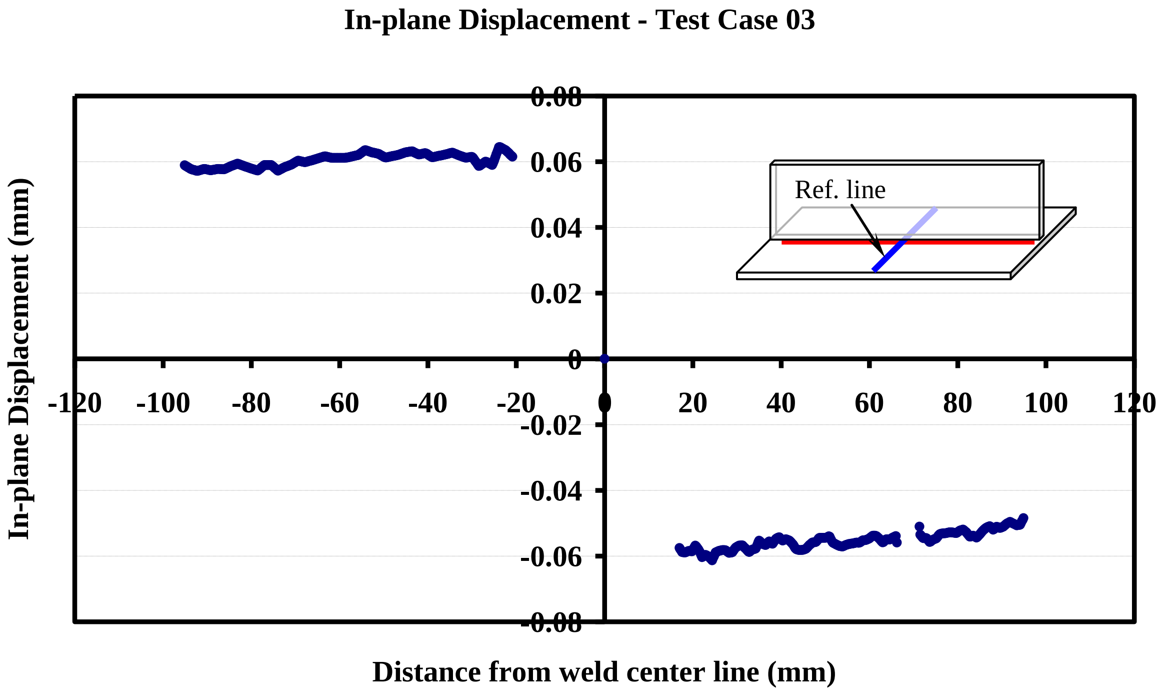

Figure 4.44. In-plane displacements – Test Case 03

4.7.3.4 Comparison of Thermal Boundary Conditions

The effect of two types of thermal boundary conditions (cooling on aluminium support and in air) over the global distortions / displacements is being presented in this section. The comparison is developed for fusion welding test cases (test case 01A and 01B), since it is established in section 4.7.1.7 that both the test cases involve almost equal amount of heat energy contained by the test plates. Moreover, filler welding cases are complex in a sense that the amount of heat energy consumed by the filler wire is unknown.

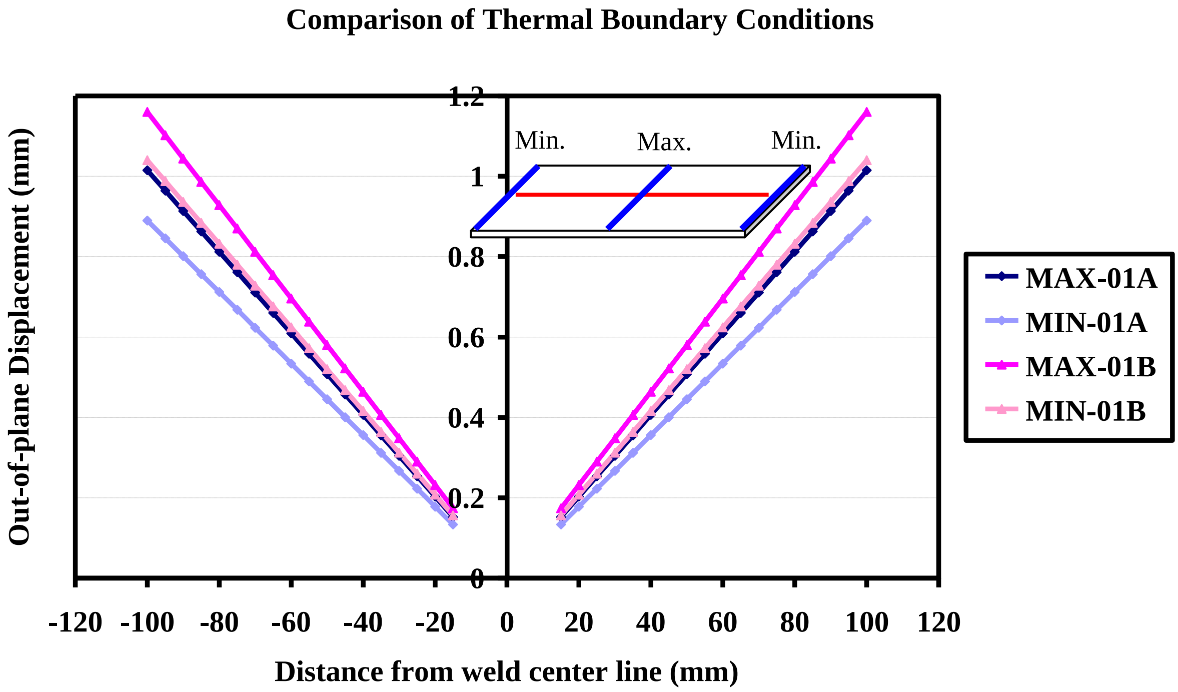

Figure 4.45. Comparison of thermal boundary conditions – Out-of-plane displacements

Figure 4.45 presents the comparison of test cases 01A and 01B for out-of-plane displacements. It is noticed that test case 01A (fusion welding case with beam power of 2300W and cooling on aluminium support) shows the displacement values slightly lesser than 01B (fusion welding case with beam power of 2300W and cooling in air). The cooling curves of these test cases (Fig. 4.26) illustrate that the test plates welded using aluminium support experience a rather rapid decrease in temperatures at thermocouple positions, thus indicating a rapid heat loss due to the plate/support contact. Since the distortions / displacements are directly proportional to the net input heat energy, the test case 01A demonstrates lower level of out-of-plane displacements as compared to 01B.

Figure 4.46 presents the comparison of the test cases for in-plane displacements. A similar trend is observed here also, where test case 01A shows slightly lesser displacement values due to rapid heat loss in aluminium support as compared to 01B.

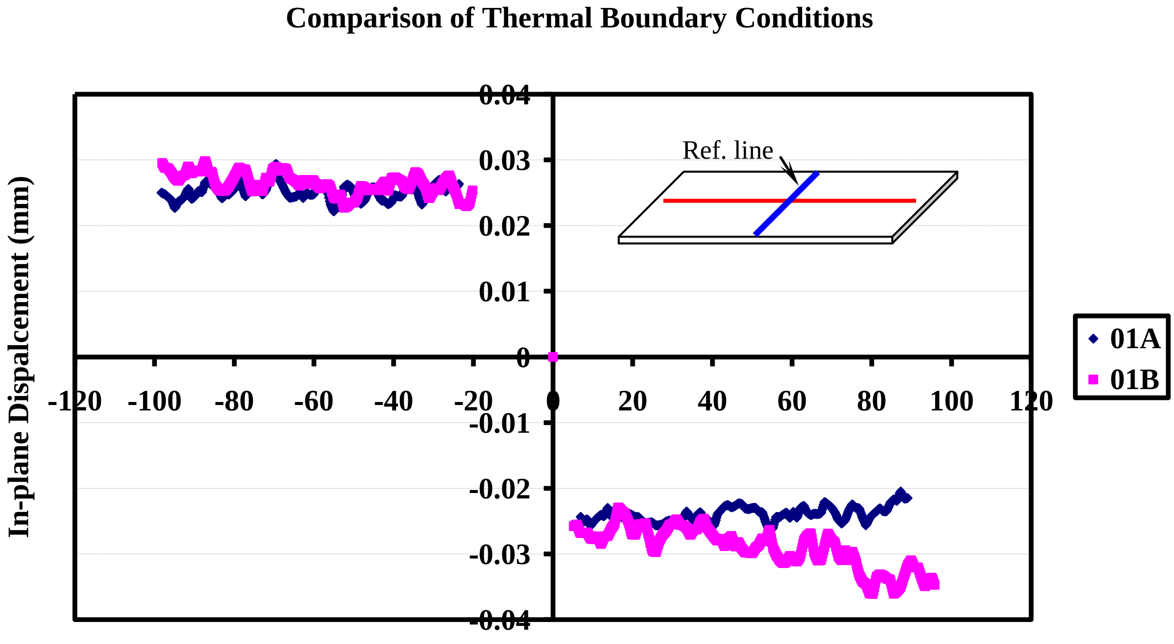

Figure 4.46. Comparison of thermal boundary conditions – In-plane displacements

4.7.4 Micrography

The weld pool dimensions are measured by means of micrography. Specimens from all the test plates and T-joints were cut at the locations immediately next to the thermocouples TC1 and TC4, and were called as micrograph-1 and micrograph-2, respectively. These specimens were then ground with the abrasive papers of increasing fineness and mounted on the moulds using a thermosetting resin. Fine polishing was performed using diamond grit (9µm – 1µm) in suspension on a napless cloth to produce a scratch-free mirror finish. Etching was done with 40% NaOH solution to increase the contrast between fusion zone and base metal. Finally, a light optical microscope equipped with camera was used to take micrographs.

Table 4.6 gives an overview of micrographs of all the test cases. Figures 4.47 and 4.48 provide graphical representation of various dimensions of test cases 01 and 02, respectively. The weld pool geometries are shown in terms of width and penetration and the average values are also taken. Differences in these dimensions for various test cases are an obvious outcome of different loading and boundary conditions. Moreover, slight variations in dimensions for the same type of test cases are a result of the ejection of material from the key-hole during welding. As far as selection of weld pool dimensions to perform the comparative analysis with simulation results is concerned, two approaches are in practice. Either the averaged values are taken as standard, or one of the micrographs with suitable dimensions (close to averaged values) is selected.

<table>
<tr><th></th><th>Micrograph – 1</th><th>Micrograph – 2</th></tr>
<tr><td>Test Case 01A</td><td>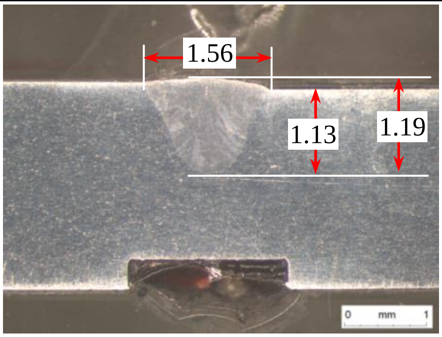
</td><td>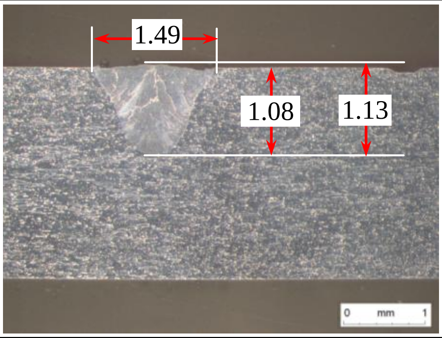
</td></tr>
<tr><td>Test Case 01B</td><td>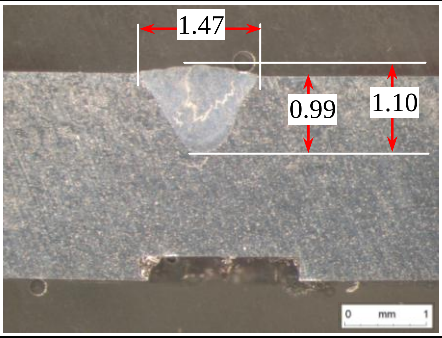
</td><td>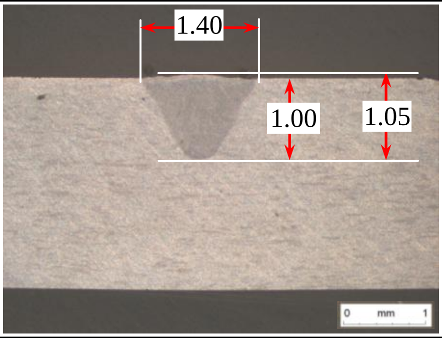
</td></tr>
<tr><td>Test Case 02A</td><td>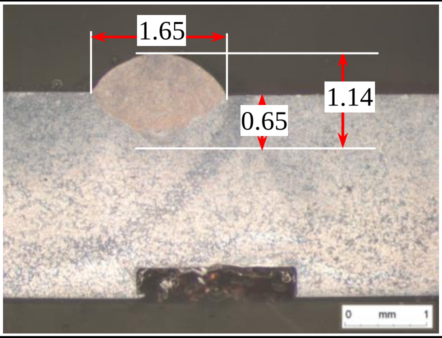
</td><td>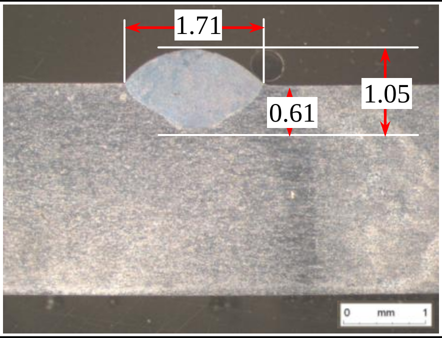
</td></tr>
<tr><td>Test Case 02B</td><td>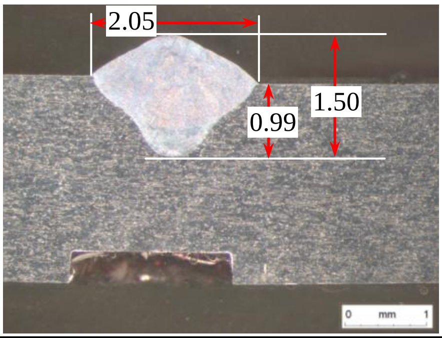
</td><td>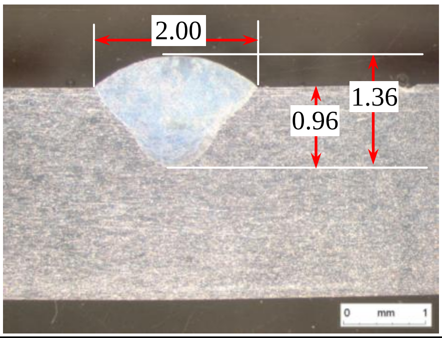
</td></tr>
<tr><td>Test Case 03</td><td>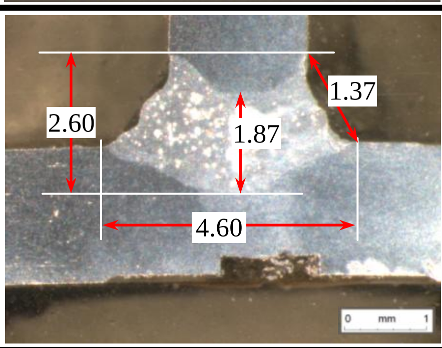
</td><td>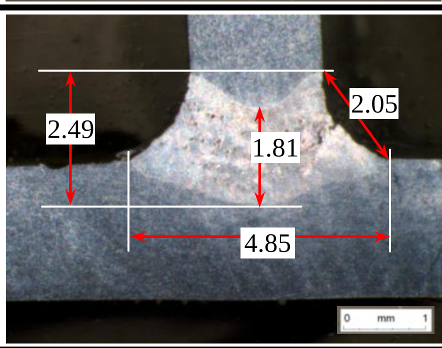
</td></tr>
</table>

Table 4.6. Micrographs of all the test cases

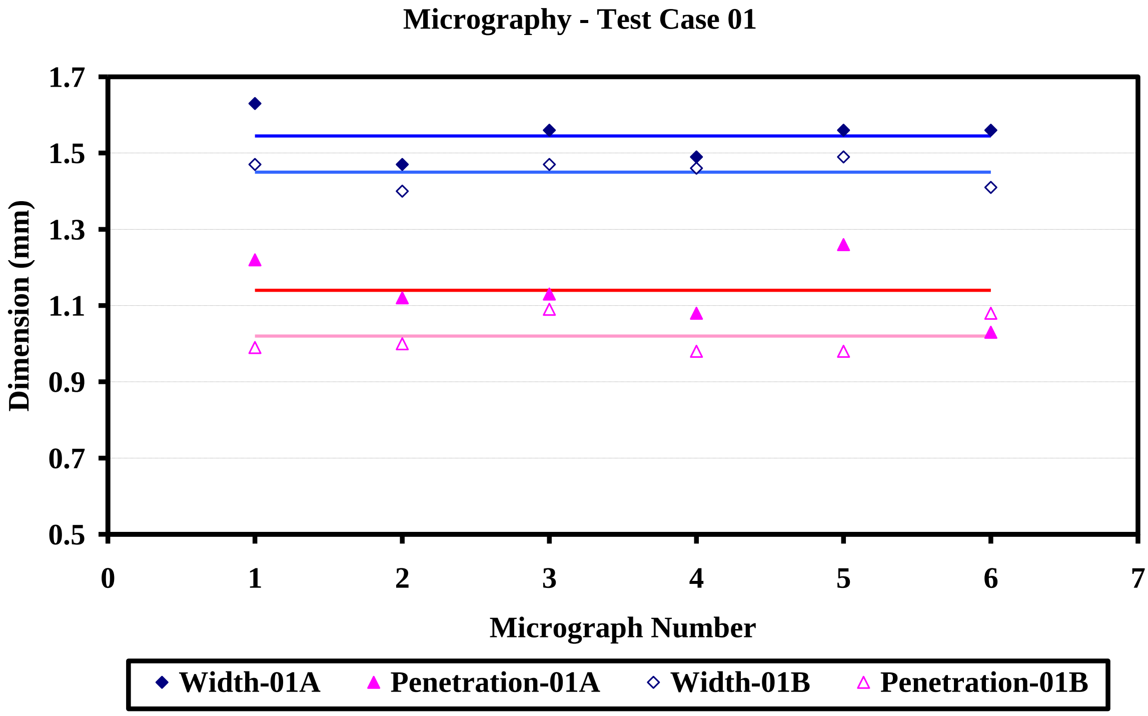

Figure 4.47. Weld pool dimensions – Test Case 01

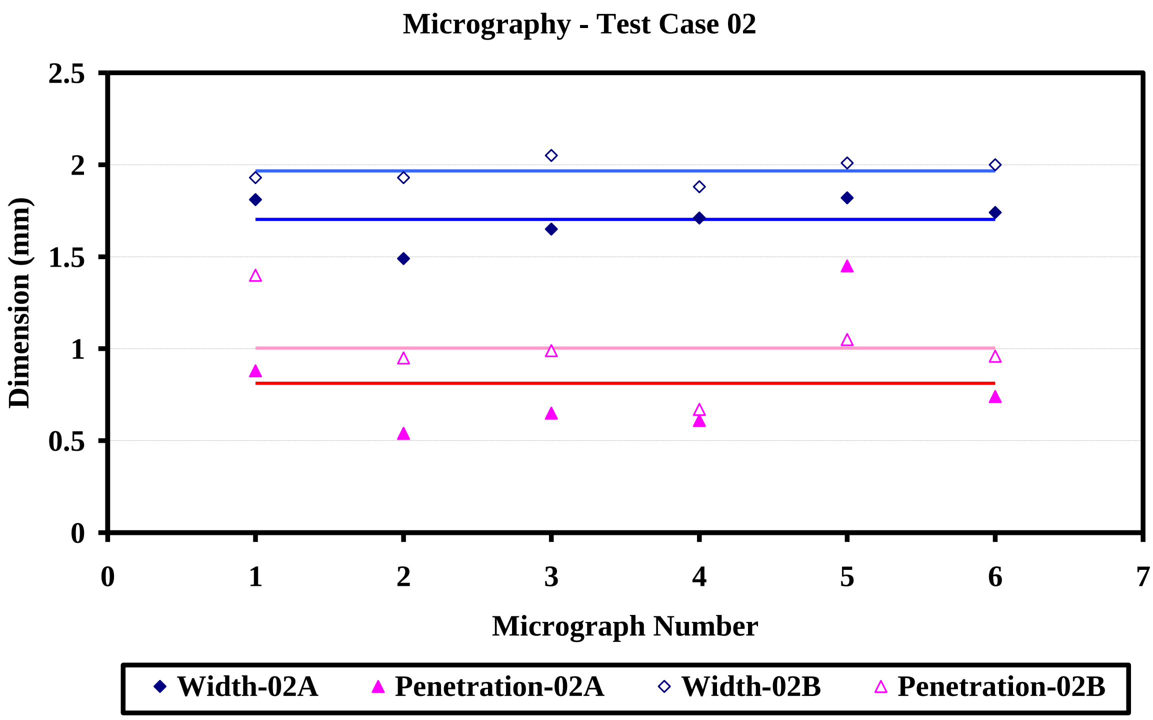

Figure 4.48. Weld pool dimensions – Test Case 02

Figure 4.49 shows weld pool dimensions graphically for test case 03. It is to be noted that in addition to width and penetration, the T-joint fusion zone have some more dimensions which should be taken into account. The letters a, b, c, d, e and f denote various dimensions.

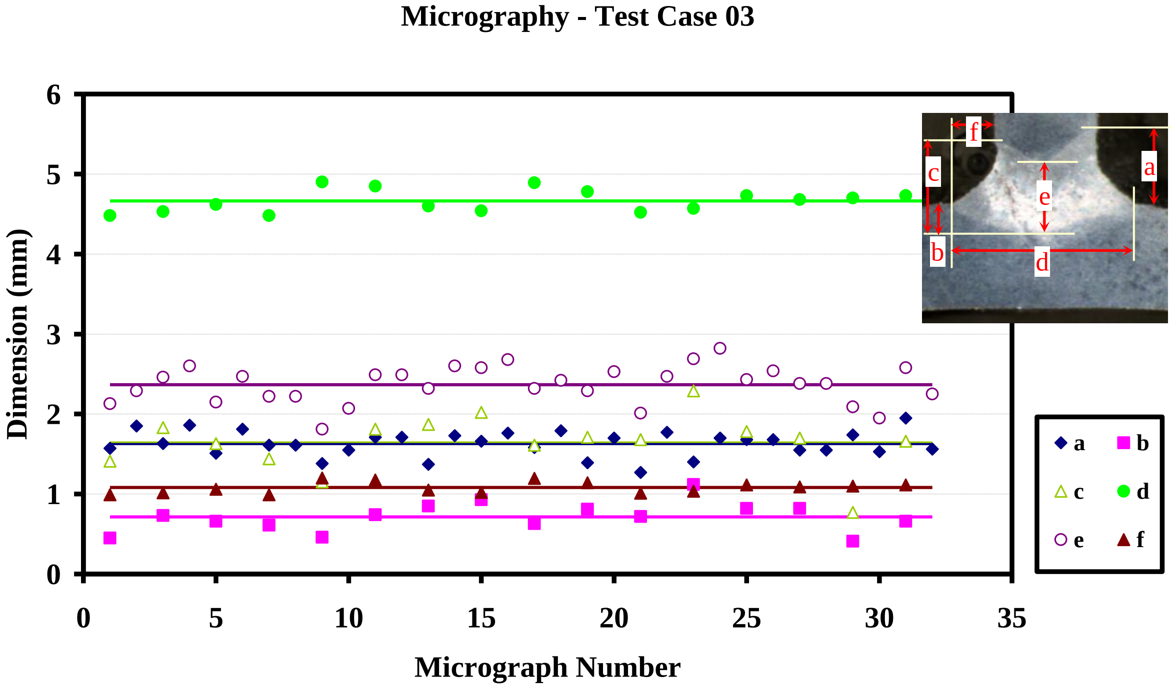

Figure 4.49. Weld pool dimensions – Test Case 03

4.7.5 Infra-red Camera

Since it is almost impossible to keep the track of weld pool dimensions at every instant of time simply by carrying out micrography; the infra-red camera is employed to qualify indirectly the stability of FZ by analysing the evolution of weld pool surface temperature as a function of time. The results of infra-red camera are termed as qualitative in table 4.3 because of two reasons. Firstly, it is difficult to establish the emissivity of constantly circulating liquid aluminium pool; and secondly, the filter used for camera could measure the temperatures up to 1700°C only. Therefore, in order to observe the surface temperature evolution, an artificial emissivity value is used to keep the temperature values within the permissible limit of 1700°C. The emissivity values used are as follows:

- *Test Cases 01 and 02: Emissivity = 0.09*
- *Test Case 03: Emissivity = 0.25*

4.7.5.1 Test Case 01A (Fusion welding on support)

Figure 4.50 presents the evolution of weld pool surface temperature for test case 01A. As this test case involves only fusion (without filler wire addition), it is found that the surface temperature remains almost constant throughout the welding. A slight increase in temperature is observed at the time when welding torch passes next to TCs. This is because of the burning of adhesive agent meant to protect the TCs.

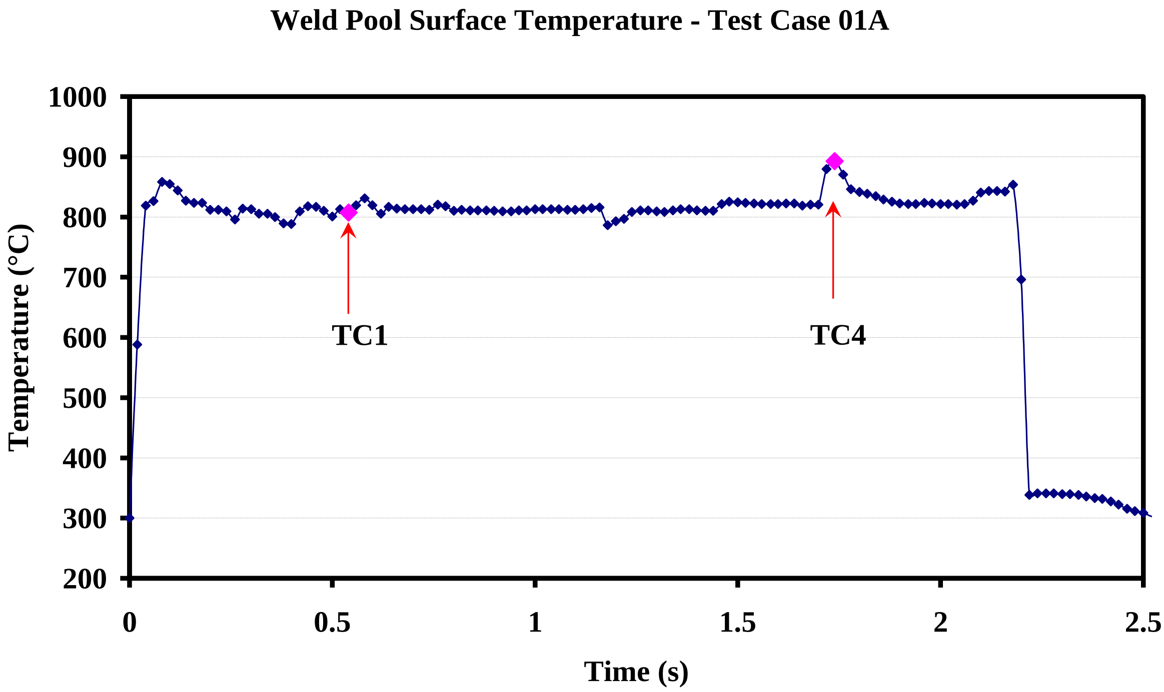

Figure 4.50. Evolution of weld pool surface temperature – Test Case 01A

4.7.5.2 Test Case 02A (Filler welding on support)

Figure 4.51 presents the evolution of weld pool temperature for test case 02A. A high level of perturbations is observed for all the three test plates used (P07, P17 and P19). One of the reasons, as mentioned above, is burning of the adhesive agent at positions TC1 and TC4; however, its effect is mainly localised.

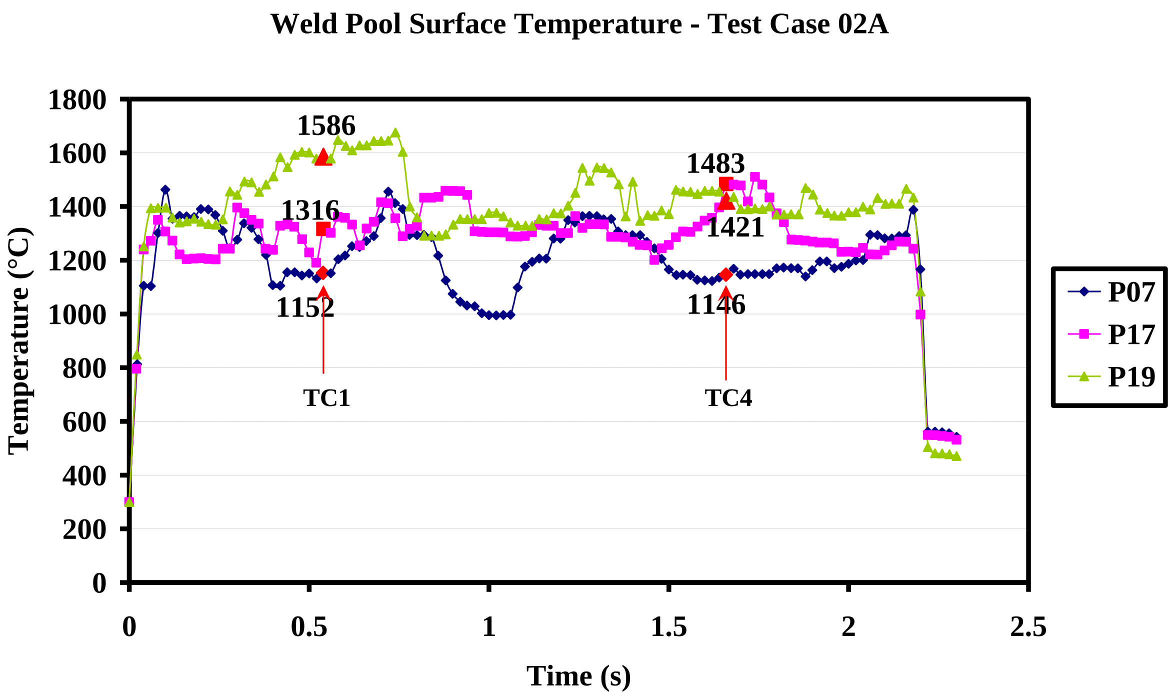

Figure 4.51. Evolution of weld pool surface temperature – Test Case 02A

The reason for continuous perturbations is the disturbed feeding of filler wire in molten pool. Though a constant wire feed rate is used for all the test cases, it is also required that filler wire be guided till its very entrance in the weld pool. In general, this is partially achieved by the feeding nozzle and partially by placing the filler wire in the weld groove. As for this test case no groove was initially made in the test plates; the filler wire is likely to change its location of entrance in the weld pool throughout the welding process. It is, therefore, expected that the temperature of weld pool drops when the wire comes directly underneath the laser-beam; while it increases when the wire displaces a little.

4.7.5.3 Test Case 03 (T-joint welding)

The evolution of weld pool surface temperature for test case 03 is being presented in Fig. 4.52. It is observed for all the T-joints that the temperature values follow an identical pattern. Results of three of the T-joints (T03, T08 and T09) are shown in Fig. 4.52.

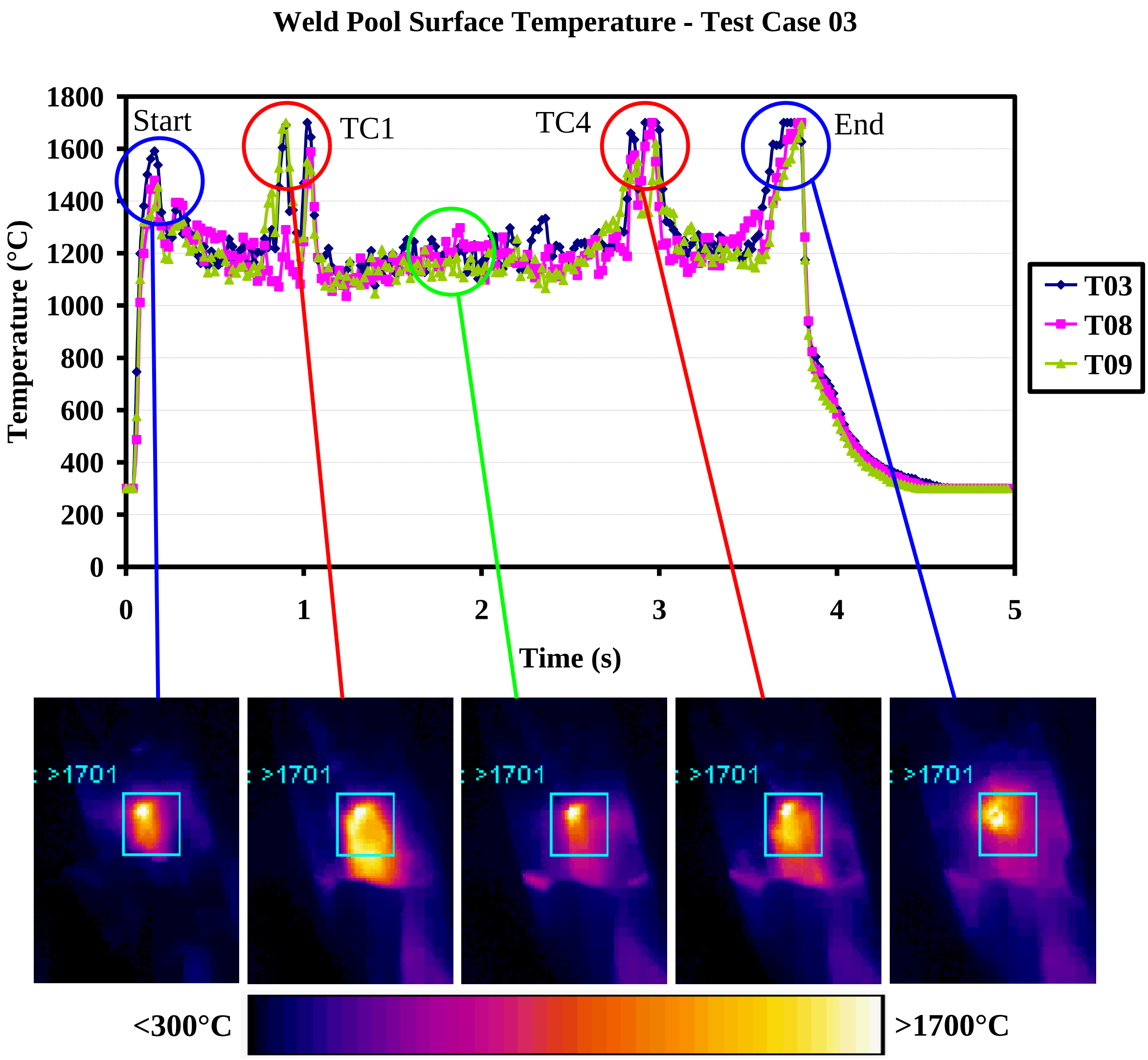

Figure 4.52. Evolution of weld pool surface temperature – Test Case 03

Four distinct temperature peaks are observed in all the cases where the first peak shows start of welding while the last peak indicates the end of welding. The second and third peaks are the ones noted next to TC1 and TC4, respectively. Figure 4.52 also presents the contours of temperature distribution in and near the fusion zone as observed from infra-red camera. As already mentioned, the peaks observed next to thermocouples are due to burning of adhesive agents applied on the thermocouples. However, the ones observed at the start and end of welding are due to the formation and closure of key-hole, respectively.

Excluding the temperature peaks, the remaining part of the curve shows a constant evolution of temperature throughout the welding process. It has been observed in the previous section that the unguided addition of filler wire due to the absence of weld groove may lead to high level perturbations. In case of T-joint welding, the fillet joint between the base plate and stiffener serves as weld groove. The filler wire adjusts itself in the fillet and smoothly becomes the part of weld pool as welding progresses.

4.7.6 High Speed Camera

The high speed camera is used to establish the material ejection from the weld pool during welding. Figure 4.53 presents various images with random spatter of molten metal. There are some instances where weld pool remains calm with no spatter at all (Fig. 4.53.b.), while most of the times molten metal exploding from the pool is observed. These random eruptions do not allow quantifying the material loss from fusion zone.

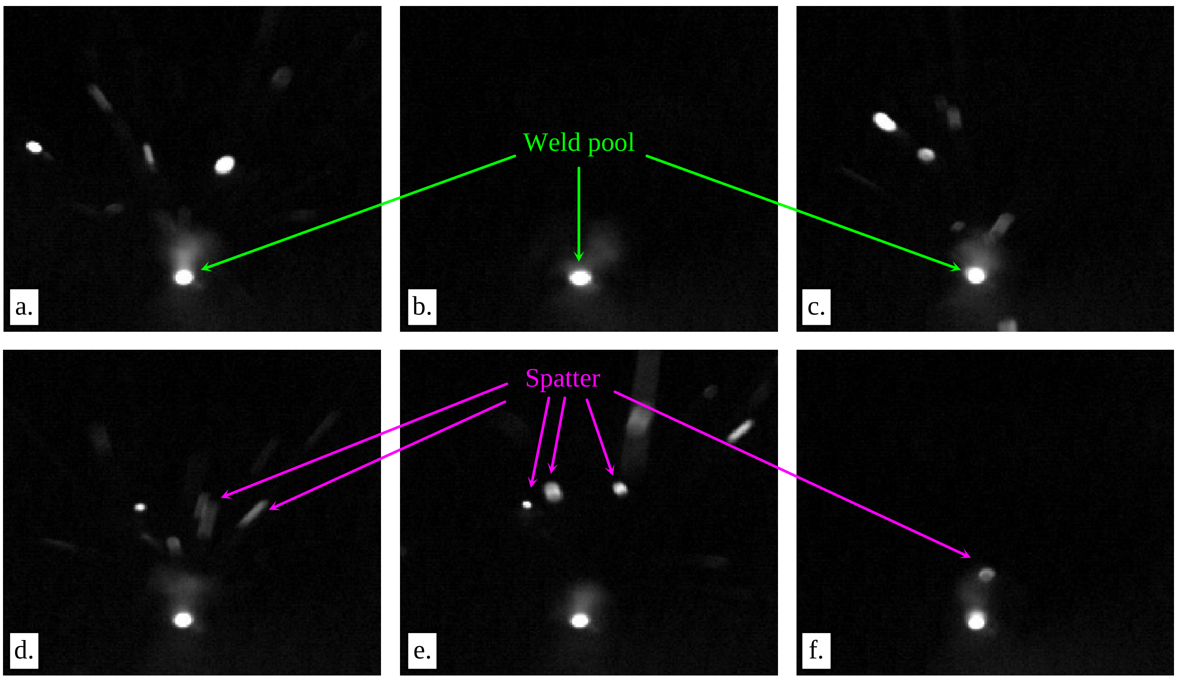

Figure 4.53. High speed camera images – Material ejection from weld pool

4.8 Conclusions

Following conclusions are inferred from the experimental investigation of laser welded test plates and T-joints.

- The three step approach used for performing various test cases (01, 02 and 03) helped in decoupling the complexities involved in laser beam welding of T-joint assembly. Fusion welding (Test Case 01) of test plates suggests the thermo-mechanical response of the material during welding. Filler welding case (Test Case 02) helps understanding the effect of filler wire addition. While, T-joint welding (Test Case 03) attempts to replicate the real situation in practice.

- To study the effect of different thermal boundary conditions, test plates were welded using aluminium support (test cases 01A and 02A) and simply supporting conditions (test cases 01B and 02B). It is found that the boundary conditions not only affect the temperature fields, but they also influence the distortion pattern of the test plates.

- For identical temperature fields of the fusion (test case 01A) and filler (test case 02A) welded test plates, the comparison of out-of-plane and in-plane displacements show that the melting of filler wire consumes significant amount of heat energy while becoming the part of weld bead.

- The effect of rapid heat loss from the test plates (using aluminium support) is such that the distortion level is reduced to some extent.

- In-plane displacement measured as a function of time using LVDT sensors help qualifying expansion and contraction occurrences during welding. It is noticed that these measurements are highly sensitive to the positioning of LVDTs, in-plane slip / glide of test specimens, out-of-plane deformation of FZ and HAZ etc.

- Stereo-image correlation technique efficiently captures the 3D global initial and final surface profiles of the test specimens. In addition to that it also provides precise measurement of residual in-plane and out-of-plane displacements. It has been observed that changing welding parameters result in different in-plane and out-of-plane displacement levels.

- Microscopic analysis and infra-red camera observations suggest the distribution of heat energy along the weld joint. It is found that a uniform average temperature of the weld pool leads to consistent fusion zone geometry, which, in turn, is likely to induce uniform displacements within the test specimens.

- Qualitative analysis of high speed camera shows the material loss from the weld pool due to the spatter produced in the keyhole regime.

CHAPTER 5

FINITE ELEMENT SIMULATIONS

Contents

SUMMARY

This chapter comprises of finite element (FE) simulations of various test cases performed during experimental campaigns. FE simulations are performed with the commercial FE software Abaqus and the conical heat source with Gaussian volumetric distribution of flux is programmed in Fortran. Owing to the symmetry of welded test specimens, only the symmetric models are assumed throughout. A very fine mesh size is used in and near the fusion zone, while the mesh density reduces gradually outside the fusion zone. Three-dimensional solid continuum brick and prism elements are used to build the geometry of the model. DC3D6 and DC3D8 type elements are used for thermal analysis; and C3D6 and C3D8R type elements are used for mechanical analysis.

An uncoupled or sequentially coupled temperature-displacement analysis is performed in each case. Heat transfer analysis is carried out first in order to achieve the required weld pool geometry and thermal histories. Thermal boundary conditions include free convection and radiation in air, forced convection due to air suction and heat transfer at the interface of test plates and aluminium support. The temperature fields so obtained are integrated in the structural analysis as predefined fields. Mechanical analysis is performed next while integrating the mechanical loading and boundary conditions. The material is assumed to follow elasto-plastic / elasto-viscoplastic law with isotropic hardening (von Mises plasticity model). The effect of filler wire addition is also integrated during simulation, where activation and deactivation of elements are achieved by changing the thermo-mechanical properties of the material depending upon the increase and decrease in current localised temperature.

MAJOR CONCLUSIONS

The comparative analysis between the experimental and simulation results is developed to validate the FE models. A good agreement is found amongst both the results for thermal as well as mechanical analysis. Some discrepancies may be attributed to the simplifications assumed during simulation.

It is observed that longitudinal residual stresses dominate all the remaining stress components and hence shall have the strongest influence over the distortion of the component. Moreover, with increasing beam power the longitudinal stresses show increasing trend. The residual in-plane and out-of-plane displacements are also efficiently predicted. The residual plastic strain components are found to be highly localised in the fusion and heat-affected zones.

FINITE ELEMENT SIMULATIONS

Numerical methods have been used since the beginning of the 1970's to simulate welding processes. The focus has been to predict thermal histories, residual stresses and distortion induced by the welding process. Finite element (FE) simulations have been the most common numerical method and many papers have been presented over a period of time [TOSI][BERD][UEDY][HIBH][BOUP][BOU1][BOU2]. Large complex simulation models of three-dimensional (3D) components are, however, still rare, mainly due to the lack of computational power. One reason is that to be able to compute the temperature and residual stress fields in the affected zones a very fine discretization of the space variable is required.

It is generally understood that welding involves highly complex phenomena, arising from interaction between thermal transients and the elasto-plastic (EP) structural responses of the assembly, together with the metallurgical transformations of the material being welded. However, Lindgren [LIN2] and Dong [DONP] have both shown that several simplifications are admissible in predicting welding residual stresses and deformations, with minimal loss in accuracy. For instance, the thermo-elasto-plastic welding process can be uncoupled into a thermal transient analysis and an EP structural analysis. Jiang [JIAW] has shown that considerable reduction in computational time can be achieved by uncoupling the welding process mechanics and the predicted welding residual stresses do not differ much from those given by a fully coupled analysis.

Early welding simulations were confined to analyses based on two-dimensional (2D) cross-sections, for example in the work performed by Friedman [FRIE]. These simulations gave an indication of the welding residual stresses which would be generated according to a plane strain assumption, but were unable to show out-of-plane deformations, for which a full-scale 3D welding simulation would have been necessary. Increasing computational power over the years led to welding simulations which could include most of the complex aspects of welding. A bibliography of finite element analyses and welding simulations presented between 1976 –1996 [MACJ] and 1996 – 2001 [MAC1] has been produced by Mackerle. These may be divided into complex models; which on one hand, address the complete transient thermo-elasto-plastic responses of welded structures and simplified models, while on the other hand, do not simulate the welding process completely but focus on the prediction of welding distortion.

However, reduction in computational time is a major target in both strategies. For example, dynamic remeshing and later on adaptive meshing was introduced in the welding simulations of Lindgren [LIN6] and Runnemalm and Hyun [RUN1], thereby reducing the number of elements and nodes in the stiffness matrix. In a further effort to reduce the number of elements Nasstrom [NAS1] used a combination of solid and shell elements to model welded structures. Younan [YOUM] developed a means of depositing the weld material by means of an element movement technique, aimed at reducing the time associated with element 'birth and death' techniques and overcoming computational instabilities.

Attention has also been given to establishing the significance of the different material properties involved, so that unnecessarily complex material modelling requirements may be avoided. Lindgren [LIN3] concludes that if welding residual stresses are to be determined, the simulations must account for elastic strains, thermal strains and an inelastic strain component, the latter usually being treated as a plastic strain. Radaj [RAD1] states that the main driving forces responsible for welding residual stresses derive from the thermal strains, suggesting that the most important material parameter is the coefficient of thermal expansion. Lindgren, in [LIN4], suggests that volume changes due to material phase changes should also be included in the thermal strain component and argues in [LIN2] that the final weld cooling phases are the important stages leading to residual stresses and distortion. In a study on low carbon steels by Free and Goff [FREJ], strong agreement with the experimental results was achieved, even when simple, fixed conductivity, specific heat, density, elastic modulus and coefficient of thermal expansion, together with temperature-dependent yield strength material properties, were used. The success of the simpler approach may simply be a function of the volume change behaviour in the particular steel used. Zhu and Chao [ZHUX] also reported successful use of fixed material properties in a study of aluminium welded joints.

All the above cases are based on transient thermo-mechanical simulation. Michaleris and DeBicarri [MICP] describe an alternative route which combines a small-deformation, eigenvalue buckling analysis with a 2D cross-section, thermo-elasto-plastic analysis and a 3D large deformation, structural analysis. In the first instance, a transient, uncoupled, two-dimensional thermo-elasto-plastic welding analysis is performed to identify the residual thermal strains due to welding and this is used to derive an applied welding load. These strains are subsequently applied to a 3D large-deformation, structural analysis. To supplement the analysis, a 3D small-deformation, eigenvalue analysis is performed to establish the critical buckling load. If this load is lower than the applied welding load, buckling is to be expected.

Random imperfections are applied to the large deformation analysis to simulate the buckling mode.

Tsai [TSAC], Deo [DEOM] and Huang [HUAT] adopted a similar procedure and applied it to multiple stiffened plate structures. Good agreement with the experimental results was achieved in all cases. These numerical simplifications are often referred to as ‘inherent strain methods’ and in all cases, the applied forces are derived from a 2D cross-section, transient, thermo-elasto-plastic analysis. The term ‘inherent strain method’ was applied earlier by Ueda [UED1] and Yuan [YUAM] to establish the longitudinal residual stress fields in butt and fillet welds. Examination of finite element model results (for welding conditions and material properties) guided the formulation of analytical solutions, based on a time-independent simplification of the transient thermal field. These were used to identify a yielded region and an elastic region. The yielded region was taken to be a zone bounded by points where the maximum temperature was greater than an arbitrary melting temperature of the parent material, while the elastic region was found via an iterative solution of analytical equations.

The FE simulations, which are being presented in this chapter, focus on the development of 3D models on FE code Abaqus. The efforts are made to simulate the temperature and displacement fields for all the test cases presented in previous chapter. The comparative analysis is developed with quantitative experimental results. The welding induced residual distortions and stresses are also predicted.

5.1 Principle of Finite Element Analysis

The principal of numerical simulation of welding entails the know-how of a comprehensive database with reference to geometry, thermo-mechanical properties, initial conditions, boundary and loading conditions. The essentials of numerical simulation of welding are shown in Fig. 5.1. The more the information regarding these parameters is accurate, the more the simulation is robust. Once the input database is furnished FE simulation may now be performed, however, an experimental database is almost always required to establish the comparison with simulation results and validate the numerical model.

An uncoupled / sequentially-coupled thermo-mechanical analysis is performed for all the test cases. The term sequentially-coupled implies that the thermal and mechanical analyses are performed in a sequence one after the other and are coupled in a way that the temperature histories calculated during thermal analysis are applied as predefined field in mechanical analysis. Here, it is assumed that mechanical response of the test specimens depends upon the thermal loading; while there is no inverse dependency. This is because the amount of heat generated due to the mechanical dissipation, if any, is negligibly small as compared to the heat energy supplied by the heat source. The description of thermal and mechanical models has already been presented in chapter 2 in detail. The heat transfer problems are generally highly non-linear because the material properties are temperature-dependent. In some cases, the boundary conditions are also temperature-dependent; while, in some other cases, they are assumed independent of temperature.

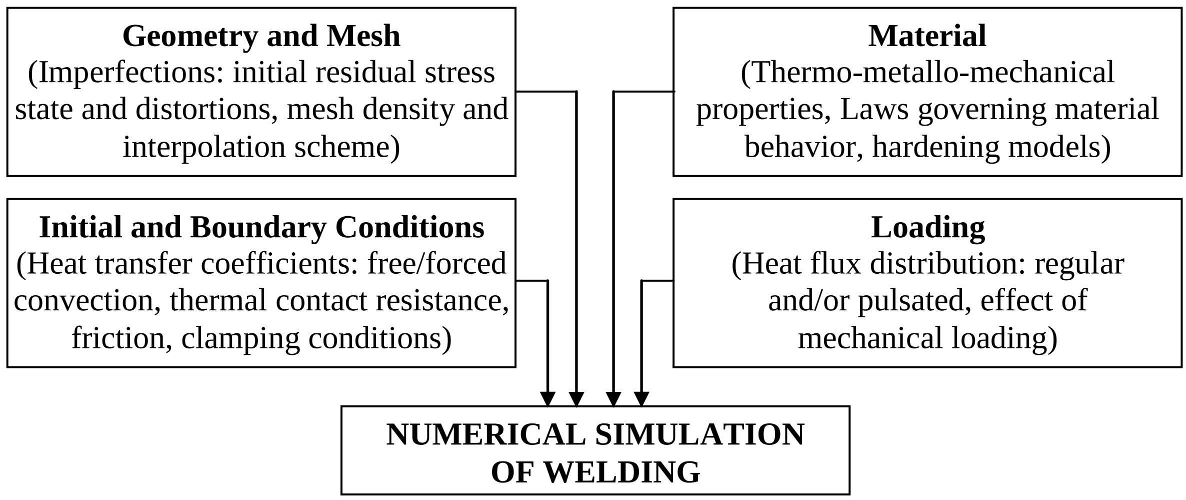

Figure 5.1. Essentials of numerical simulation of welding

5.2 Finite Element Mesh

Simulation of stresses and distortion of welding components by means of finite element method (FEM) initially requires that the component is meshed with finite elements, on the basis of the component geometry. The mesh density is generally controlled by the applied loading and/or boundary conditions. Since welding processes involve high temperature gradient in and near the FZ, a very fine mesh is required to capture the FZ boundary and temperature distribution in the HAZ. However, too fine a mesh may lead to unnecessary increase in computation time. An optimum mesh density is, therefore, used without compromising the quality of results. As the temperature gradient is considerably low outside the heat-affected zone (HAZ), a relatively coarser mesh is deemed sufficient for the analysis. Therefore, the mesh density is required to reduce progressively away from the fusion line; as an abrupt increase in mesh size may lead to discontinuous contours and poor interpolation of temperatures, displacements and stresses etc.

The FE model of the test specimens and support consists of continuum solid three-dimensional linear elements. The symmetric models are assumed due to the symmetry of the specimens' geometry, loading and boundary conditions. The choice of the symmetric models also helps reducing the number of degrees of freedom thereby decreasing the overall computation time. The test plates and T-joint mesh consists mostly of 8-nodes brick elements (type: DC3D8, C3D8R) completed by some 6-nodes prism elements (type: DC3D6, C3D6); while the support mesh consists only of 8-nodes brick elements with a relatively coarse mesh size. The mesh in the FZ and HAZ contains mostly brick elements. To compensate for the increase in the size of brick elements, prism elements are used selectively. Lengthwise, there are 600 elements at the fusion line for test cases 01, 02 and 03; which then reduce to only 30 at the far end for test cases 01 and 02 and to 60 for test case 03. Further mesh details are mentioned in Table 5.1. The mesh of test plate, T-joint and support for test cases 01, 02 and 03 are presented in Figs. 5.2, 5.3 and 5.4, respectively.

Test Case	Nodes	Elements	Smallest Element Dimensions
01 (Test plate)	58,639	50,328	0.5 mm x 0.31 mm x 0.3 mm
02 (Test plate)	63,287	53,808	0.5 mm x 0.31 mm x 0.25 mm
03 (T-joint)	76,788	63,600	0.5 mm x 0.38 mm x 0.24 mm

Table 5.1. Mesh Details

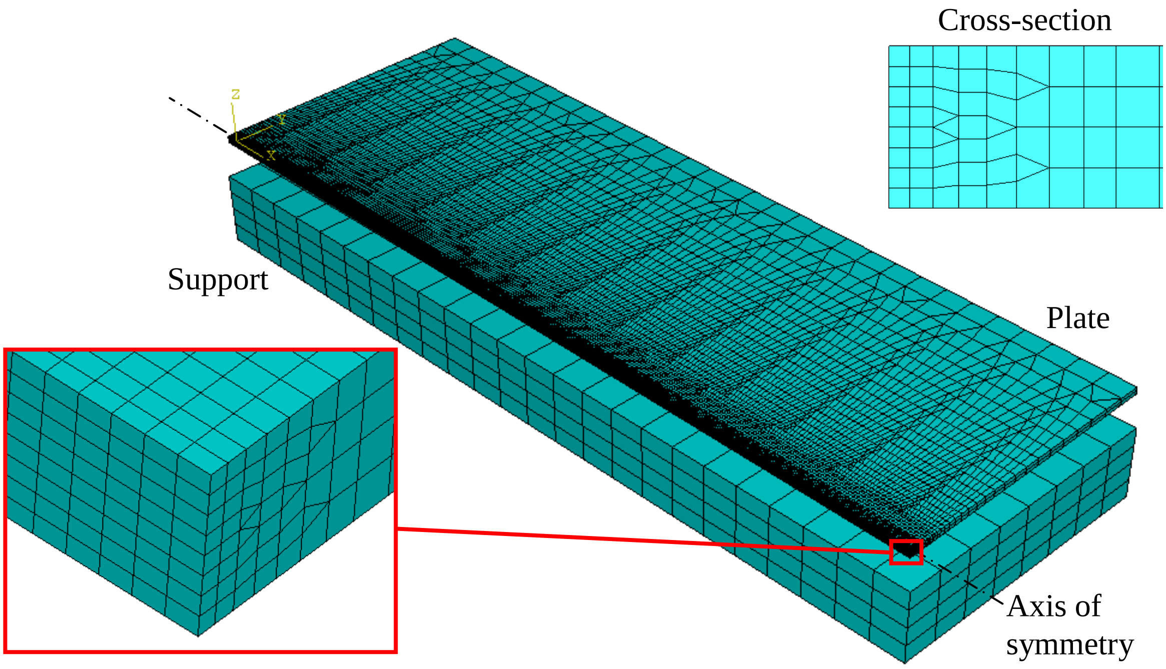

Figure 5.2. Mesh details – Test Case 01

Figures 5.3 and 5.4 also show some of the highlighted elements which are the representatives of filler metal wire. The elements activation and deactivation is achieved on these elements during welding.

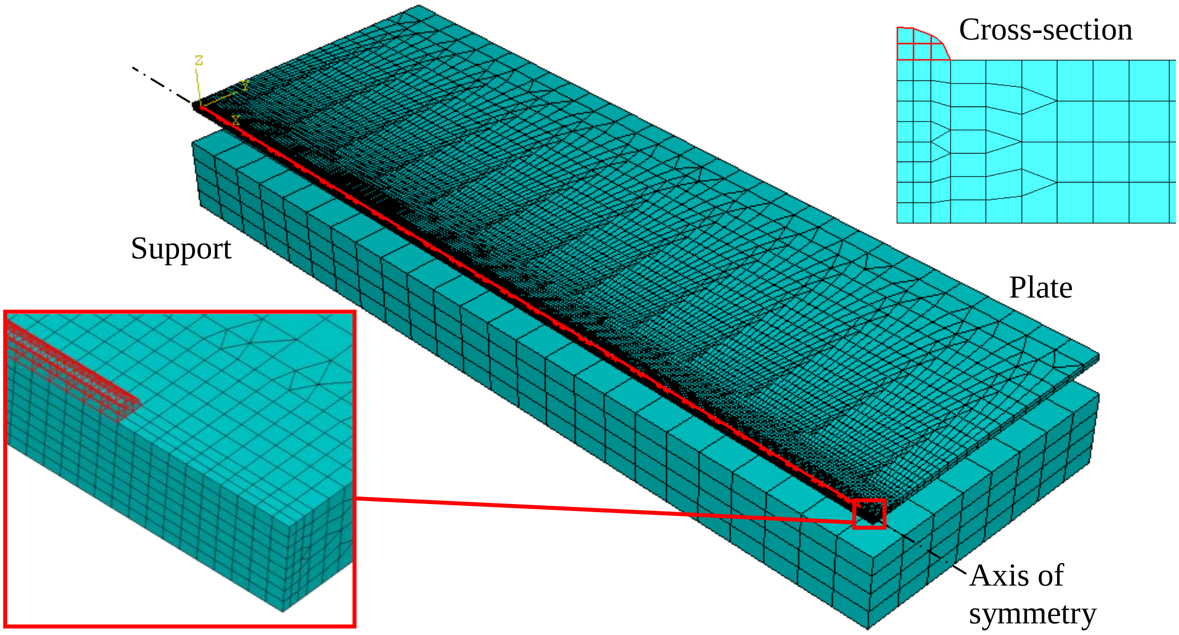

Figure 5.3. Mesh details – Test Case 02

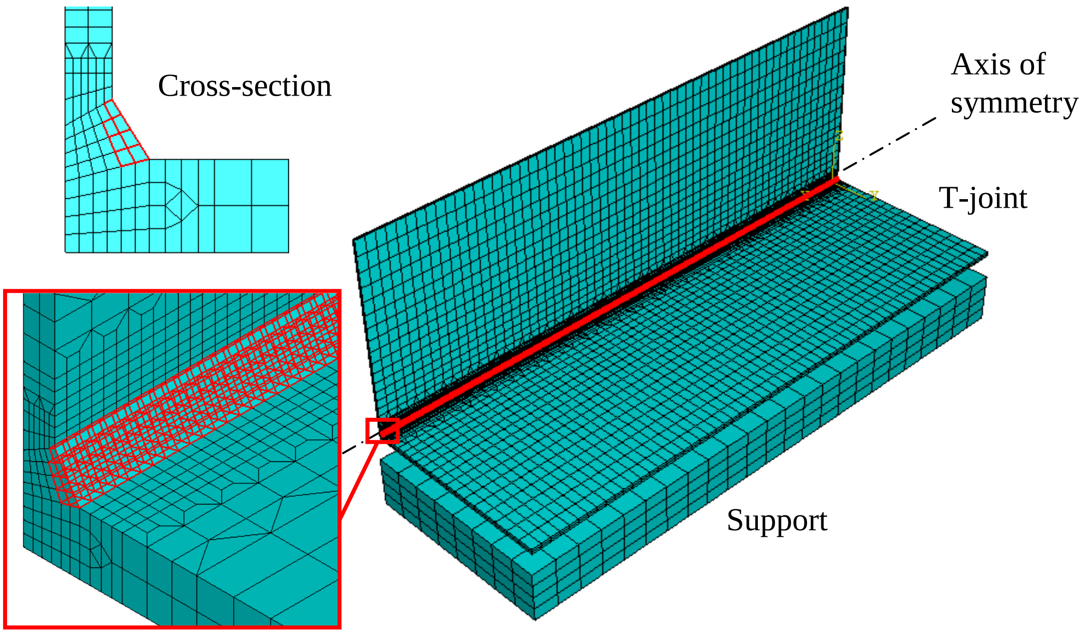

Figure 5.4. Mesh details – Test Case 03

5.3 Material Properties

The temperature dependent thermal and mechanical material properties are crucial to the successful development of numerical models. The thermo-mechanical properties, which are used for Abaqus simulations (discussed in chapter 3), are being summarized in this section. With respect to thermal properties, latent heat of fusion is defined to include the effect of solid/liquid phase transformation. A value of 4 x 10^5 $J.kg^{-1}$ is used as latent heat of fusion between the solidus ($T_{solidus}$) and liquidus ($T_{liquidus}$) temperatures of 587°C and 644°C, respectively. The thermal properties are provided by EADS.

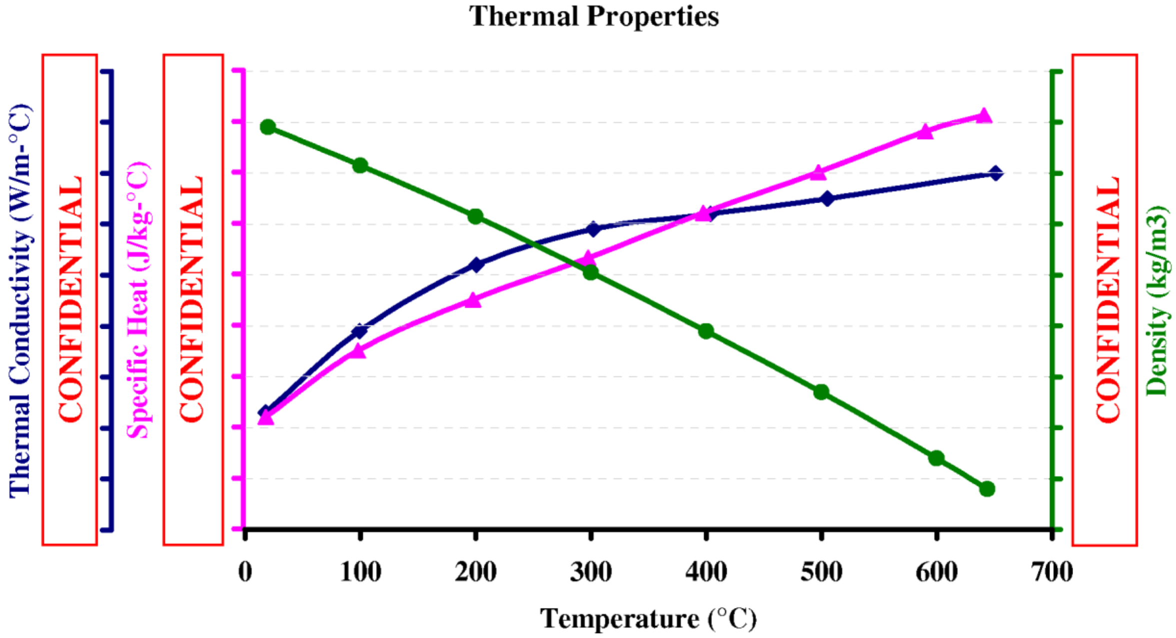

Figure 5.5. Thermal properties as a function of temperature

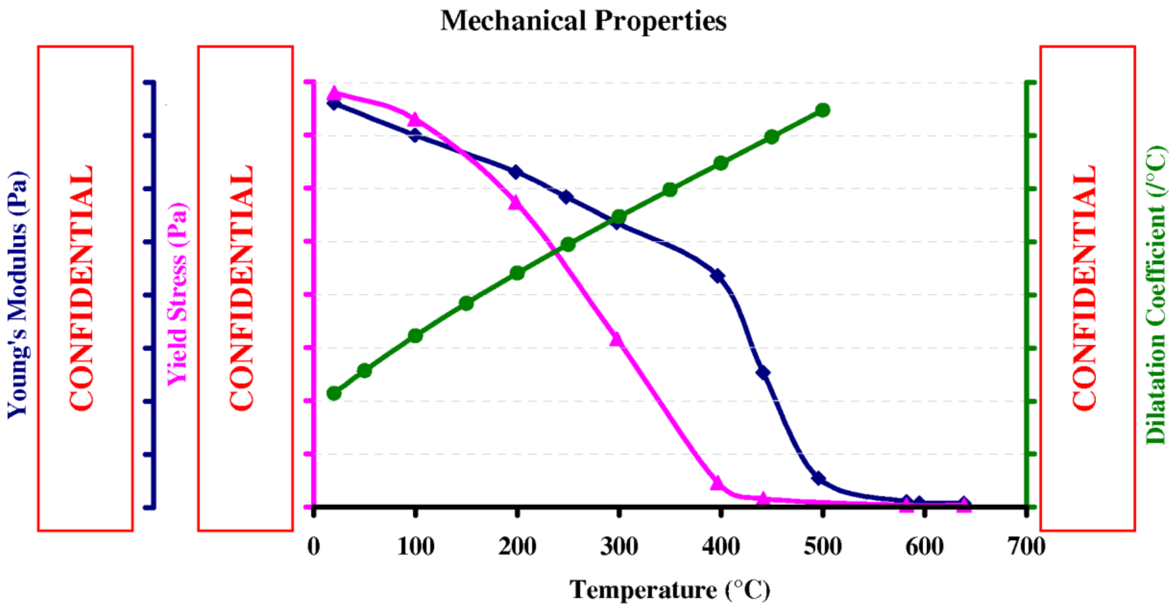

Figure 5.6. Mechanical properties as a function of temperature

Other thermal and mechanical material properties used for simulation are presented in Figs. 5.5 and 5.6, respectively. A constant value of 0.34 is used as Poisson's ratio, ν. Strain hardening curves at the strain rates of 0.0001 s^{-1} and $1s^{-1}$ with several temperatures are presented in Figs. 5.7 and 5.8, respectively. The material properties with varying strain rates help integrating the viscosity effects in the FE model. The mechanical properties are adopted from the results of conventional tensile testing machine (Chapter 3).

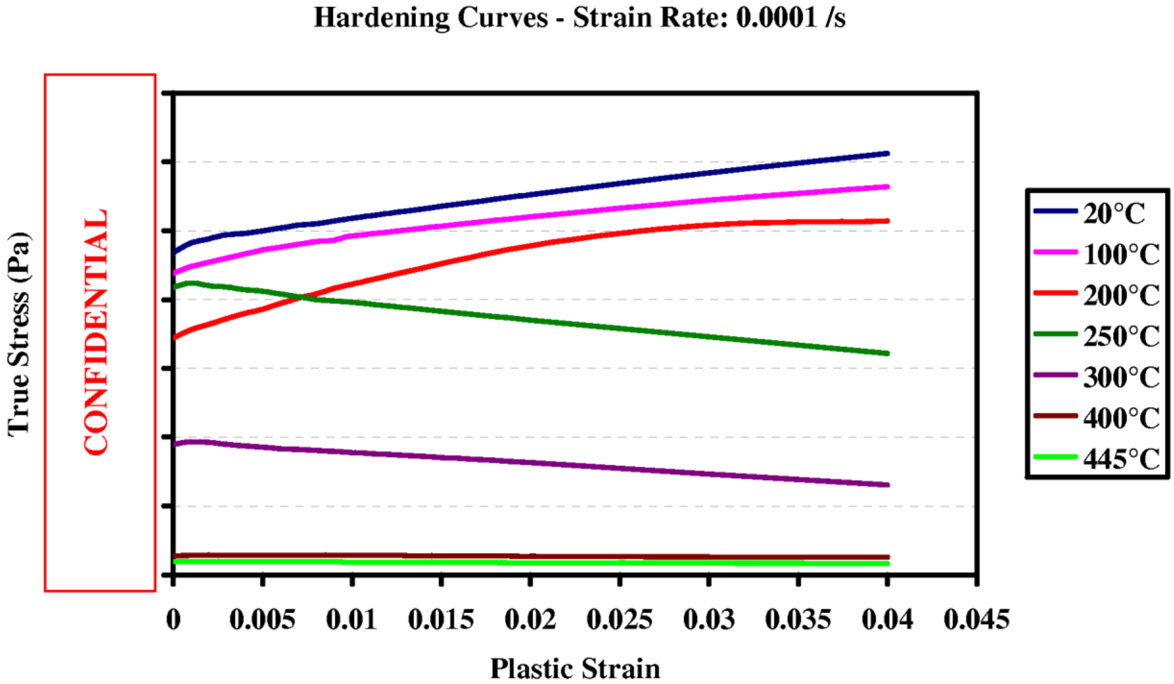

Figure 5.7. Hardening curves at various temperatures and at strain rate of $0.0001s^{-1}$

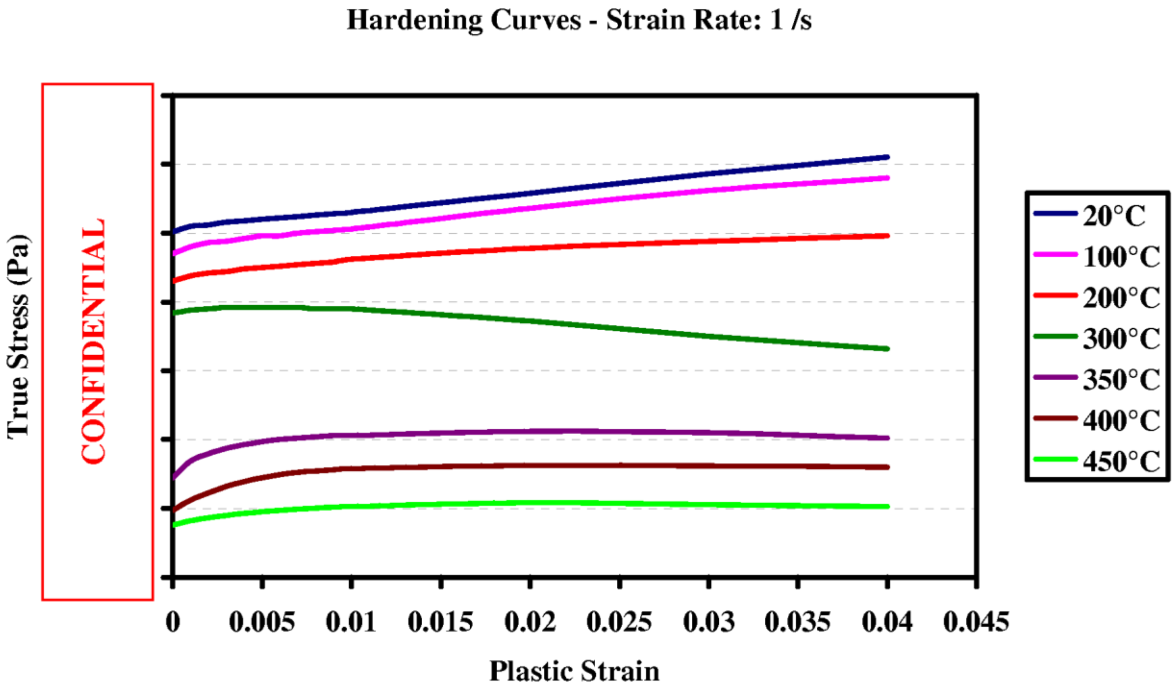

Figure 5.8. Hardening curves at various temperatures and at strain rate of $1s^{-1}$

Although the negative slope (softening) makes it difficult to converge the mechanical analyses, yet with some increase in computation time and increased number of increments the solution converges for test case 01 and 02. For test case 03 (T-joint welding), however, perfectly plastic behaviour is assumed for all the strain softening curves.

5.4 Thermal Analysis

In order to compute the temperature histories, heat transfer analysis is performed using temperature dependent thermal properties. The transient temperature field (*T*) in time (*t*) and space (*x, y, z*) is achieved by solving the following heat transfer equation:

$$\frac{\partial}{\partial x}\left(\lambda(T)\frac{\partial T}{\partial x}\right)+\frac{\partial}{\partial y}\left(\lambda(T)\frac{\partial T}{\partial y}\right)+\frac{\partial}{\partial z}\left(\lambda(T)\frac{\partial T}{\partial z}\right)+Q_v \;=\; \rho(T)C_p(T)\left(\frac{\partial T}{\partial t}\right) \tag{5.1}$$

Here, $\lambda(T)$ is the thermal conductivity as a function of temperature in $W.m^{-1}.K^{-1}$, $\rho(T)$ is the density as a function of temperature in $kg.m^{-3}$, $C_p(T)$ is the specific heat as a function of temperature in $J.kg^{-1}.K^{-1}$ and Q_v is the volumetric heat flux in $W.m^{-3}$.

The problems considered here do not take into account the temperature dependence of the surface heat transfer coefficient. By this means that the heat transfer problem is mildly non-linear. ABAQUS uses an iterative scheme to solve non-linear heat transfer problems. This scheme is based on the Newton iteration method. In ABAQUS, time integration in transient problems is done with the backward Euler method (sometimes also referred to as the modified Crank-Nicholson operator). This method is unconditionally stable for linear problems. Time incrementation used in the analysis is of both types; fixed and automatic. The analysis is performed in two steps; where first step uses fixed time increments and the second step makes use of automatic incrementation. These steps are as follows:

- *Step 1*: meant to integrate the heat flux through a Fortran subroutine DFLUX.
- *Step 2*: intended to incorporate cooling due to thermal boundary conditions.

The heat source is moved along the axis of symmetry where it travels with respect to the nodal coordinates. The choice of fixed time increment is based upon the nodal distance and welding speed. Once the heat source is removed, automatic time increments may be used, as in Step 2. For automatic incrementation, ABAQUS chooses the time step such as to keep the largest temperature change at every integration point less than an allowed value, ΔT_{max}. At the very beginning of the cooling, the temperature drops rapidly due to the conduction within the work-piece. Restrained by maximum allowable temperature change (ΔT_{max}), the time increment is very small at this stage. However, as the cooling progresses, the time step grows upto the maximum allowed value defined by the user. The combination of fixed and automatic incrementation helps reducing the computation time to a great extent. Table 5.2 shows the fixed time increments chosen for different test cases.

Test Case	Nodal distance on the fusion line	Speed of heat source movement	Fixed time increment
01 (Test plate)	0.5 mm	8 m/mn	3.75×10^{-3} s
02 (Test plate)	0.5 mm	8 m/mn	3.75×10^{-3} s
03 (T-joint)	0.5 mm	5 m/mn	6.0×10^{-3} s

Table 5.2. Time incrementation during welding

5.4.1 Initial and Boundary Conditions

All FE analysis problems are defined in terms of initial and boundary conditions. A typical type of initial condition for a welding application is the initial temperature that, in most cases, is set to room temperature. Initial conditions for these simulations are as follows:

At $t = 0$ sec

$T(t) = 20°C$

Examples of the most important thermal boundary conditions are heat transfer due to free / forced convection in air, radiation from the surface of the work-piece, heat transfer due to the contact between work-piece and the support / clamping devices. Figures 5.9, 5.10 and 5.11 show the schematic representation of thermal boundary condition for symmetric models of test plates welded on aluminium support (test cases 01A and 02A), in air (test cases 01B and 02B) and T-joint welded using aluminium support (test case 03), respectively.

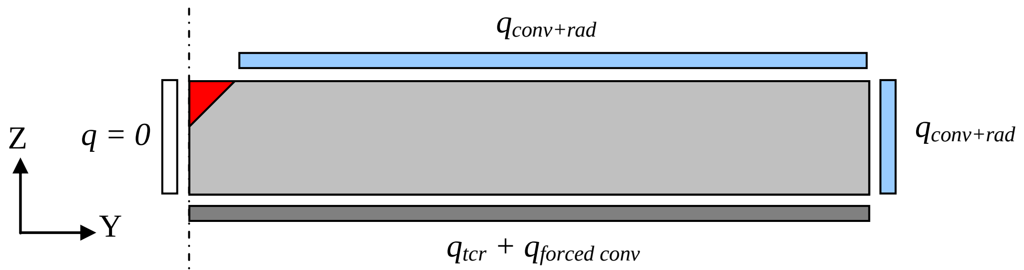

Figure 5.9. Thermal boundary conditions – Test case 01A, 02A

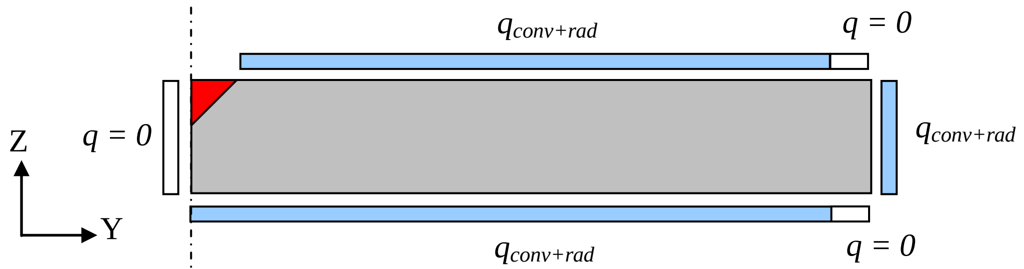

Figure 5.10. Thermal boundary conditions – Test case 01B, 02B

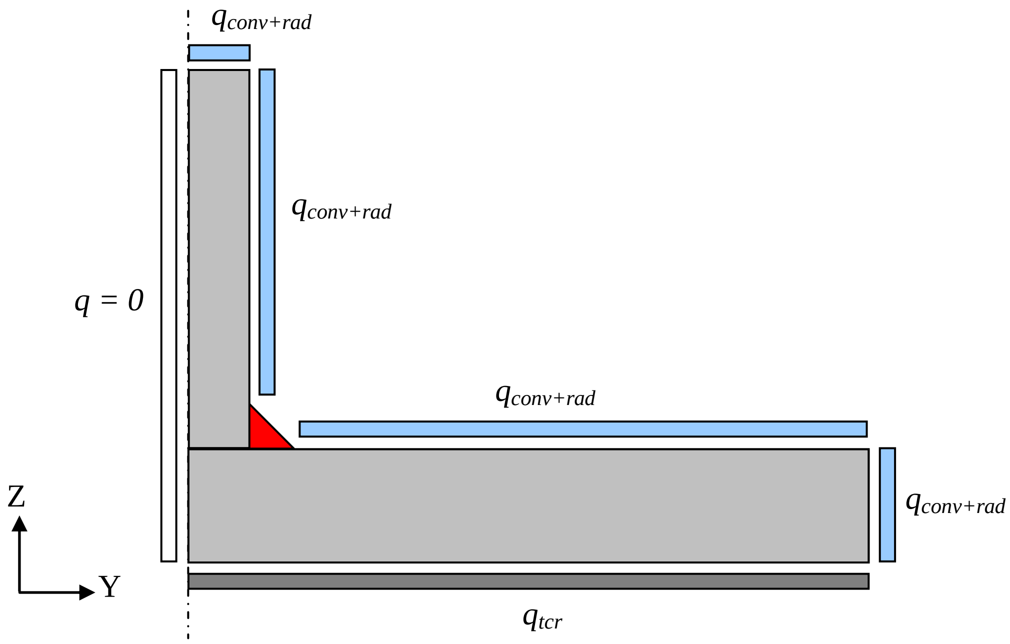

Figure 5.11. Thermal boundary conditions – Test case 03

Owing to the complex nature of thermal boundary conditions at the bottom surface of the test plate; forced convection and thermal contact resistance are used. Forced convection is assumed to be present due to air suction through aluminium suction table and leakage at the boundaries of the test plate. Furthermore, as the test plate comes in contact with aluminium suction table due to the air suction, thermal conductance as a function of pressure is introduced at the interface of the test plate and the suction table. Free convection and radiation to atmosphere are used at all the remaining surfaces except the symmetric plane and the point of contact of insulated clamps. Since, heat transfer coefficients are adjusted in order to calculate the similar temperature fields as the ones measured experimentally; only the thermal contact resistance is used on the bottom surface of T-joint. Equations 5.2, 5.3 and 5.4 define $q_{conv+rad}$, q_{tcr} and $q_{forced\ conv}$ as general boundary conditions.

$$q_{conv+rad} = h_{conv}(T - T_0) + \sigma_{SB}\xi((T - T_{abs})^4 - (T_0 - T_{abs})^4) \tag{5.2}$$

$$q_{forced\,conv} = h_{forced\,conv}(T - T_0) \tag{5.3}$$

$$q_{tcr} = h_{tcr}(T_s - T) \tag{5.4}$$

where, T, T_0, T_{abs} and T_s are the temperature of the work-piece, ambient temperature, absolute zero and temperature of the support, respectively.

The values used for the heat transfer coefficients and radiation constants are as follows.

- Convective heat transfer coefficient of air: h_{conv} = 15 $W.K^{-1}.m^{-1}$,
- Emissivity of aluminium surface: $\xi = 0.08$,
- Emissivity of speckle pattern: $\xi = 0.71$,
- Stefan-Boltzmann constant: $\sigma_{SB} = 5.68 \times 10^{-8}$ $J.K^{-4}.m^{-2}.s^{-1}$,
- Convective heat transfer coefficient for air suction: $h_{forced\ conv}$ = 200 $W.K^{-1}.m^{-2}$,
- Heat transfer coefficient at the interface of the test plate and support (test case 01A, 02A): h_{tcr} = 50 $W.K^{-1}.m^{-2}$ at 0 bar, 84 $W.K^{-1}.m^{-2}$ at 1 bar,
- Heat transfer coefficient at the interface of the T-joint and support (test case 03): h_{tcr} = 250 $W.K^{-1}.m^{-2}$ at 0 bar, 284 $W.K^{-1}.m^{-2}$ at 1 bar.

The heat transfer coefficients h_{conv} and $h_{forced\ conv}$ are adopted from [JOSE]. h_{tcr} is calibrated for each test case from the TCs at bottom surface (TC6 – TC9). Emissivity values were obtained during infra-red camera measurements.

The physical phenomena occurring at the level of weld pool like formation of keyhole, ionization and vaporization of material, circulation of molten material within the weld pool due to electromagnetic and buoyancy forces, solidification at the liquid–solid interface, etc. are difficult to model. Various simplifications are, therefore, required to be assumed. In this work the weld pool is treated as a solid phase for calculating the temperature fields.

5.4.2 Heat Source Model

The heat source model plays a critical role in achieving the precise application of heat flux, which in turn helps acquiring required weld pool dimension and desired thermal histories. The selection of an appropriate model is, therefore, a matter of great concern and depends greatly upon the factors like weld pool dimensions, geometry of the weld-joint, temperature fields in and near the FZ, welding process being simulated etc. There exist various models in literature ranging from surface heat source with Gaussian distribution to double-ellipsoidal volumetric heat source in accordance with Goldak [GOL2]; while sometimes a heat source composed of two different models is also integrated. For example, Lundback [LUNA] used Goldak's double ellipsoid with double elliptic cone to simulate the electron beam welding process with keyhole. Ferro [FERP] used conical distribution of heat flux with an upper and lower hollow sphere to incorporate the keyhole phenomenon of electron-beam welding process. Similarly, Gilles [GILP] used prismatic surface heat source with linear distribution to model the TIG welding process.

It is generally understood that the amount of heat energy contained by the work-piece is different from that produced at the tip of welding torch during the welding process. It is safe to assume that the heat input be calculated from the welding parameters like current, voltage and power. However, a part of this energy goes to heat dissipation (losses to the surroundings, shielding gas etc.) before being absorbed by the work-piece. The net heat input may, therefore, be expressed as follows:

$$Q_0 = \eta UI = \eta P \tag{5.5}$$

Where, Q_0 is the net heat input in W, η is the efficiency of process, U is voltage in V, I is current in Amp, and P is power in W. The values of the process efficiency, η, for different welding processes are presented in table 5.3.

Welding Process	**SAW,** Steel	**SMAW,** Steel	**GMAW,** CO_2-steel	**GMAW,** Ar-steel	**GTAW,** Ar-steel	**GTAW,** He-Al	**GTAW,** Ar-Al
η	0.91-0.99	0.66-0.85	0.75-0.93	0.66-0.70	0.25-0.75	0.55-0.80	0.22-0.46

Table 5.3. Efficiency factors for different welding process [GRON]

It can be observed from the table 5.3, that the efficiency of the process depends greatly upon the type of welding, shielding gas or flux, material being welded, reflections from work-piece surface and surrounding environment etc. Various authors [HONK][TISF][CARD] suggest different values of efficiency ranging from 30% to 90% for the same processes. El-Ahmar [ELAW], however, suggests a value of 75% of efficiency for TIG welding of 316L steel. In this work two different efficiency values are used for different type of test cases. The efficiency of 37% is used for laser beam welding of test plates (test cases 01 and 02), whereas a value of 80% is used for welding of T-joints (test case 03).

The heat source model integrated for the application of heat flux on test plates (test cases 01 and 02) makes use of a conical heat source with Gaussian distribution along with an upper hollow sphere with linear distribution. However, for T-joint welding (test case 03) the conical heat source with Gaussian distribution is used only.

Conical heat source is a 3D volumetric heat source that considers the heat intensity distribution along the work-piece thickness. As shown in Fig. 5.12, the heat intensity deposited region is maximum at the top surface, and is minimum at the bottom surface of the work-piece. Along the thickness of the work-piece, the diameter of the heat density distribution region is linearly decreased. But the heat density at the central axis (z-direction) is kept constant. At any plane perpendicular to z-axis, the heat intensity is distributed in Gaussian form. Thus, in fact, conical source is the repeated addition of a series of Gaussian heat sources with different distribution parameters and the same central maximum values of heat density along the work-piece thickness.

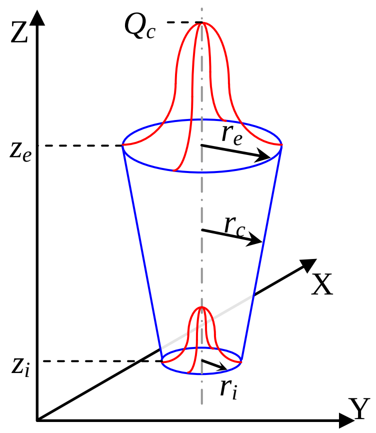

Figure 5.12. Conical heat source model

At any plane perpendicular to the z-axis, the heat intensity distribution may be written as follows [DEPL]:

$$Q_v(r,z) = Q_c \exp\left(-\frac{3r^2}{r_c^2}\right) \tag{5.6}$$

Where Q_v is the total volumetric heat flux in W.m^{-3}, Q_c is the maximum value of heat intensity in W.m^{-3}, r_c is the distribution parameter in m, and r is the radial coordinate in m. The key problem is how to determine the parameters Q_c when the decay rule of r_c is known. The thermal energy conservation implies:

$$\eta P = \int_0^H \int_0^{2\pi} \int_0^{r_c} Q_V(r,z) r dr d\theta dh \tag{5.7}$$

With $H = z_e - z_i$ and $h = z - z_i$

Or,

$$\eta P = \int_0^H \int_0^{2\pi} \int_0^{r_c} Q_c \exp\left(-\frac{3r^2}{r_c^2}\right) r dr d\theta dh \tag{5.8}$$

Which then leads to,

$$\eta P = \frac{\pi \cdot Q_c (1 - \exp(-3))}{3} \int_0^H r_c^2 dh \tag{5.9}$$

r_c decreases linearly for conical heat source. The height of the cone is defined in terms of z-coordinates of the top and bottom surfaces, viz. z_e and z_i, respectively. Similarly, the radii at the top and bottom of the cone are r_e and r_i, respectively. The distribution parameter r_c can be expressed as:

$$r_c(z) = r_i + (r_e - r_i)\frac{z - z_i}{z_e - z_i} = r_e - (r_e - r_i)\frac{z_e - z}{z_e - z_i} \tag{5.10}$$

From where,

$$r_c^2 = \left[r_i + (r_e - r_i)\frac{h}{H} \right]^2 \tag{5.11}$$

Or,

$$\int_0^H r_c^2 dh = \int_0^H \left[r_i + (r_e - r_i)\frac{h}{H} \right]^2 dh \tag{5.12}$$

Which gives,

$$\int_0^H r_c^2 dh = \frac{H}{3} \cdot \left[r_i^2 + r_e r_i + r_i^2 \right] \tag{5.13}$$

Substituting Eq. 5.13 in Eq. 5.9,

$$\eta P = \frac{\pi \cdot Q_c H (1 - \exp(-3))}{9} \cdot \left(r_e^2 + r_e r_i + r_i^2 \right) \tag{5.14}$$

From where,

$$Q_c = \frac{9\eta P \exp(3)}{\pi(\exp(3) - 1)} \cdot \frac{1}{(z_e - z_i)\left(r_e^2 + r_e r_i + r_i^2\right)} \tag{5.15}$$

Substituting Eq. 5.15 in Eq. 5.6,

$$Q_v = \frac{9\eta P \exp(3)}{\pi(\exp(3) - 1)} \cdot \frac{1}{(z_e - z_i)\left(r_e^2 + r_e r_i + r_i^2\right)} \cdot \exp\left(-\frac{3r^2}{r_c^2} \right) \tag{5.16}$$

Equation 5.16 allows the application of conical volumetric heat flux with Gaussian distribution. The schematic sketch of conical heat source application in the T-joint configuration is shown in Fig. 5.13.

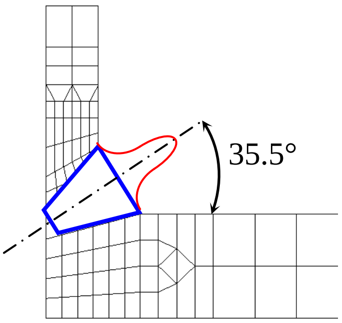

Figure 5.13. Application of conical heat source in T-joint (test case 03)

As already mentioned, the heat source model used for test plate welding (test cases 01 and 02) involves the use of a hollow sphere with linear distribution of flux in addition to the above defined conical heat source. For the case of the test plate welding, the laser beam penetrates the work-piece creating a capillary-shaped keyhole to the required depth. Here, the beam impingement zone experiences extensive material evaporation and ejection and, hence, a comparatively wider fusion zone appears. The conical part of the heat source is, therefore, meant to capture the effect of keyhole formation due to laser beam penetration; and the upper hollow sphere is incorporated to achieve the desired width of fusion zone. The heat source model is shown in Fig. 5.14.

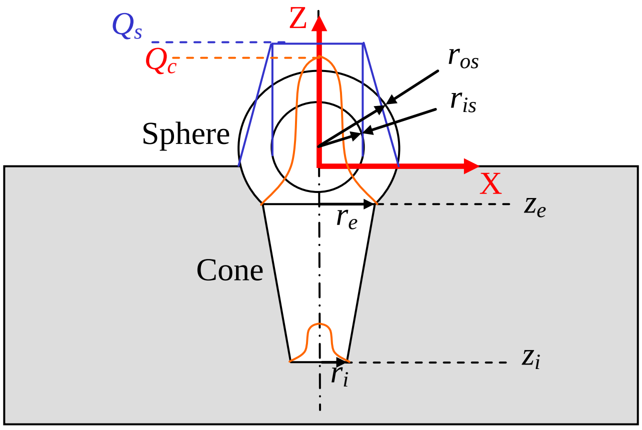

Figure 5.14. Conical heat source with upper hollow sphere (test cases 01 and 02)

The total volumetric heat flux is, therefore, split in two parts; conical and spherical.

$$Q_v = Q_{vc} + Q_{vs} = Q_c \exp\left(-\frac{3r^2}{r_c^2}\right) + Q_s \cdot 1 \cdot d_s \tag{5.17}$$

Such that, $Q_{vc} = Q_c \exp\left(-\frac{3r^2}{r_c^2}\right)$ and $Q_{vs} = Q_s \cdot 1 \cdot d_s$

Also,

$$\eta P f + \eta P(1-f) = \int_0^H \int_0^{2\pi} \int_0^{r_c} Q_c \exp\left(-\frac{3r^2}{r_c^2}\right) r\,dr\,d\theta\,dh + \int_0^{2\pi} \int_0^{\pi} \int_{r_{is}}^{r_{os}} Q_s r^2 \sin\phi\,dr\,d\phi\,d\theta \tag{5.18}$$

Where, Q_{vc} and Q_{vs} are the volumetric heat flux in W.m^{-3} for conical and spherical parts, respectively, Q_s is the maximum value of heat intensity in sphere in W.m^{-3}, r_{os} is outer spherical radius in m, r_{is} is inner spherical radius in m and d_s is the flux distribution parameter for the hollow sphere such that its value is 1 at r_{is} and 0 at r_{os}. f is the fraction of heat flux attributed to the conical part and the remaining *(1– f)* is attributed to the spherical part such that:

$$\eta Pf = \int_0^H \int_0^{2\pi} \int_0^{r_c} Q_c \exp\left(-\frac{3r^2}{r_c^2} \right) r dr d\theta dh \tag{5.19}$$

$$\eta P(1-f) = \int_0^{2\pi} \int_0^{\pi} \int_{r_{is}}^{r_{os}} Q_s r^2 \sin\phi dr d\phi d\theta \tag{5.20}$$

Solutions of Eq. 5.19 and 5.20 give,

$$Q_{vc} = \frac{9\eta P.f}{\pi(1-\exp(-3))} \cdot \frac{1}{(z_e - z_i)(r_e^2 + r_e r_i + r_i^2)} \cdot \exp\left(-\frac{3r^2}{r_c^2} \right) \tag{5.21}$$

$$Q_{vs} = \frac{3\eta P(1-f)}{4\pi(r_{os} - r_{is})^3} \cdot d_s \tag{5.22}$$

Substituting Eqs. 5.21 and 5.22 in Eq. 5.17,

$$Q_v = \frac{9\eta P.f}{\pi(1-\exp(-3))} \cdot \frac{1}{(z_e - z_i)(r_e^2 + r_e r_i + r_i^2)} \cdot \exp\left(-\frac{3r^2}{r_c^2} \right) + \frac{3\eta P \cdot (1-f)}{4\pi(r_{os} - r_{is})^3} \cdot d_s \tag{5.23}$$

Equations 5.23 and 5.16 are programmed in a Fortran subroutine called DFLUX. The parameters r_e, r_i, z_e, z_i, r_{os}, r_{is} and f are adjusted to achieve the experimentally observed weld pool geometry (see Annex B for heat source parameters).

5.5 Mechanical Analysis

A good reliable mechanical analysis requires precise calculation of temperature fields and fusion zone geometry during thermal analysis. The comparative analyses of results of thermal and mechanical simulations with those of experimental ones will be presented in the subsequent sections. Various mechanical analyses are performed in order to calculate the distortion and stress state induced during welding, while taking care of industrially employed mechanical loading and boundary conditions. The nodal temperature values calculated during heat transfer analysis are integrated as predefined field.

For all the test cases, the material is assumed to follow either the elasto-plastic (EP) or elasto-viscoplastic (EVP) behaviour with isotropic hardening law (von Mises plasticity model). The strain tensor decomposition states:

$$\boldsymbol{\varepsilon} = \boldsymbol{\varepsilon}^e + \boldsymbol{\varepsilon}^p + \boldsymbol{\varepsilon}^{th} \tag{5.24}$$

Which may be written in incremental form as:

$$\dot{\boldsymbol{\varepsilon}} = \dot{\boldsymbol{\varepsilon}}^{e} + \dot{\boldsymbol{\varepsilon}}^{p} + \dot{\boldsymbol{\varepsilon}}^{th} \tag{5.25}$$

Where, $\boldsymbol{\varepsilon}$ is the total strain tensor, $\boldsymbol{\varepsilon}^{e}$ is the elastic strain tensor, $\boldsymbol{\varepsilon}^{th}$ is the thermal strain tensor and $\boldsymbol{\varepsilon}^{p}$ is the plastic or inelastic strain tensor. The elastic strain tensor ($\boldsymbol{\varepsilon}^{e}$) is related to the stress tensor ($\boldsymbol{\sigma}$) with the help of compliance tensor, $\boldsymbol{\Lambda}^{-1}(T)$, which is the inverse of 4th order stiffener tensor, $\boldsymbol{\Lambda}(T)$ and is further defined by the two elastic coefficients namely Young's modulus, $E(T)$, and Poisson's ratio, $\nu(T)$, for an isotropic material.

$$\boldsymbol{\varepsilon}^{e} = \boldsymbol{\Lambda}^{-1}(T) : \boldsymbol{\sigma} \tag{5.26}$$

The thermal strain tensor ($\boldsymbol{\varepsilon}^{th}$) is defined in terms of thermal dilatation coefficient, $\alpha(T)$, current temperature (T) and reference temperature (T_0).

$$\boldsymbol{\varepsilon}^{th} = \alpha(T)(T - T_0)\boldsymbol{I} \tag{5.27}$$

The yield function, f, defines the limit to the elastic domain.

$$f(\boldsymbol{\sigma}, T, R) < 0 \tag{5.28}$$

Where $\boldsymbol{\sigma}$, T and R represents stress tensor, temperature and isotropic hardening parameter, respectively. The stress at the limit of elastic domain is defined as yield strength, σ_y, such that $\sigma_y = \sigma_y(\varepsilon^p, T)$. When the material flows plastically, the plastic part of the strain is defined by the flow rule:

$$\dot{\boldsymbol{\varepsilon}}^{p} = \dot{\lambda}\frac{dg}{d\boldsymbol{\sigma}} = \dot{\lambda}\frac{3}{2}\cdot\frac{\boldsymbol{S}}{\sigma_{eff}} \tag{5.29}$$

Where, $\sigma_{eff} = \sqrt{3J_2} = \sqrt{\frac{3}{2}\boldsymbol{S}:\boldsymbol{S}} = \sqrt{\frac{1}{2}\left[(\sigma_1 - \sigma_2)^2 + (\sigma_2 - \sigma_3)^2 + (\sigma_3 - \sigma_1)^2\right]}$

And, $J_2 = \frac{1}{2}\boldsymbol{S}:\boldsymbol{S}$ also $\boldsymbol{S} = \boldsymbol{\sigma} - \frac{tr(\boldsymbol{\sigma})}{3}\boldsymbol{I}$

Here, $g(\boldsymbol{\sigma}, T, R)$ is the flow potential, is $\dot{\lambda}$ the plastic flow rate whose value is determined by the requirement to satisfy the consistency condition $f = 0$, σ_{eff} is the von Mises effective stress, $\boldsymbol{S}$ is the deviatoric stress tensor, J_2 is the second deviatoric stress invariant, and σ_1, σ_2 and σ_3 are the three principal stresses.

The default plasticity models used for calculations in ABAQUS are termed as Rate independent models which essentially imply that the yield stress depends only upon plastic strain and temperature values i.e. $\sigma_y = \sigma_y(\varepsilon^p, T)$.

However, in order to take into account the viscoplastic effects, the rate-dependent models may be incorporated, where in addition to plastic strain and temperature the yield strength also depends upon the strain rate such that $\sigma_y = \sigma_y(\varepsilon^p, \dot{\varepsilon}^p, T)$.

In Abaqus, the rate-dependent stress strain data can be provided in tabular form with yield stress values versus equivalent plastic strain at different equivalent plastic strain rates. Owing to this capability of Abaqus, the viscoplastic material parameters *K* and *n* are not required to be calculated separately.

5.5.1 Sources of Non-linearities

As mentioned earlier, a suction pressure of 1 bar is applied at the bottom surface of the plates through an aluminium suction table so as to avoid out-of-plane distortions during welding and cooling; yet the in-plane distortions due to expansion and contraction of the work-piece are not restricted which, in turn, give rise to friction at the interface of the test plate and the suction table. Moreover, the suction pressure may also reduce to certain extent due to the leakage at the fine rubber joint of the support and the plate. The sensitivity of mechanical simulation results is, therefore, studied with respect to the following:

- Various friction coefficient values with constant suction pressure.
- Various pressure values provided the friction coefficient is constant.

Contact analysis, however, introduces additional boundary nonlinearity into the model with material and geometric nonlinearity, thus gathering all three sources of nonlinearity into the mechanical part of simulations. It is observed from the large number of simulation runs that including this type of analysis significantly complicates the problem, extending the computation time up to two-three times. In addition, contact modelling introduces some model developing difficulties, such as over-constraining the model and preventing rigid body motion. An overconstraint occurs when a contact constraint on the displacements at a slave node conflicts with a prescribed boundary condition on that degree of freedom at the node.

The source of material nonlinearity lies in the included plastic behaviour of the work-piece material described above (Figs. 5.6, 5.7 and 5.8). In the thermal and the mechanical analyses all the material properties depend on the temperature introducing nonlinearity into the thermal and mechanical problem. The characterisation of thermo-mechanical properties is described in chapter 3 for the base material (AA 6056-T4). The filler wire material (4047) used during experimentation was different from the material of the specimens (6056-T4). During simulations, however, the filler wire material is assumed to be the same as that of base material. The effect of filler wire addition is realized by initially deactivating some of the elements (Figs. 5.3 and 5.4), which represent wire material, and then by activating them during cooling. The activation and deactivation of elements are achieved by integrating the change in material properties; where the thermo-mechanical material properties are kept negligibly small during heating, while they are switched to actual material properties during cooling. From practical point of view, when filler wire becomes part of solidifying weld bead only then it may affect the distortion and stress level; this is why the elements representing wire material activate during cooling only and contribute towards the final residual stress state.

If geometrically non-linear behaviour is expected (as in all the models included in this dissertation), the *STEP, NLGEOM option is used. Representing large-displacement effects by including the NLGEOM parameter is an alternative to a ‘small-displacement’ analysis. When NLGEOM is specified, most elements are formulated in the current configuration using current nodal positions. Elements, therefore, distort from their original shapes as the deformation increases. Omission of the NLGEOM parameter means that geometric non-linearity is ignored – the kinematic relationships are linearized. The elements are formulated in the reference (original) configuration, using original nodal co-ordinates.

5.5.2 Solving Non-linear Problem

ABAQUS combines incremental and iterative procedures for solving non-linear problems. This process involves:

- using Newton's method to solve the non-linear equations;
- determining convergence;
- defining loads as a function of time;
- choosing suitable time increments automatically.

In a non-linear analysis the solution can not be calculated by solving a single system of linear equations, as would be done in a linear problem. Instead, the solution is found by specifying the loading as a function of time and incrementing time to obtain the nonlinear response. Therefore, ABAQUS breaks the simulation into a number of time increments and finds the approximate equilibrium configuration at the end of each time increment. Using Newton's method, it often takes ABAQUS several iterations to determine an acceptable solution to each time increment.

The mechanical analyses are performed in three steps; where all the steps use automatic time incrementation. The step times of the first and second steps are equal to those used in heat transfer analyses. The loading and boundary conditions are applied in the first two steps, whereas in third step they are relaxed while maintaining the minimum boundary conditions to achieve convergence. The relaxation of loading and boundary condition is done to observe the residual stress and distortion state of the specimens. These steps are as follows:

- *Step 1*: meant to calculate the mechanical response during welding.
- *Step 2*: meant to calculate the mechanical response during cooling.
- *Step 3*: intended to calculate the residual stress and distortions after relaxation.

5.5.3 Initial, Loading and Boundary Conditions

Other than the pre-defined temperature field, a field variable is used to define the activation and deactivation of filler metal wire (test case 02 and 03). An initial condition for this field variable, implying deactivation, is defined such that the material properties are negligibly small at the beginning of the analysis. Activation is achieved using a Fortran subroutine UFIELD, which helps switching between various sets of material properties. Following type of mechanical loads and boundary conditions are used.

- Uniformly distributed pressure, p = 0.8 bar: applied on the bottom surface of the base plates to include the effect of suction force applied through the aluminium suction table;
- Gravity, g = 9.8 m.s^{-2}: used to include the effect of gravitational forces, acting on the welding details;
- Concentrated force, F = 50N: applied on both ends of stiffener to avoid its separation from base plate during welding (test case 03 only);
- Friction coefficient, μ = 0.57: due to the contact between the test specimens and aluminium suction table,
- Symmetric plane condition, Uy = 0: applied on the plane of symmetry along the weld axis for test specimens and support;
- Fixed nodes, Ux = Uz = 0: applied at a node of test specimens near the weld start end and on several nodes of support;
- Upper and lower clamps, Uz = 0: applied at nodes where the clamps come in contact with work-piece in order to hold it (test cases 01B and 02B only).

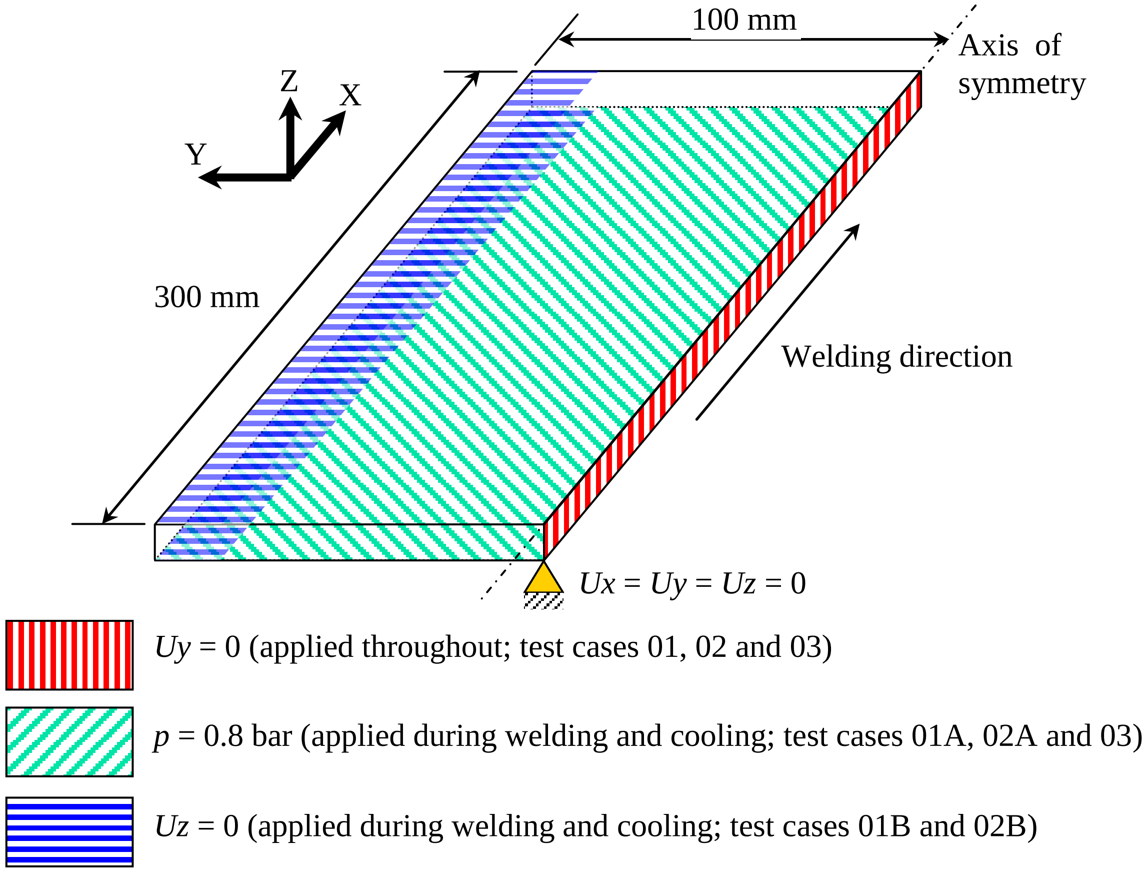

Figure 5.15. Mechanical loading and boundary conditions

Figure 5.15 presents the mechanical loading and boundary conditions used for different simulations. Symmetric plane condition ($Uy = 0$) is extended through the mid-plane of stiffener in case of T-joint welding (test case 03).

5.6 Simulation Results

Based on experimental database presented in chapter 4, FE models are validated by comparing the simulation and experimental results. The subsequent sections develop the comparative analysis for thermal and mechanical simulations for fusion zone geometry, thermocouple measurements, LVDT measurements and image correlation observations. The residual stress and strain states are finally predicted for various test cases.

5.6.1 Temperature Fields

The temperature distribution at various time instances of heating and cooling cycle for test cases 01A, 02A and 03 are shown in Figs. 5.16, 5.17 and 5.18, respectively. The contours in through-thickness and transverse directions are also presented. The fusion zone is shown as grey-coloured region throughout.

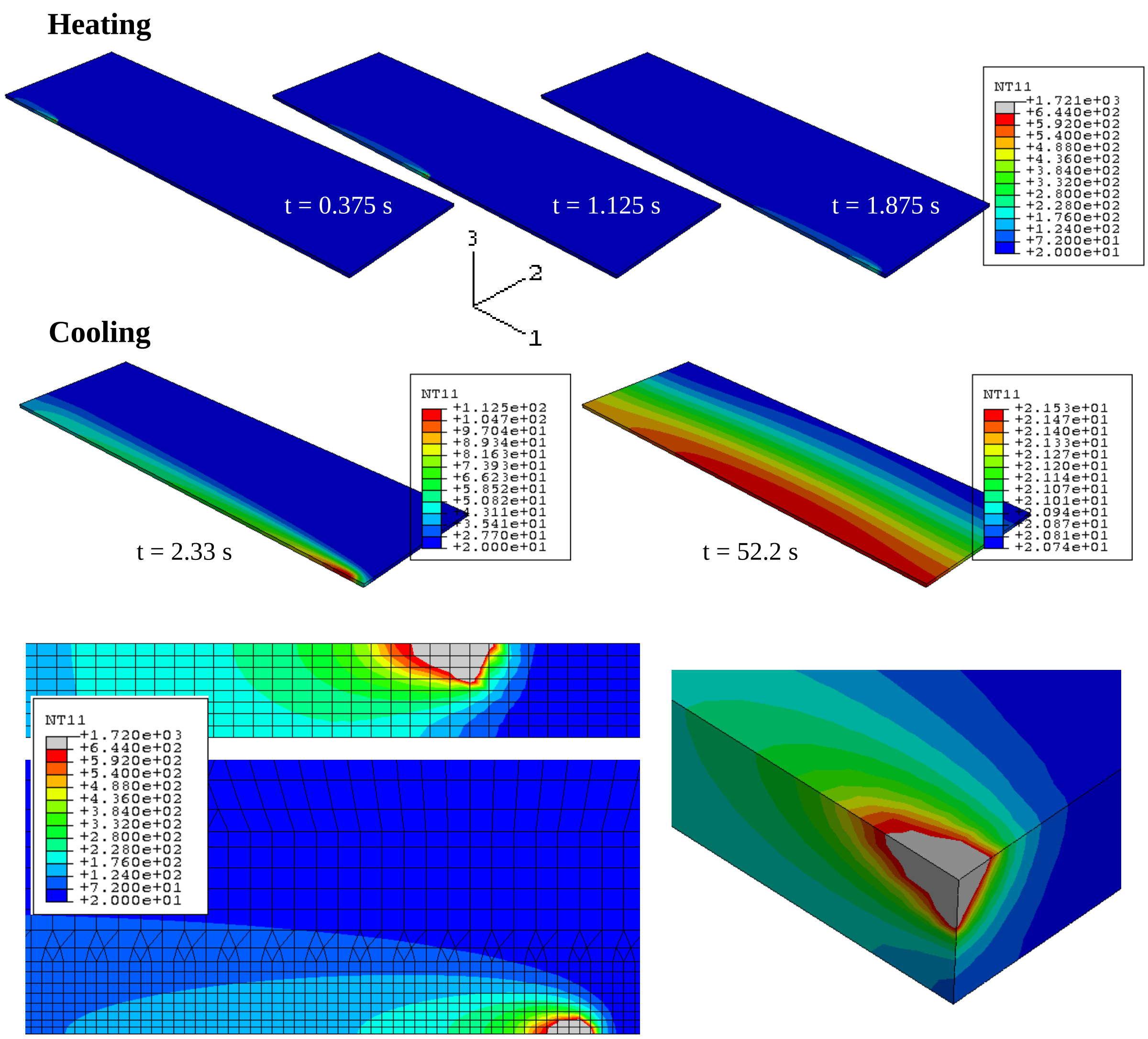

Figure 5.16. Temperature contours – Test Case 01A

Figure 5.16 demonstrates the thermal fields for test case 01A. A very fine discretization of mesh is used in and near the FZ; where, in FZ, 2 to 3 elements are present in the transverse direction, 3 to 4 elements are in the through-thickness direction and 4 to 5 elements are in the longitudinal direction. The depth of the FZ is maximum at the location of keyhole formation which is actually obtained by the conical part of the heat source; however, the molten metal that follows does not reach the fullest depth of keyhole. This is interesting from practical point of view where the penetration of the following liquid metal is seldom as deep as the keyhole. Owing to the very high speed of welding and high thermal conductivity values, the heat dissipation within the test plate is quite rapid. It is for these reasons that the temperature contours during the heating stage confine to a rather small region. Figure 5.16 also depicts fast cooling of the plate, as the temperature of the whole model drops down to 21°C in a time period of 50 s only.

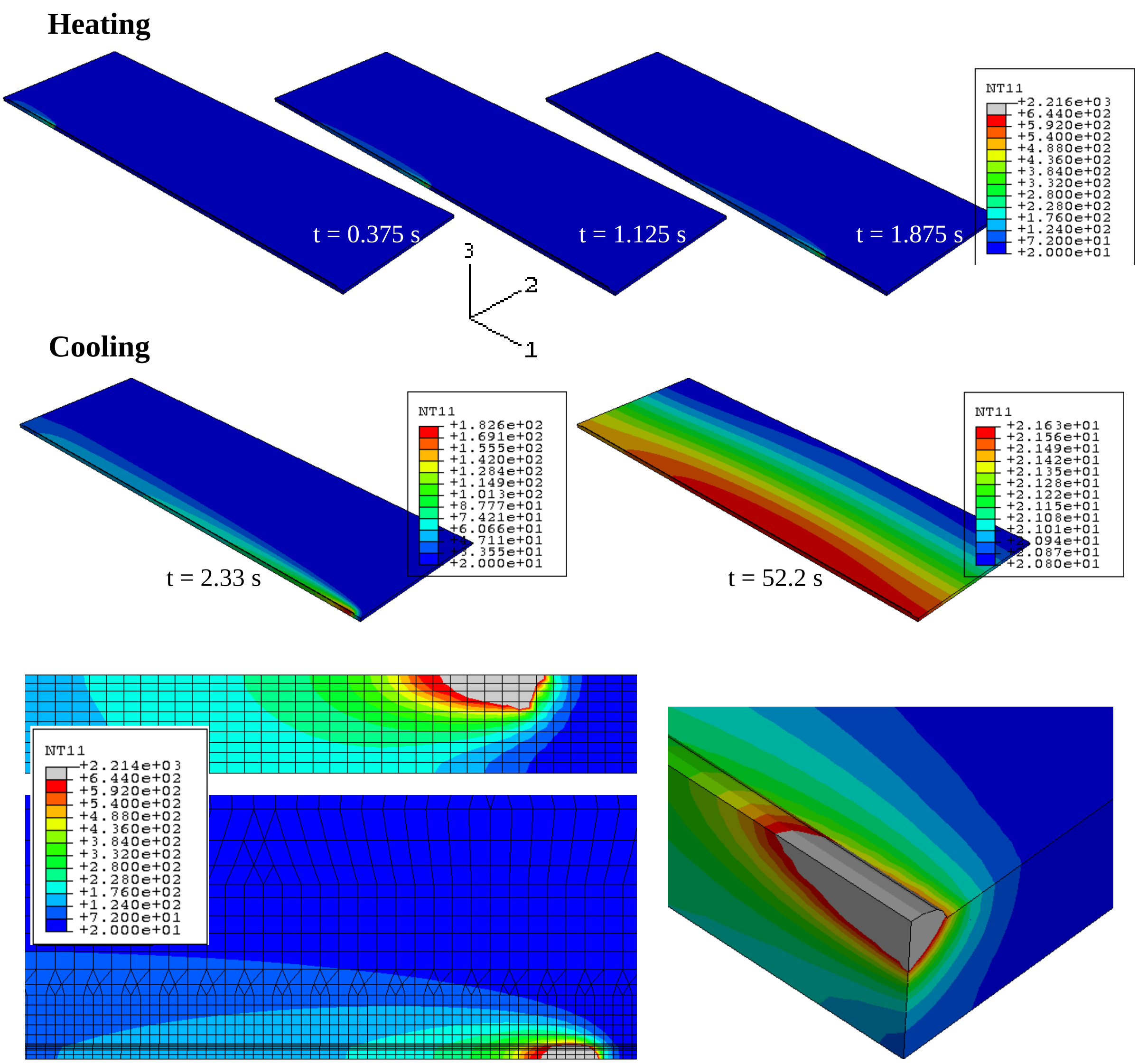

Figure 5.17. Temperature contours – Test Case 02A

Figure 5.17 shows temperature contours of test plate for test case 02A. Unlike the test case 01A, the FZ is more elongated in the welding direction (comprising over 5 to 6 elements); whereas the depth and width of FZ remain almost identical to those of 01A. However, a large fraction of the FZ includes elements used for filler material, which, in turn, reduces the actual amount of heat energy transmitted to the test plate.

Figure 5.18 presents temperature distribution in T-joint model for test case 03. Since the amount of heat input in this case is comparatively more than 01A and 02A, the high temperature contours are wider than other test cases. The FZ, here, penetrates the complete thickness of stiffener, while the cooling of the whole model takes over 100 s to reach a temperature of 27°C. The temperature contours in the support are also shown where the temperature at the end of cooling reaches 22°C.

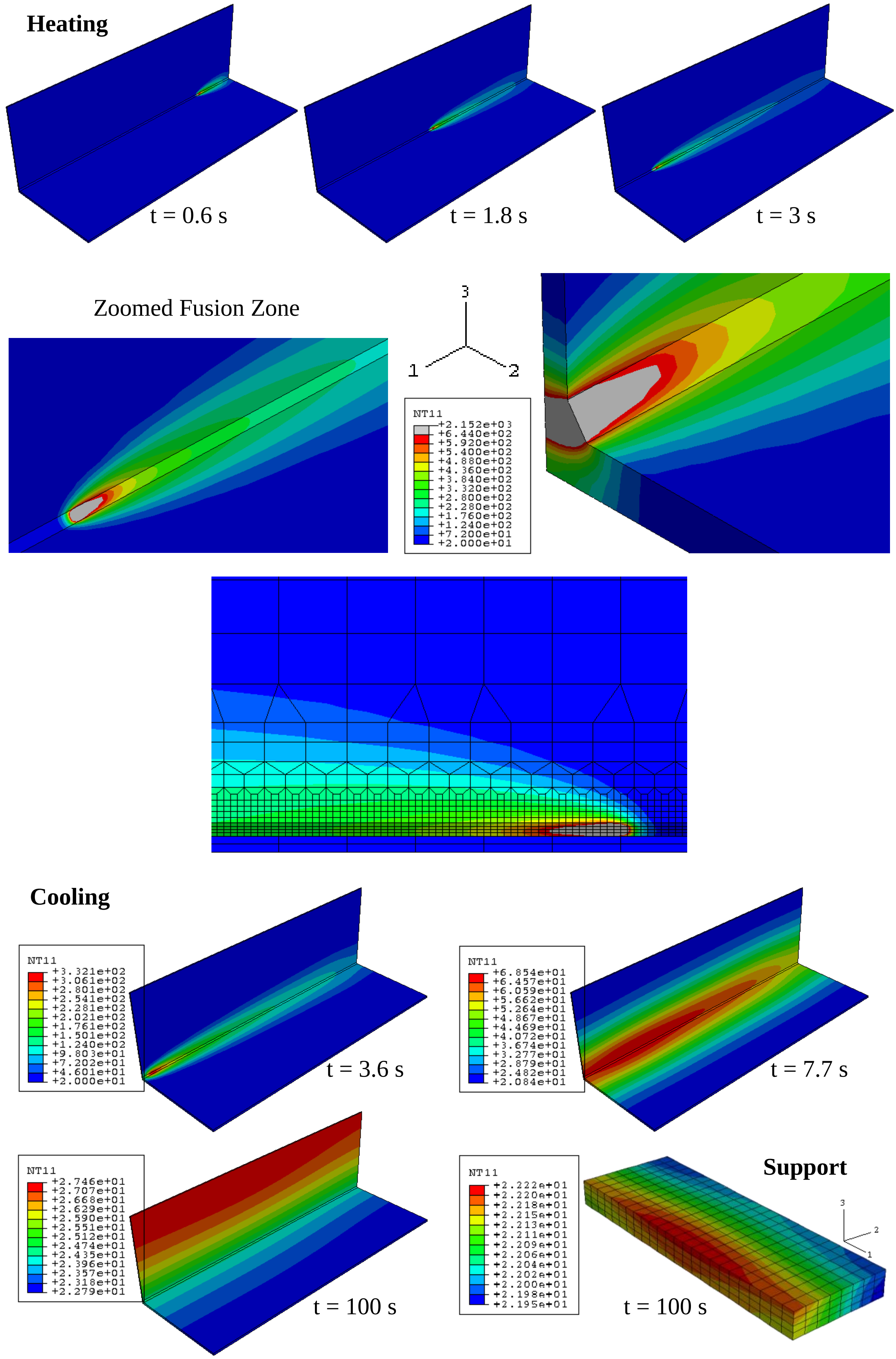

Figure 5.18. Temperature contours – Test Case 03

5.6.2 Fusion Zone Geometry

The weld fusion zone geometry for test case 01A, 02A and 03 are shown in Figs. 5.19, 5.20 and 5.21, respectively. The simulated and experimental FZ are juxtaposed as well as quantified graphically in the figures. Since the test cases 01B and 02B differ from 01A and 02A, respectively, with reference to thermal boundary conditions only; the fusion zone geometry does not change considerably and hence are not presented here. Although width and penetration of all the test cases are found in good agreement with simulated FZ geometry; yet the graphical representation shows some differences while tracking the fusion boundary.

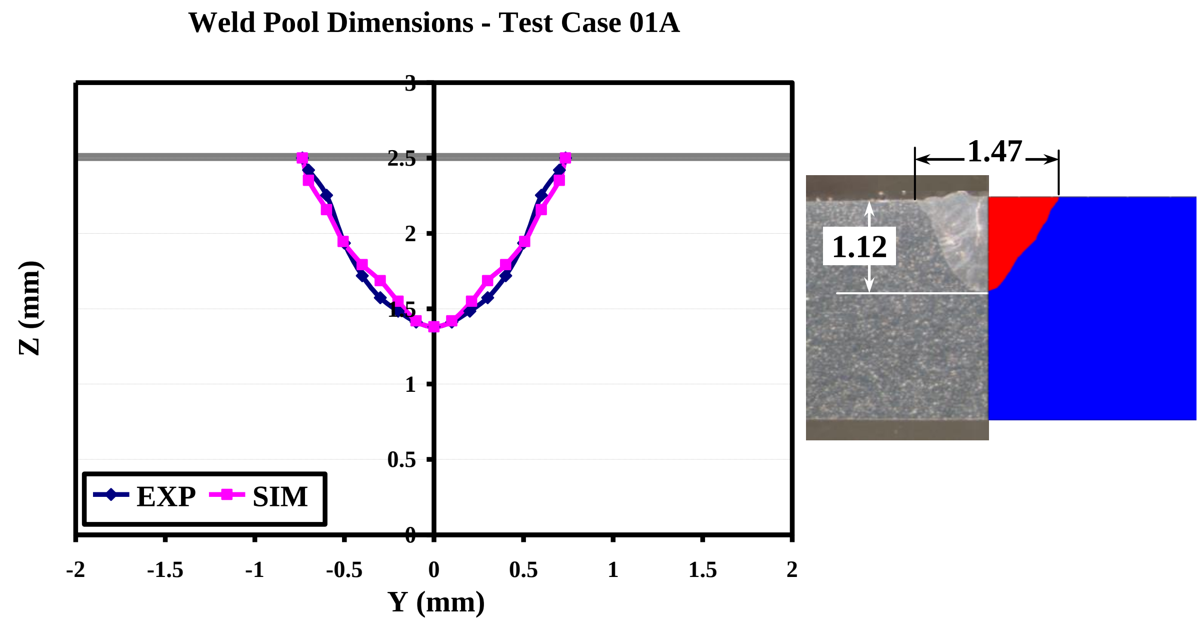

Figure 5.19. Comparison of fusion zone geometry – Test Case 01A

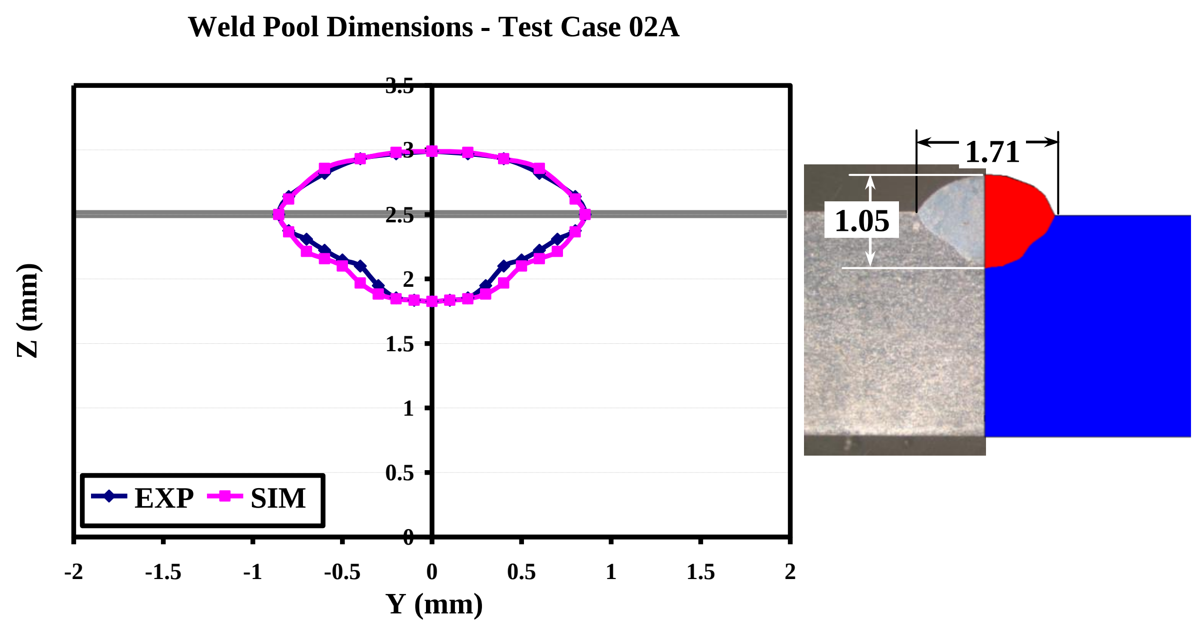

Figure 5.20. Comparison of fusion zone geometry – Test Case 02A

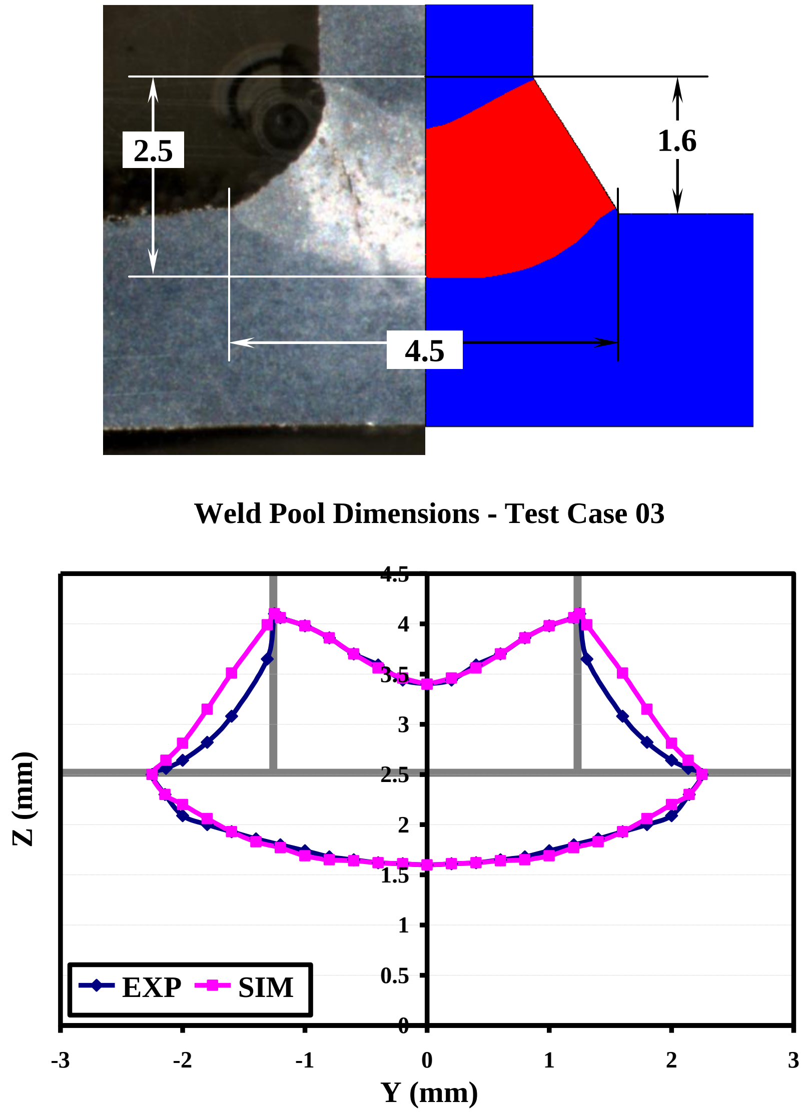

Figure 5.21. Comparison of fusion zone geometry – Test Case 03

The micrograph of T-joint shows slight depression of FZ; which is ignored in case of simulation. The remaining FZ boundary within the base plate and stiffener is, however, in good accordance with the experimental one.

5.6.3 Thermal Histories

The thermal histories recorded on thermocouple positions (Figs. 4.6 and 4.7) are compared with numerically calculated ones in Figs. 5.22 to 5.32 for various test cases. The time-temperature curves presented in these figures help establishing the accuracy of heating rates, peak temperatures and cooling rates at various distances from the FZ. The heating rates and peak temperatures are the functions of heat input per unit time and thermal properties; while cooling rates largely depend upon the thermal boundary conditions.

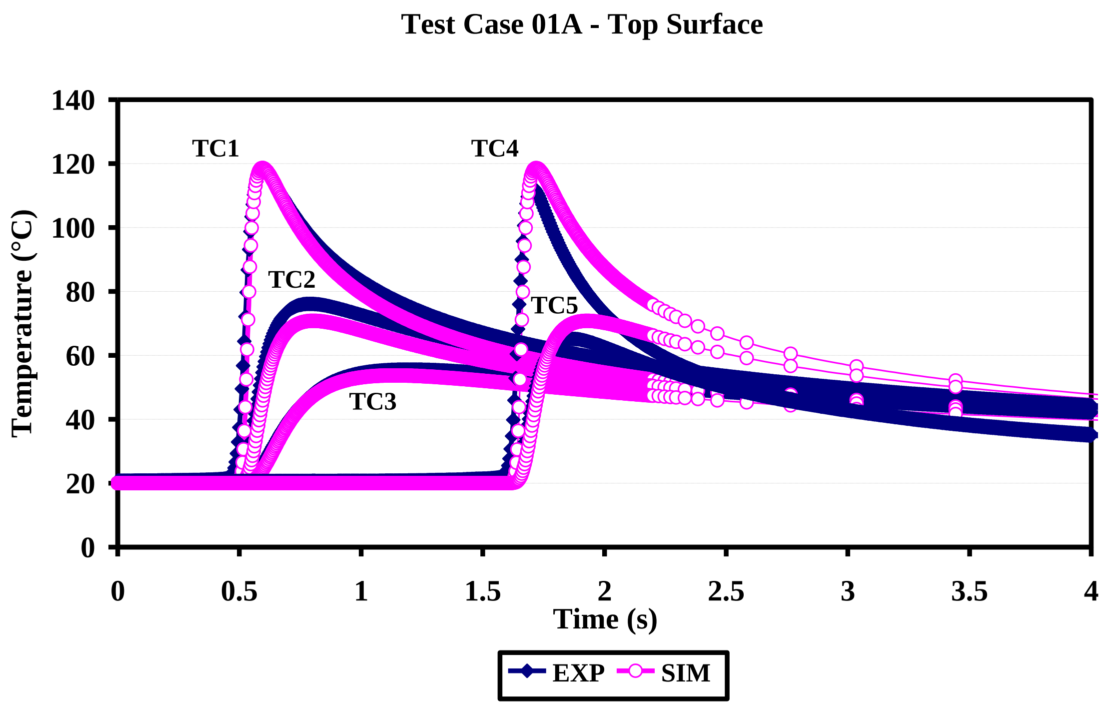

Figure 5.22. Thermal histories comparison – Test Case 01A (top surface)

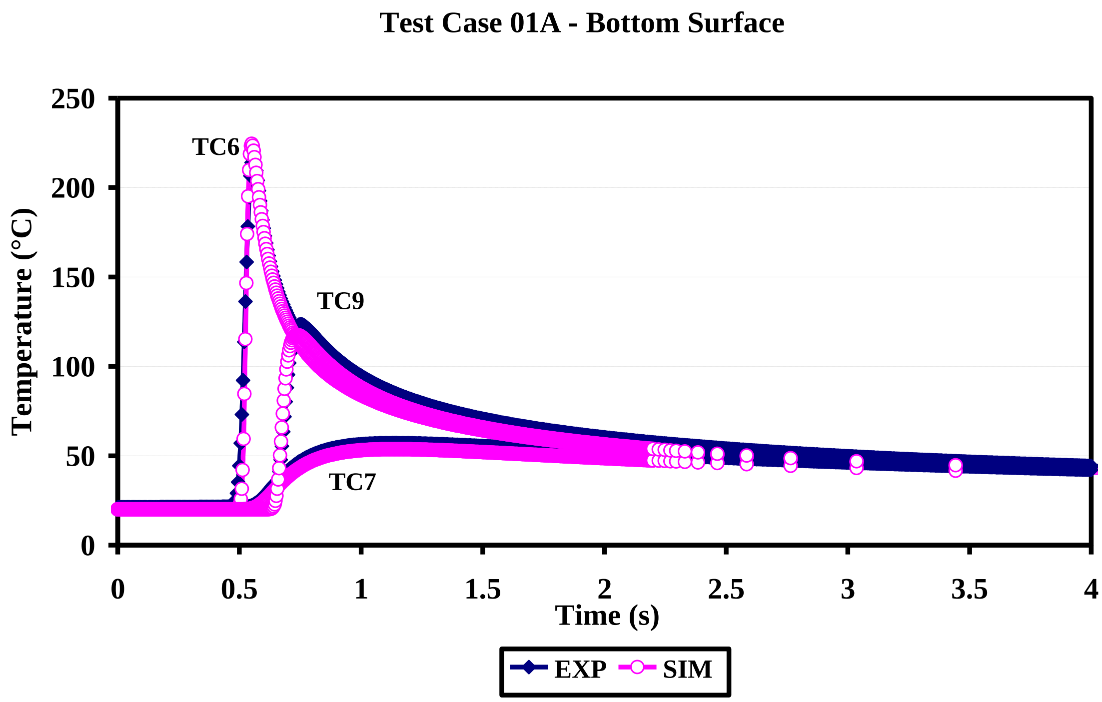

Figure 5.23. Thermal histories comparison – Test Case 01A (bottom surface)

Figures 5.22 and 5.23 present the time-temperature curves for test case 01A. The heating rate, peak temperature and cooling rate for most of the thermocouple positions is well captured. The difference for peak temperature value at TC2 may, however, result from inaccurate positioning of thermocouple. The cooling part of the experimental curve at TC4 and TC5 indicate a rather fast decrease in temperature than simulated curves; the difference may be attributed to the constant value of thermal contact resistance used between plate and support for FE simulation. Figures 5.24 and 5.25 illustrate the time-temperature curves for test case 01B. The simulated curves seem to capture the experimental results satisfactorily.

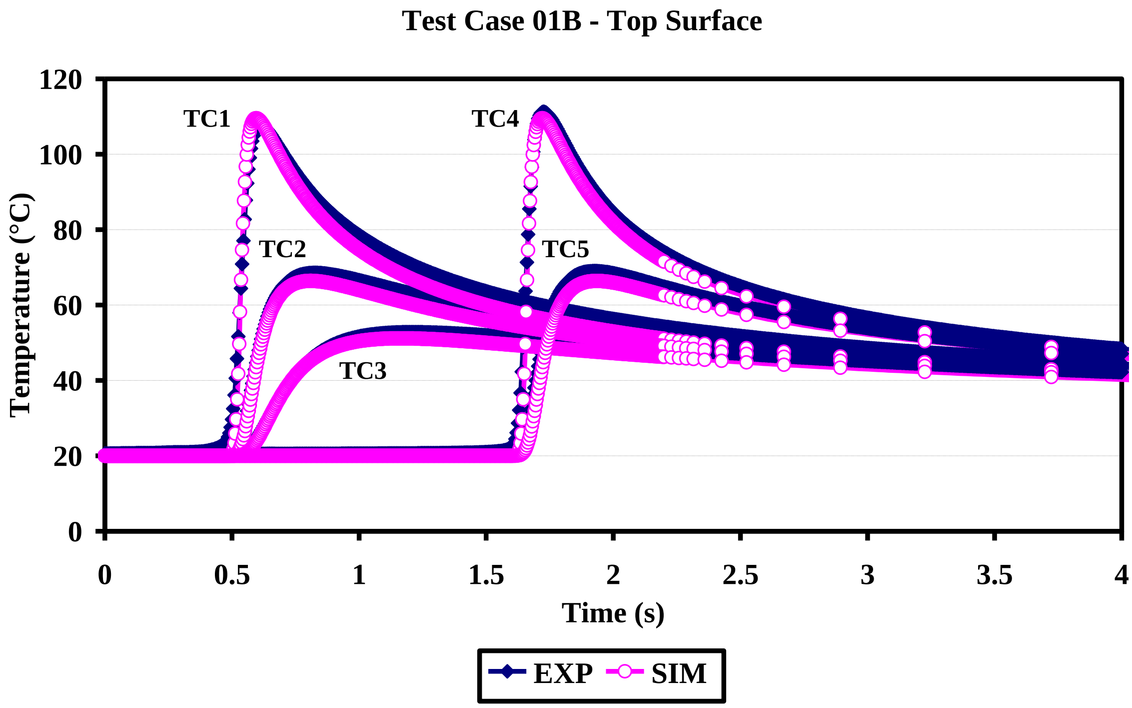

Figure 5.24. Thermal histories comparison – Test Case 01B (top surface)

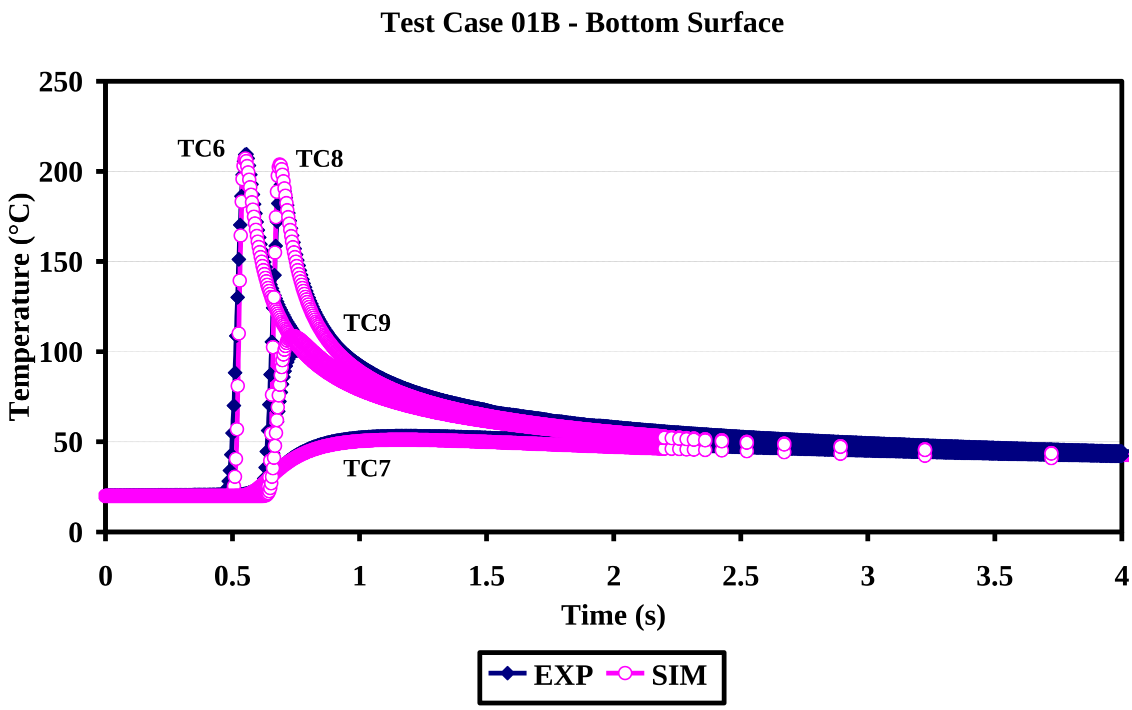

Figure 5.25. Thermal histories comparison – Test Case 01B (bottom surface)

Figures 5.26 and 5.27 present the time-temperature curves for test case 02A on the top and bottom surfaces, respectively. The heating rates and peak temperatures at various thermocouple positions lie in close approximation to each other; however, little differences are observed once again for the cooling parts of the curves due to the constant value of thermal conductance between the plate and support.

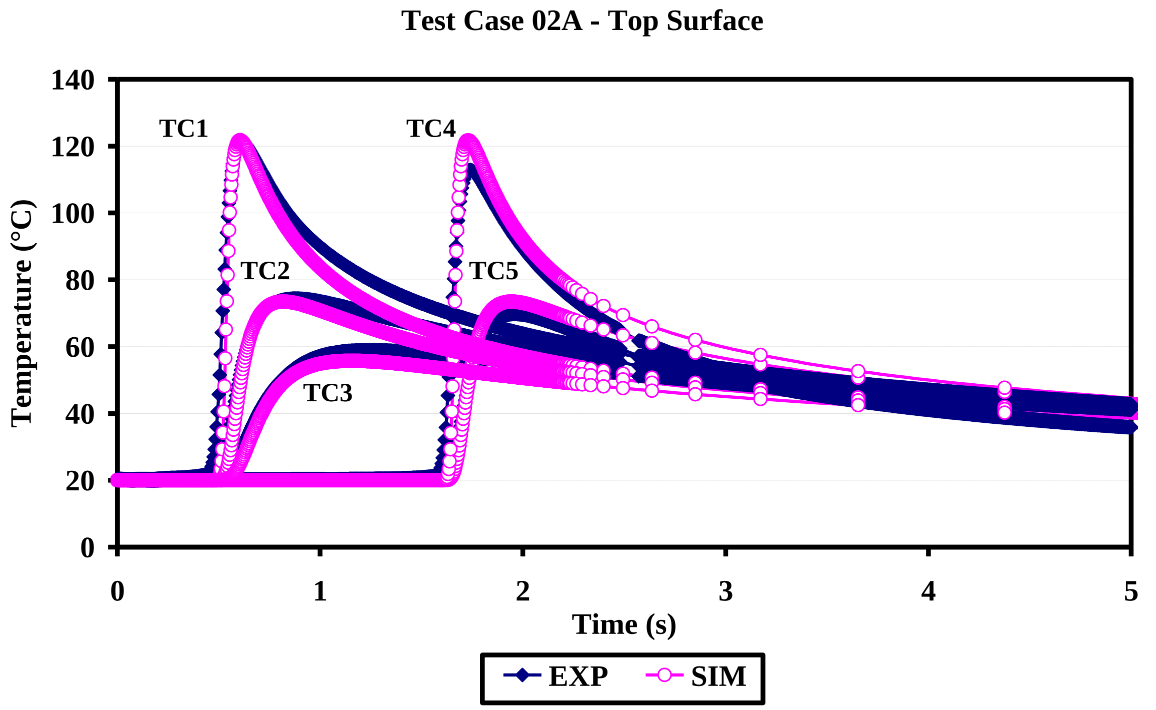

Figure 5.26. Thermal histories comparison – Test Case 02A (top surface)

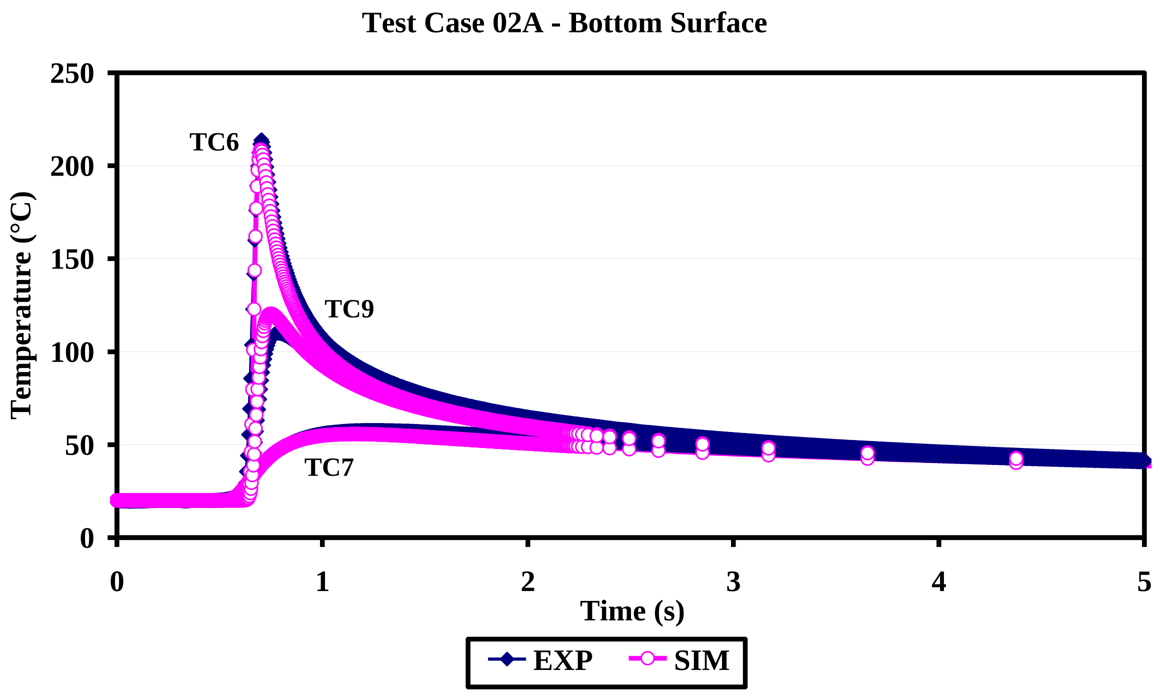

Figure 5.27. Thermal histories comparison – Test Case 02A (bottom surface)

Figures 5.28 and 5.29 show time-temperature curves for test case 02B. The simulated curves close to the weld stop end (TC4 and TC5) present slow cooling rate. The probable reason for this difference is the use of convective heat transfer coefficient independent of temperature; however, in most of the welding problems convection coefficient is temperature dependent.

Test Case 02B - Top Surface

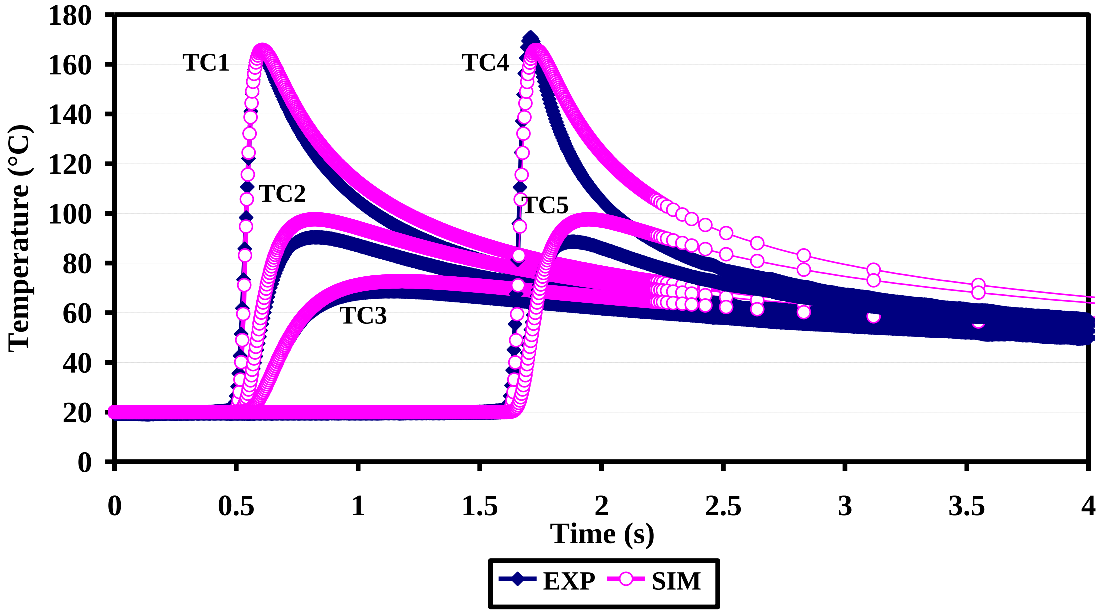

Figure 5.28. Thermal histories comparison – Test Case 02B (top surface)

Test Case 02B - Bottom Surface

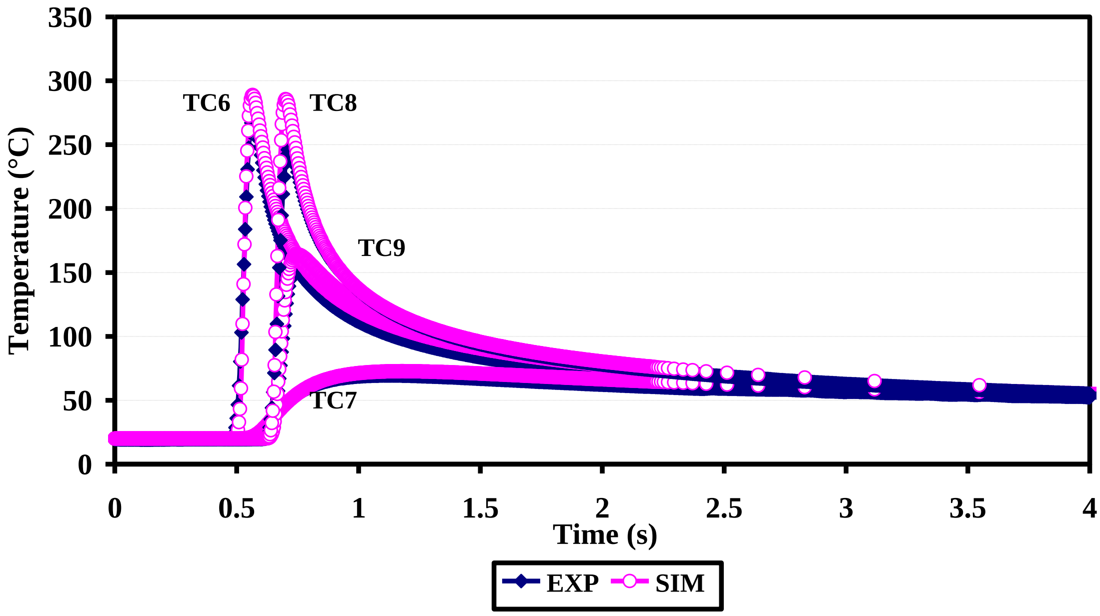

Figure 5.29. Thermal histories comparison – Test Case 02B (bottom surface)

Figures 5.30 and 5.31 demonstrate the comparison of time-temperature curves for the thermocouples on the top and bottom surfaces of base plate, respectively; while Fig. 5.32 shows curves for thermocouples installed upon stiffener. The experimentally recorded heating rate, peak temperature and cooling rates are all found in good accordance with the simulated results (see Annex B for peak temperatures comparison).

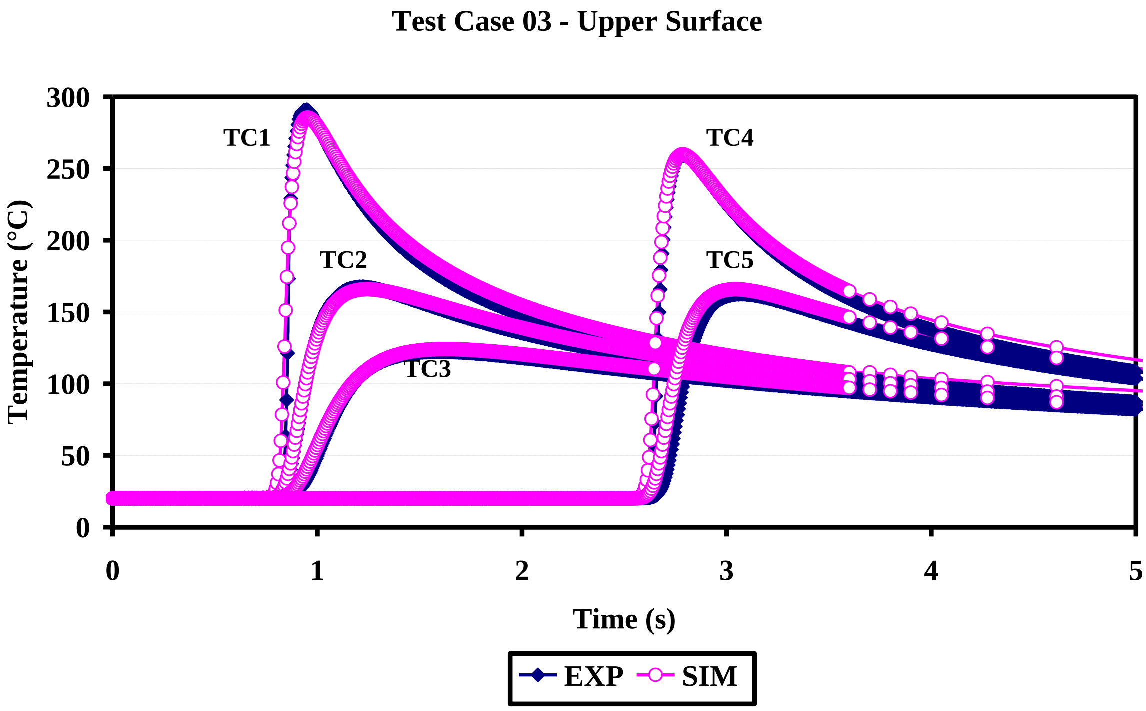

Figure 5.30. Thermal histories comparison – Test Case 03 (top surface)

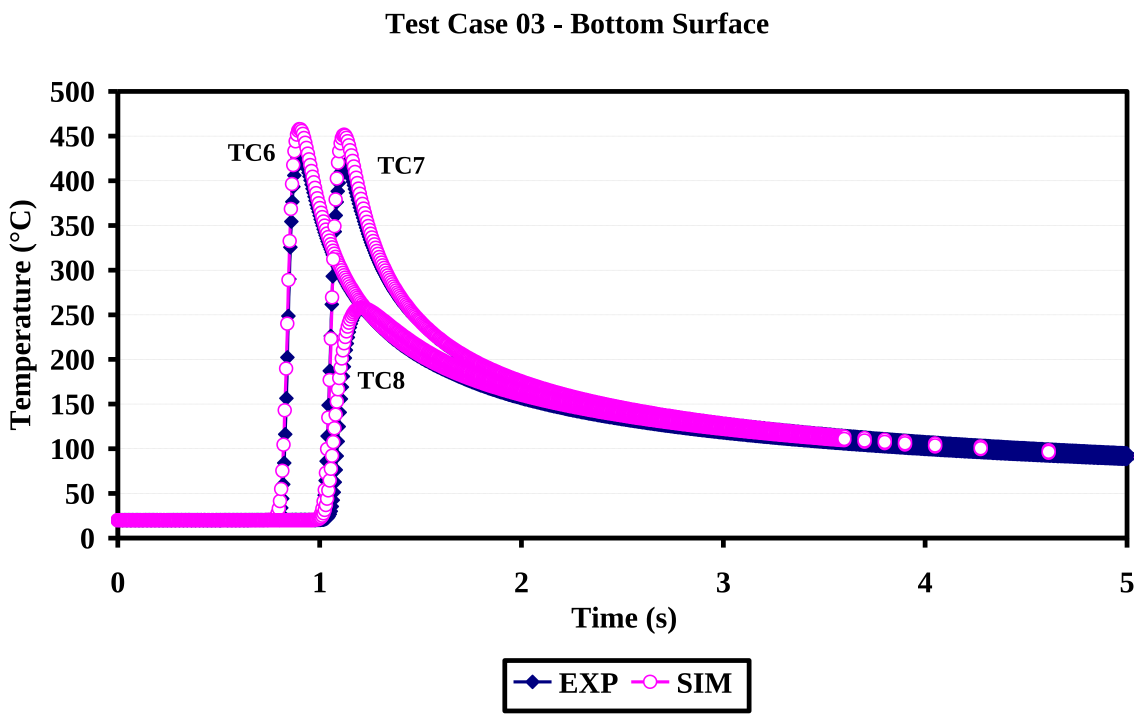

Figure 5.31. Thermal histories comparison – Test Case 03 (bottom surface)

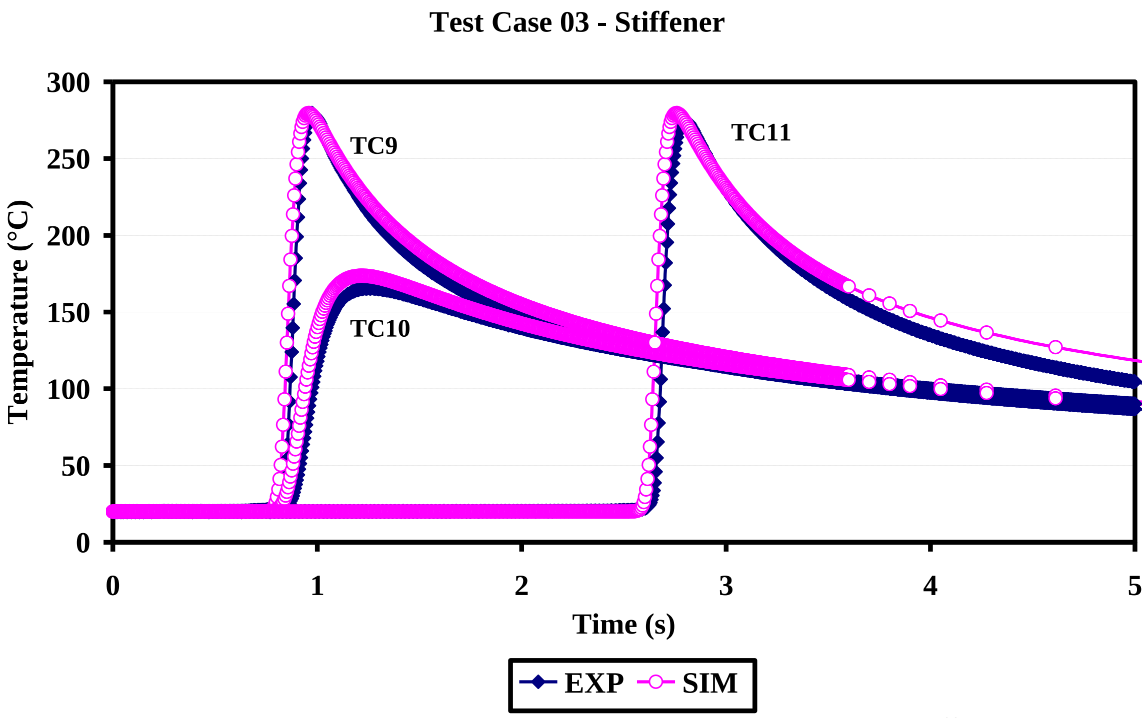

Figure 5.32. Thermal histories comparison – Test Case 03 (stiffener)

With respect to TC locations (Fig. 4.7), the peak temperature of TC1 and TC4 should necessarily be identical. It was, however, mentioned in chapter 4 that TC1 was located 0.5 mm closer to weld center line than TC4. This observation is taken care of during simulation.

5.6.4 In-plane Displacements at LVDT Positions

The experimental and simulated in-plane displacements at LVDT positions (Figs. 4.6 and 4.7) are presented as a function of time in Figs. 5.33, 5.34 and 5.35 for test cases 01A, 02A and 03, respectively. The LVDT sets have already been defined in chapter 4. Set A (LVDT1+2) and Set B (LVDT3+4) give the averaged in-plane displacements and are appropriate for comparison with simulated results of a symmetric model. Averaged values also help minimising the possiblility of error due to slippage in the direction transverse to welding. However, the slippage in the direction of welding causes difficulties in locating the updated position of LVDTs. This is because the LVDTs are fixed on the support and when the test specimen slides in the direction of welding, the Set A tends to measure the displacements close to the edge of base plate while the Set B records the displacements more towards the mid of the plate. This is the reason for the difference amongst the peak displacement values observed for both the sets.

Figures 5.33 and 5.34 illustrate that the simulated displacements follow the evolution pattern identical to LVDT measurements during heating. However, during cooling the simulated curves depart from experimental ones for both the test cases. The probable reason for the deviation of simulated values from the experimental results is the localised out-of-plane and rotational distortions in and near the FZ during solidification shrinkage. Since these localised distortions are largely restricted in T-joint model due to the stiffener, Fig. 5.35 demonstrates a rather satisfactory displacement evolution during cooling. However, peak displacement value of Set B is largely restricted at the same time.

Test Case 01A - Exp vs Sim

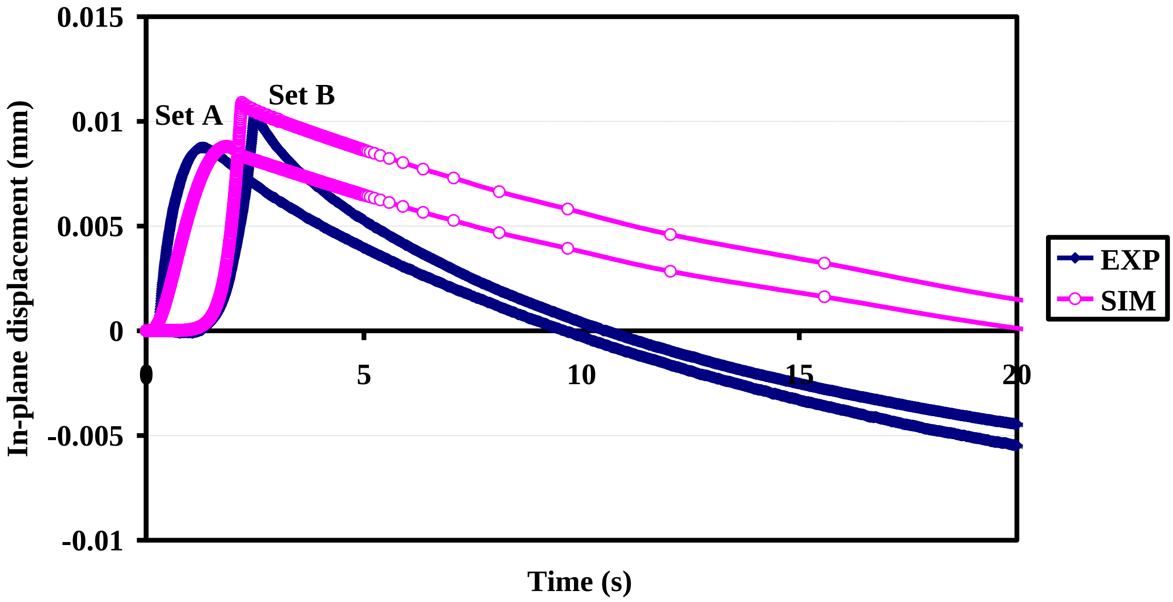

Figure 5.33. In-plane displacements at LVDT positions – Test Case 01A

Test Case 02A - Exp vs Sim

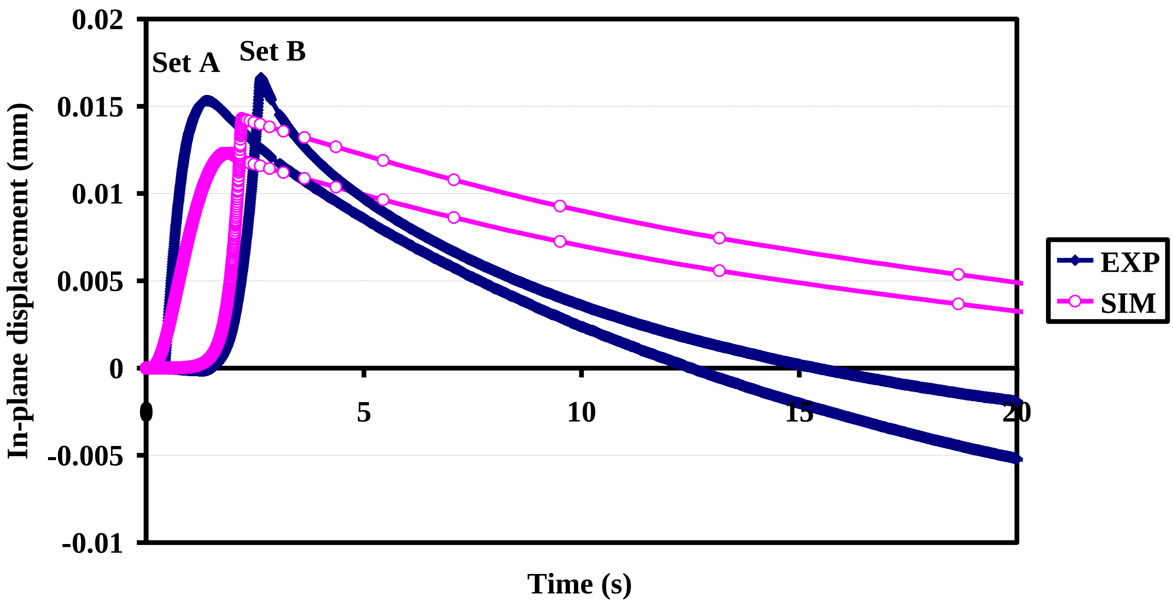

Figure 5.34. In-plane displacements at LVDT positions – Test Case 02A

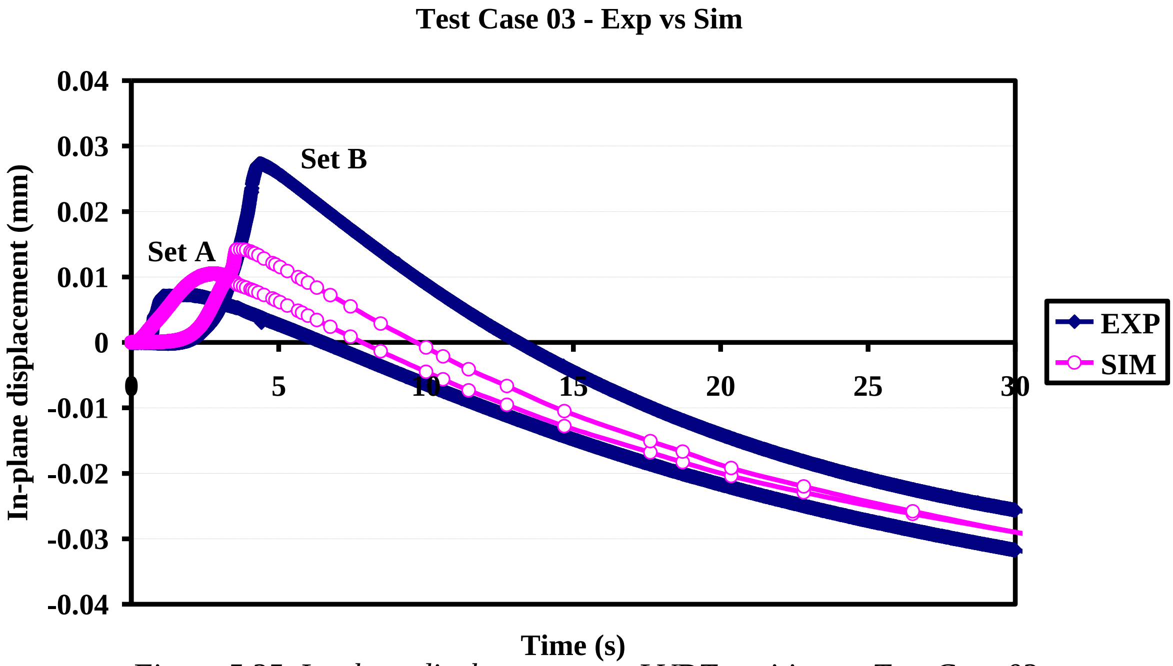

Figure 5.35. In-plane displacements at LVDT positions – Test Case 03

5.6.5 Residual Out-of-plane Displacements

The out-of-plane distortions are induced due to non-uniform heating and cooling during welding. These deformations, also known as angular deformations, result due to the existence of temperature gradient in the through-thickness direction.

The residual out-of-plane displacements are critical to welded components; since they not only distort the structures but also introduce severe problems during assembly process. However, the correct arrangement of the pre-fabrication and welding procedures (selection of appropriate welding parameters, use of clamping devices and fixtures etc.) may help preventing unwanted deformations. Such dimensional inaccuracies also necessitate the weld post-treatments (post-heating, shot peening etc.).

These problems highlight the importance of out-of-plane displacement development modelling on the design and manufacturing stages. It is important for the estimation of the reliability of structure, and development of suitable methods for improving the dimensional accuracy of the welded structure.

5.6.5.1 Evolution of Out-of-plane Displacements

Figures 5.36, 5.37 and 5.38 illustrate evolution of out-of-plane displacements for test cases 01A, 02A and 03, respectively, during the complete heating, cooling and relaxation cycle. The images are shown at a deformation scale factor of 100 along z-axis.

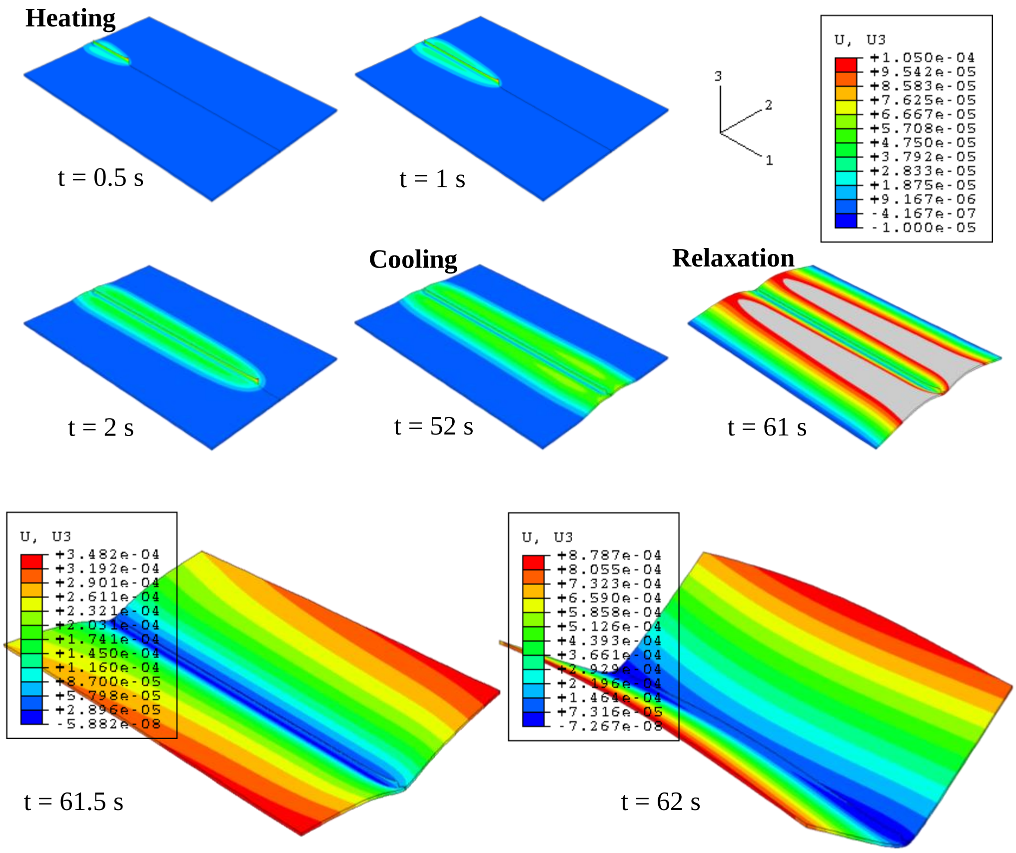

Figure 5.36. Out-of-plane displacement evolution – Test Case 01A

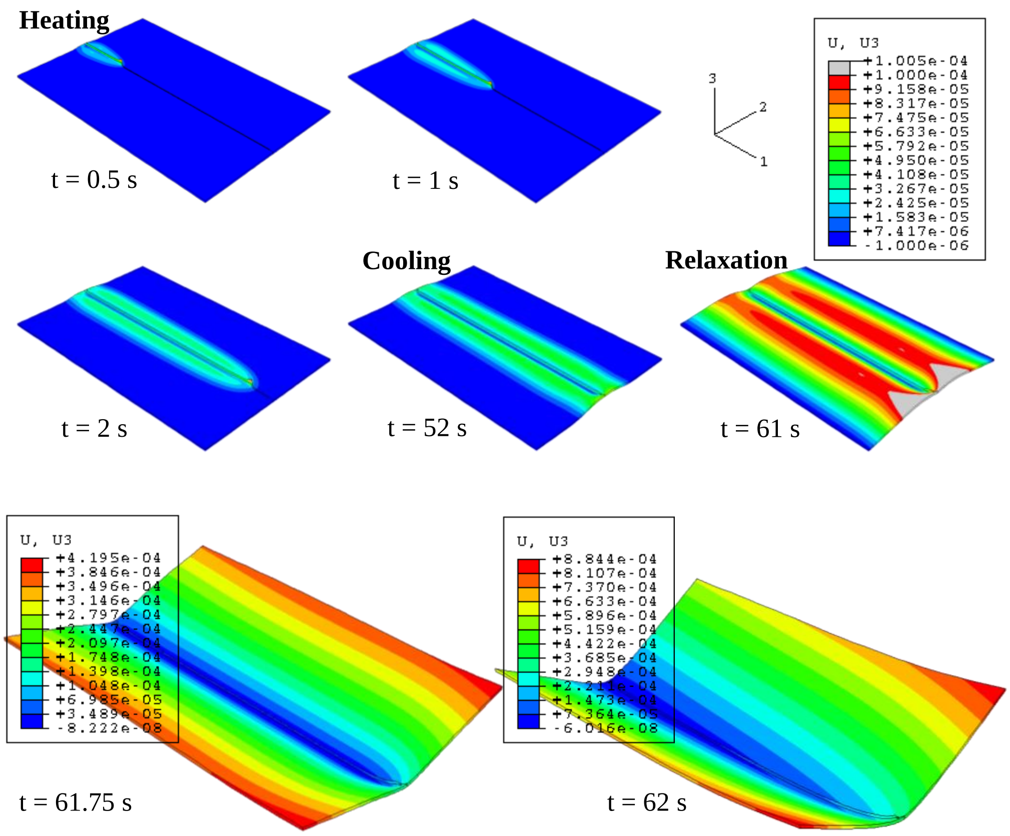

Figure 5.37. Out-of-plane displacement evolution – Test Case 02A

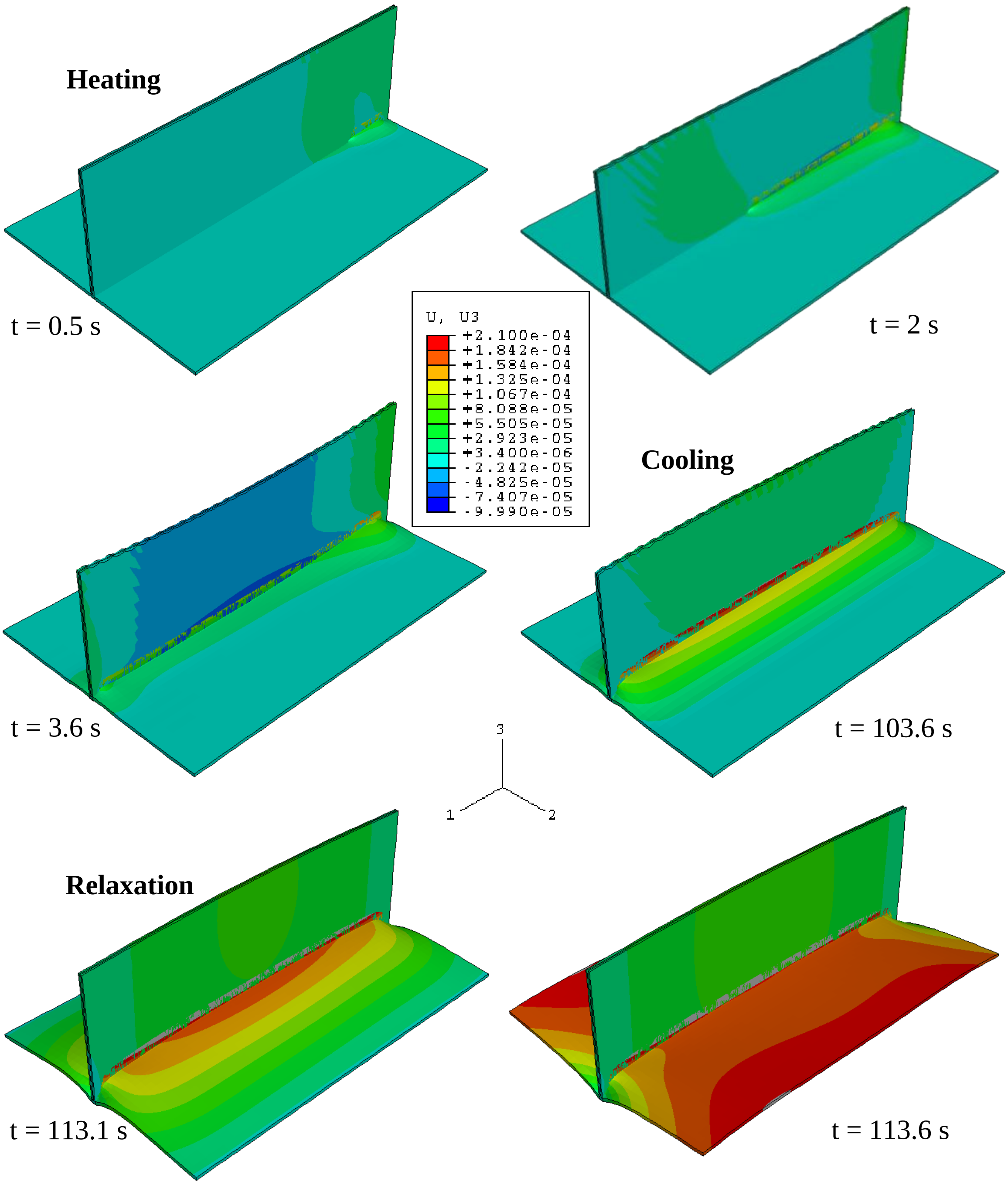

Figure 5.38. Out-of-plane displacement evolution – Test Case 03

The displacement evolution pattern shows that due to the application of pressure on the bottom surface, the test plates and T-joint deform in and near the FZ during heating and cooling. However, the far edges of the base plates deform only after the removal of pressure i.e. after relaxation. The final deformation levels result due to the release of elastic stresses. It may be observed that the out-of-plane displacements are maximum towards the mid of the plates and minimum at the edges. Test case 02A apparently shows maximum displacements at one of the edge; however, adjusting weld line at zero level reaffirms the observation of maximum displacement towards the mid of the plate. The bending distortion of the T-joint appears to be different from that of test plate (Fig. 5.38). Unlike the stiffener and base plate assembly, the test plates are free to deform in out-of-plane direction and, hence, a rather regular distortion pattern is observed. However, the stiffener part of the T-joint assembly restricts the local out-of-plane displacements occurring due to expansion and contraction of the FZ and HAZ. The combined effect of material softening in FZ and stiffener positioning deforms the base plate greatly in the vicinity of FZ; while the remaining parts of the base plate (test case 03) deform less as compared to the test plates (test cases 01 and 02).

5.6.5.2 Effect of Friction Coefficients

As already mentioned, a suction pressure of 1 bar is applied at the bottom surface of the test plate through an aluminium suction table to avoid out-of-plane distortions during welding and cooling; yet the expansion and contraction of the test plates and T-joint give rise to friction at the interface of the plate and the suction table. Effect of various friction coefficient values on the out-of-plane displacements while keeping the suction pressure constant for test case 01A is being presented in this section.

From literary sources [BEAR], the value of the friction coefficient between two aluminium surfaces could be approximated to 0.57 when one of the surfaces is moving while the other is static. To observe the effect of various coefficient values, a separate simulation was run while keeping the pressure value equals to 1 bar. The following values were used:

- Friction coefficient, μ = 0.4, 0.57, 0.8 and 1.0

Simulation results are compiled and compared with the experimental ones for out-of-plane displacements and are shown in Fig. 5.39. Owing to the symmetry of the test plate, only the results on the right half of test plate are shown. Moreover, all the displacements are set to zero at a distance of 5 mm from the center of the test plate. This is because the experimental results for displacement measures are not available in the FZ and HAZ.

It can be observed from Fig. 5.39 that in spite of using different friction coefficients, the simulation results for out-of-plane displacements are least affected. The probable reason for this observation is that the mean contact pressure – of the order of 1 bar i.e. 0.1 MPa – and the surface shear stress during heating and cooling are too less to cause any significant effect over the final distortion level. The choice for an appropriate value of the friction coefficient is, therefore, made as 0.57 [BEAR].

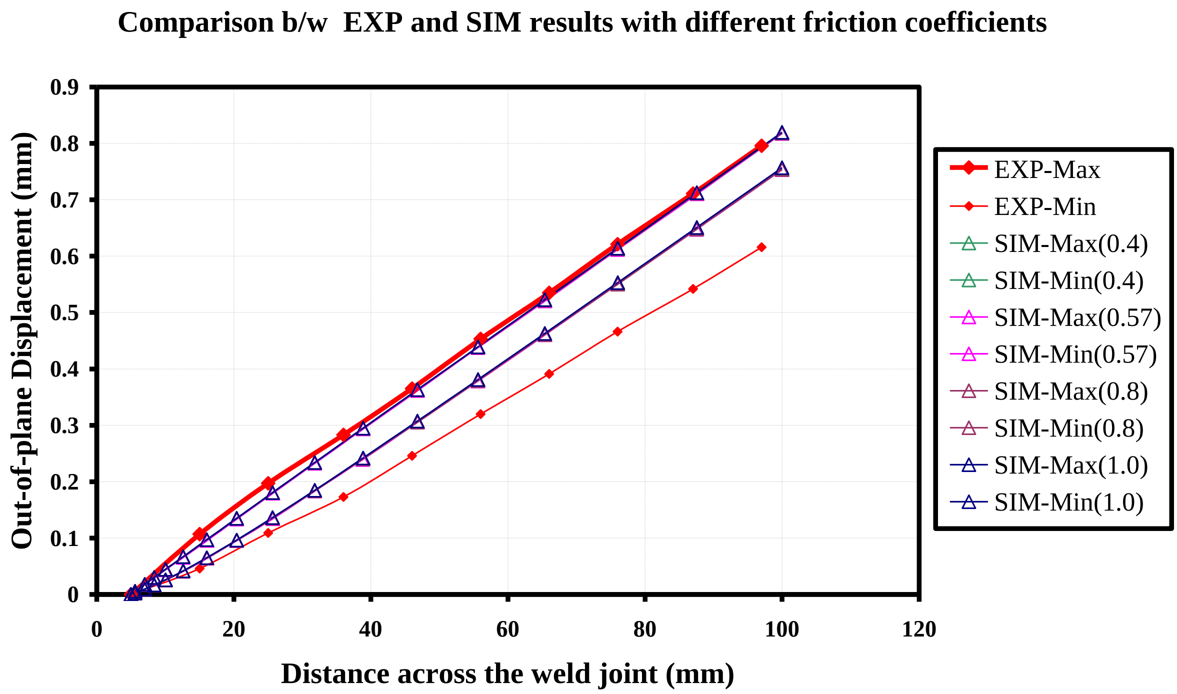

Figure 5.39. Out-of-plane displacement with various friction coefficients – Test Case 01A

5.6.5.3 Effect of Suction Pressure

Having established the friction coefficient value of 0.57, the effect of various suction pressures is investigated. The possibility of leakage at the rubber joint between the test plate and the suction table implies that the overall pressure present at the bottom surface of the test plate is less than 1 bar. Simulations are, therefore, performed for the following pressure values to include the leakage effect:

- Pressure, p = 1 bar, 0.8 bar, 0.6 bar and 0.4 bar

Comparison of all these simulations and experimental result for test case 01A is presented in Fig. 5.40. It is found that despite the large variations in pressure values, the effect over the out-of-plane displacement values is less. Nevertheless, this effect is quite systematic; the lesser the pressure, the larger the displacement. It can also be observed that the experimental results lie somewhere in between the simulation results at 1 bar and 0.8 bar. This means that in spite of leakage at the rubber joint the effective pressure value is more than 80% of the applied pressure.

These observations, however, are only valid with respect to the maximum out-of-plane displacement values. The minimum out-of-plane displacement values recorded experimentally are somewhat different from those calculated numerically. The probable reason for this difference is that the simulation assumes uniform distribution of pressure upon the entire bottom surface; however, the complex grooved and drilled shape of suction table essentially applies non-uniform pressure.

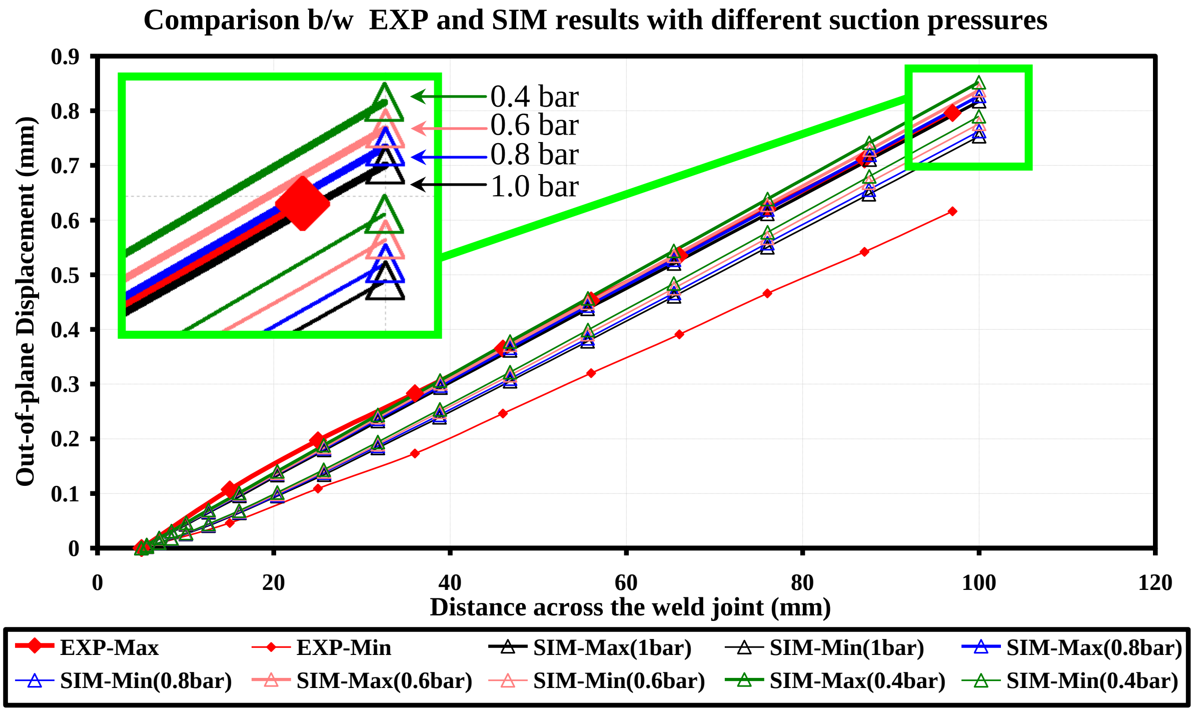

Figure 5.40. Out-of-plane displacement with various suction pressures – Test Case 01A

5.6.5.4 Effect of Initial Surface Profiles

As already discussed in the previous chapter, the initial surface profiles play an important role in defining the distortion pattern of the test plates. In order to observe the effect of initial geometric imperfections, simulations are performed with an initial curvature in plate geometry. Following two cases are studied:

- ➢ Convex model, where the test plate when placed on the support maintains a curvature of 1 mm at the center while touches the support at the edges.
- ➢ Concave model, where the test plate when placed on the support maintains a curvature of 1 mm at the edges while touches the support at the center.

Figure 5.41 shows the residual out-of-plane displacement contours for both the convex (CVX) and concave (CCV) models and also presents the graphical comparison for maximum displacement with the simulated results of a straight (STR) plate model and the experimental results.

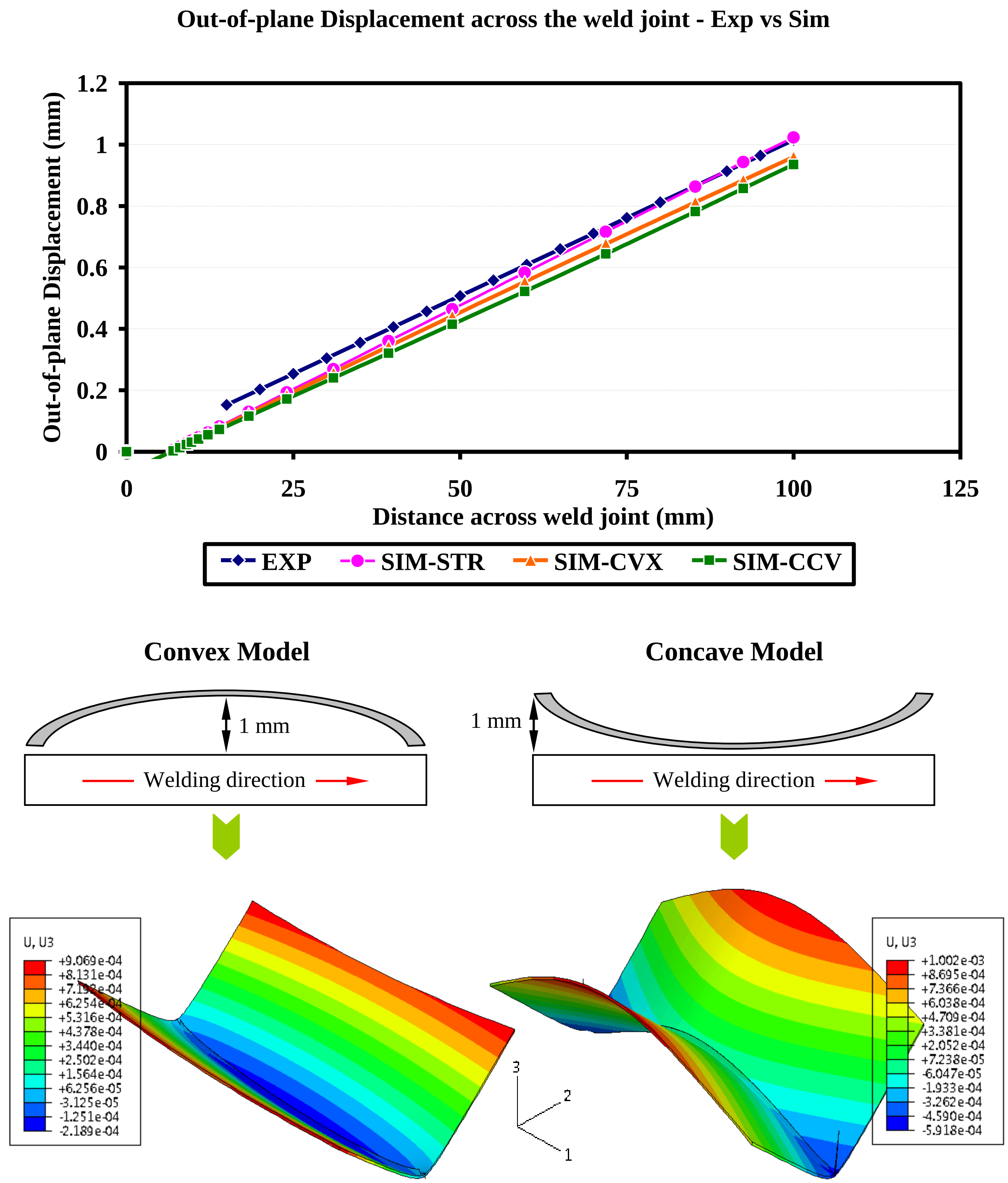

Figure 5.41. Out-of-plane displacement with different initial surface profiles – Test Case 01A

It may be noticed that the initial surface profiles not only affect the maximum displacement level but they also influence the distribution pattern of deformation, thereby giving rise to different distorted shapes of the test plates. However, as maximum out-of-plane displacement values mainly depend upon the heat energy input, the effect of geometric imperfections over these values is small.

5.6.5.5 Effect of EP and EVP Models

The thermo-mechanical material properties of AA 6056-T4 suggest that viscosity effects dominate only at high temperatures e.g. within or in the immediate vicinity of FZ. This essentially means that some of the stresses are released due to high temperature viscous flow of the material. Figure 5.42 compares the maximum out-of-plane displacements for EP and EVP models. Although the displacement level achieved using EP model is higher than that of EVP model; the difference between the two is negligibly small. This observation establishes that in order to predict the out-of-plane deformations both the EP and EVP models yield equally good results for the material AA 6056-T4.

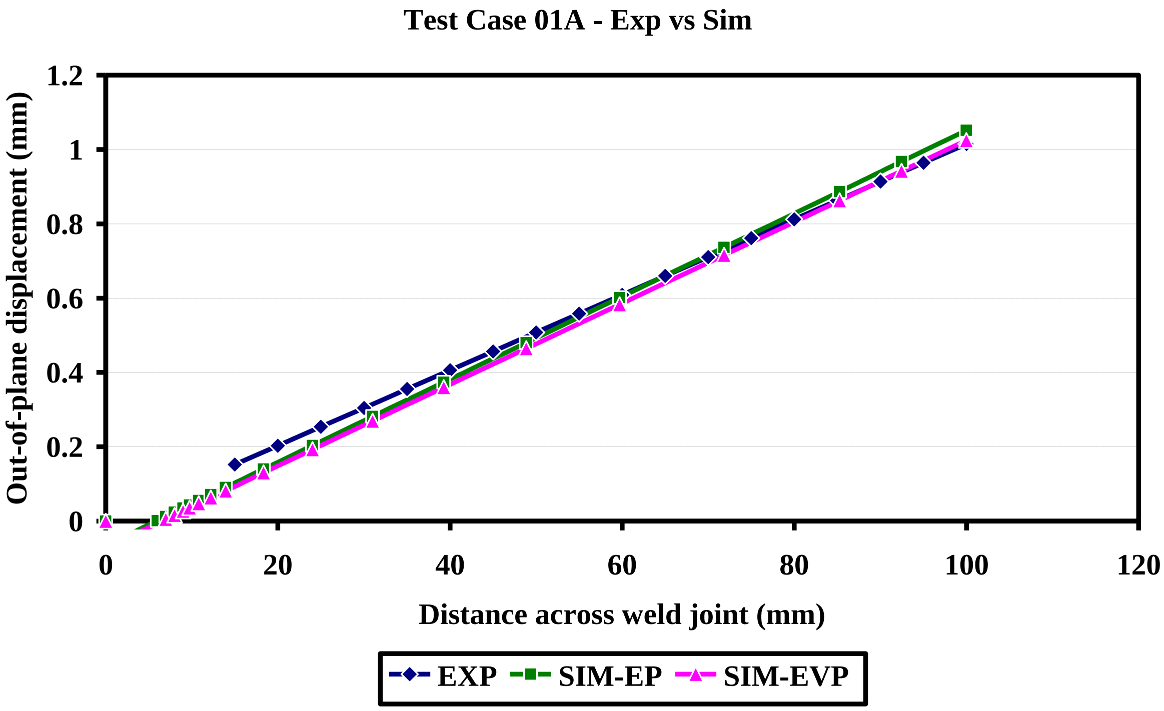

Figure 5.42. Out-of-plane displacement with EP and EVP models – Test Case 01A

5.6.5.6 Comparison between Test Cases 01A (Fusion welding) and 02A (Filler welding)

The experimental and simulated out-of-plane displacement envelopes indicating maximum and minimum values for test cases 01A and 02A are presented in Fig. 5.43. The maximum displacement values for test case 01A reach up to 1 mm, while for test case 02A they reach up to 0.8 mm only. Consistency amongst experimental and simulated results is observed. The observation made in previous chapter, regarding additional beam power used in test case 02A and yet a lower level of out-of-plane displacements in comparison to test case 01A, is also verified here with reference to simulation results. In test case 02A, a considerable fraction of additional heat energy is dissipated in heating the filler wire material.

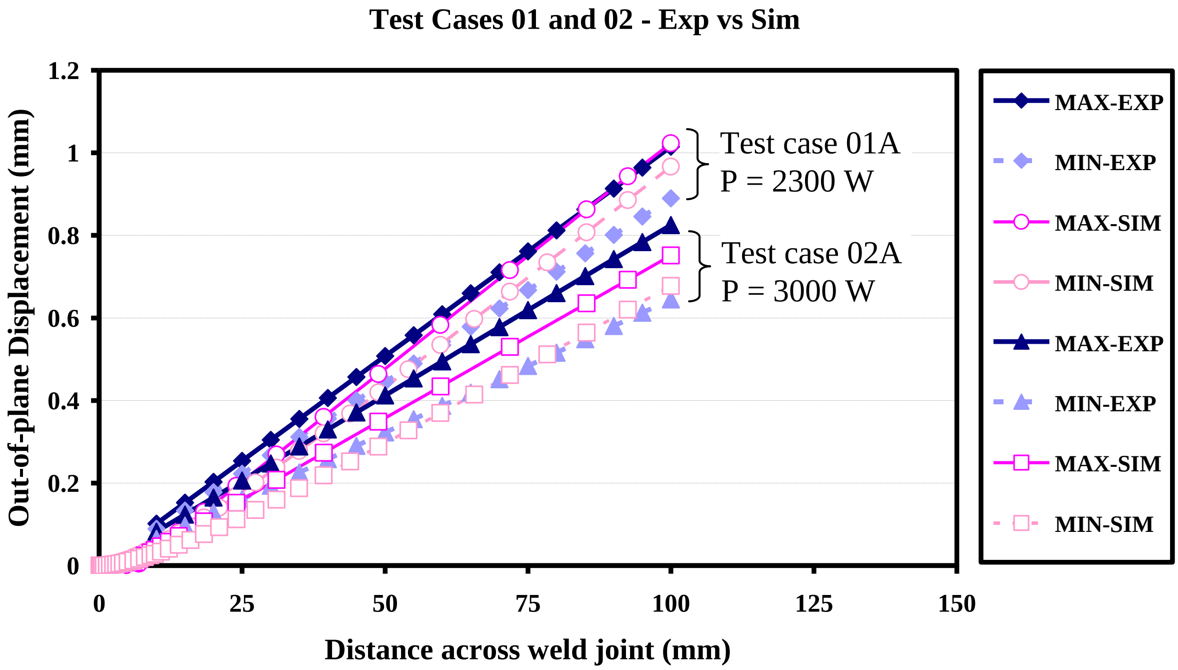

Figure 5.43. Out-of-plane displacements – Test Cases 01A and 02A

5.6.5.7 Test Case 03 (T-joint welding)

The residual out-of-plane displacement distribution for T-joint differs from those of test plates due to the presence of stiffener. As the image correlation technique was employed in the regions 15 mm away from the weld center line (Figs. 4.6 and 4.7), the distortion due to the presence of stiffener could not be recorded. The displacements were assumed to be originating linearly from the center of the FZ for all the test cases. This assumption though worked well for test plates; it fails to capture the deformations of T-joint in FZ and HAZ.

Figure 5.44 shows red-coloured encircled zone of experimental results where the displacement values are not available. However, the simulated displacement contours of T-joint indicate that the distortion pattern follow a rather curved path in the vicinity of FZ. Such an evolution pattern limits the quantitative comparison of simulated out-of-plane displacements with the experimental ones. Some additional image correlation results, for example displacement fields measured from the bottom surface of the base plate, may provide sufficient amount of data that could be used for comparison with simulated results. This could, however, not be done since the bottom side of the base plate had to remain in contact with the support. Qualitative analysis, however, may still be performed. The experimental results show that the maximum out-of-plane displacements reach up to 0.25 mm; while the simulated displacements reach up to 0.21 mm. It may, therefore, be established that a reasonable agreement is present amongst experimental and simulated results.

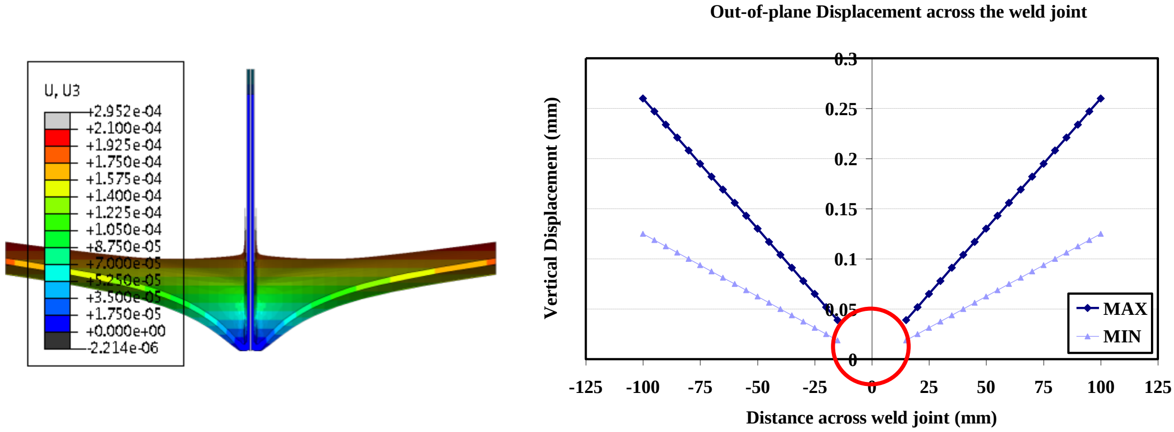

Figure 5.44. Out-of-plane displacements; Sim (left) and Exp (right) – Test Case 03

5.6.6 Residual In-plane Displacements

In-plane displacements are principally induced during expansion and contraction of the test plates in the transverse and longitudinal direction. For the test cases under investigation, the in-plane displacements were not restricted by any clamping arrangement. When the heat source moves away from its origin, the material within the FZ expands in all directions; while the trailing solidifying FZ experiences contraction due to solidification shrinkage. With reference to the transverse in-plane displacements, these expansion and contraction occurrences are directly related to heat input and the peak temperature acquired in the transverse direction. Since the peak temperature distribution increases and decreases gradually near the weld start and stop ends, respectively; the in-plane displacement level remains trivial at these locations. However, once the uniform heat input and a constant temperature in FZ is reached, these displacements remain uniform for most part of the weld length. This is where a constant magnitude of in-plane displacement is observed. Owing to the symmetry of the test specimens, the displacement magnitude should necessarily be identical on each side of the symmetric half. Once the complete heating and cooling cycle is performed, the displacements sustaining after relaxation (removal of loading and boundary conditions) may be regarded as residual in-plane displacements.

Figures 5.45, 5.46 and 5.47 present the comparison of measured and calculated in-plane displacements for test cases 01A, 02A and 03, respectively. These displacements are taken from the upper surface, towards the mid of the plates in the direction transverse to weld joint. The negative and positive sign conventions are used to indicate opposite sides of specimens with respect to weld line; yet the displacement magnitude is found to be identical on both sides. A good comparison is observed for all the test cases; however the acquired displacement level in each case differs from the other. For instance, test cases 01A and 02A reach up to the displacement levels of 0.025 mm and 0.015 mm, respectively. Consistency amongst the results may well be noticed at this stage. As for out-of-plane displacement, test case 02A has shown lesser values than case 01A; a similar pattern for in-plane displacement is observed here as well.

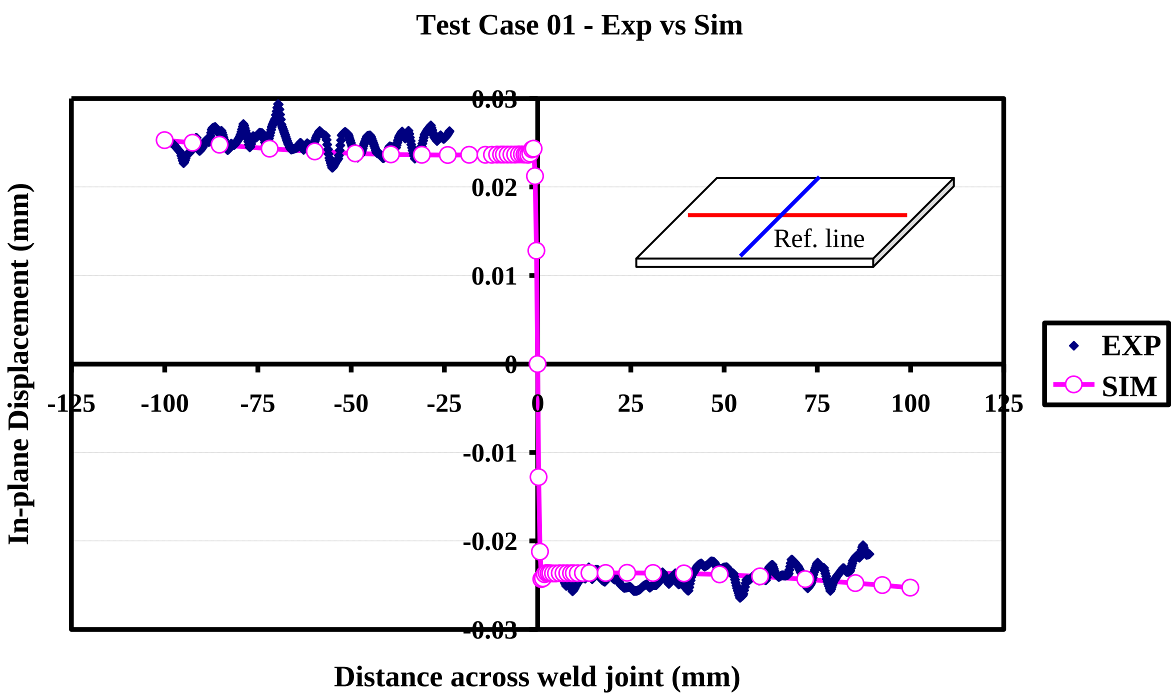

Figure 5.45. In-plane displacements – Test Case 01A

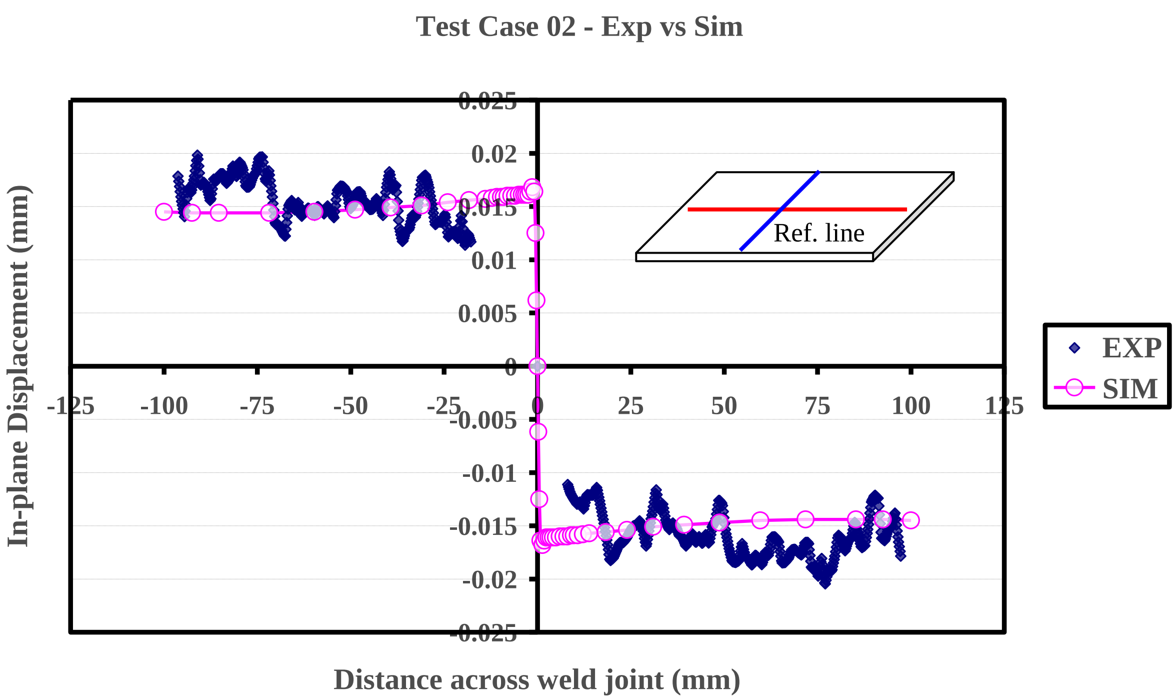

Figure 5.46. In-plane displacements – Test Case 02A

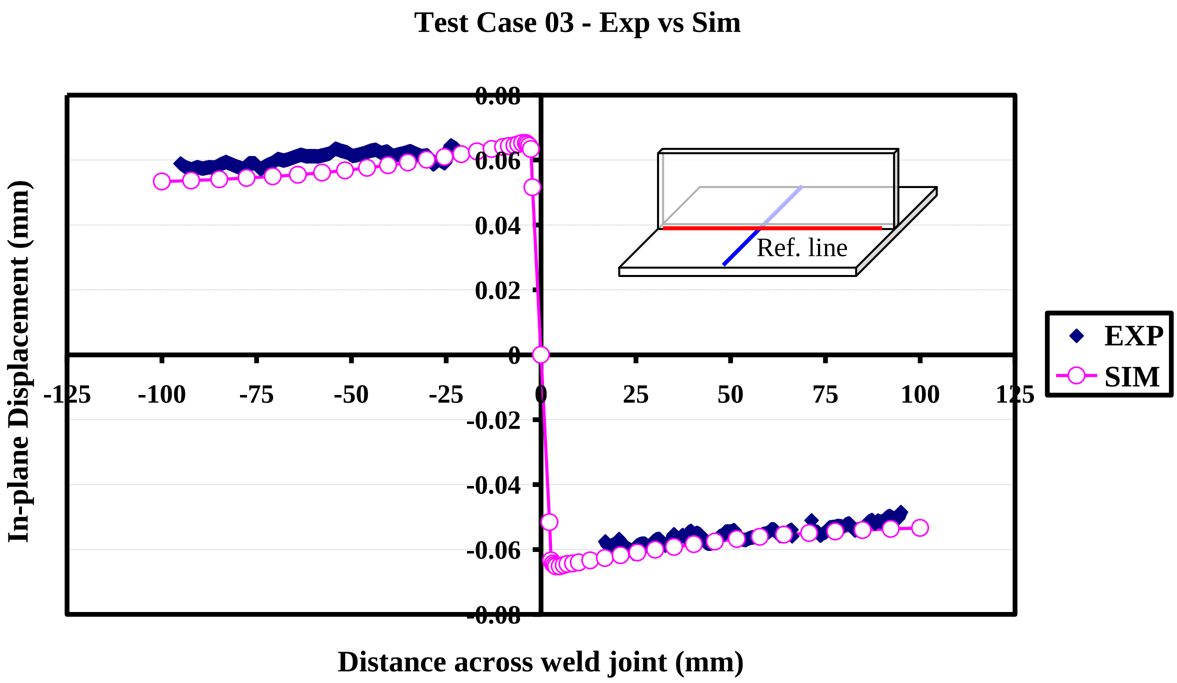

Figure 5.47. In-plane displacements – Test Case 03

Test case 03 shows a net in-plane displacement value of 0.06 mm; which is 2.5 and 4 times as high as those of test cases 01A and 02A, respectively. Such a higher displacement level is a direct consequence of corresponding high energy input supplied to the T-joint during welding through two welding heads each with a beam power of 2500 W.

5.6.7 Residual Stresses

As mentioned earlier, the residual stresses are the self-balanced internal stresses that exist in the welded structure without any external load. Due to the localised heating of the component, welding induces highly non-homogeneous stresses during its application. These stresses are at times as high as the yield strength of the material either in FZ, in HAZ or in both. In most of the welding processes, the longitudinal stresses (stresses in the direction of welding) have the maximum influence over the distortions and failure of the material. The next significant stresses are the transverse stresses; while the remaining stress components generally have insignificant effect.

5.6.7.1 Evolution of Longitudinal and Transverse Stresses

Figure 5.48 presents the development of the longitudinal stresses (σ_{xx}) in the component, where the stress distribution in the top surface of the base plate during welding is shown. At any instant of time during welding, the regions surrounding the molten pool experience compression due to the thermal expansion of FZ; whereas the stresses are released in the FZ. The regions further away from the plastic compression zone experience tension; however, the stress level outside the tension zone remains considerably low. During solidification, the FZ tends to contract, however restrained by adjacent solid material it experiences tension. These tensile stresses may increase to as high as yield limit of the base material. Figure 5.49 shows transverse stress (σ_{yy}) development, which follows the similar pattern as longitudinal stress till the beginning of cooling. However, upon further cooling they pass into compression in FZ, so as to maintain the equilibrium with longitudinal stresses.

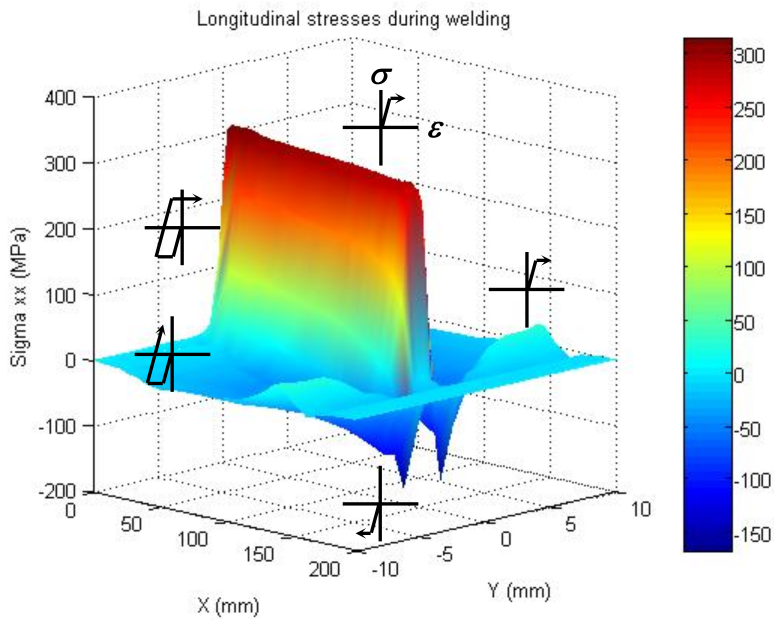

Figure 5.48. Evolution of longitudinal stresses – Test Case 01A

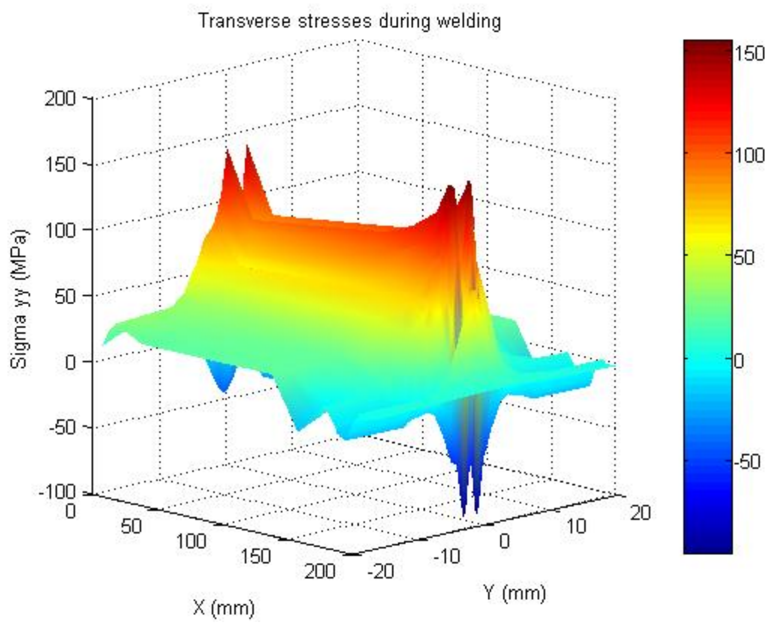

Figure 5.49. Evolution of transverse stresses – Test Case 01A

The stress evolution for all the test cases follows an identical pattern. Further discussion is developed with respect to the individual elements selected in FZ and HAZ. Figure 5.50 shows the longitudinal stress (σ_{xx}) and temperature (T) as a function of time for three of the elements selected in the fusion zone (FZ), heat-affected zone in tension (HAZT) and heat-affected zone in compression (HAZC). It may be noticed that all the elements pass in compression as the heat source approaches; however, the element in HAZT experiences maximum compression until the one in FZ releases its stresses above the fusion temperature. Since the elements in FZ and HAZT experience very high temperatures, upon cooling they respond accordingly and hence pass into tension. This, in turn, exerts compression upon the element in HAZC.

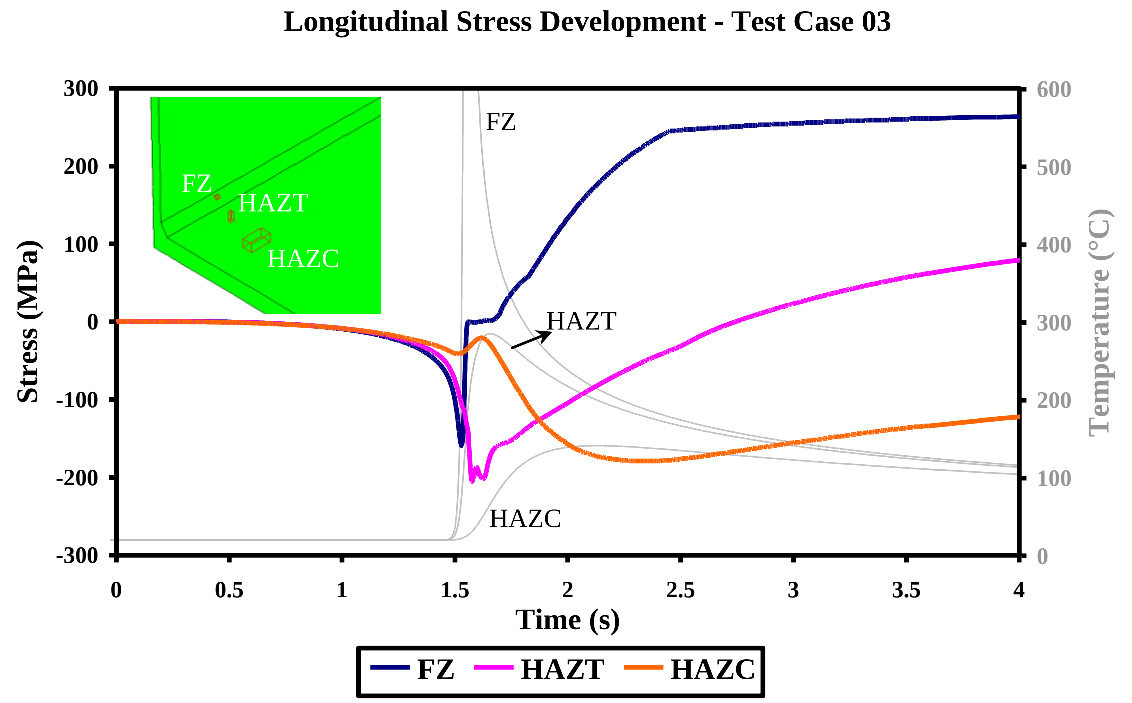

Figure 5.50. Longitudinal stress (σ_{xx}) development in FZ and HAZ elements – Test case 03

The stresses developing during heating and cooling cycle reside in the material and may result in unwanted distortions. The applied mechanical boundary conditions may further increase the level of stresses; however some of these stresses are released upon relaxation of boundary conditions.

The residual stress tensor for the test case 01A is presented in Fig. 5.51. It is found that the only significant stress components are the longitudinal (σ_{xx}) and transverse (σ_{yy}) stresses; while all other stress components (σ_{zz}, σ_{xy}, σ_{yz} and σ_{zx}) remain insignificant.

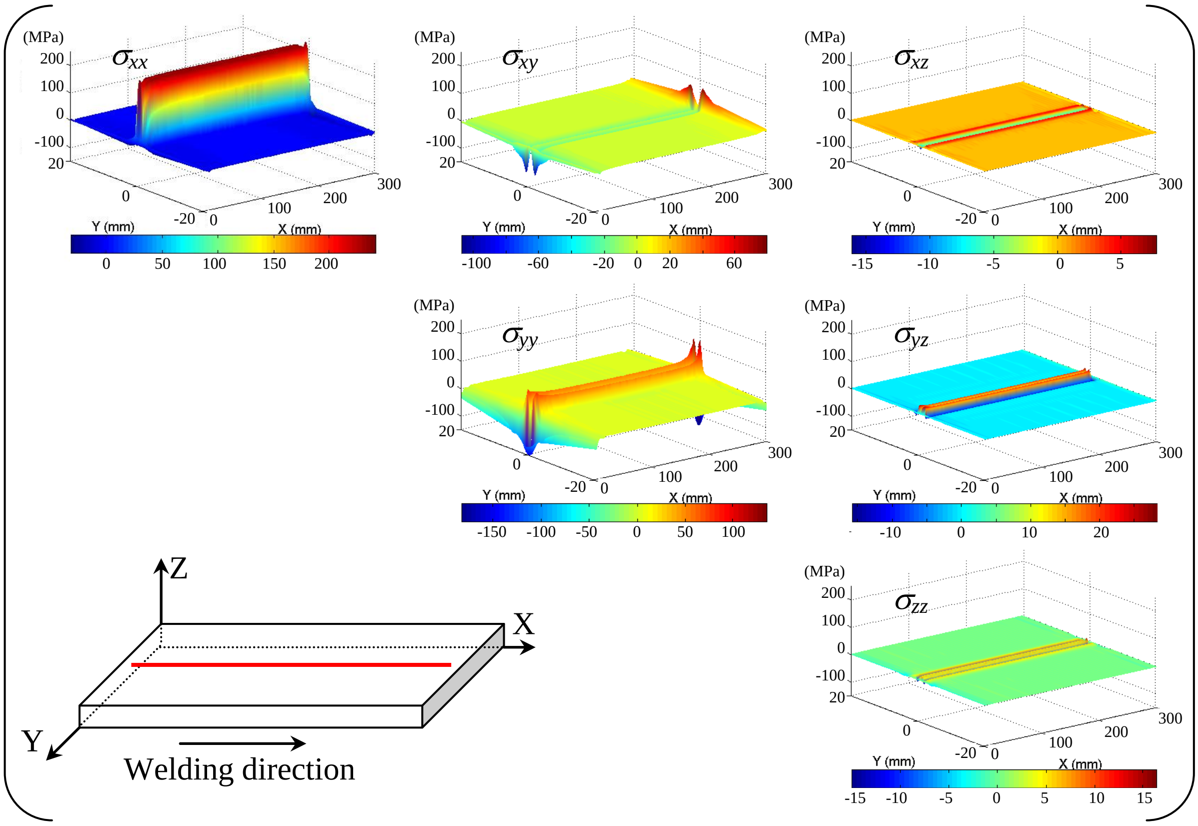

Figure 5.51. Residual stress tensor on upper surface – Test case 01A

For most part of weld length, the residual stresses remain uniform in the welding direction. It is only at the start and stop ends of the welding where stresses gradually reduce to zero level.

Further analysis of the stress state is presented on various lines drawn in and near the FZ in the longitudinal, transverse and through-thickness directions. Figure 5.52 shows the location of these lines drawn on test plate and T-joint models.

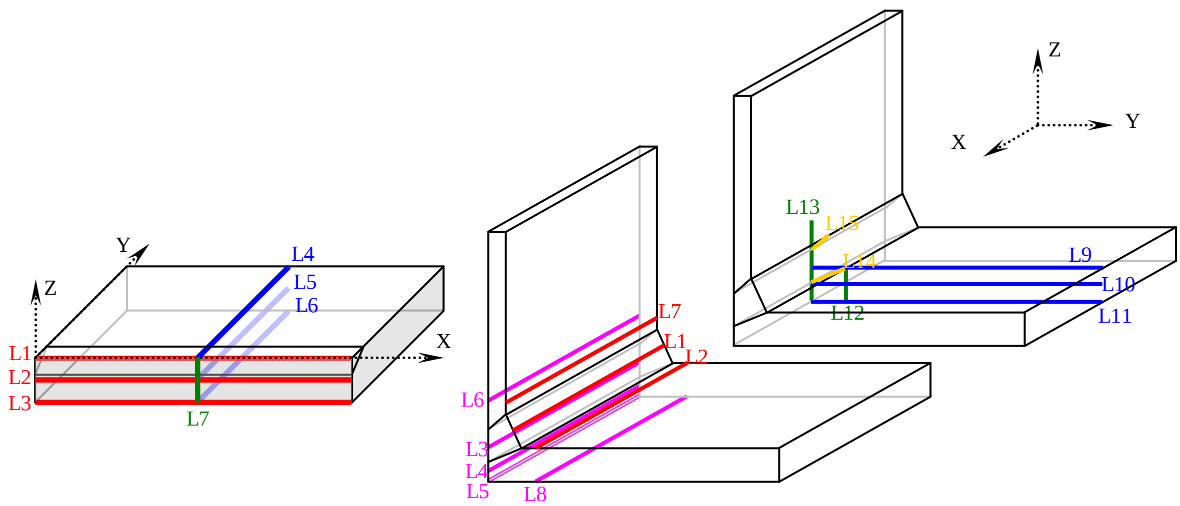

Figure 5.52. Location of various lines on test plates and T-joints

5.6.7.2 Stresses at the End of Heating, Cooling and Relaxation

Figure 5.53 presents the longitudinal (σ_{xx}) and transverse (σ_{yy}) stresses at the end of heating (EOH), end of cooling (EOC) and end of relaxation (EOR) at line L4 for test case 01A. The longitudinal tensile and compressive stress level is found to be the maximum at the EOH, while it gradually reduces first towards the EOC and then after relaxation. The transverse compressive stress changes a little from EOH to EOC, while at the EOR the compressive stress grows and tensile stress reduces relieving elastic stresses due to the removal of suction pressure.

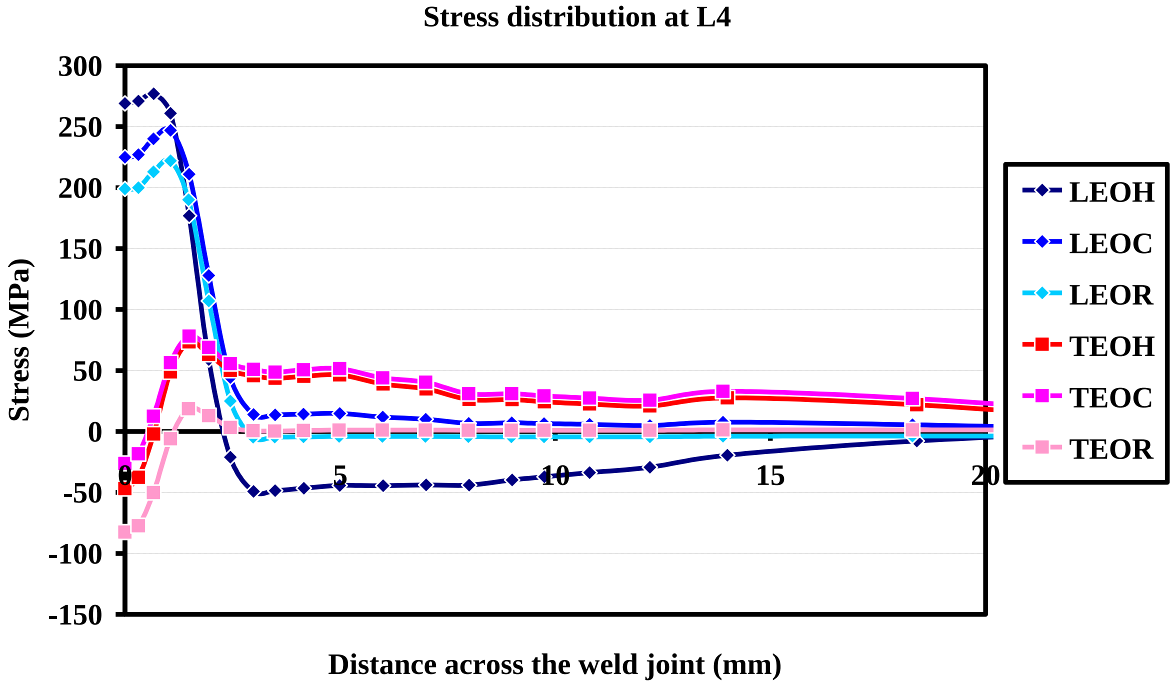

Figure 5.53. Stresses during welding cycle – Test case 01A

5.6.7.3 Effect of EP and EVP Models

The elasto-plastic (EP) behaviour of most of the materials changes to elasto-viscoplastic (EVP) at higher temperature. As discussed in chapter 3, AA 6056-T4 follows the similar trend at temperatures greater than 300°C. However, due to its high thermal conductivity the heat energy dissipates rapidly, and the high temperature zone confines to a very small region. Figure 5.54 presents the comparison between EP and EVP for longitudinal (σ_{xx}) and transverse (σ_{yy}) residual stresses at L4 for test case 01A. The difference in stress level is observed in FZ and in its immediate vicinity (approx. 3 mm). A relatively reduced level of stresses is present for EVP model due to the viscous flow of material at high temperature. Here, the maximum stress value of EVP model remains 20% lower than that of EP model.

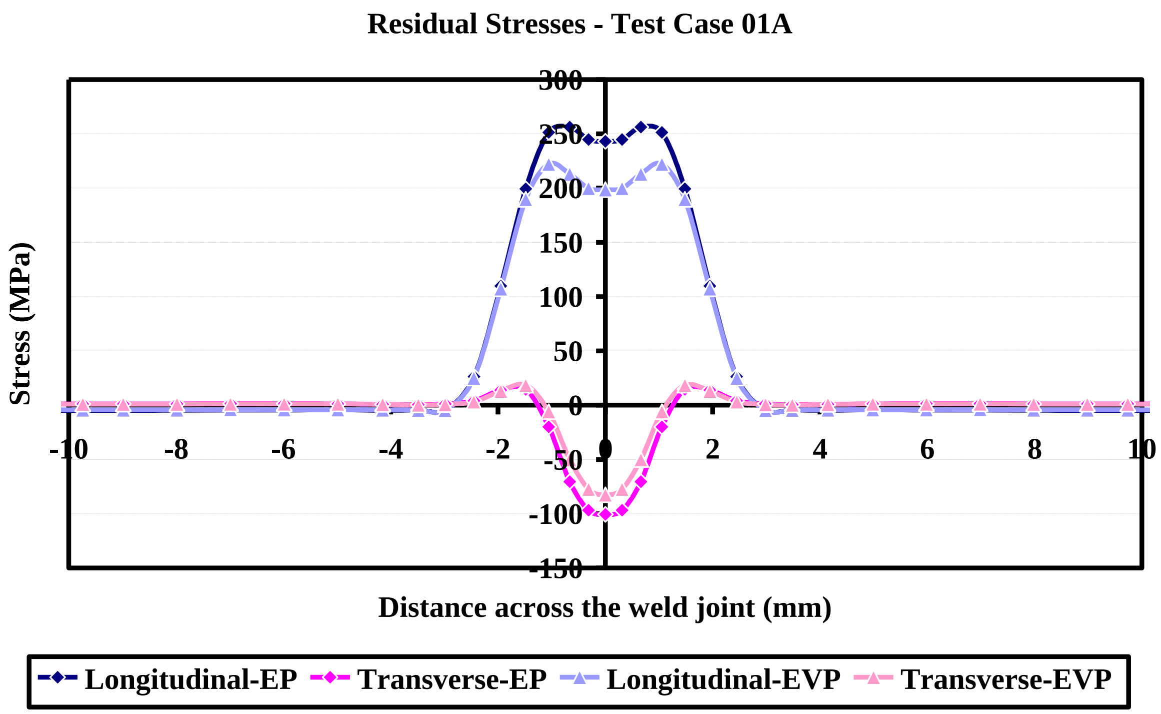

Figure 5.54. Residual stresses for EP and EVP models – Test case 01A

5.6.7.4 Effect of Thermal Boundary Conditions

Unlike the test case 01B, the use of aluminium support in test case 01A introduces forced heat transfer from the bottom surface of the specimens. This essentially means that the heat loss in 01A is faster than in 01B. A slightly higher level of longitudinal (σ_{xx}) stresses in Fig. 5.55 for 01B illustrates the effect of slower heat transfer.

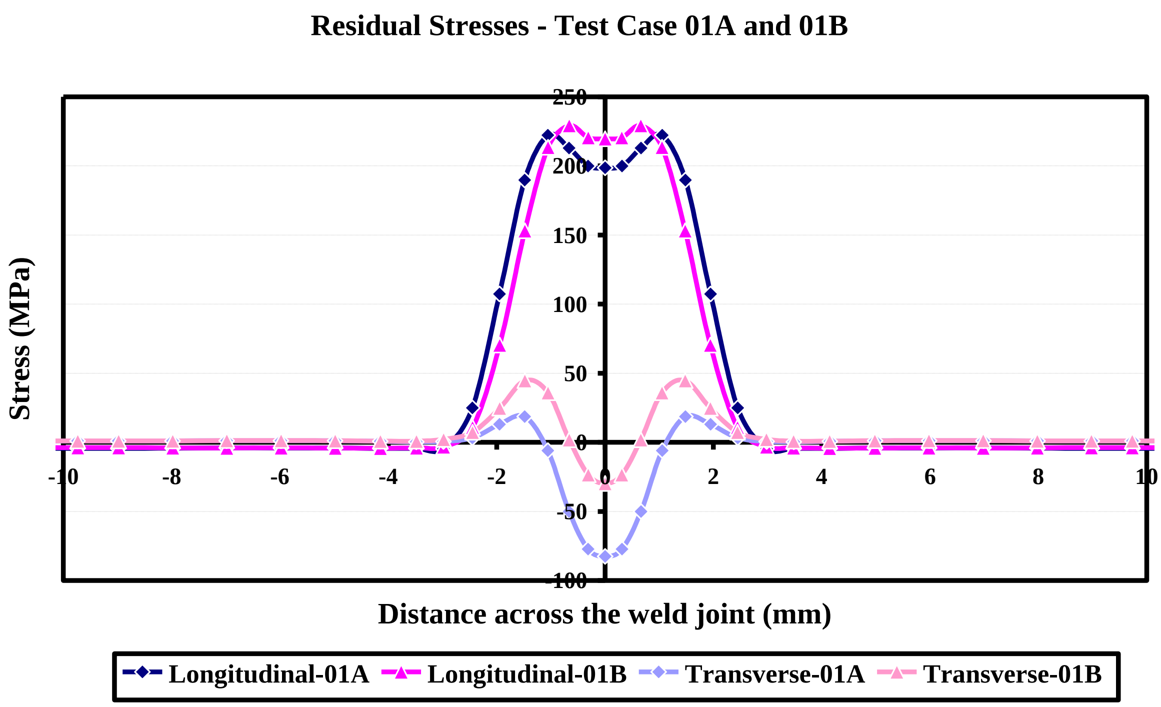

Figure 5.55. Residual stresses with different thermal BCs – Test cases 01A and 01B

In addition, a combination of forced heat transfer at the bottom surface and natural heat transfer at the top surface imparts non-uniformity and directionality to the heat loss in test case 01A; while the test case 01B experiences uniform heat loss from its surfaces. This difference in BCs also affects the resultant temperature fields, which, in turn, influence the distribution of stresses. For instance, a slightly wider zone of stress distribution for test case 01A is observed in Fig. 5.55 than for test case 01B.

5.6.7.5 Residual Stress State – Test Case 01A (Fusion welding on support)

The residual stress state of test case 01A obtained using EVP law is presented at various lines in Figs. 5.56 and 5.57. Figure 5.56 shows the stress distribution in the longitudinal direction at lines L1, L2 and L3 drawn on the top surface, mid-plane and bottom surface, respectively. Since the heat source is applied over a length of 290 mm leaving aside a distance of 5 mm at each end, the stress peaks are observed in these regions due to high temperature gradient in the longitudinal direction. The elements that experience heating above or close to the fusion temperature attain a uniform level of stresses at the end of relaxation. Longitudinal (σ_{xx}) and transverse (σ_{yy}) stress levels at line L1 (located in FZ) are less than L2 (located in HAZ) because of the visco-plastic behaviour of the material at high temperatures. L3 attains the stress level lower than L1 and L2, because it experiences relatively lower level of temperature during heating.

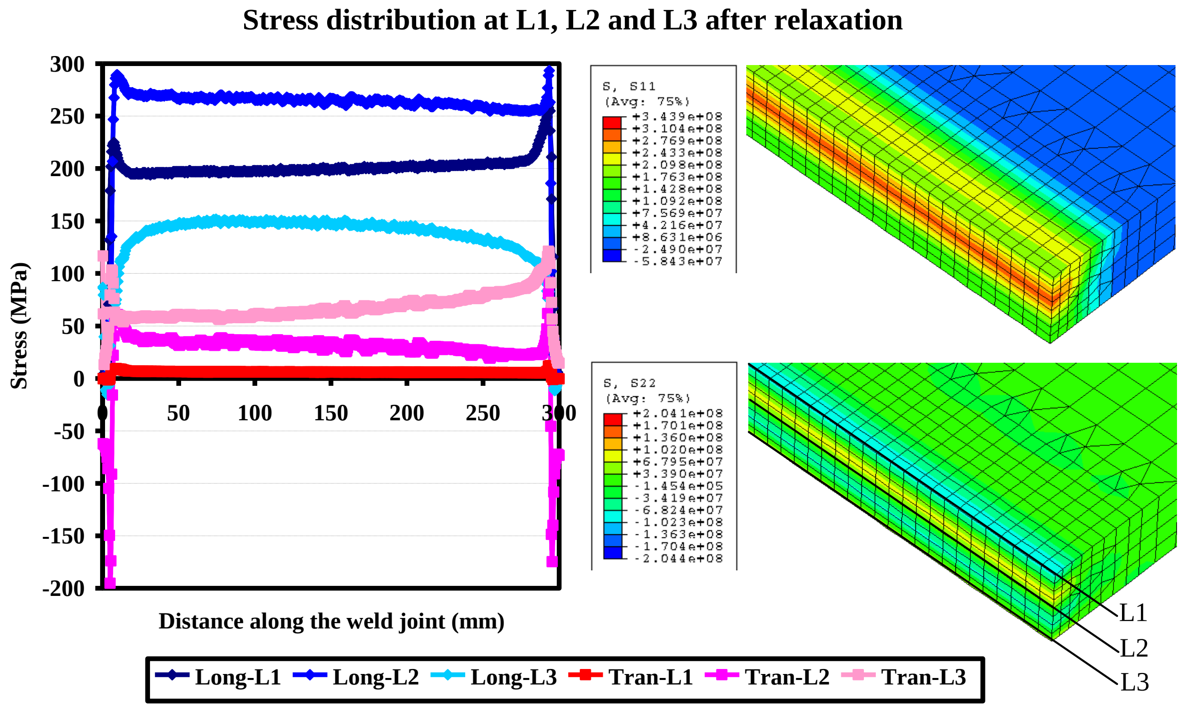

Figure 5.56. Residual stresses along lines L1, L2 and L3 – Test case 01A

Figure 5.57 illustrates the stress distribution in the transverse direction at lines L4, L5 and L6 drawn on the top surface, mid-plane and bottom surface, respectively. The stress magnitude for longitudinal (σ_{xx}) and transverse (σ_{yy}) stresses at symmetric plane is presented above in Fig. 5.56. In the transverse direction, the stress distribution zone at L4 is comparatively wider than the ones at L5 and L6 due to wider FZ at top surface. Outside the FZ, the longitudinal stresses (σ_{xx}) are higher at L4 than at L5 and L6. Here, the transverse stresses (σ_{yy}) at L4 are compressive in FZ while at L5 and L6 they tend to be tensile.

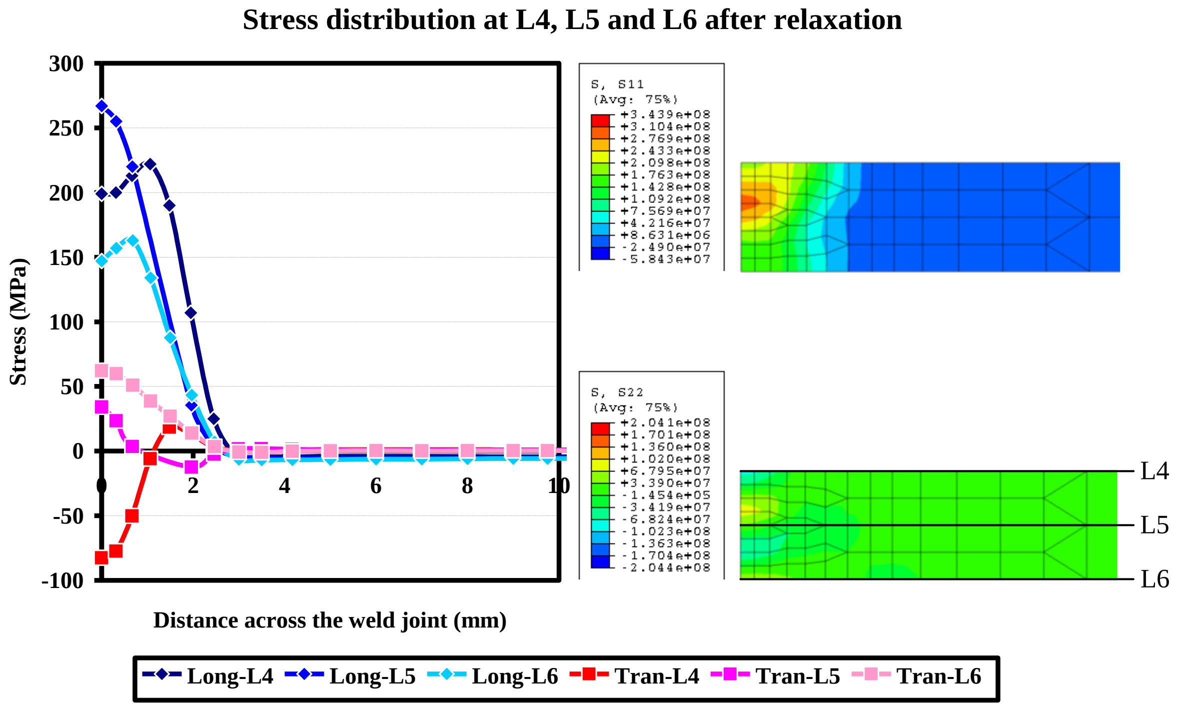

Figure 5.57. Residual stresses along lines L4, L5 and L6 – Test case 01A

5.6.7.6 Residual Stress State – Test Case 02A (Filler welding on support)

The residual stress state of test case 02A obtained using EP law is presented at various lines in Figs. 5.58 and 5.59. Figure 5.58 shows the stress distribution in the longitudinal direction at lines L1, L2 and L3 drawn on the top surface, mid-plane and bottom surface, respectively. The stress distribution is similar to the test case 01A. However, unlike the test case 01A, the longitudinal stresses (σ_{xx}) at L1 are greater than those at L2 and L3. This is because the viscosity effects of the material at high temperatures are not taken into consideration for this analysis. Additionally, the stress levels at L1 and L2 remain close to each other. Transverse stresses (σ_{xx}) pass into compression at L1 and L2 and tend to be tensile at L3.

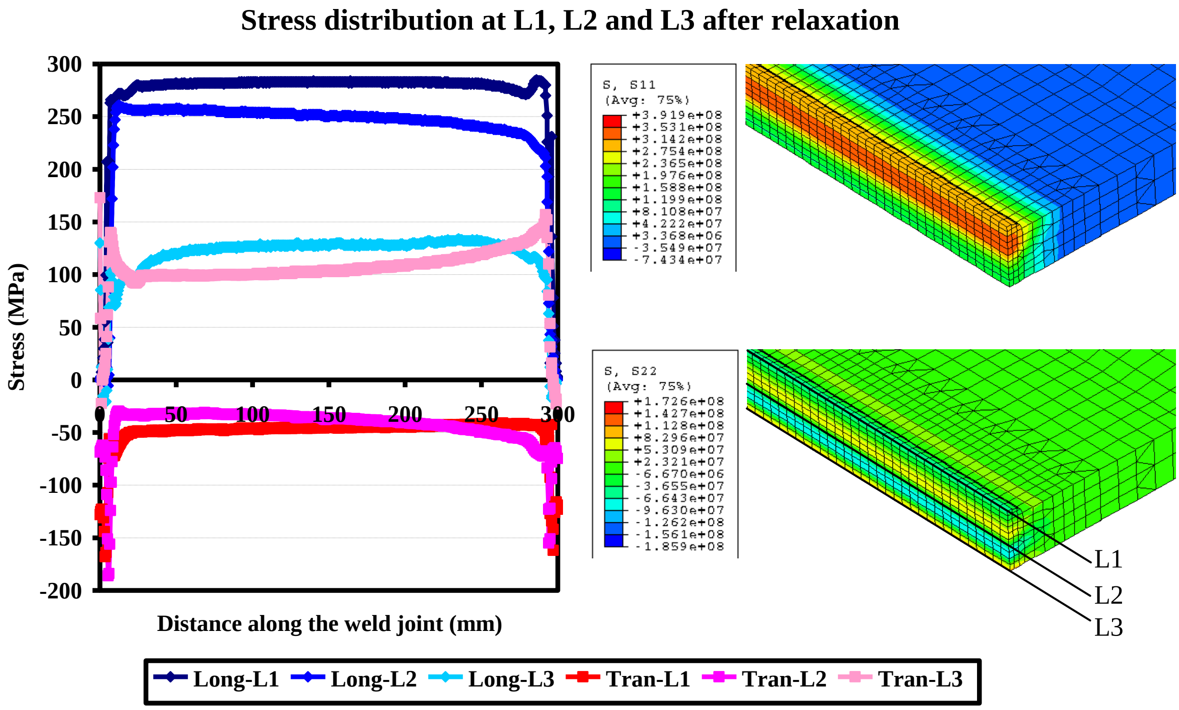

Figure 5.58. Residual stresses along lines L1, L2 and L3 – Test case 02A

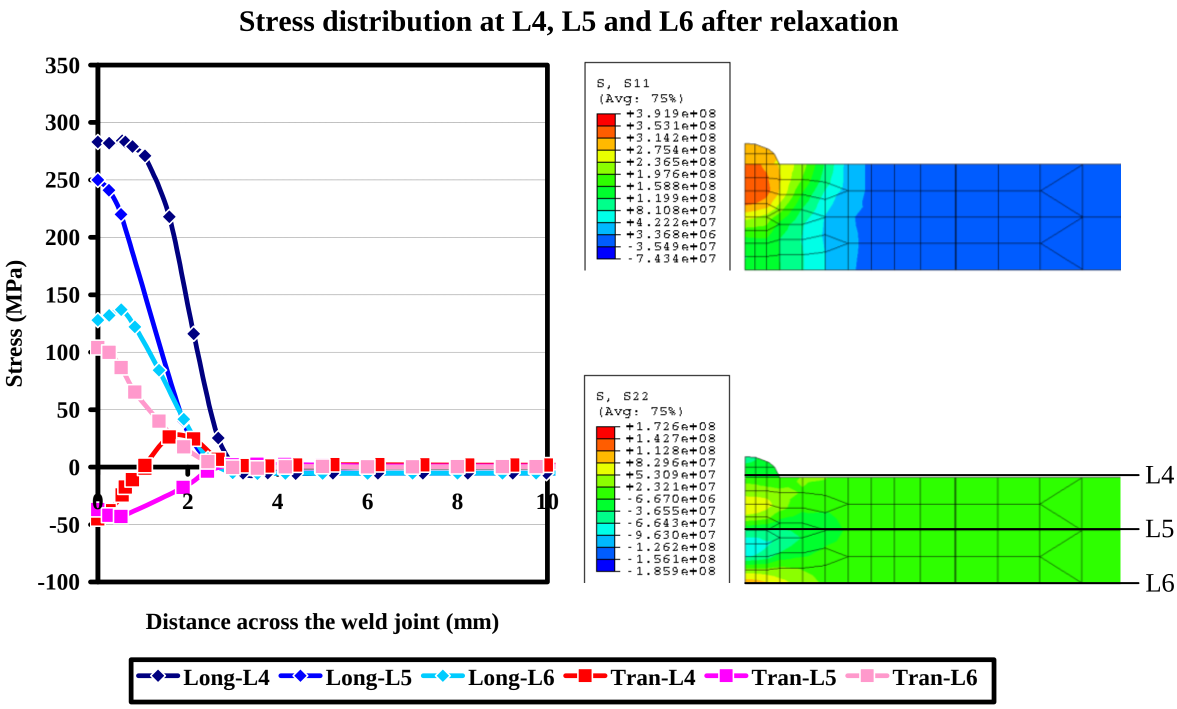

Figure 5.59. Residual stresses along lines L4, L5 and L6 – Test case 02A

Figure 5.59 shows the stress distribution in the transverse direction at lines L4, L5 and L6. Here, the stress distribution zone reduces gradually from L4 to L6. A relatively higher level of longitudinal (σ_{xx}) stresses is observed at L4 and L5.

5.6.7.7 Comparison between Test Cases 01A (Fusion welding) and 02A (Filler welding)

The longitudinal (σ_{xx}) and transverse (σ_{yy}) residual stresses for the test cases 01A and 02A at L4 are shown in Fig. 5.60. The FZ and HAZ boundaries are marked to develop the comparison. Longitudinal stress (σ_{xx}) level of test case 02A in FZ is approximately 10% higher than that of test case 01A. The increased level of σ_{xx} replicates the effect of increased laser beam power in test case 02A. Transverse stress (σ_{yy}) level of test case 02A in FZ is almost 50% less than that of test case 01A. This observation implies that with increasing laser beam power, the longitudinal tensile stresses (σ_{xx}) increase while the transverse compressive stresses (σ_{yy}) decrease. Similar trend is observed for the stresses in HAZ; however, the difference in stress levels amongst both the test cases becomes insignificantly small.

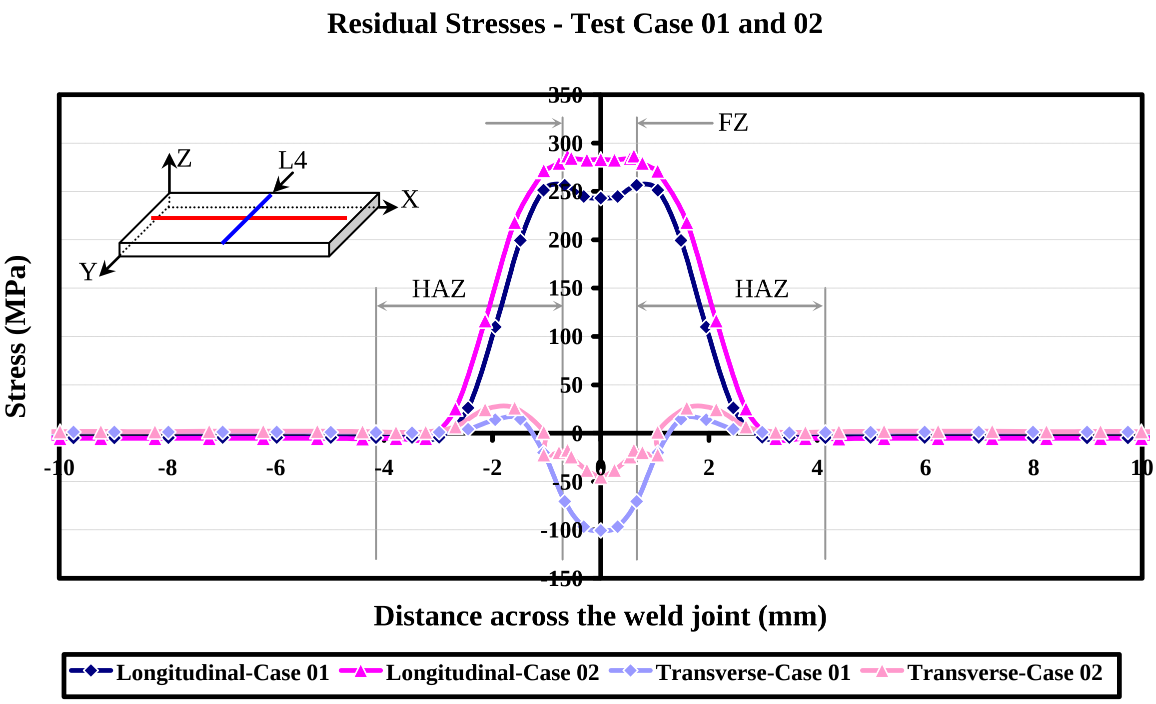

Figure 5.60. Longitudinal and transverse residual stresses – Test cases 01A and 02A

Additionally, it is found in both the cases that the longitudinal residual stresses (σ_{xx}) have magnitudes approaching 250 – 280 MPa in FZ and are largely tensile in nature, while these stresses tend to be compressive in HAZ; the compression zone, however, is very small. On the other hand, transverse stresses (σ_{yy}) are mainly compressive in FZ and tend to be tensile in HAZ. All the remaining components (σ_{zz}, σ_{xy}, σ_{yz} and σ_{zx}) of the stress tensor remain negligibly small.

5.6.7.8 Residual Stress State – Test Case 03 (T-joint welding)

The residual stress state of test case 03 at L9 (Fig. 5.52) is presented in Fig. 5.61. It is observed that the longitudinal stresses (σ_{xx}) are predominantly higher than the transverse stresses (σ_{yy}). It may also be noticed that not only the maximum stress level attained is higher than those of test cases 01A and 02A, but a comparatively wider HAZ is also present. This is because the amount of heat input in case of T-joint welding is higher than the test plates welding; since for the former the beam power is almost 2 times as high as for the latter and the welding speed of the former is 1.6 times as low as the latter (Tables 4.1 and 4.2).

As mentioned in the previous section, the effect of increased laser beam power is such that the level of longitudinal stresses (σ_{xx}) increases while that of transverse stresses (σ_{yy}) decreases. Compared to test cases 01A and 02A, the transverse compressive stresses (σ_{yy}) in FZ reduce to such an extent that they pass slightly into tension.

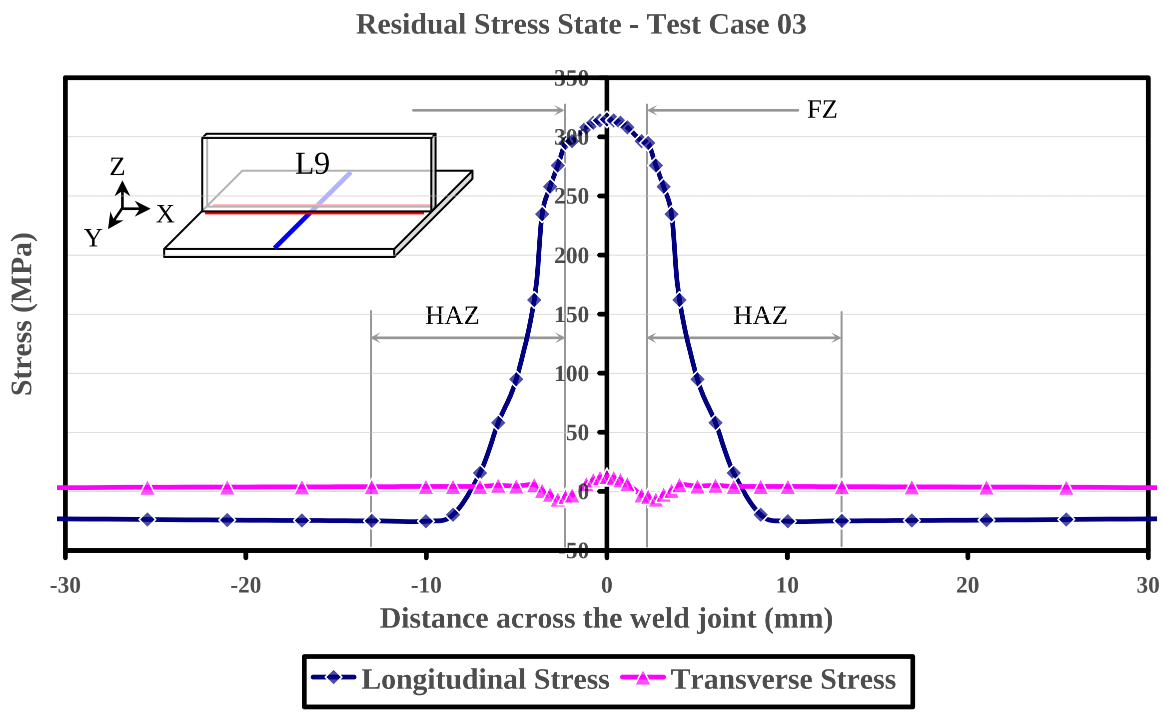

Figure 5.61. Longitudinal and transverse residual stresses – Test case 03

Since the longitudinal residual stresses (σ_{xx}) play crucial role in suggesting the distortion pattern of the T-joint; they are being presented in detail in Figs. 5.62, 5.63 and 5.64. Figure 5.62 shows the lines drawn in the direction of welding in and near the FZ, viz. L1, L3, L5, L6 and L8. It may be observed that the stress level remains not only constant, rather it also stays uniform over the entire length of the FZ except for the weld start and stop ends.

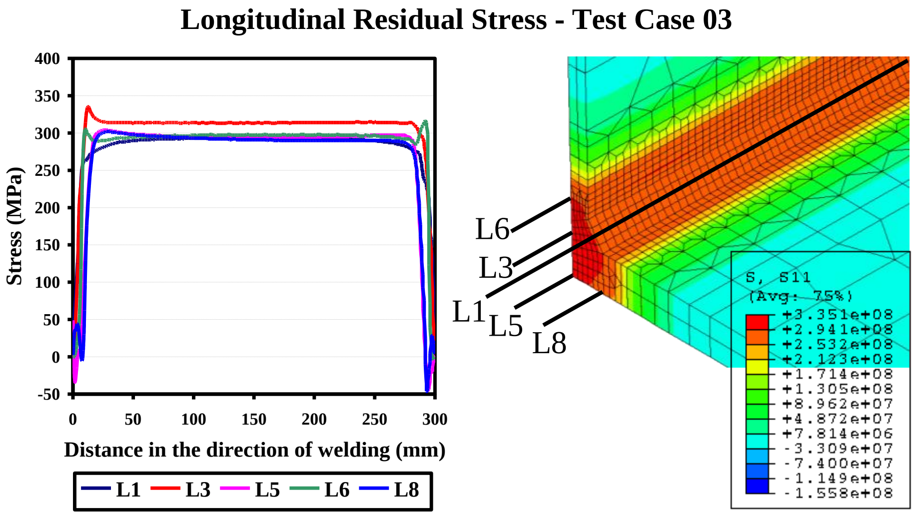

Figure 5.62. Longitudinal residual stresses at L1, L3, L5, L6 and L8 – Test case 03

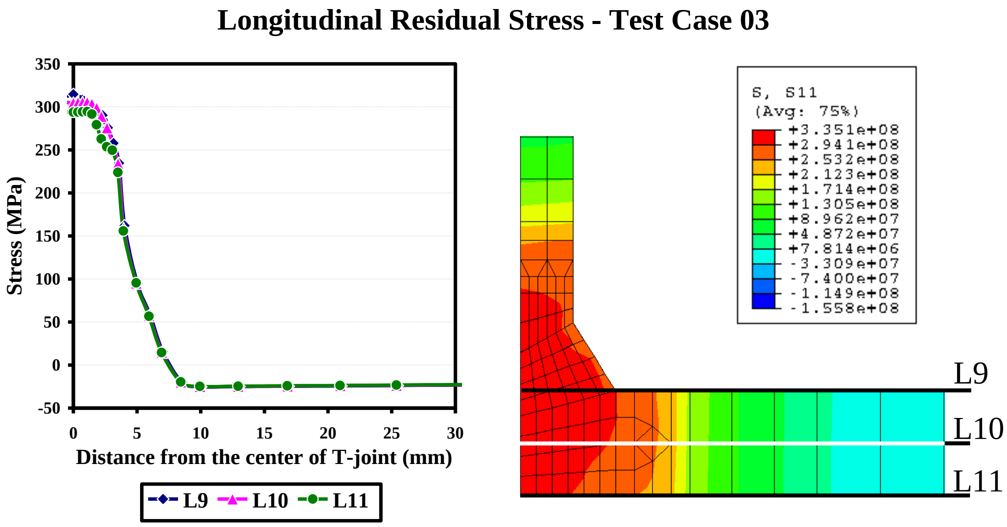

Figure 5.63. Longitudinal residual stresses at L9, L10 and L11 – Test case 03

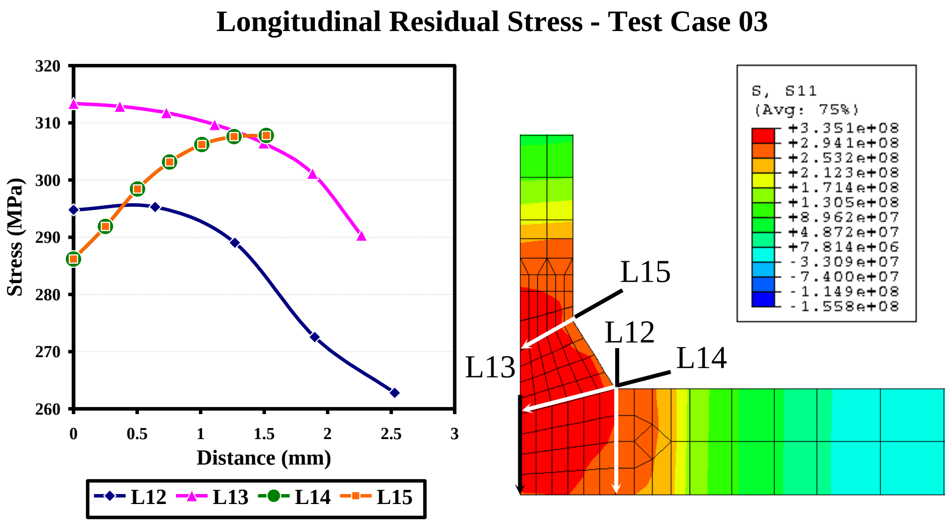

Figure 5.64. Longitudinal residual stresses at L12, L13, L14 and L15 – Test case 03

Figure 5.63 illustrates the longitudinal stress values obtained from the lines drawn on top surface (L9), mid-plane (L10) and bottom surface (L11) in the direction transverse to the weld joint. It is noticed that the stress values do not vary in the thickness direction except in FZ, where the difference remains insignificantly small. Figure 5.64 presents stress values in the through-thickness direction (lines L12 and L13) and at the FZ boundary (lines L14 and L15). In the through-thickness direction along the lines L12 and L13, the stress values decrease a little; yet they remain tensile in nature. The stress values remain identical on each side of the FZ boundary (L14 and L15), while they increase to some extent towards the center of the FZ. Irrespective of the directionality of stresses they remain tensile in nature everywhere in and near the FZ. However, as observed in Fig. 5.63, the longitudinal compressive stresses exist in HAZ, where their magnitudes increase up to -35 MPa. It may, therefore, be established that these compressive stresses are, in-fact, responsible for the bending and / or buckling distortion of the T-joint.

5.6.8 Residual Strains

During a complete welding and cooling cycle, the material experiences elastic and plastic strains. These strains can either be compressive or tensile in nature. A temporary strain-free state also appears above fusion temperature; however, upon cooling plastic strains reappear due to the solidification shrinkage. The plastic strains, being irreversible, reside in the material and result as residual plastic strains.

5.6.8.1 Evolution of Plastic Strains

Evolution of plastic strains along the longitudinal (ε^p_{xx}), transverse (ε^p_{yy}) and through-thickness (ε^p_{zz}) direction is being presented in Fig. 5.65 for an element selected in the HAZ immediately next to the FZ (Test case 03). As the temperature in HAZ rises to very high values without passing the fusion temperature; the plastic strains dominate the elastic ones during heating and cooling stages. These inelastic strains, however, start to appear only when a considerably high temperature is reached. Figure 5.65 shows that the material plastification takes place around 150°C, which further implies that any level of strains induced before reaching this critical temperature will essentially be reversible. With further increase in temperature, the longitudinal (ε^p_{xx}) and the transverse (ε^p_{yy}) plastic strains grow in negative values; however, the through-thickness plastic strain (ε^p_{zz}) grows in positive values during heating, nevertheless it increases considerably only at the start of cooling. The longitudinal

(ε^p_{xx}) and transverse (ε^p_{yy}) strains increase in negative values at the start of cooling while the element is still at a higher temperature. Upon further cooling the former reduces and the latter increases to some extent; yet they do not turn into positive strains thereby indicating the effect of compressive stresses. The through-thickness strain (ε^p_{zz}), in-fact, maintains the condition of incompressibility ($\varepsilon^p_{xx}+\varepsilon^p_{yy}+\varepsilon^p_{zz} = 0$). Figure 5.65 also presents the strain summation result that remains at zero throughout the heating and cooling cycle. Furthermore, none of the plastic strain values return back to zero level, hence suggesting a significant level of residual plastic strains in the component.

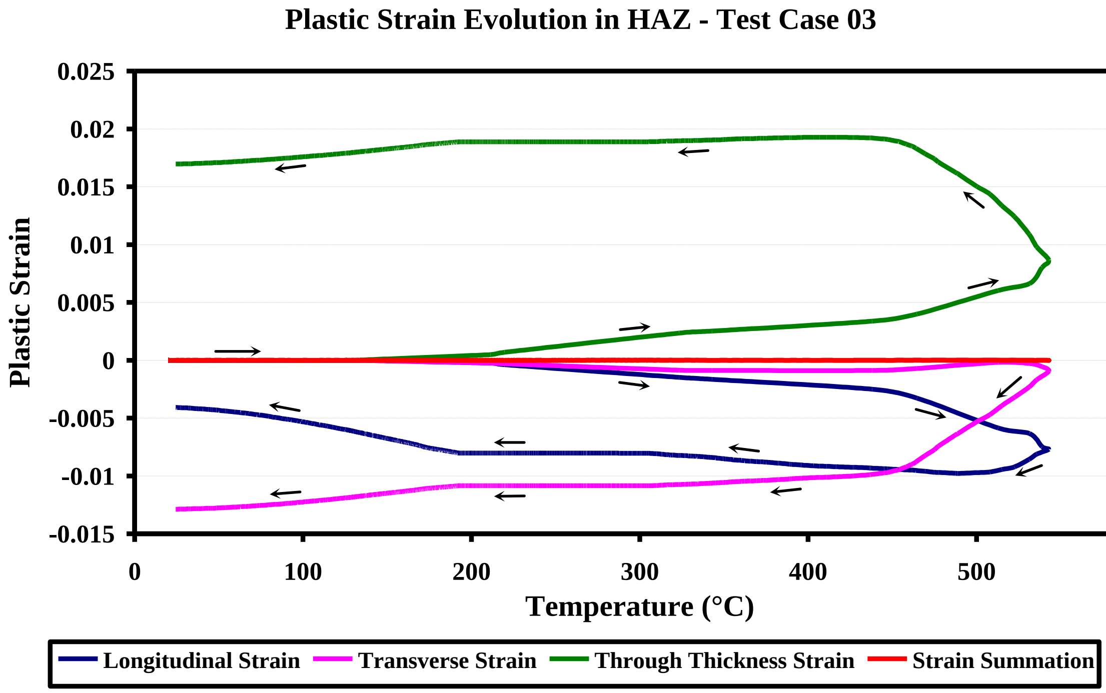

Figure 5.65. Plastic strains (ε^p_{xx}, ε^p_{yy}, ε^p_{zz}) evolution in HAZ – Test case 03

The residual plastic strain state in the top surface of test plate for test case 01A is presented in Fig. 5.66. It is observed that amongst the normal strain components, the longitudinal plastic strain (ε^p_{xx}) values remain insignificantly small; the transverse (ε^p_{yy}) and through-thickness (ε^p_{zz}) plastic strains, however, attain considerably higher levels. Here, the transverse plastic strains (ε^p_{yy}) are compressive in nature, while through-thickness plastic strains (ε^p_{zz}) are tensile in nature. Unlike the shear stress components, the plastic shear strain components, especially ε^p_{xy} and ε^p_{yz}, are predominantly high in magnitude. These shear strain components are considered to have strong influence over the plastic deformation (change in shape) of the components.

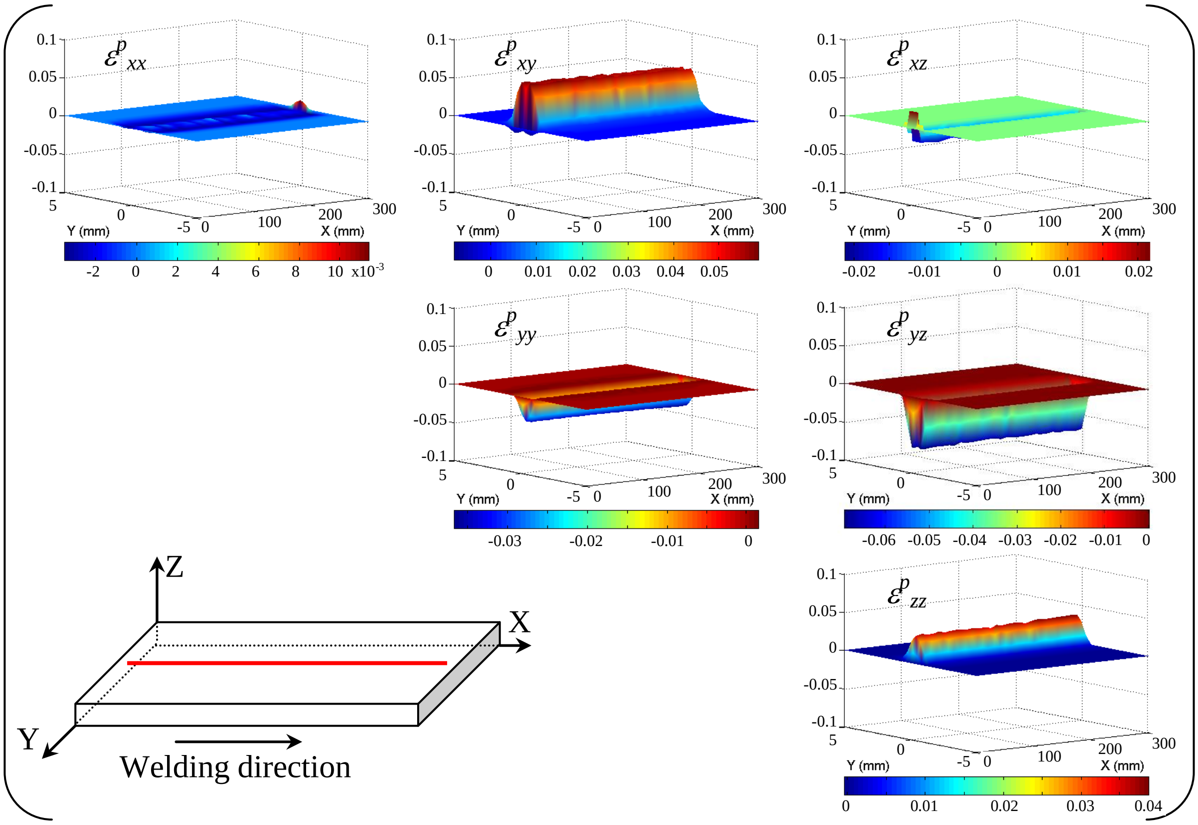

Figure 5.66. Residual strain tensor in upper surface – Test case 01A

5.6.8.2 Plastic Strain State – Test Cases 01A (Fusion), 02A (Filler) and 03(T-joint)

The residual plastic strains for test cases 01A, 02A and 03 are presented in Figs. 5.67, 5.68 and 5.69, respectively. These figures present the plastic strain contours of $\varepsilon^p{}_{yy}$ and $\varepsilon^p{}_{zz}$. Figure 5.67 shows the strain values along the line L4. It is noticed that all the plastic strains are accumulated in the center of the FZ, while they reduce to zero at a distance of 2.5 mm and 10 mm on each side of the weld center line for test plates and T-joint, respectively; thereby defining the limits of plastic deformation zone. This observation is completely in accordance with the material plastification temperature of 150°C in Fig. 5.65; because Fig. 5.30 (test case 03) shows that the thermocouple TC2 (installed at 7 mm from the weld center line) surpasses the temperature of 150°C where a very low level of plastic strains is observed; while TC3 (installed at 10 mm from the weld center line) remains below 150°C and hence no plastic strain is recorded. Similarly, the thermocouple TC1 (installed at 3 mm from the weld center line) for test cases 01A (Fig. 5.22) and 02A (Fig. 5.26) shows the peak temperature value around 120°C (less than 150°C) and hence no plastic strains are noted at a distance of 3 mm for both the test cases. Here, $\varepsilon^p{}_{xx}$ remains close to zero throughout for all the test cases; $\varepsilon^p{}_{yy}$ and $\varepsilon^p{}_{zz}$ strains, however, show considerably higher values in and near the FZ.

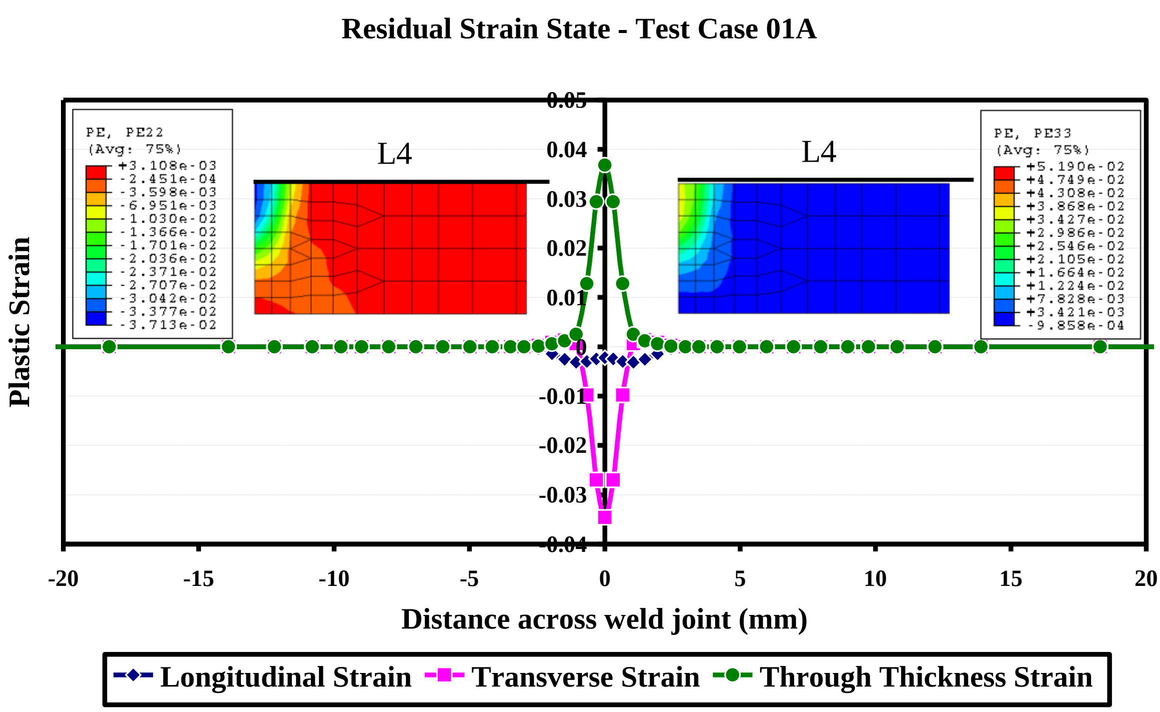

Figure 5.67. Residual plastic strain state – Test Case 01A

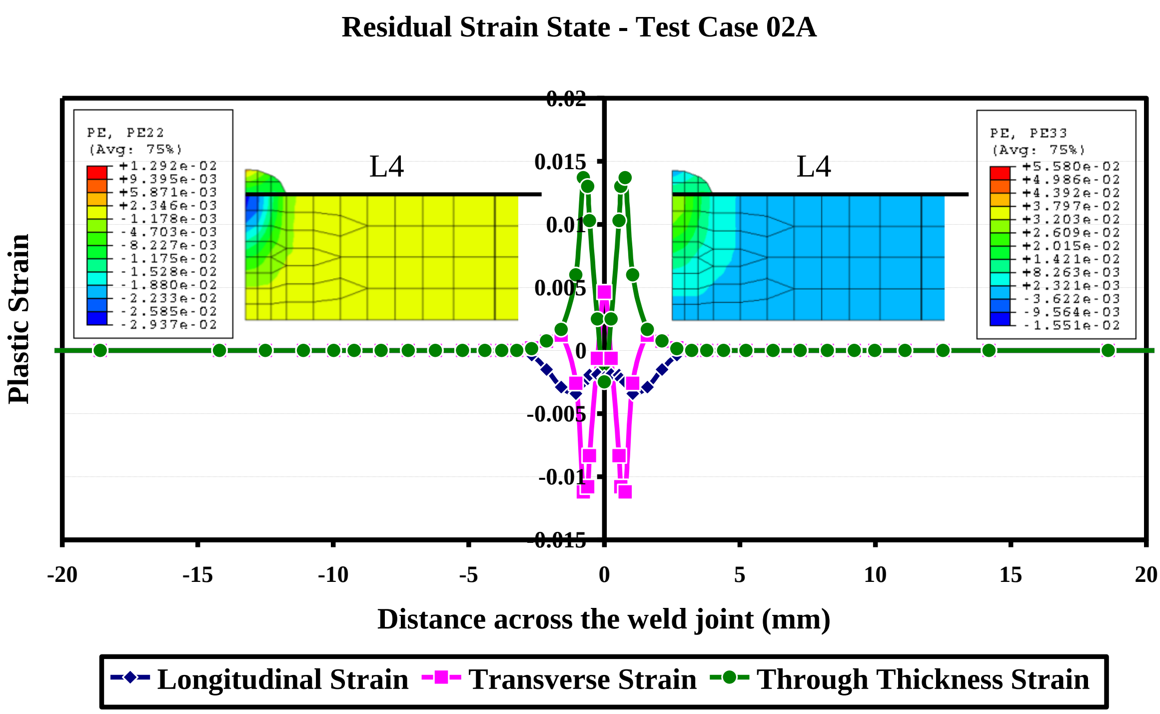

Figure 5.68. Residual plastic strain state – Test Case 02A

The effect of gradually increasing beam power from test case 01A to 03 is also evident in strain distribution pattern. For instance, ε^{p}_{yy} in test case 01A is entirely compressive in FZ; however, it tends to be tensile in test case 02A and its tensile nature is even more pronounced in test case 03. An exact opposite behaviour is observed for ε^{p}_{zz}.

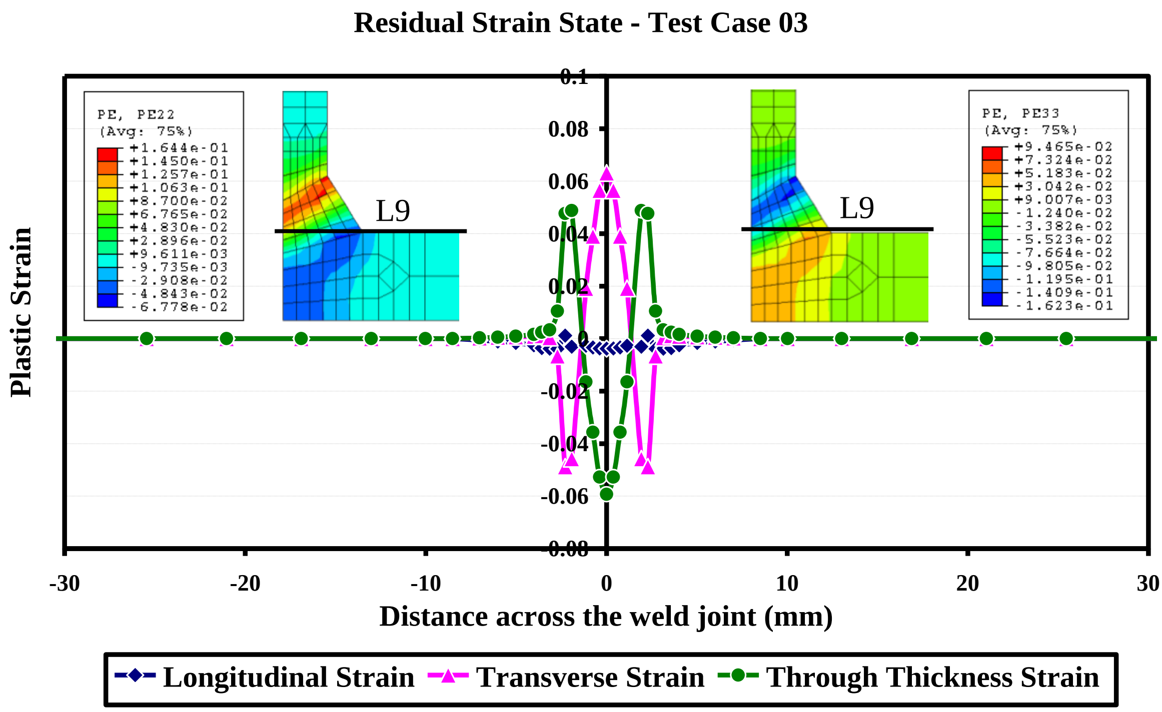

Figure 5.69. Residual plastic strain state – Test Case 03

5.7 Metallurgical Aspects – Sysweld®

The key feature of the Sysweld® 2008 code, which sets it apart from other commercial finite element software, is the ability to model metallurgical transformations. Metallurgical transformations introduce volume changes as well as the change in mechanical properties due to phase transformations. Also included is a library of metallurgical models for both steel and aluminium. The metallurgical aspects of the simulation have, therefore, studied using this software.

Sysweld contains metallurgical models for recrystallization and dissolution of precipitates for aluminium alloys. Two models are dedicated to aluminium alloys with respect to their heat-treatability. First model is dedicated to the heat treatable alloys of series 2XXX, 6XXX and 7XXX; while the second model is intended for non-heat treatable (hardened by strain hardening) alloys of series 1XXX, 3XXX, 4XXX and 5XXX. Since the aluminium alloy under investigation is 6056-T4, only the first type of model is being discussed here, which allows the simulation of precipitate dissolution kinetics. This model is described as follows:

$$x = \left(\frac{t}{t_r^*}\right)^n \exp\left[\left(\frac{Q_s}{R} + \frac{nQ_d}{R}\right)\cdot\left(\frac{1}{T_r} - \frac{1}{T}\right)\right] \qquad (5.30)$$

Where,

x : dissolute fraction of precipitates,

t : time,

n : parameter which can be dependent on x : $n(x) = 0.5 - a.x^b$,

T : temperature in Kelvin,

R : constant of perfect gas,

t_r* : time necessary for the total dissolution of precipitates at a given temperature T_r,

Q_s : enthalpy of metastable solvus,

Q_d : energy for activation of diffusion process of one of alloy elements (the less mobile).

In Sysweld the metallurgical and thermal calculations are coupled so that at each temperature the phase proportions are calculated. The thermal characteristics are determined using a linear mixture law of the amount of each phase present. The enthalpy of each phase includes the latent heat of transformation and inertia effects. The mechanical simulation is performed using temperature fields calculated during thermo-metallurgical simulation. Sysweld contains database of material properties for alloy type Al-Mg-Si for various phases.

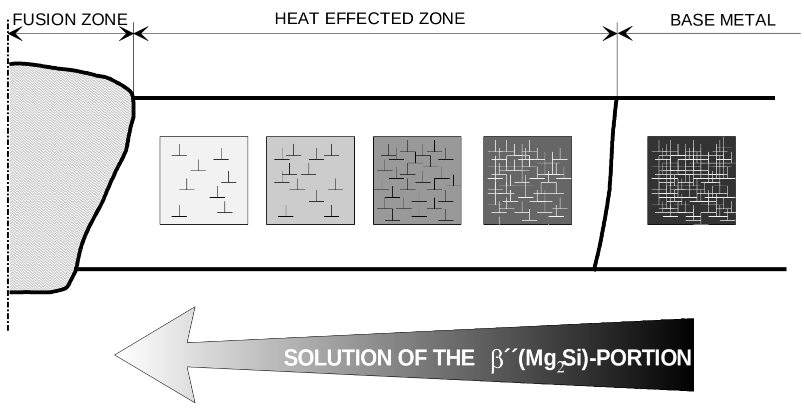

Figure 5.70. Reaction kinetics of series 6XXX

Reaction kinetics of series 6XXX is shown in Fig. 5.70, where three distinct phases are demarcated. The unaffected phase, labelled as Base Metal (BM), contains precipitates of Mg_2Si. The heat affected zone (HAZ) shows gradual dissolution of precipitates towards the fusion zone (FZ); while FZ contains different characteristics depending upon the type of filler wire used. Thermo-mechanical properties are applied based upon the phase proportions calculated during thermo-metallurgical simulation.

Test case 03D (T-joint with no tacks) has been simulated using Sysweld with three distinct phases. The material properties used for BM are similar to those of Abaqus simulation (section 5.3). The properties of HAZ and FZ are adopted from the database provided by Sysweld. Based on this criterion, the three phases can be defined as follows:

- Phase 1: BM, Precipitation hardened – initial material
- Phase 2: HAZ, Precipitates dissolution – weak material
- Phase 3: FZ, Precipitation hardened only after cooling – new (filler) material

The heat source, loading and boundary conditions used are same as those of Abaqus simulation. It is to be noted that material properties of different phases were used during mechanical simulation only, whereas thermal simulation employed similar thermal properties for each phase (section 5.3). Integration of identical thermal properties for each phase yielded similar thermal histories and FZ as observed in Abaqus simulation (Figs. 5.21, 5.30, 5.31, and 5.32). For instance, comparison of FZ as calculated through Abaqus and Sysweld are shown in Fig. 5.71. (See Annex B.3. for temperature histories at TCs)

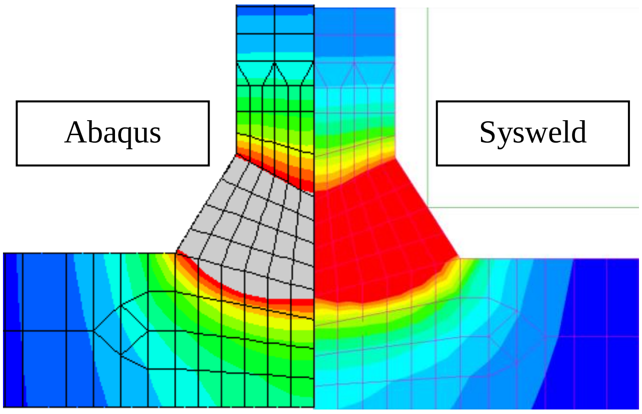

Figure 5.71. FZ comparison for Abaqus and Sysweld simulations

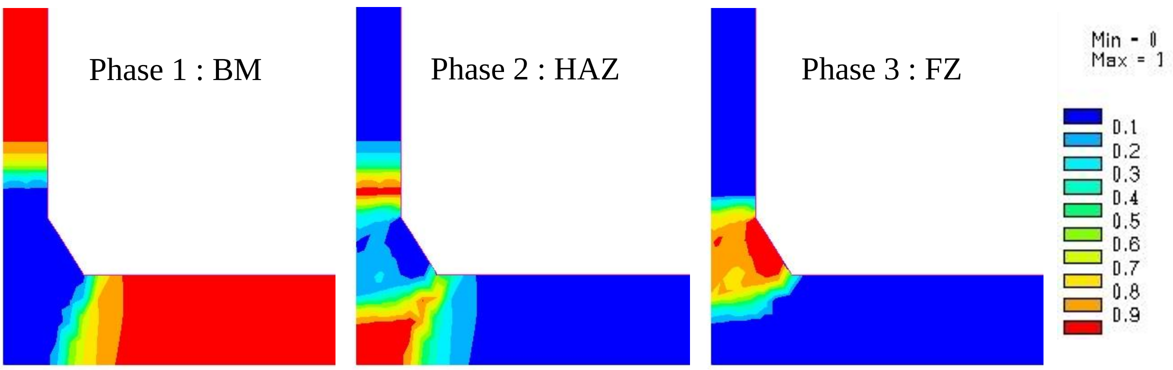

Figure 5.72. Metallurgical phase fractions

Minute differences are observed due to different mesh scale only. Grey coloured region marks FZ of Abaqus simulation while red coloured region shows FZ of Sysweld simulation. Figure 5.72 presents residual phase fractions appearing as a result of welding.

Figure 5.73 presents phase transformations as a function of time for all the three phases during a complete heating and cooling cycle. These phase transformations are shown for a point carefully selected in the region where all the three phases appear. It is observed from the curve that all the transformations take place during heating only, while no transformation is present during cooling. Moreover, these transformations start upon approaching a temperature of 272°C while they stop at the peak temperature of 562°C. In a complete transformation, phase 1 reduces from 100% to 5%; while phases 2 and 3 increase from 0% to 70% and 25%, respectively.

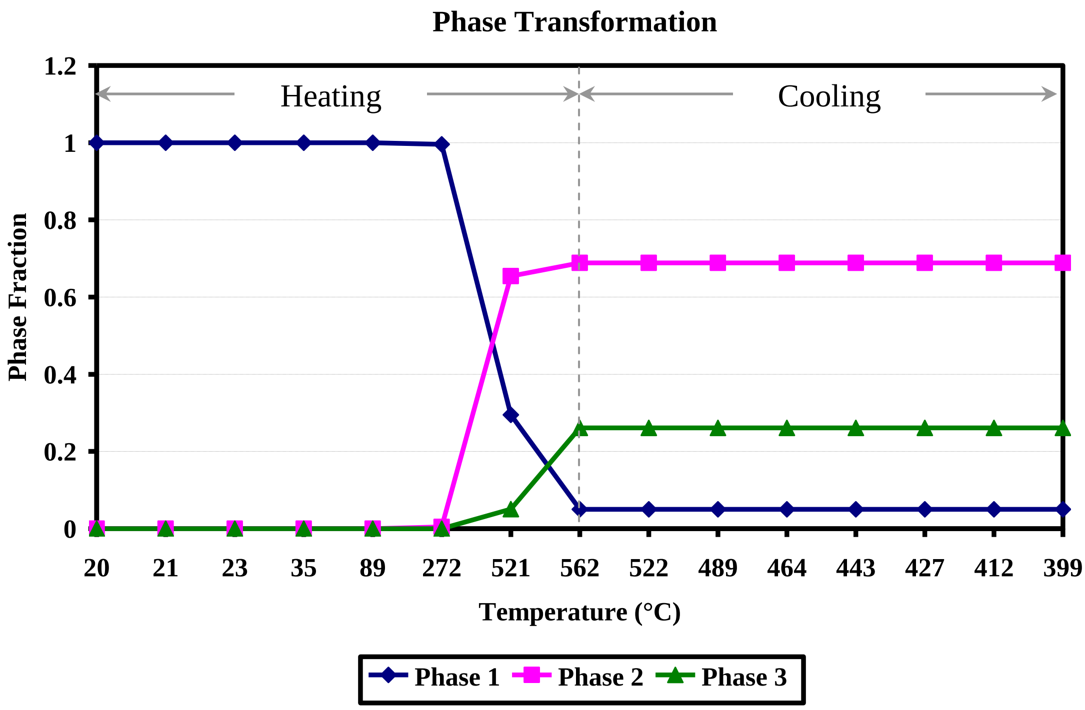

Figure 5.73. Phase transformations as a function of temperature

Figure 5.74 presents the comparison of experimental and simulated results, as obtained using Abaqus and Sysweld, for in-plane displacements. Figure 5.47 is reproduced here with an additional curve of Sysweld simulation. Good comparison is observed for both the simulated curves, however, the displacement values with phase transformations (Sysweld) are slightly higher than without transformations (Abaqus).

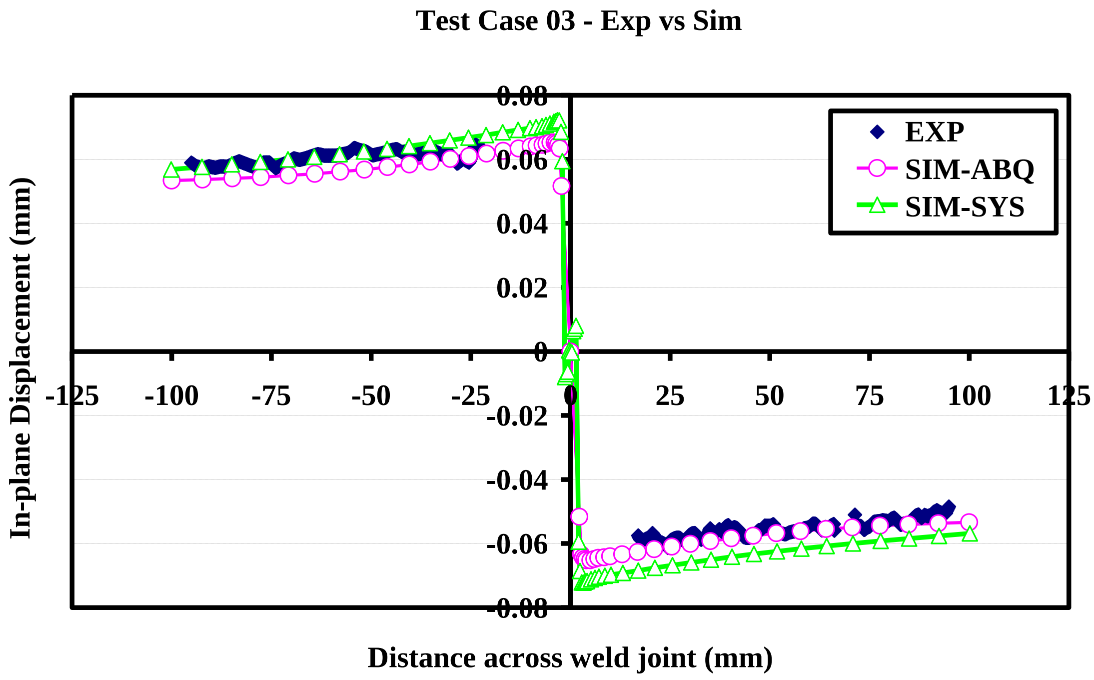

Figure 5.74. Comparison of in-plane displacements from Abaqus and Sysweld

Figure 5.75 presents contours of out-of-plane displacement. In comparison to Figs. 5.38 and 5.44, displacement values predicted from Sysweld are of the same order (~0.20 mm); however, the shape of deformed T-joint is a bit different. For example, Abaqus predicts maximum displacement towards the end of welding while Sysweld predicts the same towards the start of welding.

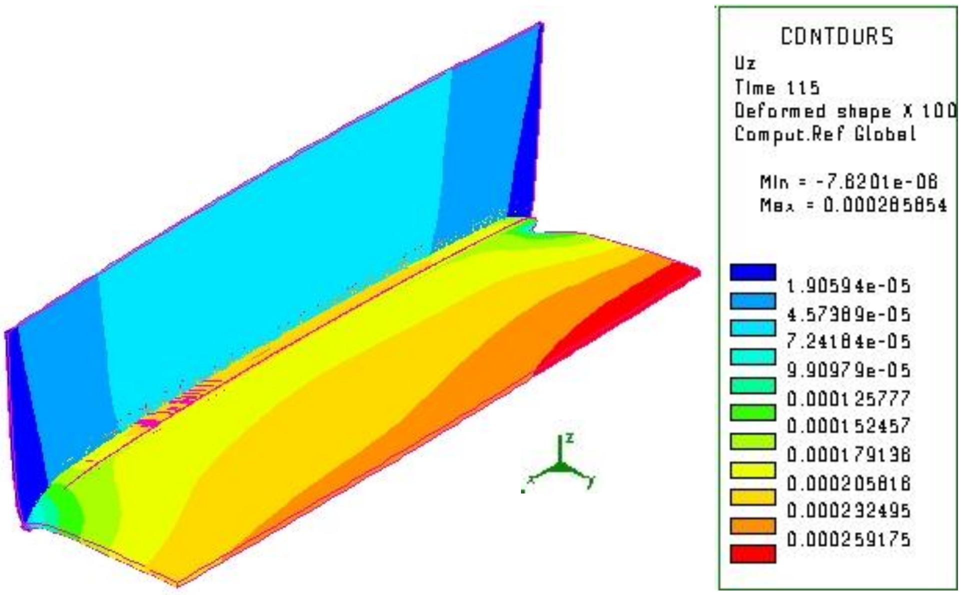

Figure 5.75. Contours of out-of-plane displacements from Sysweld

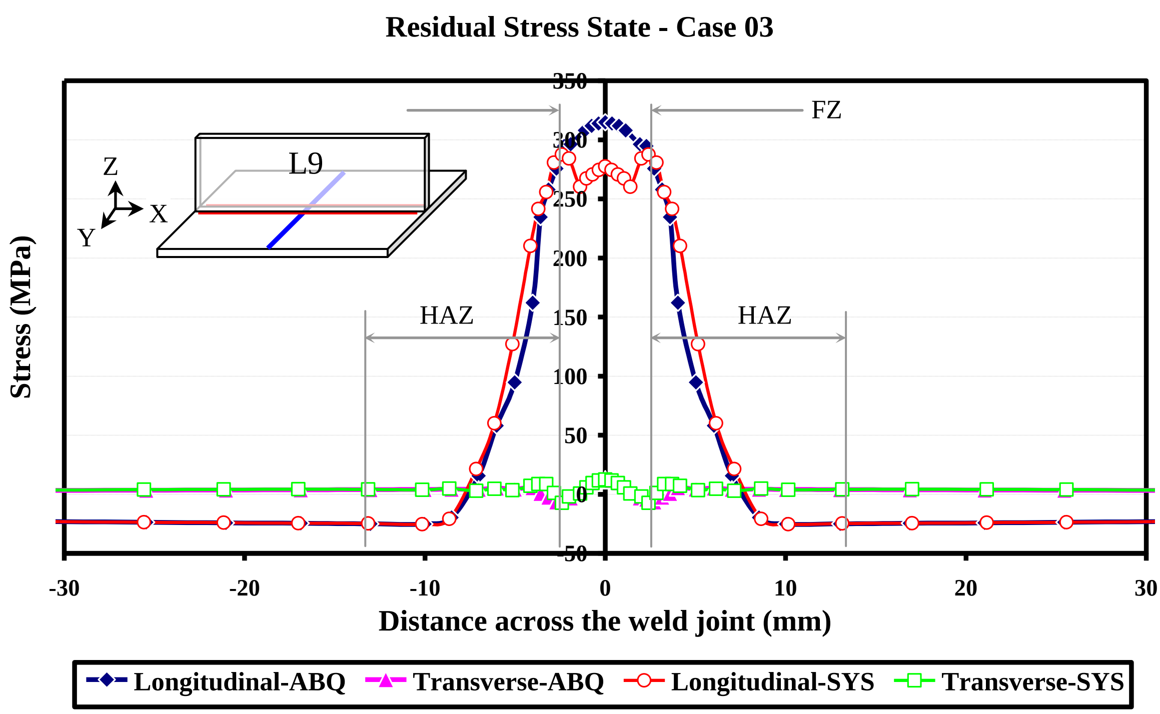

Figure 5.76. Comparison of residual stress state from Abaqus and Sysweld simulations

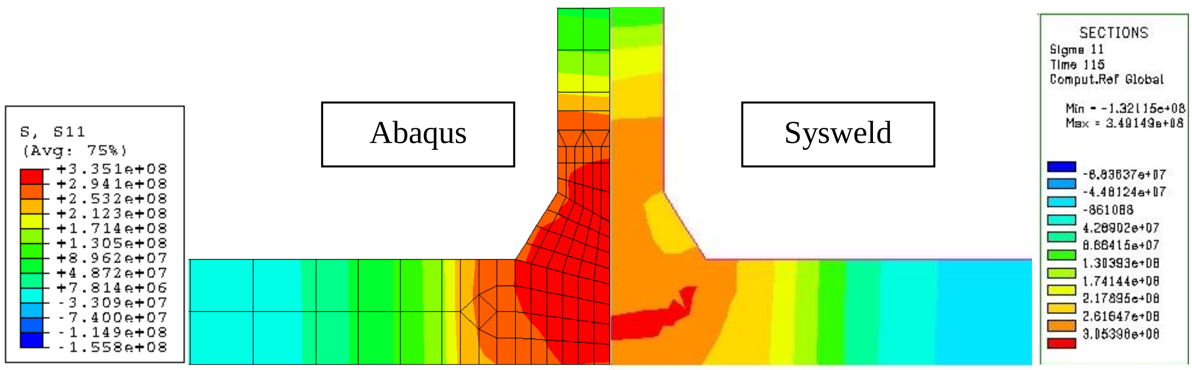

Figure 5.77. Comparison of σ_{xx} contours from Abaqus and Sysweld simulations

The comparison of predicted residual stress states from Abaqus and Sysweld is shown in Fig. 5.76. Abaqus results are reproduced from Fig. 5.61. It is observed that the residual stress state changes very little in HAZ; however, in FZ the longitudinal stresses (σ_{xx}) decrease significantly due to phase transformations. Nevertheless, the transverse stresses (σ_{yy}) show insignificant difference. The longitudinal stress (σ_{xx}) contours from Abaqus and Sysweld are juxtaposed in Fig. 5.77. It is observed that stress distribution from Abaqus simulation (without phase transformations) remains almost constant in and near the FZ; whereas Sysweld simulation (with phase transformations) demonstrates variation in stress distribution in FZ as well as HAZ.

5.8 Conclusions

The conclusions inferred from the simulation results are as follows:

- Comparisons of weld pool geometry with simulated FZ for various test cases justify the heat source models for test plates and T-joints. Likewise, the applied heat flux and thermal boundary conditions are well integrated so as to calculate the resultant temperature fields in close approximation to the experimentally recorded thermal histories. A few discrepancies may be attributed to the simplifications assumed during simulation.

- FE simulation results of mechanical analysis and the experimental results for out-of-plane and in-plane displacements are found in good agreement with each other, for a suction pressure of 0.8 bar and a friction coefficient of 0.57. This, in turn, establishes the reliability of the mechanical model, material properties, constitutive laws and mechanical boundary conditions. It is also noticed that the out-of-plane displacements are insensitive to the change in friction coefficient; however, variation in suction pressure may impart a systematic change in their magnitude, yet the effect is found to be quite low.

- The simulated in-plane displacements at LVDT positions illustrate slight mismatch with experimental values. This may also be attributed to the simplifications assumed during mechanical analysis. For instance, assuming a uniform distribution of suction pressure and no slip / glide in the direction of welding are likely to cause difference in displacement evolution. However, the qualitative analysis shows comparable expansion and contraction occurrences. Additionally, the residual displacements as measured from image correlation technique present good agreement with simulated values.

- The study of the example cases with convex and concave profiles of test plates before welding suggests that initial geometric imperfections influence the residual distortion state. However, the use of EP or EVP formulation yields negligible difference in displacement levels for the material AA 6056-T4.

- The experimental observation that a considerable amount of heat energy dissipates during melting is also validated by simulation. From both the perspectives, it is found that fusion welding case (Test case 01A) yields out-of-plane displacement values 20% higher than filler welding case (Test case 02A). The qualitative analysis of out-of-plane displacements for T-joint welding (Test case 03) shows comparable results with experimental ones.

- The simulated residual in-plane displacements demonstrate good conformance to the ones obtained through image correlation technique for all the test cases (test cases 01A, 02B and 03). It is also noticed that these displacements are proportional to the amount of heat energy supplied during welding.

- The longitudinal residual stresses, σ_{xx}, in all the cases are as high as the yield strength of the material. They are largely tensile in FZ and tend to be compressive in HAZ. Compared to all other stress components, they will have strongest influence over the distortion level and failure of the material. It is also observed that the longitudinal residual stresses, σ_{xx}, are proportional to the heat source intensity; i.e. with increasing laser beam power the stress level increases.

- The transverse residual stresses, σ_{yy}, are found to be the next important stress component that may affect the distortion pattern of the material. It is observed that they are initially compressive in FZ (test case 01A), but tend to be tensile (test case 03) in nature with increasing beam intensity.

- The through-thickness residual stresses, σ_{zz}, and other stress components namely σ_{xy}, σ_{xz} and σ_{yz} have negligible magnitudes and, hence, are not likely to contribute significantly in the deformation of the material.

- Laser-beam welding with keyhole formation is characterised by a more pronounced dominance of the longitudinal residual stresses over the transverse residual stresses.

- Residual plastic strains remain confined in the FZ and to a very limited part of HAZ. It is observed that plastic strains appear in the component only above a critical temperature of 150°C, which is called as plastification temperature in this work.

- The study of metallurgical aspects of simulation using Sysweld illustrates the presence of various precipitate / dissolution phases within the FZ and HAZ.

- The comparison of in-plane displacements of Abaqus and Sysweld simulations yield almost identical results. Slight differences, however, may be attributed to the effect of phase transformations.

- The distribution of out-of-plane displacements is somewhat different for Abaqus and Sysweld simulations. Here, the former suggests maximum displacements towards the end of welding, while the latter predicts the same towards the start of welding.

- In comparison to Abaqus simulation, the difference in stress distribution is observed within the FZ only; while outside the FZ, the stress distribution remains almost identical for both the simulation strategies.

CHAPTER 6

SYNOPSES AND PERSPECTIVES

Contents

Synopses and Perspectives

The work presented in this dissertation focuses upon the selective aspects of the problem under investigation. Like any other research work produced in the field of science and technology, there always remains a margin for improvement; this dissertation is not an exception to the rule. Brief synopses of the efforts made, along with the perspectives for future work are described in this chapter.

6.1 Thermo-Mechanical Characterisation – AA 6056-T4

Monotonic tensile tests were performed on the specimens made out of AA 6056-T4 sheets (thickness: 2.5 mm) in order to characterise thermo-mechanical properties of the material at various temperatures and strain rates. These tests were performed at temperatures ranging between 20°C and 450°C with high and low strain rates. A conventional tensile testing machine with induction heating and Gleeble system with Joule heating were used to realize the tests. It is observed that heating rate plays an important role in affecting the material properties of the precipitation hardened alloys.

Although monotonic tensile tests provide sufficient information regarding the material properties; yet the hardening behaviour either isotropic or kinematic may only be investigated through cyclic tests i.e. by tensile and compression loadings. Since the specimens were cut out of thin sheets of AA 6056-T4, compression tests could not be performed due to the risk of buckling. It is, therefore, recommended that either the cylindrical specimens be used for cyclic testing or torsion tests be carried out on same specimens to capture the hardening behaviour of material. Further material characterisation may also be performed for different phases that appear during heating and cooling of specimens. This requires very fast heating to the desired temperature and then performing the tests based upon various dwell times so as to allow partial or complete transformation of phases. Thermal shock type loading may also be provided to the specimens before carrying out actual tensile tests in order to study the effect of thermal histories.

6.2 Experimental Campaigns of Laser Beam Welding

Highly instrumented experimental campaigns of laser beam welding of test plates and T-joints were carried out in collaboration with IUT du Creusot. Efforts were made to gather as much experimental data as possible. Measurements were taken before, during and after the welding operation. An extensive database of experimental results was prepared so as to serve as a benchmark for numerical models.

Some observations with respect to temperature and displacement measurements are being addressed in this section, which are required to be taken care of for any further work. For example, the infra-red camera used to determine the weld pool surface temperature was equipped with a filter that could only record the temperatures in the range of 300-1700°C. Since keyhole welding of aluminium alloys is likely to surpass the boiling point (~2400°C) of the material, the precise measurement of weld pool temperature may be achieved using a filter capable of measuring temperatures up to 2500°C.

Similarly, the results of high speed camera may only be used for qualitative analysis of material loss from weld pool due to random spatter produced over the length of weld seam. It could be of interest, especially from simulation point of view, to know the exact amount of material loss from the welded specimen. This may further help developing a more reliable numerical model.

LVDT sensors are found to be highly sensitive to the slip / glide of test specimens and the out-of-plane rotation of test plates. The problem arose because the in-plane movements of test specimens were not restricted. It was only due to the combined effect of pressure applied at the bottom surface of plates and the friction at the plate-support interface that the test specimens remained in position while welding. It is, therefore, expected that constraints applied to in-plane slip may improve the displacement results at LVDT positions.

The results of image correlation technique led to excellent capturing of 3D global in-plane and out-of-plane displacements. This technique was, however, employed only upon the regions 15 mm away from the weld center line on the upper surface of plates. The assumption that out-of-plane displacements would evolve linearly within this 15 mm wide region worked well for welding of test plates; but for T-joints this assumption fell short of capturing the effect of 'seating' phenomenon of stiffener. It is, therefore, recommended that image correlation of the entire bottom surface be also performed in order to determine the displacement evolution immediately beneath the FZ and HAZ.

6.3 Numerical Simulation of Laser Beam Welding

Numerical simulation was performed for most of the test cases assuming elasto-plastic and elasto-viscoplastic law with isotropic hardening behaviour. FE models were validated using experimental database and the residual stress and strain states of test plates and T-joints were predicted.

Three dimensional elements with linear interpolation between the nodes were used both for thermal and mechanical analyses. Improvement in results may be expected with quadratic interpolation between nodes for mechanical analysis, yet this would require a highly powerful computer and increased computation time. In addition, the use of shell elements may help reducing the overall computation time.

Literature survey [JOSE][DARC] suggests that isotropic hardening behaviour be used for numerical simulation of AA 6056-T4. The use of the isotropic hardening model assumes that the yield surface will expand with increasing plastic strain but will retain the same initial shape. This could lead to over-prediction of the residual stresses. The effect of kinematic hardening model over the residual stress state may also be investigated through simulation. A better choice, however, may only be made upon the availability of experimentally measured stress values.

Some simulation work is also produced as regards to T-joints with tack welds, but is not presented in this dissertation. This is because the effect of tack welds requires special care during modelling as they depending upon their position and length significantly influence the distortion pattern and stress distribution within the model. Due to the complex nature of welded and un-welded locations in a single weld bead, the separation and contact of plate-stiffener assembly needs to be taken care of properly. The preliminary simulations are available within the hard-disk of database for AA 6056-T4 (see Annex A).

This dissertation deals with laboratory scale specimens; however, in manufacturing industry the specimen size is seldom so small. Therefore, the numerical models detailed here may be considered as local models and may serve as building blocks for a global model with configuration closer to the one used industrially.

Bibliography

[ABAQ] ABAQUS Ver 6.6, 6.7. User's manual. Hibbit, Karlsson & Sorensen.

[ADRT] Adrien, 2004. Airbus A380: l'épopée d'un géant du ciel. Available online from : http://www.techno-science.net/?onglet=articles&article=2 (accessed on 14th Jan. 09)

[ANDB] Andersson, B.A.B., 1978. Thermal Stresses in a Submerged-arc Welded Joint considering Phase Transformations. ASME J. Engg. Mater. Technol., 100, pp. 356 – 362.

[ASSA] Asserin-Lebert, A., 2005. Etude Expérimentale et Prévision des Mécanismes de Rupture des Tôles et des Joints Soudés Bout à Bout en Alliage d'Aluminium. Ph.D. Thesis, Ecole Nationale Supérieure des Mines de Paris.

[BEAR] Beardmore, R., 2007. Tribology index, friction coefficients. Site address: http://www.roymech.co.uk/Useful_Tables/Tribology/co_of_frict.htm (accessed on 4 April 2007).

[BECT] Beck, T., Rau, K., 2008. Int. J. Fatigue, 30, pp. 226–233.

[BELG] Bel'chuk, G.A., Gatovskii, K.M., Polishko, G.Yu., Rybin, Yu.I., Nov; 1977. Application of the Finite Element Method to Solve Problems of Welding Deformations and Stresses. Avtomaticheskaya Svarka, N11.

[BERD] Berglund, D., 2001. Simulation of Welding and Stress Relief Heat Treating in the Development of Aerospace Components. Licentiate Thesis, Lulea Tekniska Universitet.

[BERJ] Bergheau, J.M., 2004. Modélisation Numérique des Procédés de Soudage. Doc. BM7758, St. Etienne, France.

[BER1] Bergheau, J.M., Robin, V., Boitout, F., 2000. Finite Element Simulation of Processes involving Moving Heat Sources. Application to Welding and Surface Treatment, J. Shanghai Jiaotong University, E-5, 1, pp. 114 – 122.

[BRUD] Bru, D., Devaux, J., Bergheau, J.M., Pont, D., 1997. Influence of Material Properties at High Temperatures on the Modelling of Welding Residual Stress and Deformation State. Mathematical Modelling of Weld Phenomenon, 3, pp. 456 – 463.

[BOUP] Bouchard, P.J., 2007. Validated residual stress profiles for fracture assessments of stainless steel pipe girth welds. Int. J. Press. Vessel. Pip., 84, pp. 195 – 222.

[BOU1] Bouchard, P.J., 2008. Code characterisation of weld residual stress levels and the problem of innate scatter, International Journal of Pressure Vessels and Piping, 85, pp. 152 – 162.

[BOU2] Bouchard, P.J., 2009. The NeT bead-on-plate benchmark for weld residual stress simulation. International Journal of Pressure Vessels and Piping, 86, pp. 31 – 42.

[CAST] Cast3m, Finite Element Code, CEA France.

[CAVN] Cavallo, N., 1998. Contribution à la Validation Expérimentale de Modèles Décrivant la ZAT lors d'une Opération de Soudage. Ph.D. Thesis, Institut National des Sciences Appliquées de Lyon.

[CARD] Carrouge, D., 2002. TIG Welding of Supermartensitic Stainless Steel. Ph. D. Thesis, University of Cambridge.

[CHIS] Chiang, S., Albright, C.E., Aug 1998. Light-material Interactions in Laser Materials Processing. Gas Flow and Chemical Lasers Proceedings, 7th International Symposium. Vienna, Austria. pp. 522 – 531.

[CODA] Code_Aster, Finite Element Code, EDF France.

[CORM] Coret, M., 2001. Etude Expérimentale et Simulation de la Plasticité de Transformation et du Comportement Multiphasé de l'Acier de Cuve 16MnD5 sous Chargement Multiaxial Anisotherme. Ph.D. Thesis. Ecole Normale Supérieur de Cachan.

[DARC] Darcourt, C., 2005. Simulation Numérique du Soudage Laser de Structures Aéronautiques. Ph.D. Thesis, Université de Technologie Compiègne, France.

[DEPL] Depradeux, L., 2004. Simulation Numérique du Soudage en vue de la Prédiction des Distorsions et Contraintes Résiduelles – Validation Expérimentale sur Cas Tests de Référence – Acier 316L. Ph.D. Thesis, Institut National des Sciences Appliquées de Lyon.

[DEOM] Deo, M. V., Michaleris, P., Sun, J., 2003. Prediction of buckling distortion of welded structures. Sci. Technol. Weld. Joining, 8, pp. 55 – 61.

[DITJ] Dittberner, J-J., 2004. Laser Welding of Light Alloys. Presentation, Aluform Congress. Paris.

[DONP] Dong, P., 2005. Residual Stresses and Distortion in Welded Structures: A Perspective for Engineering Applications. Sci. Technol. Weld. Joining, 10, pp. 389 – 398.

[DUAY] Duan, Y., 2008. Modélisation Numérique des Distorsions Résiduelles de Soudage de Structures Minces. Ph.D. Thesis, Ecole Nationale Supérieure des Mines, Saint-Etienne.

[ELAW] El-Ahmar, W., 2007. Robustesse de la Simulation Numérique du Soudage TIG de Structures 3D en Acier 316L. Ph.D. Thesis, Institut National des Sciences Appliquées de Lyon.

[ELA1] El-Ahmar, W., Jullien, J.F., Gilles, P., Jul. 2006. Robustness of Residual Stress Computation : From Satoh Test To Welding Plate. ASME Pressure Vessels and Piping Division Conference, Vancouver.

[FABD] Fabrègue, D., 2004. Microstructure et Fissuration à Chaud lors du Soudage Laser d'Alliages d'Aluminium 6000. Ph.D. Thesis, Institut National Polytechnique de Grenoble.

[FERP] Ferro, P., Zambon, A., Bonollo, F., 2005. Investigation of Electron-beam Welding in Wrought Inconel 706 – Experimental and Numerical Analysis. Materials Science and Engineering A 392, pp. 94 – 105.

[FRAJ] Francis, J.D., 2002. Welding Simulations of Aluminum Alloy Joints by Finite Element Analysis. Masters Thesis, Blacksburg, Virginia.

[FREJ] Free, J.A., Goff, R.F.D.P., 1989. Predicting residual stresses in multi-pass weldments with the finite-element method. Comput. Struct., 32, pp. 365 – 378.

[FRIE] Friedman, E., 1975. Thermo-mechanical Analysis of the Welding Process using the Finite Element Method. Trans. ASME, J. Pressure Vessel Technology, pp. 206 – 213.

[GALC] Gallais, C., 2005. Joints Soudés par Friction Malaxage d'Alliages d'Aluminium de la Série 6xxx : Caractérisation et Modélisation. Ph.D. Thesis, Institut National Polytechnique de Grenoble.

[GATK] Gatovskii, K.M., 1973. Determination of Welding Stresses and Strain with Allowance for Structural Transformations of the Metal. Welding Production (English translation of Svarochnoe Proizvodstvo), 20, N11.

[GILP] Gilles, P., El-Ahmar, W., Jullien, J-F., 2009. Robustness Analyses of Numerical Simulation of Fusion Welding NeT-TG1 Application: ''Single Weld-Bead-on-Plate". International Journal of Pressure Vessels and Piping, doi:10.1016/j.ijpvp.2008.11.012.

[GOLJ] Goldak, J., Oddy, A., Gu, M., Ma, W., Mashaie, A., Hughes, E., 1992. Coupling Heat Transfer, Microstructure Evolution and Thermal Stress Analysis in Weld Mechanics. Proc. of IUTAM Symp. Mechanical effects of welding, Springer Verlag, Berlin.

[GOL1] Goldak, J., Breiguine, V., Dai, N., Zhou, J., Jul. 1996. Thermal Stress Analysis in Welds for Hot Cracking. American Society of Mechanical Engineers, PVP, ASME Pressure Vessels and Piping Conference, Montreal.

[GOL2] Goldak, J., Chakravati, A., Bibby, M., 1984. A New Finite Element Model for Welding Heat Sources. Metallurgical Transactions, 15B, pp. 299 – 305.

[GRON] Grong, 1994. Metallurgical Modelling of Welding. The Institute of Materials, Cambridge.

[HERR] Hertzberg, R.W., 1996. Deformation and Fracture Mechanics of Engineering Materials. John Wiley & Sons Inc., New York, pp. 166 – 167.

[HIBH] Hibbitt, H., Marcal, P., 1973. A Numerical Thermo-mechanical Model for the Welding and Subsequent Loading of a Fabricated Structure. Comput. Struct., 3, pp. 1145 – 1174.

[HONK] Hong, K., Weckman, D.C., Strong, A.B., 1998. The Influence of Thermofluids Phenomena in Gas Tungsten Arc Welds in High and Low Thermal Conductivity Metals. Canadian Metallurgical Quarterly, 37, No. 3 – 4, pp. 293 – 303.

[HUAT] Huang, T. D., Dong, P., DeCan., L., Harwig, D., Kumar, R., 2004. Fabrication and Engineering Technology for Lightweight Ship Structures: 1. Distortions and Residual Stresses in Panel Fabrication. J. Ship Production, 20, pp. 43 – 59.

[JIAW] Jiang, W., Yahiaoui, K., Hall, F.R., Laoui, T., 2005. Comparison of Sequentially and Fully Coupled Generalised Plane Strain FE Modelling of Multi-pass Welding. Proc. NAFEMS World Congr., Malta.

[JOSE] Josserand, E., Jullien, J.F., Nélias, D., Deloison, D., 2007. Numerical Simulation of Welding-induced Distortios taking into account Industrial Clamping Conditions. Mathematical Modelling of Weld Phenomenon, 8, pp. 1105 – 1124.

[KANM] Kane, M., 1996. Caractérisation du Plasma d'interaction Laser-matière obtenu lors du Soudage de Cibles Métalliques – Contribution au Contrôle du Procédé. Ph.D. Thesis, Université de Strasbourg 1, France.

[LEBJ] Leblond, J.B., 1989. Simulation Numérique du Soudage, Modèle de Viscoplasticité. FRAMASOFT, N°CSS.L.N.T.89/4015.

[LEB1] Leblond, J.B., Devaux, J.C., 1989. Mathematical Modelling of Transformation Plasticity in Steels I – Case of Ideal Plastic Phases. Int. J. of Plasticity, 5, pp. 551 – 572.

[LEB2] Leblond, J.B., 1989. Mathematical Modelling of Transformation Plasticity in Steels II – Coupling with Strain Hardening Phenomena. Int. J. of Plasticity, 5, pp. 573 – 591.

[LEB3] Leblond, J.B., Mottet, G., Devaux, J.C., 1986. A Theoretical and Numerical Approach to the Plastic Behaviour of Steels during Phase Transformation II – Study of Classical Plasticity for Ideal-Plastic Phases. J. Mech. Phys. Solids, 34, N°4, pp. 411 – 432.

[LEDH] Ledbetter, H.M., 1982. Cryogenics, 22, pp. 653 – 656.

[LEMJ] Lemaître, J., Chaboche, J.L., 1985. Mécanique des Matériaux Solides. France.

[LINL] Lindgren, L.-E., 1985. Deformations and Stresses in Butt Welding of Plates. Ph.D. Thesis. Luleå, Sweden.

[LIN1] Lindgren, L.-E., Haggblad, H.A., Josefson, B.L., Karlson, L., 2002. Thermo-mechanical FE-analysis of Residual Stresses and Stress Redistribution in Butt Welding of a Copper Canister for Spent Nuclear Fuel. Nuclear Engineering and Design, 212, pp. 401 – 408.

[LIN2] Lindgren, L.-E., 2002. Modelling for Residual Stresses and Deformations due to Welding – Knowing What Isn't Necessary to Know. Mathematical Modelling of Weld Phenomena, 6, H. Cerjak ed., pp. 491 – 518.

[LIN3] Lindgren, L.-E., 2001. Finite Element Modelling and Simulation of Welding, Part 1 : Increased Complexity. Journal of Thermal Stresses, 24, pp. 141 – 192.

[LIN4] Lindgren, L.-E., 2001. Finite Element Modelling and Simulation of Welding, Part 2 : Improved Material Modelling. Journal of Thermal Stresses, 24, pp. 195 – 231.

[LIN5] Lindgren, L.-E., 2001. Finite Element Modelling and Simulation of Welding, Part 3 : Efficiency and Integration. Journal of Thermal Stresses, 24, pp. 305 – 334.

[LIN6] Lindgren, L.-E., Haggblad, H.A., McDill, J.M.J., Oddy, A.S., 1997. Automatic Remeshing for Three-dimensional Finite Element Simulation of Welding. Comput. Methods Appl. Mech. Eng., 147, pp. 401 – 409.

[LUNA] Lundback, A., Runnemalm, H., 2005. Validation of Three-dimensional Finite Element Model for Electron Beam Welding of Inconel 718. Science and Technology of Welding & Joining 10(6), pp. 717 – 724(8).

[MACJ] Mackerle, J., 1996. Finite Element Analysis and Simulation of Welding: A Bibliography (1976–1996). Modelling Simul. Mater. Sci. Eng., 4, pp. 501 – 503.

[MAC1] Mackerle, J., 2002. Finite Element Analysis and Simulation of Welding – An Addendum: A Bibliography (1996–2001). Modelling Simul. Mater. Sci. Eng., 10, pp. 295 – 318.

[MAKV] Makhnenko, V.I., Oleinik, V.A., Nov. 1974. Analytical Evaluation of Nominal Stresses and Deformations Preceding the Failure of Round Plates. Prikladnaya Mekhanika, 10, N11, Rus.

[MAK1] Makhnenko, V.I., Velikoivanenko, E.A., Apr. 1975. Elasto-Plastic Deformations in the Thermal Effect Zone during Butt-Welding of Plates. Avtomaticheskaya Svarka, N4, Rus.

[MASK] Masubuchi, K., 1980. Analysis of Welded Structures – Residual Stresses, Distortions and their Consequences. Pergamon Press, New York.

[MAZJ] Maumder, J., 1993. Laser Beam Welding. ASM Handbook, Welding Brazing and Soldering, 6, pp. 262 – 269.

[MICP] Michaleris, P., DeBicarri, A., 1996. A Predictive Technique for Buckling Analysis of Thin Section Panels due to Welding. J. Ship Prod., 12, pp. 269 – 275.

[MOLT] Moltubakk, T., 1999. Strength Mismatch Effect on the Cleavage Fracture Toughness of the Heat Affected Zone of Steel Welds. Ph.D. Thesis, Trondheim.

[MONF] Montheillet, F., Jonas, J.J., 1996. Dynamic Recrystallization. Encyclopedia of Applied Physics, VCH Publishers, 16, pp. 205 – 225.

[NASM] Näsström, M.O., 1992. Thermo-mechanical Modelling of Welding with Experimental Verification. Ph.D. Thesis, Luleå, Sweden.

[NAS1] Nasstrom, M., Wikander, L., Karlsson, L., Lindgren, L. E., Goldak, J., 1991. Combined 3D and Shell Element Modelling of Welding. IUTAM Symp. on the Mechanical Effects of Welding, Lulea, Sweden, pp. 10 – 14.

[PETM] Petelet, M., 2007. Analyse de Sensibilité Globale de Modèles Thermomécaniques de Simulation Numérique du soudage. Ph.D. Thesis, Université de Bourgogne.

[PETS] Petit-Grostabussiat, S., 2000. Conséquences Mécaniques des Transformations Structurales des Alliages Ferreux. Ph.D. Thesis, Institut National des Sciences Appliquées de Lyon.

[PILA] Pilipenko, A., 2001. Computer Simulation of Residual Stress and Distortion of Thick Plates in Multi-electrode Submerged Arc Welding – Their Mitigation Techniques. Ph.D. Thesis, Norwegian University of Science and Technology, Trondheim, Norway.

[RADD] Radaj, D., 1992. Heat Effects of Welding. Pergamon Press, New York.

[RAD1] Radaj, D., 1989. Finite-element Analysis of Temperature Field, Residual Stresses and Distortion in Welding. Weld. Res. Abroad, 35, pp. 31 – 38.

[RAD2] Radaj, D., 2002. Integrated Finite Element Analysis of Welding Residual Stress and Distortion. Mathematical Modelling of Weld Phenomenon 6, H. Cerjak ed., pp. 469 – 489.

[ROBY] Robert, Y., 2007. Simulation Numérique du Soudage du TA6V par Laser YAG Impulsionnel : Caractérisation Expérimentale et Modélisation des Aspects Thermomécanique Associées à ce Procédé. Ph.D. Thesis, Mines Paris Tech.

[ROSD] Rosenthal, D., 1935. Etude Théorique du Régime Thermique pendant la Soudure à l'Arc. Congress National des Sciences, Comptes Rendus, Bruxelles, 2, pp. 1277 – 1292.

[ROS1] Rosenthal, D., Schmerber, H., 1938. Thermal Study of Arc Welding. Welding Journal, 4, pp. 4 – 8.

[ROS2] Rosenthal, D., Schmerber, R., Apr. 1938. Thermal Study of Arc Welding – Experimental Verification of Theoretical Formulas. Am. Weld. Journ, pp. 2s – 8s.

[ROS3] Rosenthal, D., 1941. Mathematical Theory of Heat Distribution during Welding and Cutting. Welding Journal, 20, pp. 220s – 234s.

[ROS4] Rosenthal, D., 1946. Mathematical Theory of Moving Sources of Heat and its Application to Metal Treatments. Trans ASME, 68, pp. 849 – 866.

[RUNH] Runnemalm, H., 1999. Efficient Finite Element Modeling and Smulation of Welding. Ph.D. Thesis, Luleå.

[RUN1] Runnemalm, H., Hyun, S., 2000. Three-dimensional Welding Analysis using an Adaptive Mesh Scheme. Comput. Methods Appl. Mech. Eng. 189, pp. 515 – 523.

[RYKN] Rykalin, N.N., 1938. Temperature Distribution in the Elements of the Structure during Welding. Avtogennoe Delo, N5 and N7, Rus.

[RYK1] Rykalin, N.N., 1953. Berechnung der Wärmevorgänge beim Schweissen. Berlin, VEB Verlag Technik.

[RYBE] Rybicki, E. et al., 1977. A Finite Element Model for Residual Stresses in Girth-Butt Welded Pipes. Numerical Modeling of Manufacturing Processes, ASME Winter Annual Meeting.

[SHAS] Sharma, S.C., 2000. Metall. and Mater. Trans., v31A.

[SYSW] Sysweld Documentation, Finite Element Code, ESI Group, France.

[TEKP] Tekriwal, P., Mazumder, J., 1991. Transient and Residual Thermal Strain-stress Analysis of GMAW. ASME J. Engineering Materials and Technology, 113, pp. 336 – 343.

[TEMG] Tempus, G., May 2001. New Aluminium Alloys and Fuselage Structures in Aircraft Design. Presentation, Materials Day, Werkstoffe für Transport und Verkehr, ETH Zürich, Switzerland.

[TISF] Tissot, F.X., 1998. Etude Phénoménologique et Modélisation du Comportement du Bain de Fusion en Soudage TIG en vue d’une Application au Contrôle de Procédé. Ph.D. Thesis. CEA, France.

[TOSI] Toselo, I., Tissot, F. X., Barras, M., 1997. Modelling of the Weld Behaviour for the Control of GTA Process by Computer Aided Welding. Mathematical Modelling of Weld Phenomena, 4, pp. 80 – 103.

[TSAC] Tsai, C. L., Park, S. C., Heng, W. T., 1999. Welding Distortion of a Thin Plate Panel Structure. Welding Journal, 78, pp. 156s – 165s.

[UEDY] Ueda, Y., Yamakawa, T., 1971. Analysis of Thermal Elastic-Plastic Stress and Strain during Welding. Trans. Japan Welding Soc., 2, N2, pp. 90 – 100.

[UED1] Ueda, Y., Yuan., M. G. 1993. Prediction of Residual Stresses in Butt Welded Plates using Inherent Strains. ASME J. Eng. Mater. Technol., 115, pp. 417 – 423.

[VINY] Vincent, Y., 2002. Simulation Numérique des Conséquences Métallurgiques et Mécaniques induits par une Opération de Soudage – Acier 16MnD5. Ph.D. Thesis, Institut National des Sciences Appliquées de Lyon.

[VOLL] Volden, L., 1999. Residual Stress in Steel Weldments – Experiments, Mechanism and Modeling. Ph.D. Thesis, Trondheim.

[WALJ] Walter, J. C., 1963. Shrinkage Distortion in Longitudinal Welding of Beams. The Technical University of Norway, Trondheim.

[WESO] Westby, O., 1968. Temperature Distribution in the Work Piece by Welding. Ph. D. Thesis, The Technical University of Norway, Trondheim.

[WIKL] Wikander, L., 1996. Efficient Thermomechanical Modeling of Welding. Ph.D. Thesis, Luleå.

[WUTO] Wu, T., 2007. Experiment and Numerical Simulation of Welding Induced Damage – Stainless Steel 15-5PH. Ph.D. Thesis, Institut National des Sciences Appliquées de Lyon.

[YOUM] Younan, M.Y.A., Wifi, A., S., Fanous, I.F.Z., 2002. 3D Finite Element Modelling of the Welding Process using Element Birth and Element Movement Techniques. ASME Pressure Vessel and Piping Conf. Canada, 422, pp. 165 – 172.

[YUAM] Yuan, M. G., Ueda, Y., 1996. Prediction of Residual Stresses in Welded T- and I-joints using Inherent Strains. ASME J. Eng. Mater. Technol., 118, pp. 229 – 234.

[ZHUX] Zhu, X.K., Chao, Y.J., 2002. Effects of Temperature-dependant Material Properties on Welding Simulation. Computers and Structures, 80, pp. 967 – 976.

Annex A

Database AA 6056-T4

The work produced within the framework of INZAT4 is mainly comprised of thermo-mechanical characterisation of AA 6056-T4, experimental campaigns and numerical simulation of laser beam welded test plates and T-joints. The classification of various tests and simulations is described in detail in the dissertation. All the data, whether raw or treated, is provided with the hard disk available at LaMCoS, INSA-Lyon. Guide to these bases is provided in this annexure.

Figure A.1. provides the details of folder for numerical simulation in Abaqus. The folder 'Abaqus' contains two sub-folders viz., 'Simulation' and 'Misc'. The folder 'Simulation' contains all the principal analyses, mechanical and thermal, performed for various test cases; whereas the folder 'Misc' shows some of the miscellaneous simulations which were not planned initially.

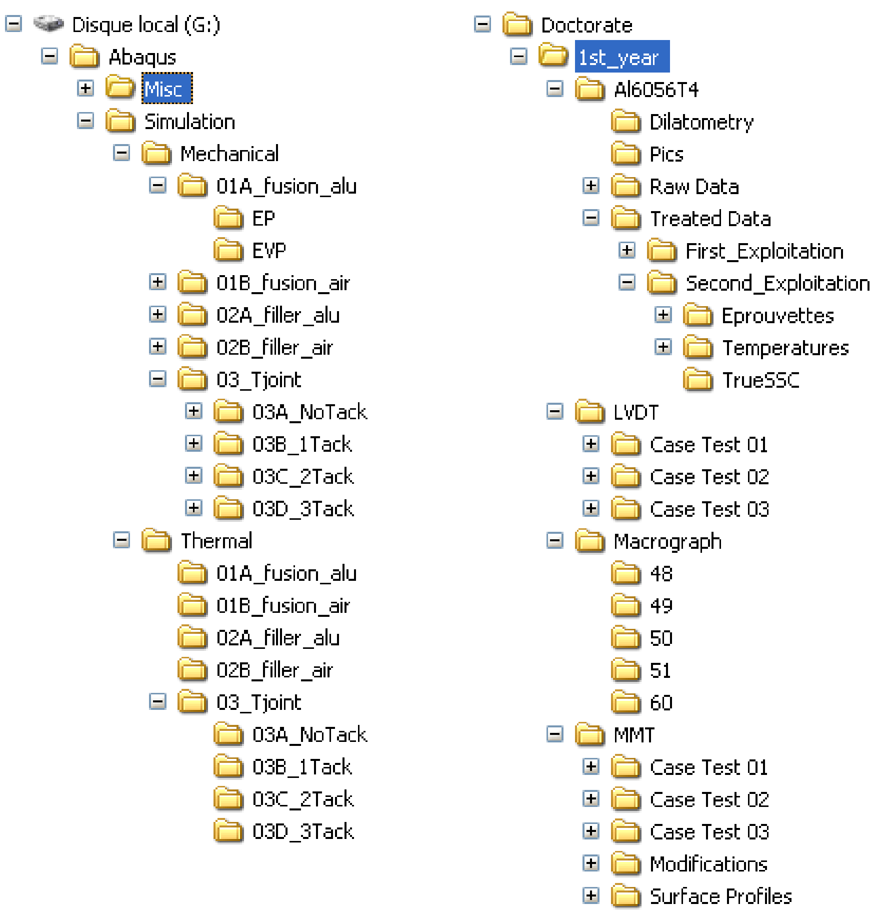

Figure A.1. Details of database, all simulations and experimental work of 1^{st} year

All the experimental works performed during the three years of thesis are placed in the main folder ‘Doctorate’. Figure A.1. also shows the details of the experimental work performed during first year of thesis. The sub-folder ‘Al6056T4’ of the folder ‘1st_year’ contains data files for thermo-mechanical characterisation of AA 6056-T4 in raw as well as treated form. The remaining sub-folders, namely ‘LVDT’, ‘Macrograph’ and ‘MMT’, give the details of the test results exploited and treated from the experimental campaigns of the previous works of Emmanuel Josserand.

Figure A.2. illustrates the folders containing experimental work performed in the second and third years of thesis. The sub-folder ‘07oct_manip’ of the folder ‘2nd_year’ contains results of laser beam welded test plates. Similarly, the sub-folder ’08jun_manip’ of the folder ‘2nd_year’ contains the results of laser beam welded T-joints.

Figure A.2. also shows a sub-folder ‘Gleeble’ of the folder ‘3rd_year’. This folder contains the details of the thermo-mechanical characterisation of AA 6056-T4 performed on the machine Gleeble equipped with the Joule Effect heating system.

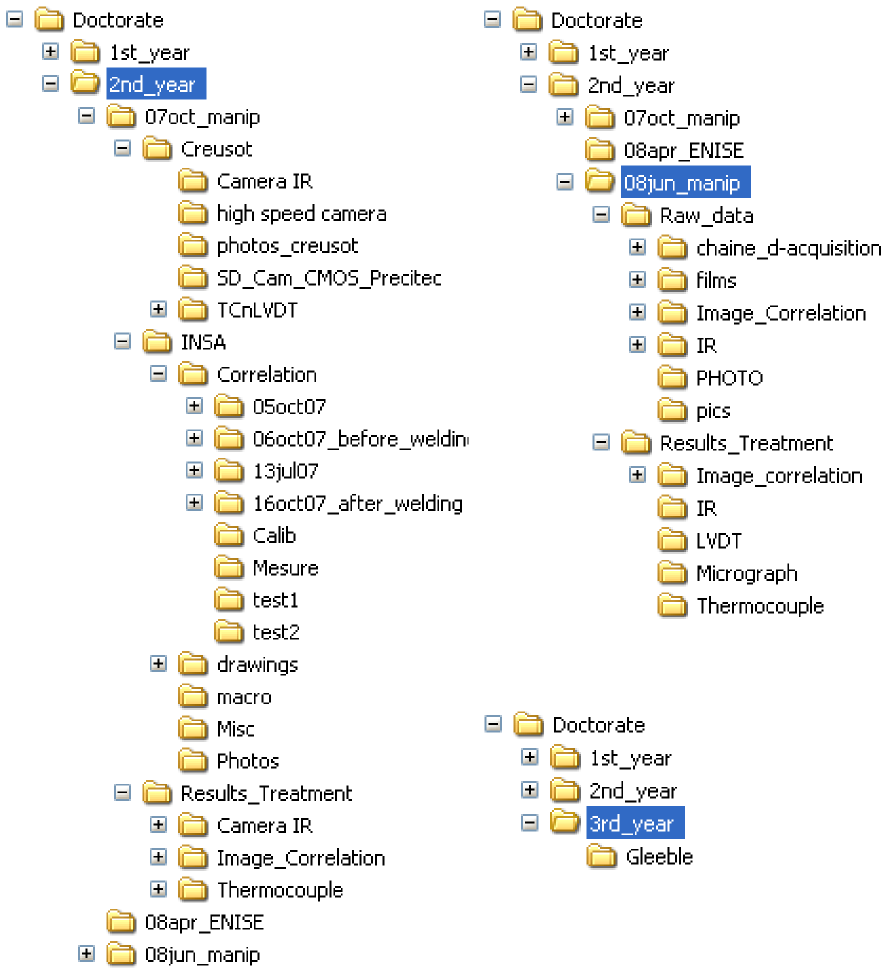

Figure A.2. Details of database, experimental works of 2nd and 3rd years

Annex B

Miscellaneous Results

B.1. Results from Previous Experimental Campaign

B.1.1 Out-of-plane Displacements by Coordinates Measuring Machine

Geometrical configurations of test plates were noted at 600 points by Coordinates Measuring Machine or MMT (Machine à Mesurer Tridimensionnelle) both before and after welding. These measurements not only provide information regarding residual out-of-plane displacements but also the initial and final surface profiles of test plates. The difference between initial and final surface profiles gives a measure of out-of-plane displacement induced during welding. Fig. B.1. shows coordinates measuring machine and the surface profiles of one of the test plate. These results are obtained from the raw data provided by E. Josserand and then treated as a supplementary part of this work in MATLAB.

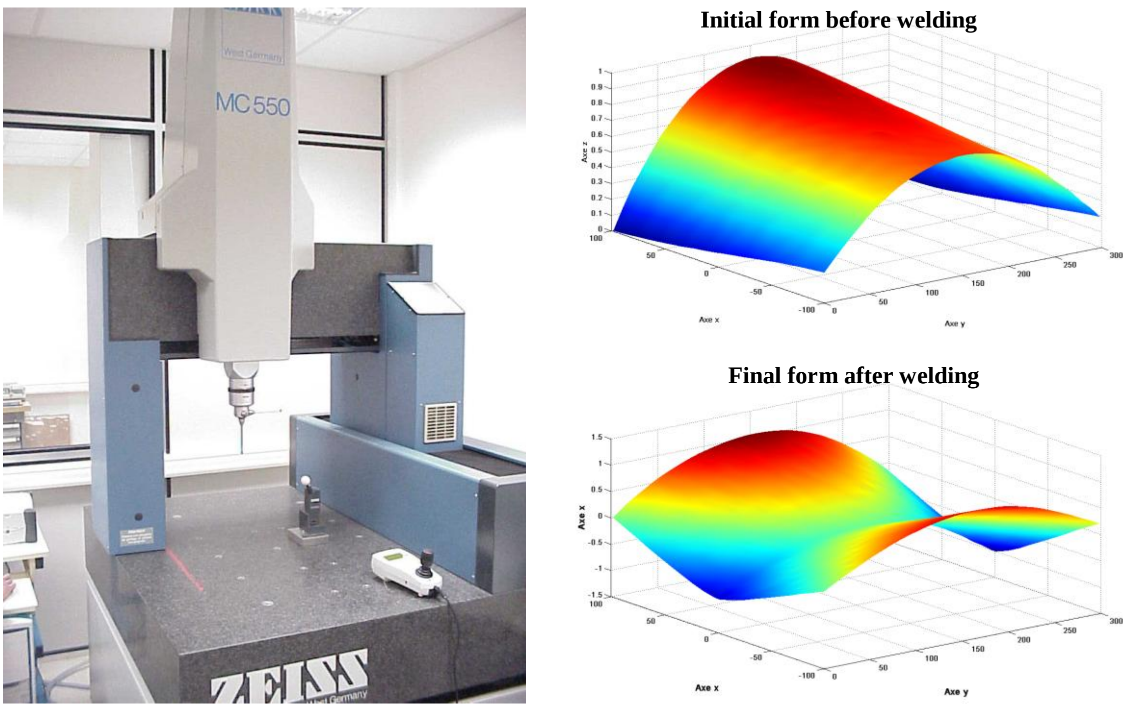

Figure B.1. Coordinates Measuring Machine (left), Surface profiles (right)

The difference profile obtained from initial and final state of surface profiles for one of a fusion welded test plate are shown in Fig. B.2. The out-of-plane displacement values are also plotted on two reference lines along (Y=105) and across (X=155) the weld joint. Results of all the test plates are treated the same way and are available in the database prepared.

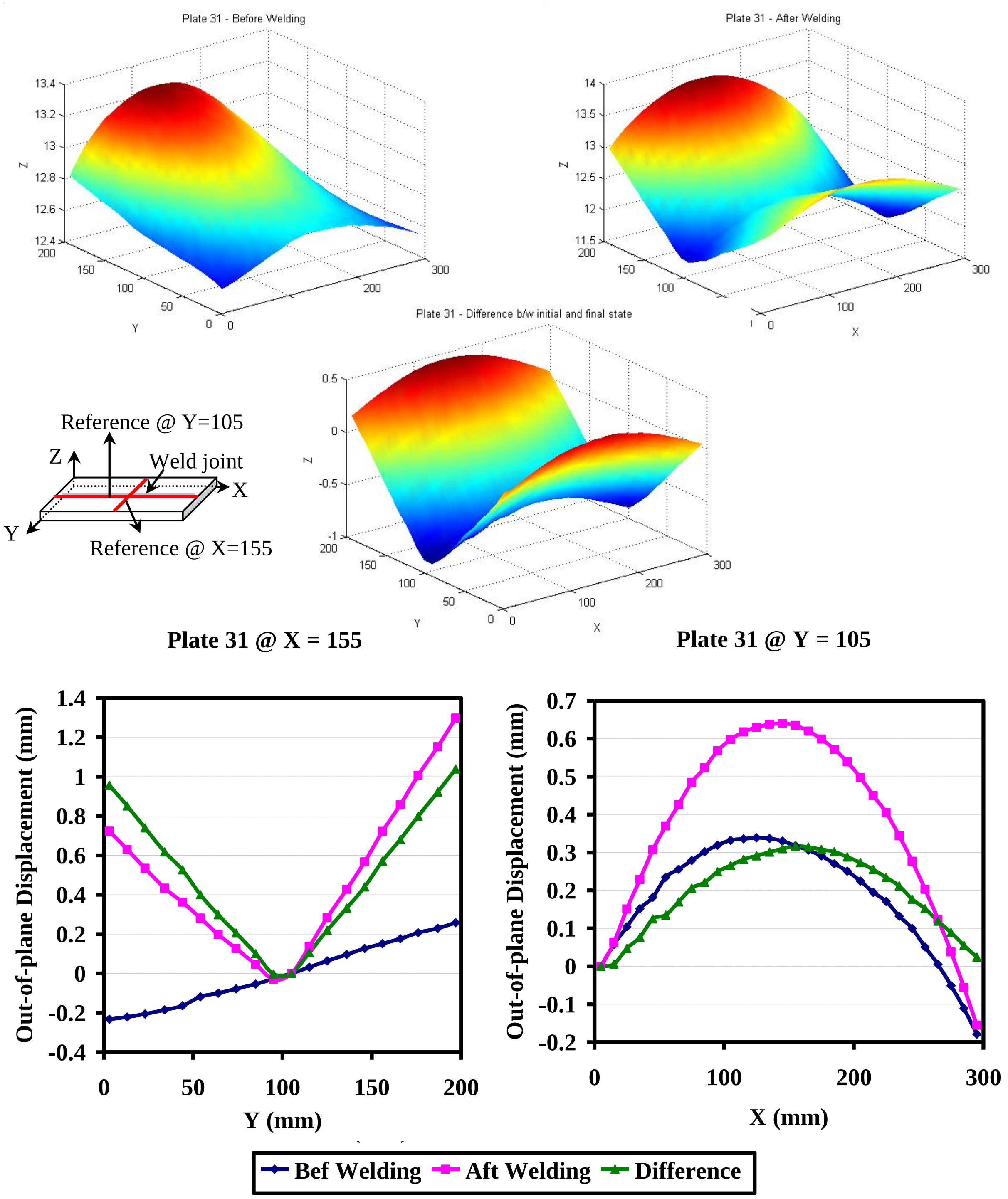

Figure B.2. Initial, final and difference surface profiles

B.1.2. Microscopic Observations

The evolution of weld pool geometry is studied from the test plates available from the previous campaign. Two types of fusion welded test plates were available where one of them was welded using aluminium suction table while the other one was welded using wooden suction table. A number of micrographs are taken from each plate within a distance of 15 – 20 mm in the direction of welding. Both the test plates were welded using identical welding parameters. Figure B.3. shows the schematic sketch of specimen positions and some of the micrographs representing varying weld bead dimensions.

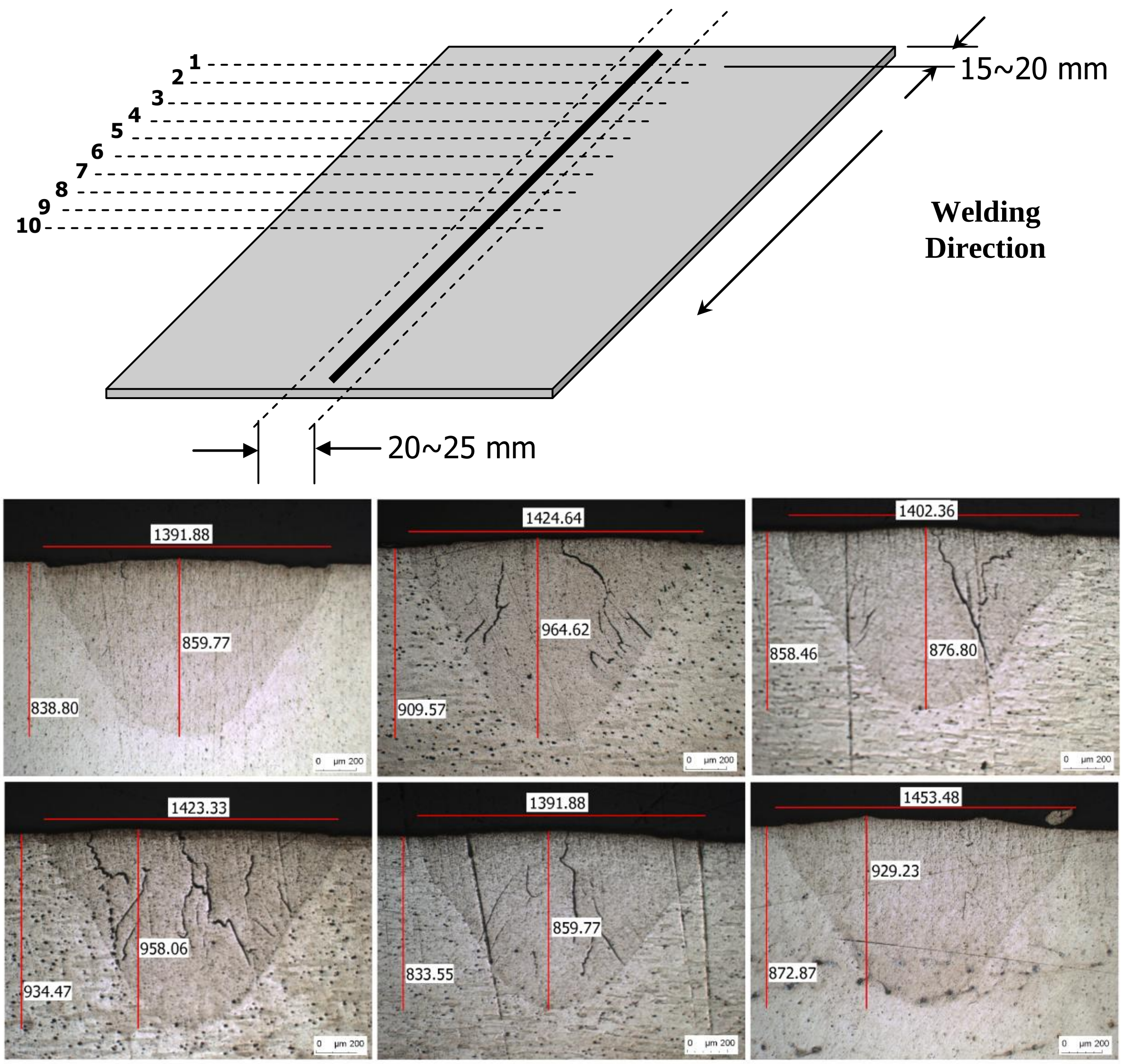

Figure B.3. Schematic representation of micrograph locations and micrographs

Figures B.4. and B.5. illustrate the graphical representation of penetration and width of weld bead, respectively, at various locations. The evolution pattern for both the plates indicate significant variations for the penetration of fusion zone, whereas the width of weld bead remains almost constant during welding. It is expected that different penetration values appear as a result of random material ejection from the molten pool during keyhole welding. However, the penetrations as achieved on wooden support are more pronounce than on aluminium support. This is because the aluminium support allows rapid dissipation of heat energy from the test plate as compared to the wooden support.

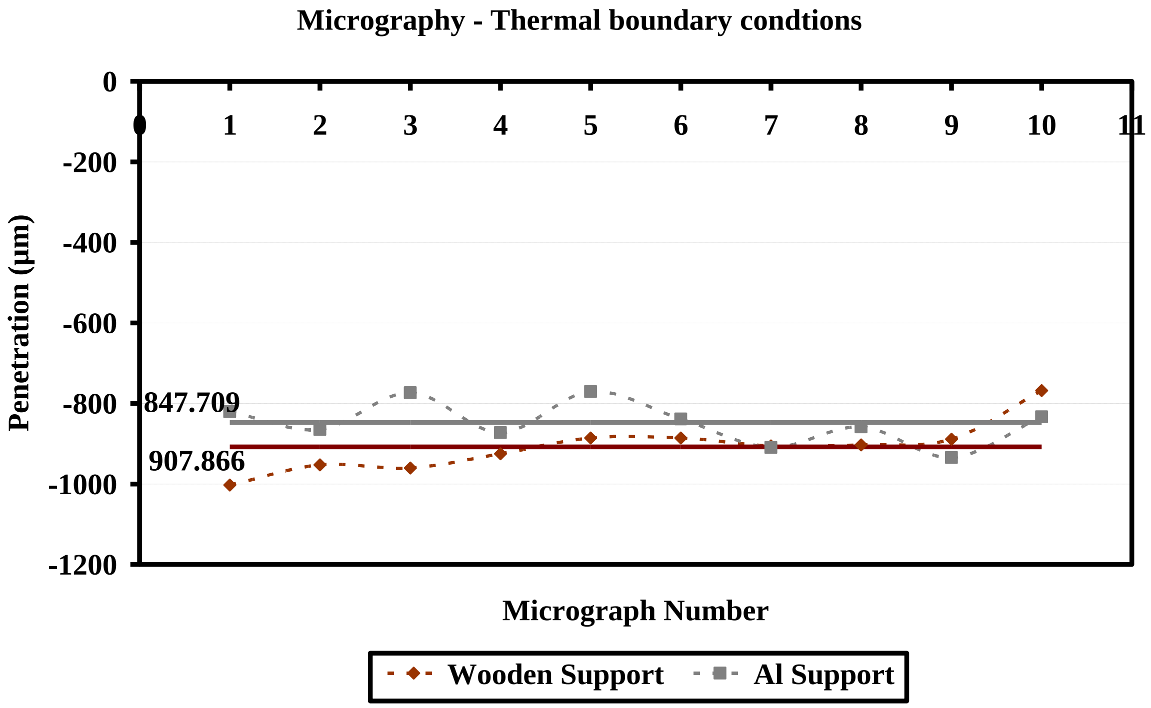

Figure B.4. Weld bead penetration from different micrographs

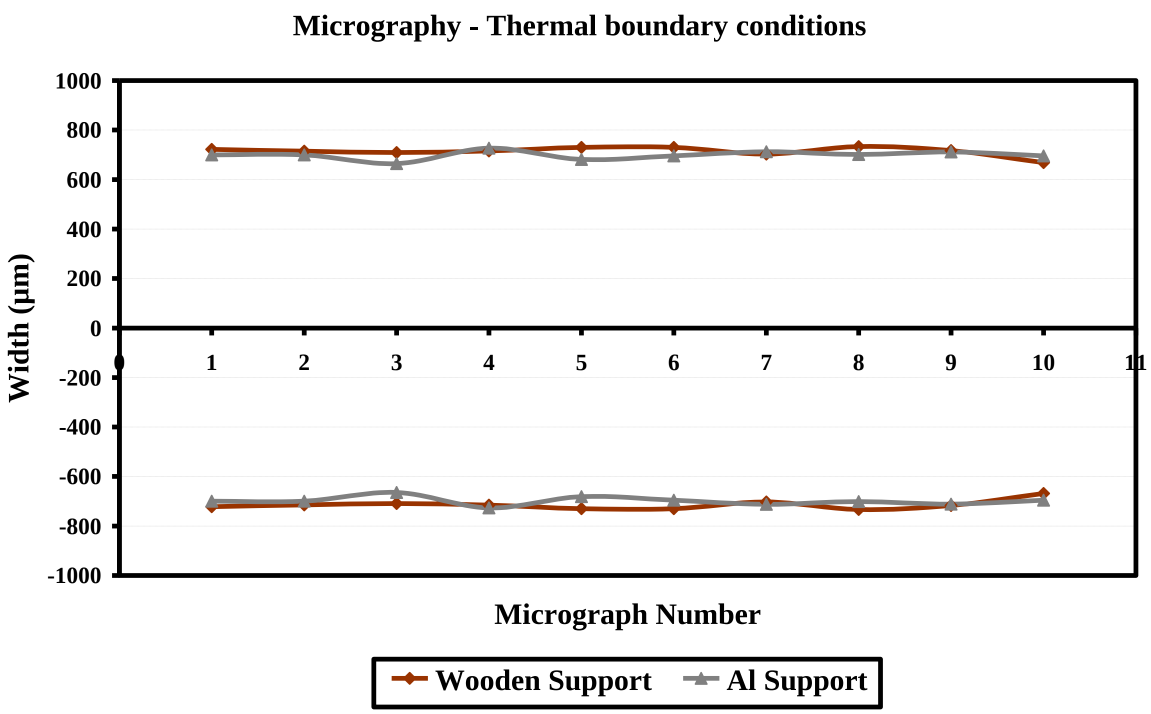

Figure B.5. Weld bead width from different micrographs

B.2. Sysweld Thermal Simulation

The results of Sysweld thermal simulation at thermocouple locations have been superimposed on Figs. 5.30 – 5.32 and presented in Figs. B.6 – B.8.

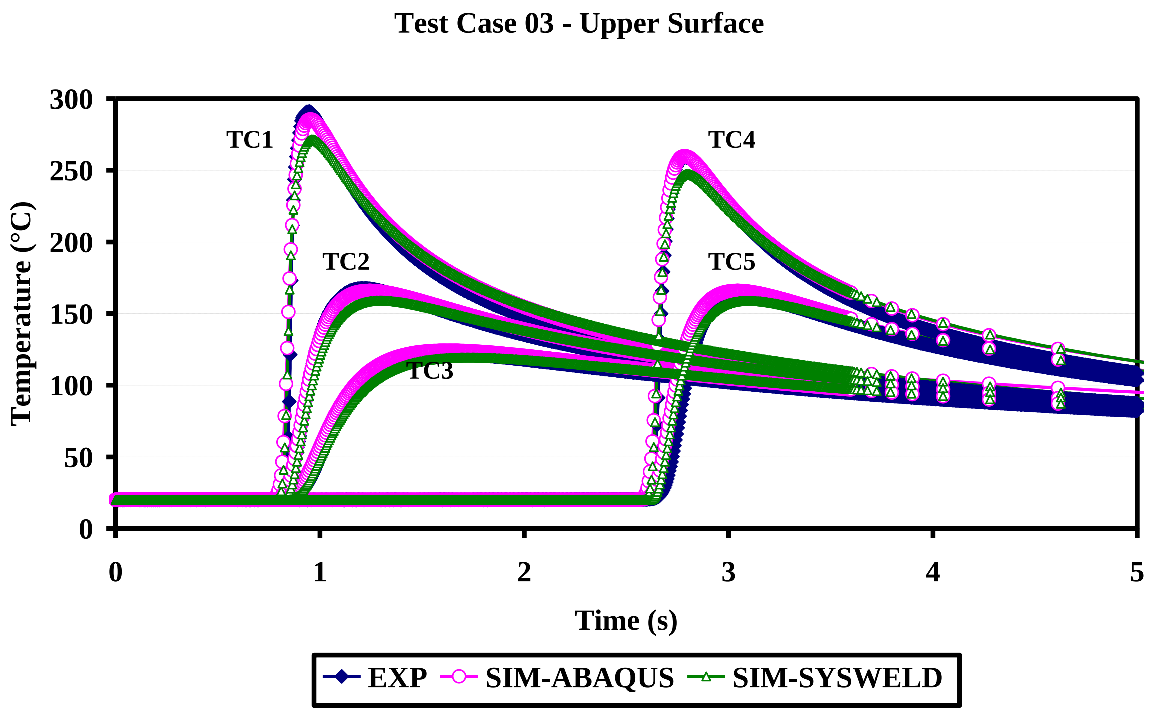

Figure B.6. Comparison of Abaqus and Sysweld simulation at TCs – Top Surface

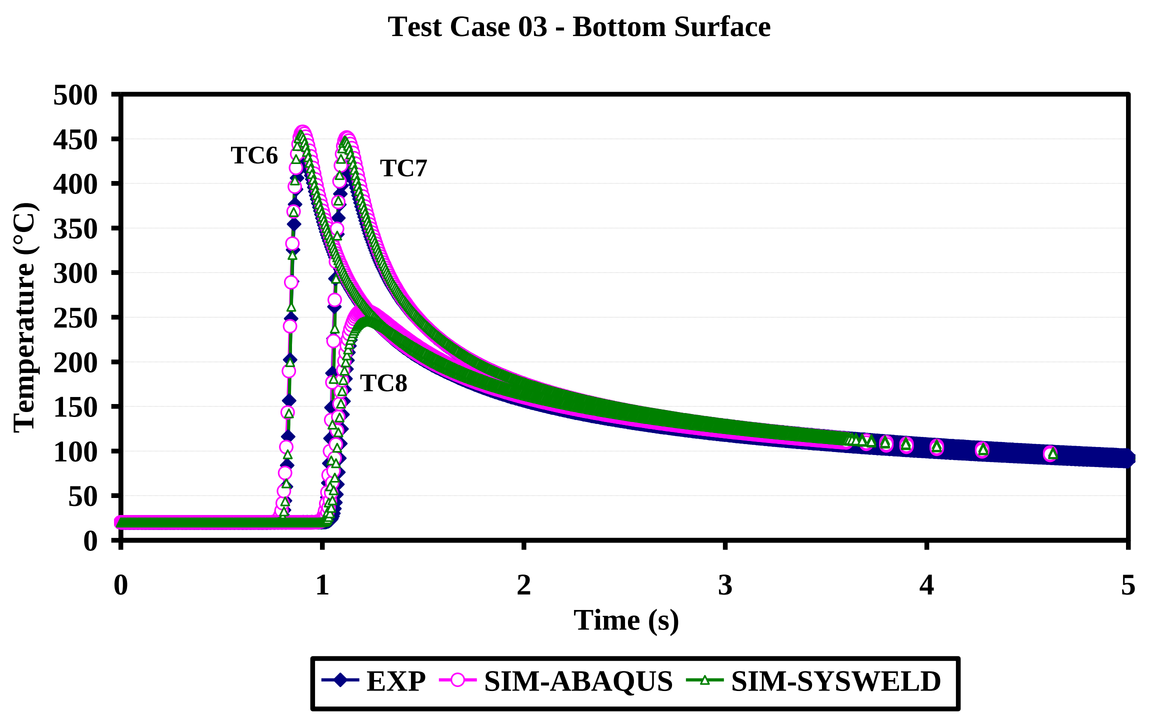

Figure B.7. Comparison of Abaqus and Sysweld simulation at TCs – Bottom Surface

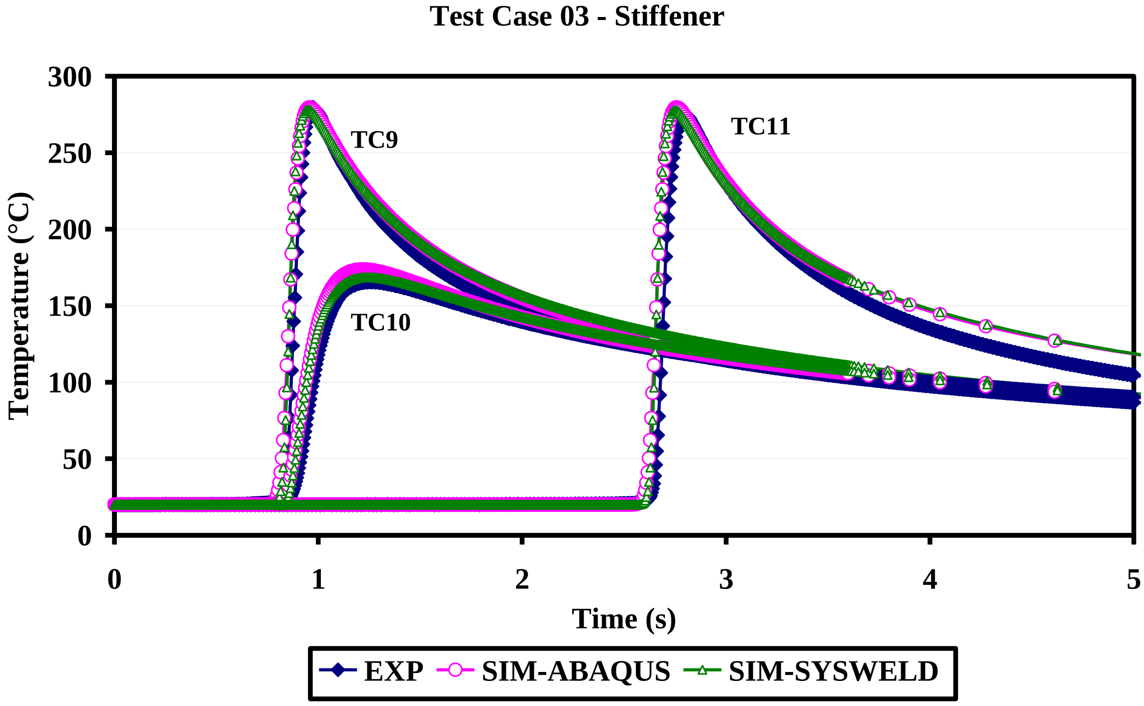

Figure B.8. Comparison of Abaqus and Sysweld simulation at TCs – Stifferener

B.3. Detailed Design of Tensile Test Specimen

The detailed design of tensile test specimen used for thermo-mechanical characterization using conventional tensile testing machine is shown in Fig. B.9.

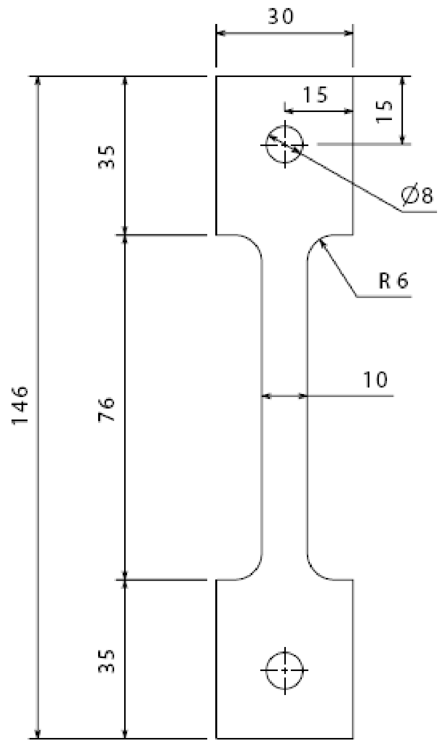

Figure B.9. Sketch of tensile test specimen (dimensions in mm)

B.4. Peak Temperatures Comparison

Peak temperatures comparison of experimental and simulated results for Figs. 5.22 – 5.32 is shown in the following tables:

Case 01A	**Peak Temperatures (°C)**		
TC	Exp	Sim	Error (%)
1	117.43	118.62	-1.01
2	76.13	70.78	7.03
3	55.56	53.71	3.33
4	112.56	118.60	-5.37
5	65.17	70.77	-8.59
6	217.13	224.49	-3.39
7	57.09	53.65	6.02
8	207.78	220.72	-6.22
9	123.57	117.56	4.87

Case 01B	**Peak Temperatures (°C)**		
TC	Exp	Sim	Error (%)
1	107.79	109.55	-1.63
2	68.54	66.38	3.14
3	52.81	51.15	3.15
4	111.28	109.54	1.57
5	69.01	66.38	3.82
6	209.53	207.07	1.17
7	53.32	51.15	4.06
8	193.20	203.84	-5.51
9	100.70	108.77	-8.02

Case 02A	**Peak Temperatures (°C)**		
TC	Exp	Sim	Error (%)
1	121.59	121.74	-0.12
2	74.38	73.46	1.23
3	58.95	55.74	5.45
4	112.87	121.72	-7.83
5	69.76	73.45	-5.30
6	239.86	211.24	11.93
7	57.79	55.68	3.65
8	213.97	208.66	2.48
9	109.92	120.35	-9.49

Case 02B	**Peak Temperatures (°C)**		
TC	Exp	Sim	Error (%)
1	164.85	165.82	-0.59
2	90.38	97.59	-7.98
3	68.62	72.65	-5.87
4	170.85	165.79	2.97
5	88.60	97.57	-10.13
6	270.82	288.95	-6.70
7	69.33	72.65	-4.78
8	247.88	285.70	-15.26
9	158.56	164.05	-3.46

Case 03	**Peak Temperatures (°C)**		
TC	Exp	Sim	Error (%)
1	290.98	285.55	1.86
2	167.62	165.81	1.08
3	122.35	124.10	-1.43
4	259.09	259.87	-0.30
5	162.48	165.81	-2.05
6	430.47	457.77	-6.34
7	418.02	451.45	-8.00
8	256.28	257.68	-0.55
9	279.69	279.59	0.03
10	165.71	173.64	-4.79
11	273.73	279.59	-2.14

B.5. Heat Source Parameters

The calibrated heat source parameters for various thermal simulations are shown in the following table. All the dimensions are in mm.

Test Case	**Heat Source Parameters**							
	r_e	**r_i**	**z_e**	**z_i**	**r_{os}**	**r_{is}**	**f**	**H(cone)**
01A	0.6	0.3	-0.25	-0.87	1.52	1.14	0.4	0.62
01B	0.6	0.4	-0.25	-0.87	1.52	1.14	0.4	0.62
02A	0.6	0.3	-0.25	-0.87	1.52	1.14	0.4	0.62
02B	0.6	0.3	-0.25	-0.87	1.52	1.14	0.4	0.62
03	0.4	0.2	-	-	-	-	1	1.72

Annex C

Peer-reviewed Journal Paper

Ref: Journal of Materials Processing Technology, 209 (2009) 2907–2917.

PREDICTION OF LASER BEAM WELDING-INDUCED DISTORTIONS AND RESIDUAL STRESSES BY NUMERICAL SIMULATION FOR AERONAUTIC APPLICATION

Muhammad ZAIN-UL-ABDEIN*, Daniel NELIAS*, Jean-François JULLIEN*
Dominique DELOISON**

** LaMCoS, INSA-Lyon, CNRS UMR5259, F69621, France*
*** EADS Innovation Works, 12, rue Pasteur, BP 76, 92152 Suresnes Cedex*

Abstract

This paper focuses on the prediction of laser beam welding-induced distortions and residual stresses through numerical simulation. Fabrication of fuselage panels of latest generation civil aircraft involves welding of stringers on thin sheets of 6056 T4 aluminium alloy. The efforts are made to exercise better control over the excessive out-of-plane distortions. A series of experiments have so far been performed using small specimens. One of the test cases that include single-pass fusion welding on a 6056 T4 thin sheet with the industrially used thermal and mechanical boundary and loading conditions is being studied in this work. Laser beam welding in the keyhole regime is employed. The test plate is maintained in position with the help of an air suction table made of aluminium. Although a pressure of 1 bar is used experimentally, yet the possibility of leakage cannot be overruled. Various magnitudes of pressures are, therefore, introduced during numerical simulation to study the effect of each. The effect of contact between test plate and support over thermal and mechanical results is also integrated. A 3D symmetric model of test plate and support is incorporated and the comparison between simulation and experimental results is developed. Finally, a good correlation is found between experimental and simulation results, on the basis of which residual stress state in the test plate is predicted.

Keywords: laser beam welding, thermo-mechanical analysis, residual stress, distortion, 6056 T4 aluminium alloy

1. Introduction

Laser beam welding is believed to be beneficial in terms of time saving and weight reduction for the manufacturing of the aeronautical structures. Riveting has so far been used industrially to assemble the fuselage panels of aircrafts with stiffeners. The laser beam welding, in fact, effectively eliminates the large quantity of material added to the aircraft structure in the form of rivets. However, accompanied with its blessings, welding always brings some inconveniences like distortions and residual stresses. In the recent years, numerical simulation has proven itself to be a useful tool in predicting these welding-induced distortions and residual stresses. The knowledge of residual stress distribution and distortions may then lead to the better control over the undesirable aspects of the process.

Laser beam welding involves several complex phenomena like formation of keyhole, weld pool geometry, plasma formation etc. Sudnik et al. (2000) discussed the mathematical model of keyhole formation and studied the simulation of weld pool geometry with key-hole formation and varying welding parameters namely laser beam power and welding speed. According to their findings, there exists a linear relationship between the length and depth of the weld pool for laser beam welding experiments with varied laser beam power and constant welding speed; while on the other hand, the weld pool length changes slightly with varying welding speed and constant laser beam power. The experimental work presented here uses constant welding speed (8 $m.min^{-1}$) and constant laser beam power (2.3 kW), so as to minimize the dependency of weld pool geometry over these factors. Jin et al. (2003) focussed upon heat transfer model based on an actual keyhole and discussed the thermal gradient and melt pool shape around the keyhole on the surface of the test specimen. Olmedo (2004) also discussed the principal of laser beam welding with special reference to aluminium alloys used for aeronautical applications. Ferro et al. (2005) proposed a cone-shaped heat source model with an upper and lower sphere to predict the shape of weld pool and thermal gradient around the keyhole formed during electron-beam welding. Heat source model used in this work also takes care of keyhole formation and temperature distribution. Comparison between experimental and simulated results for distortions is developed by Tsirkas et al. (2003) who used the commercial software SYSWELD for simulation. C. Darcourt et al. (2004) attempted to predict laser beam welding induced distortions in a T-joint configuration and suggested that a correct thermal analysis is mandatory to predict welding induced distortions and residual stresses. E. Josserand et al. (2007) have also tried to predict laser welding induced-distortions for an aeronautic aluminium alloy while working on thin test plates. They have suggested that the initial surface profiles of the test plate due to pre-processing, like rolling etc., play an important role in defining the distortions level of test plate. In this work the effort is, therefore, made to predict the residual stress state and distortion pattern by numerical simulation giving due care to the factors affecting final result. For instance, the displacement field of the test plates is measured in a way so as to minimize the effect of pre-processing phenomena. Moreover, the industrially employed complex thermal and mechanical boundary conditions are integrated, which have not previously been taken under consideration for numerical simulation.

The fuselage panels of aircraft structures are large-thin sheets of an aluminium alloy 6056T4 with stringers welded upon them. The typical total length of seam reaches 50 m or more. Industrially, these panels are kept in position with the help of suction force applied through an aluminium fixture. This is done to avoid out-of-plane displacements of the panels during welding. However, after the release of suction force i.e. at the end of welding, the out-of-plane deformations dominate. In order to uncouple the complexities involved in the process, a step-wise approach has been adopted for the small-scale experiments that include:

a. Fusion welding of test plate without filler material

b. Fusion welding of test plate with filler material
c. T-joint welding of base plate and stiffener with filler material

In this work the emphasis is given to the prediction of out-of-plane displacements and residual stress distribution during fusion welding of test plate without filler material.

2. Experimental Approach

An instrumented experimental campaign was carried out in order to have a reference database necessary for numerical simulation. Various test plates were welded with different welding parameters and with a variety of thermal and mechanical boundary conditions. The test case presented here includes single-pass fusion welding of test plate of material 6056T4 and dimensions 200 mm x 300 mm x 2.5 mm with the following welding parameters:

- Power: 2300 W
- Speed: 8 m.min^{-1}

During the experiment, a fusion line was created lengthwise in the middle of the test plate and a distance of 5 mm was left at both ends. The test plate was held in position with the help of an aluminium suction table (25 mm thick). The suction force was applied over the entire bottom surface of the test plate. A pressure of 1 bar was maintained during welding and cooling, while after sufficient cooling time the pressure was released to allow the test plate to deform freely. The temperature histories were recorded with the help of thermocouples. A total of nine thermocouples were used to record temperatures at various distances from the weld pool. Thermocouples named as TC1, TC2, TC3, TC4 and TC5 were installed on the upper surface, while TC7, TC8 and TC9 were installed on the bottom surface and TC6 was installed in the depth of 0.31 mm beneath the weld line. The displacement fields were measured with the help of 3D image correlation technique applied on the entire upper surface of the test plate, both before and after welding. The width and depth of weld pool were measured by micrography. The geometry of the test plate with thermocouple positions and the experimental setup with plate mounted on aluminium suction table are shown in Fig. 1. The red lines in Fig. 1 present the weld line and the red arrows indicate the welding direction.

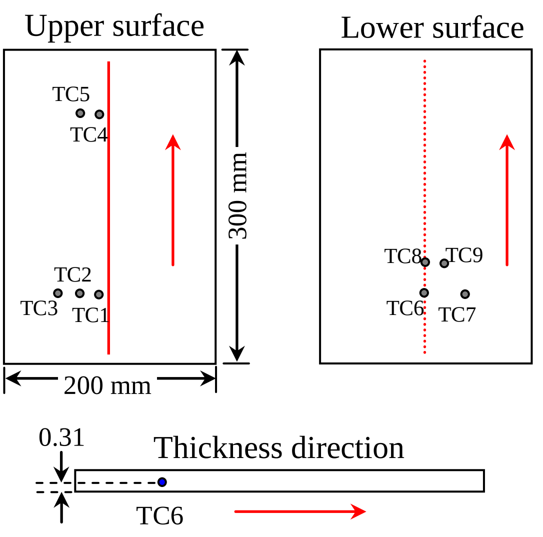

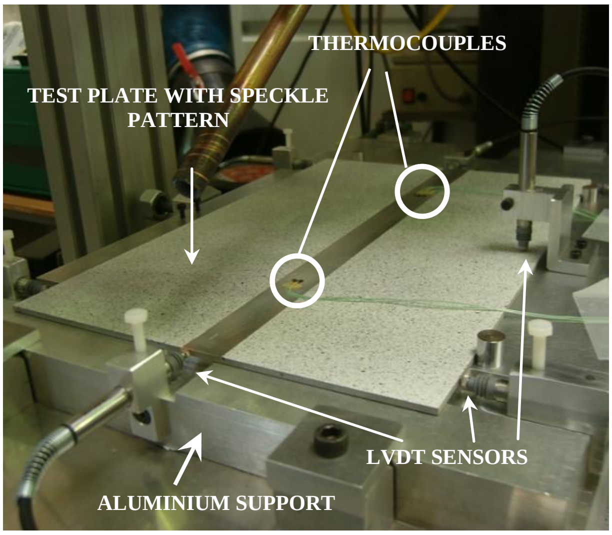

Fig 1. Geometry of test plate with thermocouple positions (left); Experimental setup (right)

Owing to the contact between the test plate and the table, it is believed that some of the heat energy is lost due to the thermal conductance. Moreover, the in-plane displacements due to expansion and contraction during welding and cooling respectively give rise to the friction at the interface between the test plate and the table.

Since it was observed with the help of 3D image correlation technique that the test plate is not perfectly straight rather there exists an initial curvature in the test plate, the difference between initial (before welding) and final (after welding) state is taken as standard to be compared later with numerical simulation results. The surface profiles before and after welding taken from the upper surface of the test plate are shown in Fig. 2. Here, 'after welding' means after complete cooling and release of the pressure from the suction table. It is observed from the difference profile (Fig. 3) that the maximum out-of-plane displacements / vertical displacements are present towards the center of the test plate, while the minimum values are at the start and stop ends of the weld seam. The probable reason being the pre-bended/buckled state of the test plate. Moreover, during welding the in-plane expansion and contraction of the central regions of the test plate are restricted by their adjacent regions and hence to compensate for these expansion and contraction occurrences the test plate deform more in the out-of-plane direction at the center than at the weld start and stop edges. These out-of-plane displacements reach up to 1.05 mm at the middle of the test plate and up to 0.89 mm at the edges, thereby defining the range for maximum and minimum values; the numerical simulation results will be compared in this range.

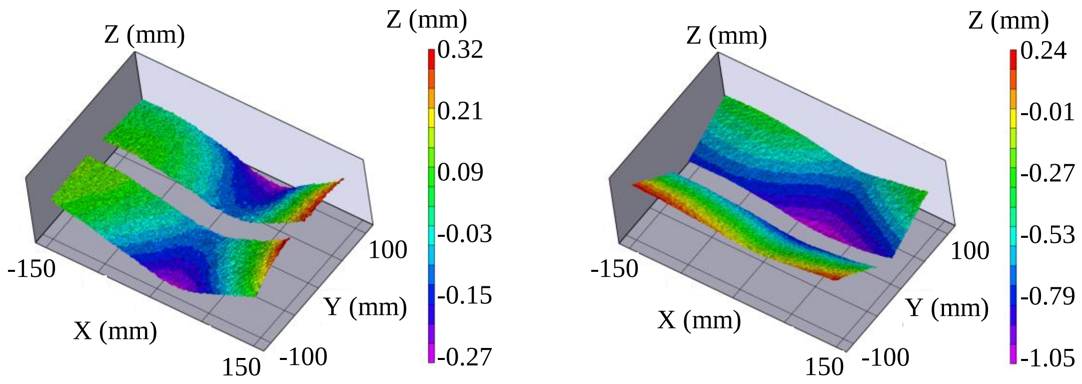

Fig 2. Initial (left) and final (right) surface profiles of test plate

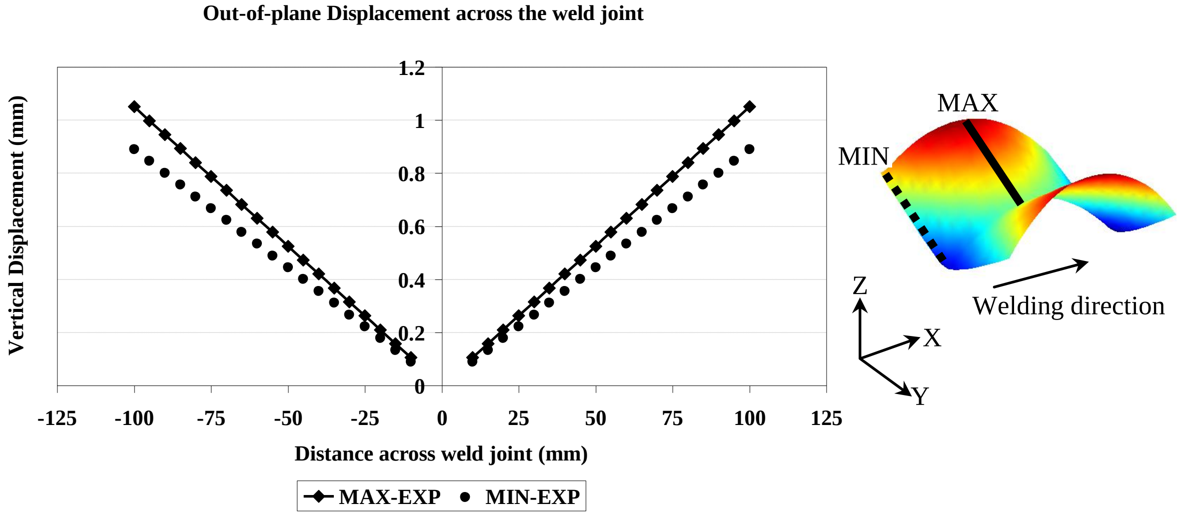

Fig 3. Maximum and minimum out-of-plane displacements

Figure 3 shows the maximum and minimum vertical displacements as a function of the distance across the weld joint, obtained from the difference profile shown on the right. The maximum and minimum values are noted at the intersection of test plate and a cutting plane passing through the test plate across the welding direction and moving in the welding direction.

Assuming weld joint an axis of symmetry, the vertical displacements of right half of the test plate will be considered only. In addition to the specimen's geometry and thermo-mechanical properties of the material, it is assumed that the magnitude of vertical displacement is influenced by the following three factors:

- The amount of heat energy absorbed by the test plate during welding which has a direct influence on the geometry of the weld pool and the temperature fields in the vicinity of the weld joint.
- The friction coefficient present at the interface of the test plate and the support.
- The actual suction pressure present at the bottom surface of the test plate; as there is a possibility of air leakage from the boundary of the test plate which is, in fact, simply placed on the suction table with a very fine rubber joint to avoid leakage. Yet during welding the leakage is observed due to in- and out-of-plane expansion and contraction of the test plate.

These factors are given emphasis in this work and are being studied for the first time with reference to friction coefficient and suction pressure. Different friction coefficients and suction pressure values will be used to analyze the affect of each on the final distortion level.

3. Finite Element Model

Numerical simulation has been performed using the commercial finite element code Abaqus /Standard. The finite element (FE) model of the test plate and support consist of continuum solid three-dimensional linear elements. The test plate mesh consists mostly of 8-nodes brick elements (type: DC3D8, C3D8R) completed by some 6-nodes prism elements (type: DC3D6, C3D6), for 58,000 nodes and 50,000 elements; while that of mesh of support consists only of 8-nodes brick elements with a relatively coarse mesh size. Taking the weld line as an axis of symmetry, a symmetric model is assumed in order to minimize the degrees of freedom and consequently the calculation time. Due to the high thermal gradient in the fusion and heat-affected zones the mesh in these regions is considerably fine where mostly brick elements are used. The dimensions of the smallest brick element are 0.5 mm x 0.3 mm x 0.31 mm (Fig. 4). As the temperature gradient is considerably low outside the heat-affected zone (HAZ), a relatively coarser mesh is deemed sufficient for analysis. The size of the mesh increases progressively away from the axis of symmetry i.e. fusion line. To compensate for the increase in size of brick elements prism elements are used selectively. Lengthwise, there are 600 elements at the fusion line which then reduce to only 30 at the far end of the test plate; while thickness-wise there are 8 elements at the fusion line which finally reduce to 2 at the far end. The model is shown in Fig. 4.

An uncoupled thermo-mechanical analysis approach is employed, where the thermal analysis is first performed independently in order to adjust the heat source parameters and incorporate the complex thermal boundary conditions including free and forced convection and thermal contact resistance between the test plate and the support. Temperature histories calculated during thermal analysis are then used as a predefined field for mechanical analysis. Other mechanical boundary conditions and loadings are applied during mechanical analysis.

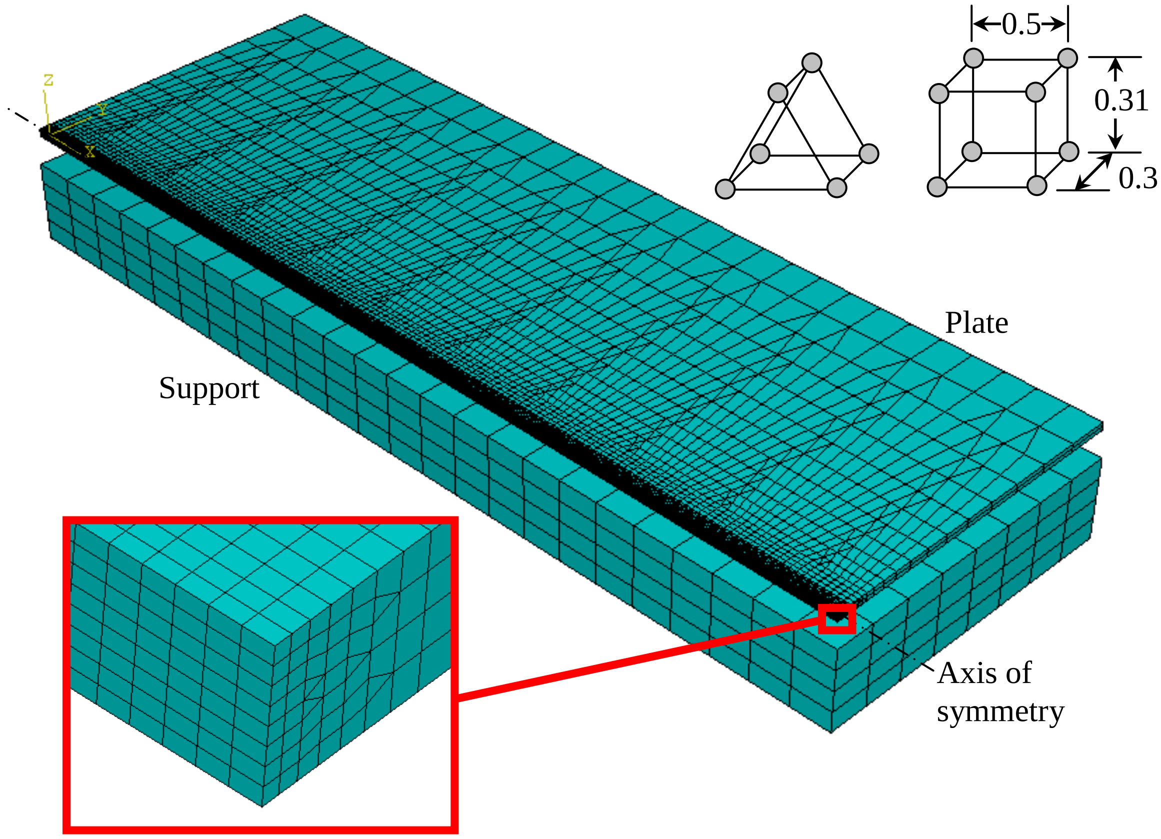

Fig 4. Plate and support mesh with dimensions (mm) of brick elements in the fusion zone

4. Thermal Analysis

The thermal analysis was performed using temperature dependent thermal material properties. The transient temperature field T in time (t) and space (x,y,z) is acquired by solving the following heat transfer equation:

$$\frac{\partial}{\partial x}\left(k(T)\frac{\partial T}{\partial x}\right)+\frac{\partial}{\partial y}\left(k(T)\frac{\partial T}{\partial y}\right)+\frac{\partial}{\partial z}\left(k(T)\frac{\partial T}{\partial z}\right)+Q_{\text{int}} = \rho(T)C_p(T)\left(\frac{\partial T}{\partial t}\right) \quad (1)$$

Here, $k(T)$ is the thermal conductivity as a function of temperature in W.m^{-1}.K^{-1}, $\rho(T)$ is the density as a function of temperature in kg.m^{-3}, $C_p(T)$ is the specific heat as a function of temperature in J.kg^{-1}.K^{-1} and Q_{int} is the internal heat generation rate in W.m^{-3}.

The heat source modeling is considered to be the most important aspect of the welding thermal analysis. Various models including cone-shaped volumetric heat source with Gaussian distribution and double-ellipsoidal volumetric heat source in accordance with Goldak et al. (1984) exist that may be employed for a variety of welding processes like TIG, MIG, electron beam welding, laser beam welding etc. The choice is, however, largely dependant upon the size of the weld pool and the temperature field recorded in or near the weld pool. For instance, Lundback et al. (2005) used Goldak's double ellipsoid with double elliptic cone to simulate the electron beam welding process with keyhole. Similarly, Ferro et al. (2005) used conical distribution of heat flux with an upper and lower sphere to incorporate the keyhole phenomenon of electron-beam welding process. A similar kind of heat source is also integrated in this work. Cone-shaped volumetric heat source with Gaussian distribution and an upper hollow sphere is used to attain the required weld pool size and temperature fields. In practice, the laser beam penetrates the test plate creating a capillary-shaped keyhole to a required depth, while the impingement zone experiences material evaporation and a comparatively wider fusion zone appears. The conical part of the heat source is, therefore, meant to capture the effect of keyhole formation due to laser beam penetration; and the upper hollow sphere is incorporated to achieve the desired width of fusion zone. The heat source model is shown in Fig. 5.

Equation 2 gives the combined heat source model where the first part represents the Gaussian distribution of the heat flux in the cone and the second part corresponds to a linear distribution of the heat flux in a hollow sphere.

$$Q_v = \frac{9\eta P.f}{\pi(1-e^{-3})} \cdot \frac{1}{(z_e - z_i)(r_e^2 + r_e r_i + r_i^2)} \cdot \exp\left(-\frac{3r^2}{r_c^2}\right) + \frac{3\eta P.(1-f)}{4\pi(r_{es} - r_{is})^3} \cdot d_s \qquad (2)$$

where
$$r_c = r_i + (r_e - r_i)\frac{z - z_i}{z_e - z_i}$$

Here, Q_v is the total volumetric heat flux in W.m^{-3}, P is the laser beam power in W, η is the efficiency of the process, f is the fraction of the heat flux attributed to conical section, r is the current radius as a function of Cartesian coordinates x and y, r_c is the flux distribution parameter for the cone as a function of depth (z), d_s is the flux distribution parameter for the hollow sphere such that its value is 1 at inner radius of sphere (r_{is}) and 0 at outer radius of sphere (r_{es}). r_e and r_i are larger and smaller radii of the cone respectively. Similarly, z_e and z_i are upper and lower z-coordinates of the cone respectively. The parameters are also shown in Fig. 5. An efficiency (η) of 37% is used for the thermal analysis with power (P) of 2300 W. The remaining parameters are adjusted to obtain the required weld pool geometry. A latent heat of fusion of 4x10^5 J.kg^{-1} is used between the solidus and liquidus temperature of 587°C and 644°C respectively.

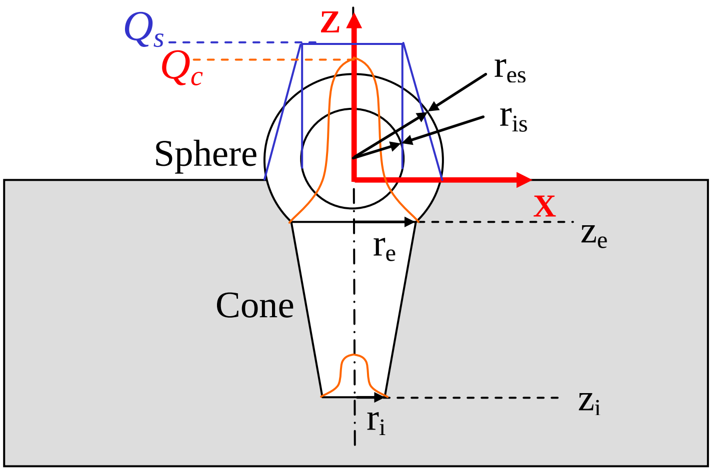

Fig 5. Conical Heat source model with an upper hollow sphere

Owing to the complex nature of thermal boundary conditions at the bottom surface of the test plate forced convection and thermal contact resistance are used. Forced convection is assumed to be present due to air suction through suction table and leakage at the boundaries of the test plate. Similarly, as test plate comes in contact with aluminium suction table due to air suction, thermal conductance as a function of pressure is also introduced at the interface of test plate and suction table. Free convection and radiation to atmosphere are used at all the remaining surfaces except the symmetric plane. A schematic sketch of thermal boundary conditions is shown in Fig. 6, where free convection and radiation is assumed to be present at all the surfaces of the plate except the bottom surface, while at the bottom surface it is assumed that forced convection is present due to air suction and leakage and thermal conductance is present at the interface of the test plate and aluminium support.

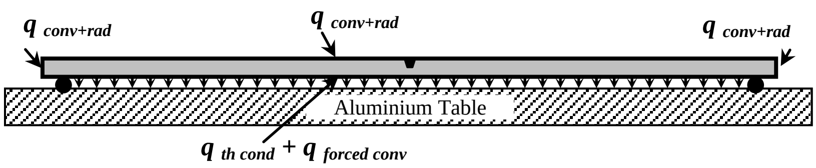

Fig 6. Schematic diagram of thermal boundary conditions

Equations 3, 4 and 5 define $q_{conv+rad}$, $q_{th\ cond}$ and $q_{forced\ conv}$ as general boundary conditions.

$$q_{free\,conv+rad} = h_{free\,conv}(T - T_0) + \sigma\varepsilon((T - T_{abs})^4 - (T_0 - T_{abs})^4) \quad (3)$$

$$q_{forced\,conv} = h_{forced\,conv}(T - T_0) \quad (4)$$

$$q_{th\,cond} = h_{th\,cond}(T_s - T) \quad (5)$$

where, T, T_0, T_{abs} and T_s are the temperature of the test plate, ambient temperature, absolute zero and temperature of the support respectively. The values used for the heat transfer coefficients and radiation constants are as follows:

- Convective heat transfer coefficient of air, $h_{free\ conv}$ = 15 W.K^{-1}.m^{-2}
- Emissivity of aluminium surface, ε = 0.08
- Emissivity of speckle pattern, ε = 0.71
- Stefan-Boltzmann constant, σ = 5.68 x 10^{-8} J.K^{-4}.m^{-2}.s^{-1}
- Convective heat transfer coefficient for air suction, $h_{forced\ conv}$ = 200 W.K^{-1}.m^{-2}
- Heat transfer coefficient at the interface of the test plate and support, $h_{th\ cond}$ = 50 W.K^{-1}.m^{-2} at 0 bar, 84 W.K^{-1}.m^{-2} at 1 bar

A volumetric heat flux Q_v, as defined in equation 2, is introduced in the Abaqus model through a user subroutine DFLUX programmed in FORTRAN. The heat source parameters are adjusted in order to achieve the experimentally observed weld pool geometry. Figure 7 compares the weld pool geometry observed experimentally and numerically.

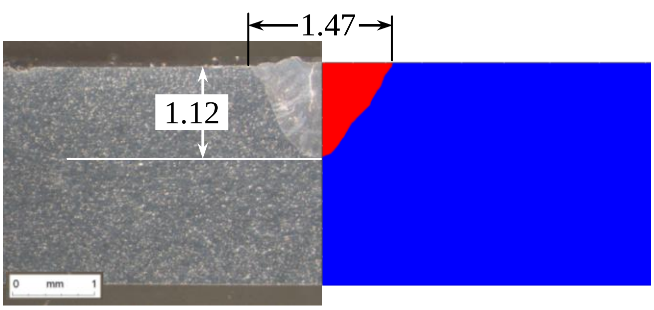

Fig 7. Comparison of the weld fusion zone, experiment vs simulation

The physical phenomena occurring at the level of weld pool like formation of keyhole, ionization and vaporization of material, circulation of molten material within the weld pool due to electromagnetic and buoyancy forces, solidification at the liquid-solid interface etc. are difficult to model. Various simplifications are, therefore, required to be assumed. In this work the weld pool is treated as a solid phase for calculating the temperature fields only. The temperature histories recorded in the vicinity of the weld pool during experimentation are then compared with the numerically simulated time-temperature curves at positions TC1 to TC9 (Fig. 1). Figures 8 and 9 present this comparison of temperature histories at the upper and lower surface and in-depth beneath the fusion line respectively.

Time-temperature Curves - Exp vs Sim (Upper Surface)

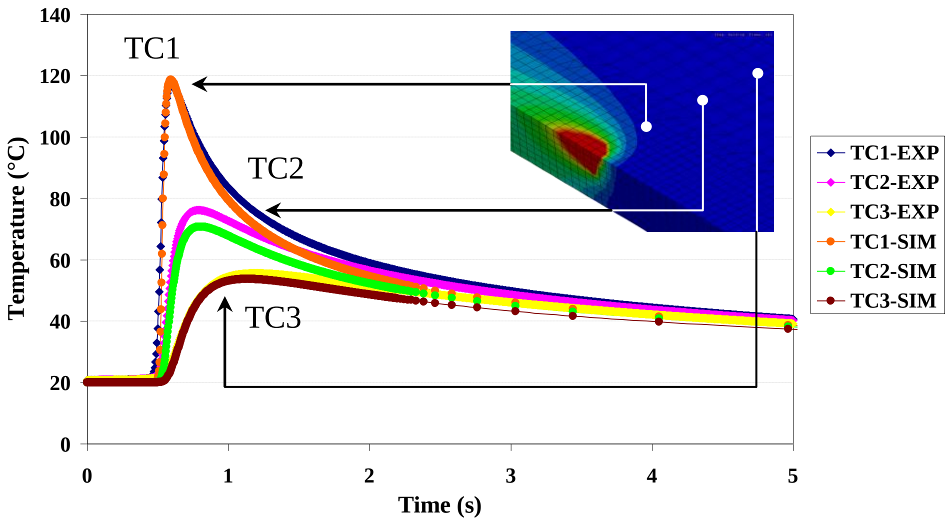

Fig 8. Time-temperature curves at TC1, TC2 and TC3 (upper surface); experiment vs simulation

Time-temperature Curves - Exp vs Sim (Lower Surface)

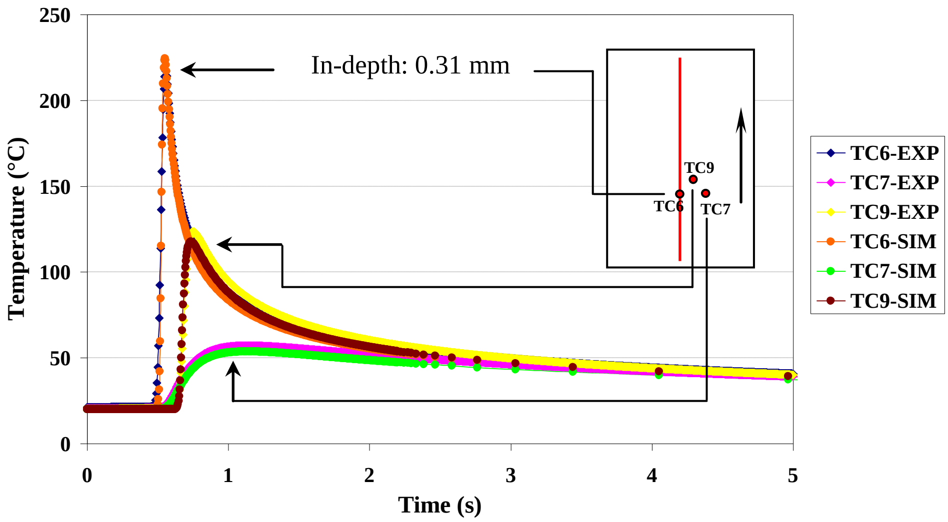

Fig 9. Time-temperature curves at TC6, TC7 and TC9 (lower surface); experiment vs simulation

A good accordance is found between experimental and simulation results. The disagreement between peak temperatures at some of the thermocouple positions, however, may be attributed to some inaccuracies in heat flux distribution – assumed constant in the model, some imprecision in the thermocouple locations with respect to the fusion line, relatively coarser mesh away from the fusion zone, and the simplifications assumed during numerical simulation.

5. Mechanical Analysis

Having obtained the result of the thermal analysis, the temperature fields are used as predefined field for the mechanical analysis. The material assumes rate-dependent elasto-viscoplastic behavior with isotropic hardening law (Mises plasticity model). The three-dimensional formulation of viscoplastic strain states:

$$f(\sigma, T, H_{iso}) < 0 \tag{6}$$

and $$\dot{\varepsilon}^{vp} = \frac{3}{2}\dot{p}\frac{S}{\sigma_{eff}}$$ where $$\dot{p} = \left(\frac{\langle f \rangle}{\eta}\right)^n$$ and $$\sigma_{eff} = \sqrt{\frac{3}{2}S:S} \tag{7}$$

Here, f is the yield function that defines the limit of the region of purely elastic response, H_{iso} shows isotropic hardening parameters, T is the temperature, σ_{eff} is the Von Mises effective stress, S is the deviatoric stress and η and n are viscosity parameters. $\dot{\varepsilon}^{vp}$ is the viscoplastic strain rate and $\dot{p}$ is the cumulative plastic strain rate. The term rate-dependent implies that the yield strength, $\sigma_y = \sigma_y(\varepsilon^p, \dot{\varepsilon}^p, T)$. The effect of plastic strain rate, $\dot{\varepsilon}^p$, is essential to take care of viscous behaviour of material, which is generally more pronounced at high temperatures, specially in fusion and heat-affected zones. This may, in turn, affect the final residual stress state of test plate.

As already mentioned, a suction pressure of 1 bar is applied at the bottom surface of the test plate through an aluminium suction table to avoid out-of-plane distortions during welding and cooling; yet the in-plane distortions due to expansion and contraction of the test plate are not restricted which, in turn, give rise to friction at the interface of the test plate and the suction table. Moreover, the suction pressure may also reduce to certain extent due to the leakage at the fine rubber joint of the support and the test plate. The subsequent discussion is, therefore, developed from two perspectives:

a. Effect of various friction coefficient values on the out-of-plane displacements while keeping the suction pressure constant.
b. Effect of various pressure values, provided the friction coefficient is constant.

5.1. Out-of-plane Displacements

5.1.1. Effect of friction coefficient

From literary sources (Beardmore, 2007), the value of the friction coefficient between two aluminium surfaces could be approximated to 0.57 when one of the surfaces is moving while the other is static. To observe the effect of various coefficient values, a separate simulation was run while maintaining the pressure equals to 1 bar. The following values were used:

- Friction coefficient, μ = 0.4, 0.57, 0.8 and 1.0

Simulation results are compiled and compared with the experimental ones for out-of-plane displacements and are presented in Fig. 10. It is to be noted that, due to the symmetry of the test plate, only the results of the out-of plane displacements for the right half of test plate are shown. Moreover, all the displacements are set to zero at a distance of 5 mm from the center of the test plate. This is because the experimental results for displacement measures are not available in the fusion and heat-affected zones.

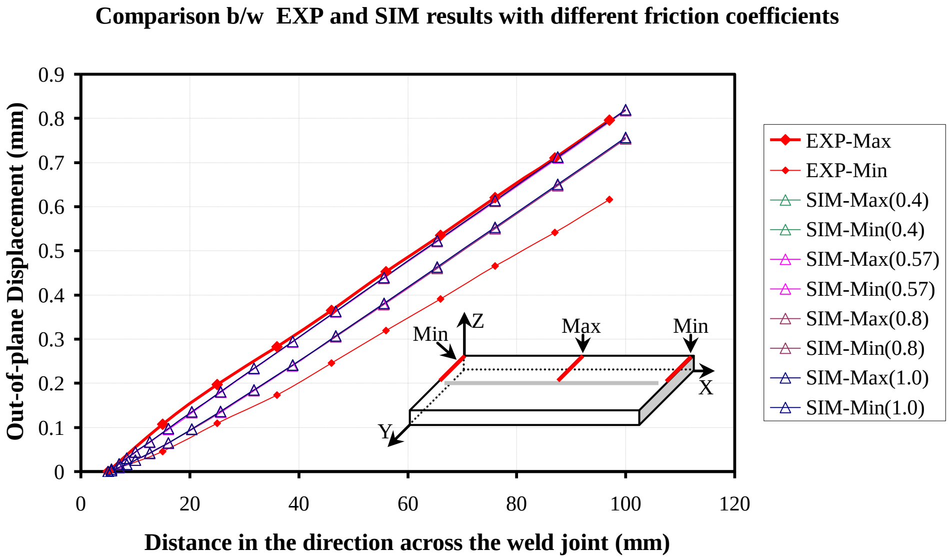

Fig 10. Maximum and minimum out-of-plane displacements for different friction coefficients; experiment vs simulation

It can be observed from Fig. 10 that in spite of using different friction coefficients, the simulation results for the out-of-plane displacements are least affected. The probable reason for this observation is that the mean contact pressure – of the order of 1 bar i.e. 0.1 MPa – and the surface shear stress during welding and cooling are too less to cause any significant effect over the final distortion level. The choice for the adequate value of the friction coefficient is, therefore, made at this stage and a value of 0.57 is taken as a standard; as the same is suggested in literary sources (Beardmore, 2007) for the case of a sliding-static interface which is actually the situation under discussion.

5.1.2. Effect of suction pressure

Having established the friction coefficient value of 0.57, the effect of various suction pressures is observed over the out-of-plane displacements. The possibility of leakage is present at the rubber joint, which provides seal between the test plate and the suction table. This means that the overall pressure present at the bottom surface of the test plate is less than 1 bar. Simulations are, therefore, run for the following pressure values to include the leakage effect:

- Pressure, p = 1 bar, 0.8 bar, 0.6 bar and 0.4 bar

Comparison of all these simulations and experimental results is presented in Fig. 11. It is found that despite the large variations in pressure values the effect over the out-of-plane displacement values is less. Nevertheless this effect is quite systematic; the lesser the pressure the larger the displacement. It can also be observed that the experimental results lie somewhere in between the simulation results at 1 bar and 0.8 bar. This means that in spite of leakage at the rubber joint the effective pressure value is more than 80% of the applied pressure. The locations for maximum and minimum displacement values on the test plate are also shown in Fig. 11.

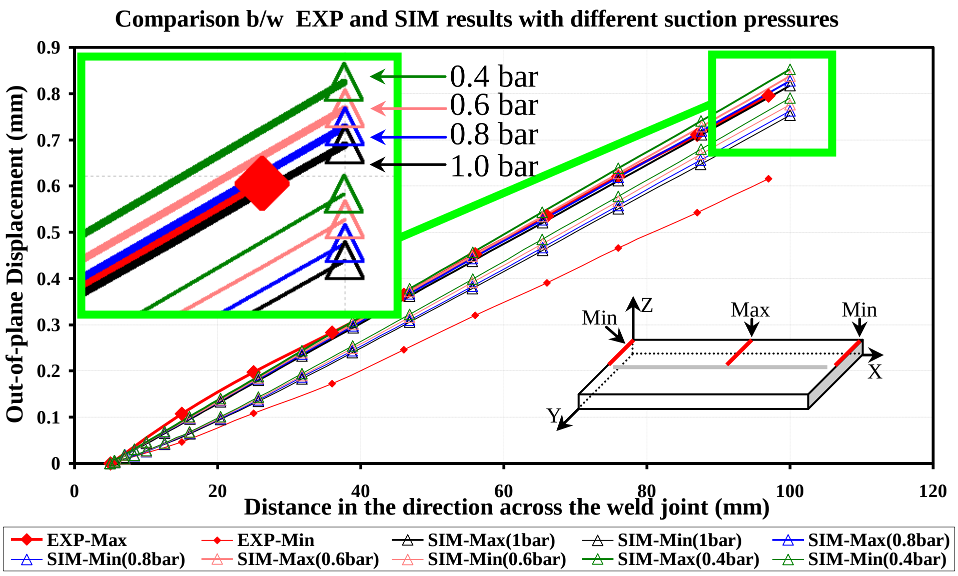

Fig 11. Maximum and minimum out-of-plane displacements at different pressures; experiment vs simulation

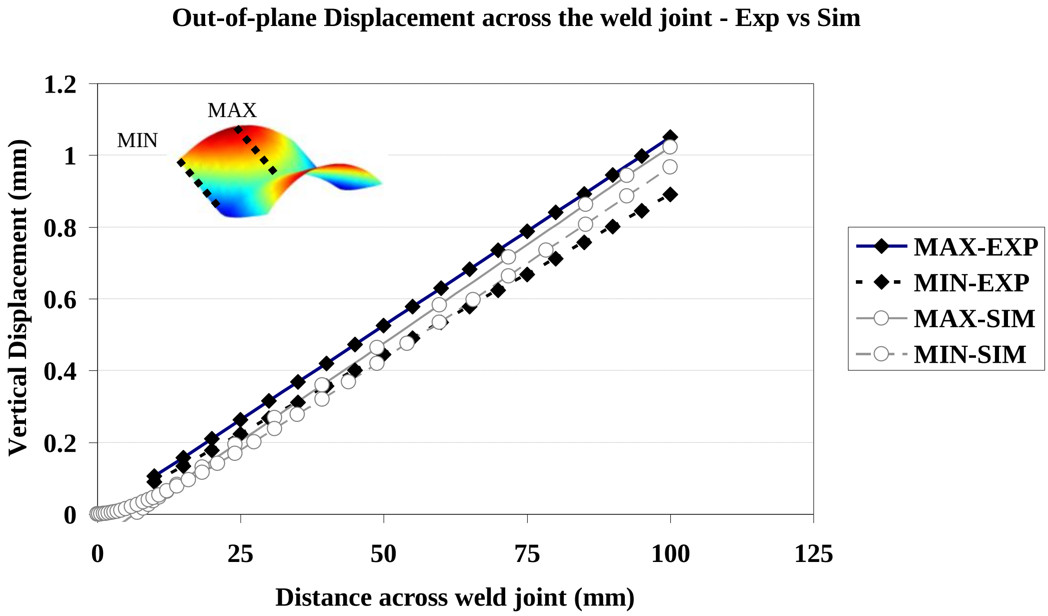

Fig 12. Maximum and minimum out-of-plane displacements; experiment vs simulation

These observations are, however, valid with respect to the maximum out-of-plane displacement values. The minimum out-of-plane displacement values recorded experimentally are considerably different from the ones found during simulation. The probable reason for this difference is the complex grooved and drilled shape of suction table. The suction is created through these grooves and drilled-holes and it is likely that the distribution of pressure at the bottom surface of the test plate during the experiment is non-uniform, while during simulation a constant pressure is assumed to be present over the entire bottom surface.

Subsequent comparison for out-of-plane displacements, U_z, with a suction pressure of 0.8 bar and a friction coefficient of 0.57 is shown in Fig. 12. A good agreement may be observed between experimental and simulated results. Displacement values are set to the scale of experimental values shown earlier in Fig. 3.

5.2. In-plane Displacements

The in-plane displacements, U_y, in the direction transverse to the fusion zone as measured with the image correlation technique are shown in comparison with the simulated values in the middle of the test plate in Fig. 13. A good correlation is observed on each side of the test plate. Due to the symmetric model of the test plate, the displacement values for the part 'not included' in the numerical model are taken as a mirror image of the values calculated in the meshed region with an opposite sign convention.

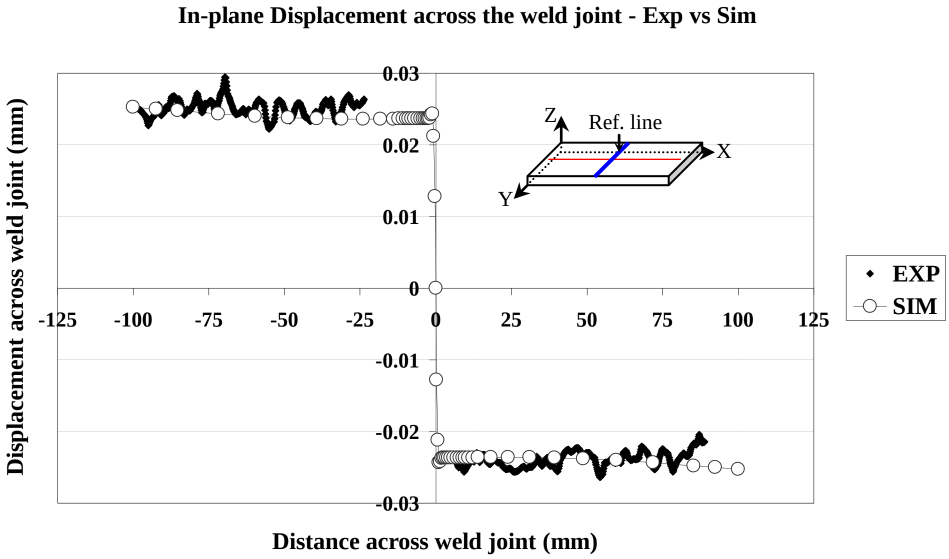

Fig 13. In-plane displacements; experiment vs simulation

5.3. Residual Stress Distribution

Welding is characterised by highly non-uniform temperature field and high heat input. The stresses induced during welding are, therefore, highly heterogeneous. In the molten weld pool the stresses are released and can be assumed to zero. However, the expansion of the fusion zone exerts compressive stresses on the regions immediately adjacent to it. Once the material starts to solidify shrinkage takes place in the weld zone, which then exerts stresses on the surrounding HAZ. These stresses reside in the material after welding and may result in unwanted distortions. The applied mechanical boundary conditions may further increase the level of stresses; however some of the stresses may be released by relaxing these boundary conditions at the end of welding. The self-balanced stresses remaining without any external load are known as residual stresses.

The 2 major components, viz. longitudinal and transverse stress, of the residual stress tensor for the case under study are presented in Fig. 14. The residual stress distribution profiles are presented for the upper surface of the test plate. It can be established from the residual stress profiles that the stresses in the direction of welding, σ_{xx}, will have the strongest influence over the distortion and/or failure of the material. These longitudinal residual stresses are largely tensile in nature. Three distinct regions are demarcated in Fig. 15 as fusion zone, HAZ and base metal. The graph is reproduced from the stress profiles of σ_{xx}, σ_{yy} and σ_{zz} on the upper surface and in the middle of the test plate lengthwise. It is to be noted that the distinction between HAZ and base metal is merely arbitrary and based on the assumption that base metal has zero level of stresses. Moreover, nodal stress values are presented in this graph, which are actually the values extrapolated from the stress values calculated at corresponding Gauss integration points.

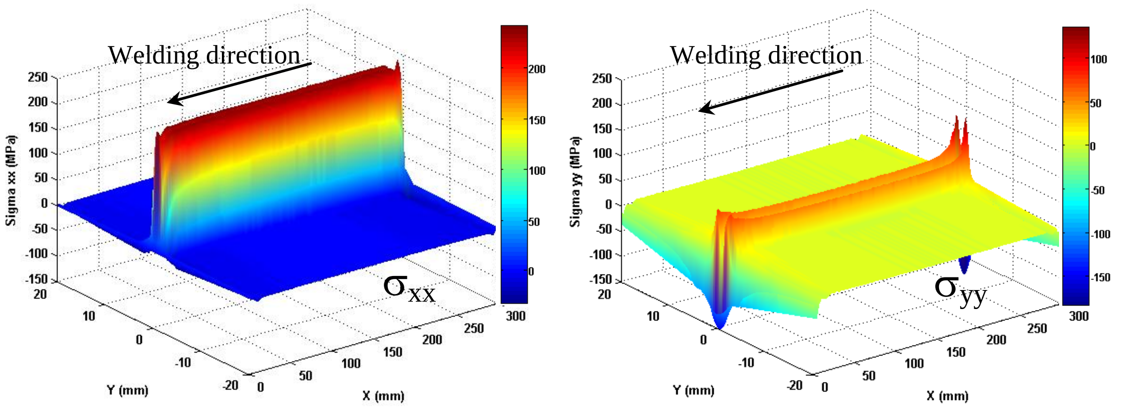

Fig 14. Longitudinal (left) and transverse (right) residual stress field on the upper surface of the test plate

The comparison between σ_{xx}, σ_{yy} and σ_{zz} is also presented in Fig. 15. It is observed that maximum stresses are present in the HAZ both in the case of longitudinal residual stresses σ_{xx} and transverse residual stresses σ_{yy}; the longitudinal stresses are, however, approximately 5 times more than the transverse ones. Moreover, the longitudinal stresses, σ_{xx}, are entirely tensile in nature; while the transverse stresses are compressive in the fusion zone and tensile in the HAZ. The through-thickness stresses, σ_{zz}, have insignificant magnitude, yet the non-zero value can be attributed to the approximations in interpolating the stress values from Gauss integration points to the surface nodes. Similarly, all the remaining stress components viz. σ_{xy}, σ_{xz} and σ_{yz}, being negligible in magnitude, will have least effect over the entire distortion of the test plate.

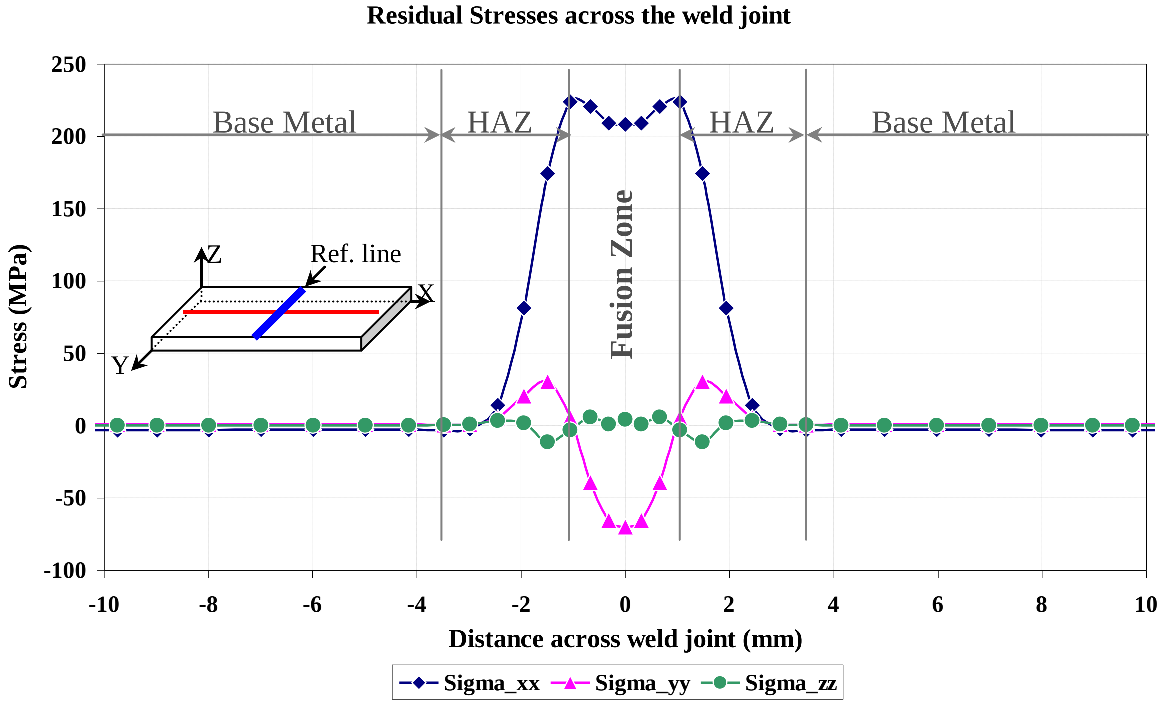

Fig 15. Residual Stresses σ_{xx}, σ_{yy} and σ_{zz} as a function of the distance from the weld line

6. Conclusion

An uncoupled thermo-mechanical analysis has been performed to predict the distortions and residual stresses for a single pass fusion welded thin test plate. A comparative study of experimental and simulation results has also been carried out. Following conclusions are inferred:

1. Comparison of weld pool geometry with simulated fusion zone (Fig. 7) justifies the heat source model with an upper hollow sphere and a subsurface cone, which are actually meant to achieve the required width and penetration of the fusion zone respectively. Likewise, the applied heat flux and thermal boundary conditions are well integrated so as to calculate the resultant temperature fields in close approximation to the experimentally recorded thermal histories (Fig. 8 and 9). A few discrepancies may be attributed to the simplifications assumed during simulation.
2. FE simulation results of mechanical analysis compared with experimental results for out-of-plane (Fig. 10, 11 and 12) and in-plane (Fig. 13) displacements are found in good agreement with each other, for a suction pressure of 0.8 bar and a friction coefficient of 0.57. This, in turn, establishes the reliability of the mechanical model, material properties, constitutive laws and mechanical boundary conditions. It is also noticed that the out-of-plane displacements are insensitive to change in friction coefficient; however, variation in suction pressure may impart a systematic change in their magnitude, yet the effect is little.
3. The longitudinal residual stresses, σ_{xx}, have values as high as the yield strength of the material. Compared to all other stress components, they will have considerable influence over the distortion level and failure of the material.
4. The transverse residual stresses, σ_{yy}, are around 20% of the yield strength in the fusion zone and are even lesser in the HAZ. Moreover, they are tensile in the HAZ and compressive in the fusion zone.

5. The through-thickness residual stresses, σ_{zz}, and other stress components namely σ_{xy}, σ_{xz} and σ_{yz} have negligible magnitudes and, hence, do not contribute significantly to the distortions.
6. Laser-beam welding with keyhole formation is characterised by a more pronounced dominance of the longitudinal residual stresses over the transverse residual stresses. In the present analysis the former is found 5 times higher than the latter.
7. Three dimensional elements with linear interpolation between the nodes are used both for thermal and mechanical analyses. Improvement in results may also be expected with quadratic interpolation between nodes for mechanical analysis.

ACKNOWLEDGMENTS

The author would like to acknowledge the financial support provided by EADS, AREVA-NP, EDF-SEPTEN, ESI Group and Rhône-Alpes Région through the research program INZAT4.

REFERENCES

[1] Sudnik, W., Radaj, D., Breitschwerdt, S., Eroeew, W., 2000. Numerical simulation of weld pool geometry in laser beam welding. J. of Physics D: Applied Physics, 33, 662-671.

[2] Jin, X., Li, L., Zhang, Y., 2003. A heat transfer model for deep penetration laser welding. Int. J. of Heat and Mass Transfer, 46, 15-22.

[3] Olmedo, M., 2004. Soudage laser en aluminium. PhD thesis, ENISE France.

[4] Ferro, P., Zambon, A., Bonollo, F., 2005. Investigation of electron-beam welding in wrought Inconel 706 – experimental and numerical analysis. Materials Science and Engineering A, 392, 94-105.

[5] Tsirkas, S.A., Papanikos, P., Kermanidis, Th., 2003. Numerical simulation of the laser welding process in butt-joint specimens. J. of Materials Processing Technology, 134, 59-69.

[6] Darcourt, C., Roelandt, J.-M., Rachik, M., Deloison, D., Journet, B., 2004. Thermomechanical analysis applied to the laser beam welding simulation of aeronautical structures. J. Physique IV, 120, 785-792.

[7] Josserand, E., Jullien, J.F., Nelias, D., Deloison, D., 2007. Numerical simulation of welding-induced distortions taking into account industrial clamping conditions. Mathematical Modelling of Weld Phenomena, 8, 1105-1124.

[8] Goldak, J., Chakravarti, A., Bibby, M., 1984. A new finite element model for welding heat sources. Metallurgical Transactions, 15B, 299-305.

[9] Lundback, A., Runnemalm, H., 2005. Validation of three-dimensional finite element model for electron beam welding of Inconel 718. Science and Technology of Welding & Joining, 10(6), 717-724(8).

[10] Beardmore, R., 2007. Tribology index, friction coefficients. On line available from: http://www.roymech.co.uk/Useful_Tables/Tribology/co_of_frict.htm (accessed 4 April 2007).

List of Figures

List of Tables